Advanced Anisotropic Hybrid Plasmonic Nano-emitters

Dandan Ge

To cite this version:

Dandan Ge. Advanced Anisotropic Hybrid Plasmonic Nano-emitters. Micro and nanotechnologies/Microelectronics. Université de Technologie de Troyes, 2021. English. NNT : 2021TROY0005 . tel-03808734

HAL Id: tel-03808734
https://theses.hal.science/tel-03808734v1

Submitted on 10 Oct 2022

HAL is a multi-disciplinary open access archive for the deposit and dissemination of scientific research documents, whether they are published or not. The documents may come from teaching and research institutions in France or abroad, or from public or private research centers.

L'archive ouverte pluridisciplinaire **HAL**, est destinée au dépôt et à la diffusion de documents scientifiques de niveau recherche, publiés ou non, émanant des établissements d'enseignement et de recherche français ou étrangers, des laboratoires publics ou privés.

Thèse
de doctorat
de l'UTT

Dandan GE

Advanced Anisotropic Hybrid Plasmonic Nano-emitters

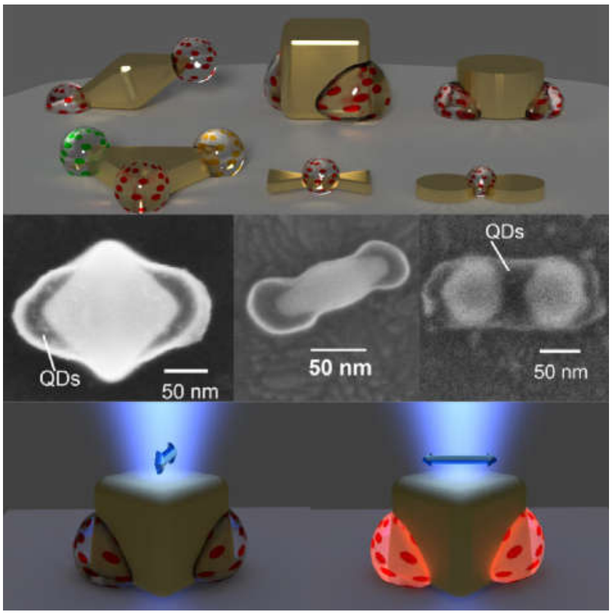

Champ disciplinaire :
Sciences pour l'Ingénieur

2021TROY0005

Année 2021

utt
UNIVERSITÉ DE TECHNOLOGIE
TROYES

THESE

pour l'obtention du grade de

DOCTEUR
de l'UNIVERSITE DE TECHNOLOGIE DE TROYES

en SCIENCES POUR L'INGENIEUR

Spécialité : MATERIAUX, MECANIQUE, OPTIQUE, NANOTECHNOLOGIE

présentée et soutenue par

Dandan GE

le 5 février 2021

Advanced Anisotropic Hybrid Plasmonic Nano-emitters

JURY

Mme C. FIORINI-DEBUISSCHERT	DIRECTRICE DE RECHERCHE CEA	Présidente
M. G. COLAS DES FRANCS	PROFESSEUR DES UNIVERSITES	Rapporteur
M. J. WENGER	DIRECTEUR DE RECHERCHE CNRS	Rapporteur
M. C. COUTEAU	PROFESSEUR ASSOCIE UTT	Examinateur
Mme V. KRACHMALNICOFF	CHARGEE DE RECHERCHE CNRS	Examinatrice
M. R. D. SCHALLER	PROFESSOR	Examinateur
M. R. BACHELOT	PROFESSEUR DES UNIVERSITES	Directeur de thèse

Personnalité invitée

M. T. XU	ASSOCIATE PROFESSOR

Acknowledgement

It is an unforgettable experience for me to complete this thesis in Laboratory Light, nanomaterials, nanotechnologies (L2n) at University of Technology of Troyes (UTT) with the funding from China Scholarship Council (CSC). Many people help me during this period.

First of all, I would like to express my sincerest thanks to Prof. Renaud BACHELOT for giving me this opportunity to work on this thesis under his supervision. He is a professional, knowledgeable, patient, and good guider. His encouragement always gives me the courage and strength to overcome any difficulty. His correct advices help me to do the experiment in the right way. His character, especially humor, is the best atmosphere modifier. I cherish every time to communicate and discuss with him, it is so proud for me to start research work under his guidance.

I would like to give my grateful thanks to Prof. Christophe COUTEAU, who gave me a lot of help during my experiments. His kindness and enthusiasm helped me through a difficult period. I want to thank him for his trust in me so that I can use his experimental equipment to complete my thesis work. His serious and responsible work attitude is worth learning.

I would like to thank prof. Safi JRADI, his genius ideas helped to develop the method for completing this thesis. His critical and valuable chemistry knowledge helped me in realizing two-photon polymerization.

Thanks to our colleagues Sylvie MARGUET, Jeremie BEAL. Thanks for providing some beautiful samples contributing to final good results. Thanks should also been given to Regis DETURCHE and Sergei KOSTCHEEV for their professional work that helped me in working with all the instruments in the lab.

I would like to thank Richard D SCHALLER from Argonne National Laboratory. He provided us perfect gold bipyramids and the discussion with him is helpful. Thanks to our collaborators Prof. Xiaowei SUN and Xuanquyen DINH who have provided different kinds of QDs.

I would like to give my thanks to the group members, Ali ISSA, Hongshi CHEN, Aurelie BROUSSIER and Xiaolun Xu. We help each other and grow together. I also want to thank my other colleagues, Ying PENG, Yingping ZHANG and Xuan Zhou, Bingbing WANG. Their help allows me to be familiar with the whole lab and carry out experiments quickly. I also want to thank all the other colleagues who helped me.

Before going to financial supports, I would like to give special thanks to my parents, my sister, and my boyfriend. Thank my parents for their love and their supporting. Thanks to my boyfriend Quan, he is not only my family, friend, colleague, but also a good listener. He also helped me a lot in my research work. Finally, I would like to thank CSC for funding my PhD study in France. The later work of this thesis also received financial support from the Planck Innovation.

Contents

NOMENCLATURE

AFM	Atomic force microscopy
APDM	azimuthally polarized doughnut mode
AuBP	Gold nanobipyramids
CCD	Charge Coupled Device
CTAB	cetyltrimethylammonium
EBL	Electron beam lithography
FDTD	Finite-difference time-domain
IPA	Isopropanol alcohol
ITO	Indium Tin Oxide
LDOS	Local density of optical states
LPRM	longitude plasmon resonance mode
LSP	localized surface plasmons
LSPR	Localized surface plasmonic resonance
MNP	Metal nanoparticles
NA	Numerical aperture
OPP	One-photon polymerization
PL	Photoluminescence
PMMA	Polymethylmethacrylate
QD	Quantum dot
RPDM	radially polarized doughnut mode
SEM	Scanning electron microscopy
SPP	Surface plasmon polariton
TEM	Transmission electron microscopy
TCSPC	Time-correlated single photon counting
TPA	Two-photon absorption
TPP	Two-photon polymerization
TPRM	transverse plasmon resonance mode

Introduction

Although the hybrid plasmonic nanosystems based on the interaction between quantum emitters and metallic nanostructures have been receiving much attention because of the possibility for developing controllable nanosources, controlling the relative position of nano-emitters and metal nanostructures remains challenging.

This thesis has aimed at developing anisotropic hybrid plasmonic nano-emitters *via* near-field two-photon polymerization that is triggered by localized field enhancement from surface plasmon supported by metal nanoparticles. By trapping the nano-emitters (QDs) inside the polymer or at its surface, distribution of the nano-emitter can be controlled accordingly by controlling the spatial distribution of the polymer in the vicinity of the metal nanostructures.

The manuscript consists of 5 chapters

In the first chapter, we introduce the basic theoretical principles used for describing a hybrid system that consists of metallic nanostructures and nano-emitters. Then, after a brief introduction to the development of hybrid systems, we review existing methods for constructing such hybrid systems. At the end of chapter 1, we introduce our method based on near-field two-photon polymerization.

In chapter 2, all experimental methods and techniques are introduced. Starting from the preparation of metal nanostructures, we describe the methods to deal with different kinds of metal nanostructures including gold nanocubes and gold bipyramids synthesized by chemical methods, as well as nanodisks manufactured by electron beam lithography. Then we describe the sample characterization methods including Atomic Force Microscopy and Scanning Electron microscopy. We also introduce the optical set-ups used for dark-field scattering measurement and photoluminescence analysis of single nanosystems: emission spectra, lifetime and second order autocorrelation function (g_2). Besides, we introduce the principles of the two-photon polymerization method used for fabricating the hybrid plasmonic nanosystems, including the preparation of the photosensitive formulation and the principles of 2-photon polymerization

In chapter 3, we present our results of the fabricated hybrid nano-emitters based on nanocubes and nanodisks. We study and compare the polarization sensitivity of emission from hybrid nano-emitters based on different exciting polarization modes and different shapes of particles. We proposed a concept of nanoscale spatial overlap between the active medium and the local excitation field to interpret the emission properties of the hybrid nano-emitters. We report also on a golf nano-cube based hybrid nano-emitter containing a single quantum dot, leading to the first polarization driven single photon switch

Chapter 4 deals with the use of our near-field two-photon polymerization method on gold bipyramids. After studying the 3D orientations of bipyramids using special focused azimuthal and radially polarized donut modes, we study the emission patterns from the hybrid bipyramid-based nanostructures with QDs inside the integrated polymer nanovolumes. We have observed some interesting phenomena, including special emission patterns and splitting emission spectra. We need more discussion and data to explain these phenomena.

In chapter 5, we describe some new works and perspectives that have not been finished. We share the preliminary observations with the readers. These uncompleted studies show promising potential involving polarization-driven multicolor nano light source, and coupled systems based on single QD and plasmonic bowties.

The manuscript ends up with a general conclusion summarizing the most important achievements and observations

Chapter 1 Nano-emitters based on composite plasmonic hybrid systems: context, principles, and state of the art

The fast development of computer industry makes the need for integrated optical paths is becoming more and more urgent. The challenge is to integrate optical elements on the same substrate in the form of a thin film. The goal is to achieve small size, low cost, stable performance, high efficiency, and low power consumption. This has driven plenty of research on nanophotonics. In particular, realization of effective and stable nanosources is one of the most important issue for integrated optics and nanophotonic. An important family of nanosources consists of hybrid plasmonic nanoemitters.

The hybrid plasmonic systems usually composed of metal nanostructures and nano-emitters provide a feasible solution for the development of integrated controllable nanosources. However, the lack of control of the nanoscale spatial distribution of the dye/QDs relative to the metal nanoparticles has always been a key issue. There are currently several methods for addressing the localization of emitters at strategic positions, such as those using DNA strands[1,2], AFM tips[3,4], or special etching methods[5], etc. The approach, based on near-field polymerization[6,7], proposed earlier by our team has the potential to control the position of QDs relative to the nanoparticles.

In this chapter, the development status of the plasmonic hybrid nano-emitters and the basic plasmon theory related to the subsequent chapters of this thesis will be introduced firstly. Following the introduction, interaction between plasmon and emitters will be discussed simply. As the most used emitter, the properties of quantum dots will also be briefly introduced. This chapter will also introduce the existing experimental implementation methods for constructing hybrid plasmonic nano-emitter systems, and briefly discuss their different advantage and drawbacks.

1.1 Introduction

Surface Plasmons are quasi-particles associated with a collective oscillation of electrons at a dielectric–metal interface. The ability of plasmonic structures to confine light field to volumes at the nanoscale offers attractive possibility to achieve strong enhancement of light-matter interactions and opens new potential applications such as biosensor[8–10], Photocatalysis[11,12], micro/nano photonic circuit[13–15] and molecular rulers[16,17]

Since the first discovery of plasmon-emitter interaction achieved when people found the enhanced absorption and emission of dye molecules adjacent metal films[18], it has become a fast growing research field. The ability of plasmons to confine electromagnetic field to subwavelength scale and get strong field enhancement contributes many relevant new phenomena when the presence of emitters is in the vicinity of plasmonic nanostructures. In general, two plasmon modes can be used for enhancing light-matter interaction: i) surface plasmon polariton (SPP) on metallic film or periodically metallic structures, ii) and the localized surface plasmons (LSP) associated with near-field enhancement on metallic nanoparticles.

Depending on the nature of the involved energy exchange, the interaction can be divided into two main states: weak coupling and strong coupling. The coupling strength depends on the characteristics of plasmonic nanostructures and emitters including the spectra overlapping between plasmon resonance and emitters' absorption and emission, the distance between emitters and plasmonic structures[19,20], and the size and shape of the metallic nanostructures. In the weak coupling regime, the plasmonic nanostructure acts as a nano-cavity that amplifies the local density of optical states (LDOS)[21] , resulting in an increase of the excitation rate, as well as an increase of the radiative and nonradiative decay rates *via* the Purcell effect[22]. Not only fluorescence enhancement but also fluorescence quenching[23,24] arising from nonradiative energy transfer have been observed in hybrid plasmon-emitters systems. During decades, there is a large number of experimental and theoretical studies of different fluorescence modification transiting from enhancement to quenching. For example, It has been reported on a large (up to 1000 times) increase in the relaxation rate of single quantum dots placed on rough metal film, which was mainly from nonradiative losses[25]. Plasmon-enhanced emission has also been used for improving the photoluminescence of quantum dot light-emitting diode (QLED) by a factor of four[26]. The Interaction between plasmons and emitters has been mainly investigated through localized surface plasmon resonances (LSPRs). Noble metal nanoparticles (MNPs), especially gold and silver nanoparticles, their LSPR depend strongly on the size and shape of the metal nanoparticles, exhibit unique and tunable optical properties in visible and Near Infrared (NIR) spectral ranges with relatively low damping As examples, silver spheres can enhance molecular fluorescence[27]. Single gold nanorod has been discovered to enhance the fluorescence of a weak emitter more than 1000-fold[28]. Strong polarization dependence of the MPNs' plasmon-enhanced localized near field distribution is beneficial to develop modulation photonic devices[29–32]. Due to the limited enhancement factor of localized field of the isolated single metallic nanoparticles, appropriate structural arrangement of metallic nanoparticles become the easiest way for improving this factor. Gap plasmons provided by the 'hot-spots' from two closed metallic nanoparticles[33–36], metal film coupled nanoparticle[37–40], or multi-particle aggregates[41] can significantly exceed the near field of individual nanoparticle resonators, and it has been applied in plasmon-mediated optical sensing applications such as surface-enhanced Raman scattering of molecules. It has been observed that the single-molecule' fluorescence can be increased 1340 times by Au bowties[35]. Kasey J. Russell and his group achieved radiative emission rate enhancements approaching 1,000 times using the gap plasmon mode between the silver nanowire and silver substrate[38]. Gleb M. Akselrod and his group showed that emitters in gap region of a film-coupled metal nanocube system can present a spontaneous emission rate enhancement over 1000 times[42]. Belacel and his group not only observed strong acceleration of spontaneous emission from QDs deposited on gold patch antenna but also observed the radiation pattern modification. The interaction strength in these weak coupling systems, which can be sometimes described by Purcell factors, largely depends on the geometrical parameters and fabrication technique, ranges from 4 to above 1000. Besides, Plasmon-induced resonance energy transfer (PIRET) of emitters can highly increase the efficiency of thin-film solar cells or photocatalysis[43].

Nearly twenty years ago, a new concept of plasmon laser called 'Spaser' (surface plasmon amplification by stimulated emission of radiation) was proposed theoretically[44,45]. Similar to a general laser, plasmonic nanostructures work as an optical cavity, and plasmon modes can provide feedback when the gain medium such as dye molecules and QDs can be pumped by the excited states of the plasmon. Spasers have been generated by many methods with the help of planar geometry supporting SPPs[46] and metallic nanostructures supporting LSPRs[47,48]. A wavelength tunable spaser was developed with narrow spectra linewidth using Au nanorods conjunct with different concentration of rhodamine 6G as gain medium[47]. The nanolaser without a pumping threshold was realizable by plasmon-based spasers with suitable gain medium concentration and plasmon cavity design. It was reported that the three-level spaser using triplet-state electrons has an emission spectral linewidth of about 3 nm, which will be quite useful as luminescent probes in many applications[49]. Since a spaser can act as a strong coherent radiative local source, this type of nanosystem has been an important research part in plasmon-emitters interactions.

When the coupling strength reaches the strong coupling regime, which is another special plasmon-emitter interaction, the modes of plasmon and emitters change essentially and generate new optical spectral modes presenting a Rabi splitting[50]. For cryogenic emitters[51,52] (laser-cooled atoms, vacancies in diamond, QDs), it is pretty easy to achieve strong coupling with plasmonic cavity because of low loss. On the other hand, strong coupling has been achieved in many kinds of emitters-plasmon coupled systems in room temperature[3,53,54]. Organic molecules coupled with periodic silver nanoparticle arrays demonstrated gradual evolution from weak coupling to strong coupling regime by increasing the molecules' concentration that is related to the effective molecular oscillation strength [55]. Strong coupling between J-aggregates and a single silver nanoprism has been leading to a Rabi splitting around 295 meV[54] . The single QD placed in the gap region of a single silver bowtie realized Rabi splitting as high as 120 meV[56]. With the fast development of nanofabrication technologies, for better photonic devices, the development of hybrid plasmon-emitters system seeks to decrease the size of the whole structure and enhance the interaction strength between plasmonic structures and emitters.

Finally, it should be mentioned that the tremendous development of quantum photonic has driven the research of single photon light-source during a few decades. Single-photo source plays an important role in quantum communication in many areas such as quantum metrology[57], quantum key distribution[58,59], quantum computing[60,61]. Coupling with plasmons can adjust and control emission properties of single-photon emitter, leading to controllable single-photon light sources. Both weak and strong coupling in single emitter/photon level have been studied.

Plasmon nanostructures help to enhance the capabilities of single photon sources including increasing the emission efficiency[62], emission directionality and collection efficiency [62–64].

The following sections remind the most important principles and achievements related to the context of the thesis.

1.2 Surface Plasmons

Surface Plasmons are collective coherent oscillations of free electrons at the metallic surfaces. From classical Drude model, there is a large number of free electrons inside the metal. When the incident electromagnetic wave strikes the metal, the conductive free electrons inside the metal are driven to shift relative to the lattice ions and form a collective charge oscillation. The oscillation is damped by collisions from the electrons bound around the nucleus and the positive ions on the metal lattice.

Assume the electrons start to oscillate with the time-dependent electromagnetic field represented as $E(t) = E_0 exp(-i\omega t)$. It is damped by collisions with a characteristic rate of Γ. Then the motion equation in this model is

$$m\ddot{\mathbf{x}} + m\Gamma\dot{\mathbf{x}} = -eE(t) \tag{1.1}$$

Here, m is the effective mass, e is the free electron charge. From classic Maxwell's equation, we can drive a solution from equation (1.1)as

$$\varepsilon(\omega) = \varepsilon_\infty - \frac{\omega_p^2}{\omega^2 + i\Gamma\omega} \tag{1.2}$$

Where ε_∞ is the high frequency limit of the dielectric constant and the ω_p is introduced as bulk plasmon frequency describing the natural oscillation frequency:

$$\omega_p^2 = \frac{Ne^2}{\varepsilon_0 m} \tag{1.3}$$

Here, ε_0 is the permittivity of vacuum. ω_p. In case of $\omega \ll \Gamma$, metals are mainly absorbing. And in case of $\gamma \leq \omega \leq \omega_p$, the free conduction electrons, the complex refractive index is predominantly imaginary, which mainly leads to reflection of the light. In the case of large frequencies, $\omega \gg \Gamma$, the damping part is negligible and $\varepsilon(\omega)$can be simplified to

$$\varepsilon(\omega) = 1 - \frac{\omega_p^2}{\omega^2} \tag{1.4}$$

In this case, when $\omega > \omega_p$, $\varepsilon(\omega)$ is a positive real permittivity, then metallic character is missing, and waves propagate without decay (metal transparency in the UV). But when $\omega < \omega_p$, $\varepsilon(\omega)$ is negative leading to an imaginary refractive index. There is no propagation of electro-magnetic waves in this situation. The plasma frequency ω_p is thus a frontier between metallic and dielectric behaviors.

For real metals, especially noble metal (e.g. Ag, Au), the Drude model becomes inaccurate for higher frequency because the interband transitions of the bound electrons excited by the photons with higher photonic energy are not considered by this model. In other to take into account this effect, the Drude model has to be supplemented by one or several Lorentz oscillations terms. In particular, the solution of the dielectric function can become[65,66]

$$\varepsilon(\omega) = \varepsilon_\infty - \frac{\omega_p^2}{\omega^2 + i\Gamma\omega} + \frac{f_1\omega_1^2}{\omega_1^2 - \omega^2 - i\omega\Gamma_1} \tag{1.5}$$

Where f_1 is the strength of the Lorentz oscillator with center frequency ω_1, Γ_1 is the damping relaxation rate related to the interband transition. All the damping gives limitation to the quality of the plasmon resonance and on the extent of the associated near- field enhancement and interaction with excitons.

1.2.1 Localized surface plasmon resonances

The above model is based on the plasma gas formed by free electrons in an ideal bulk metal. When we consider a space-constrained metal, the collective oscillation of electrons driven by the outside electromagnetic field is distributed on the surface of metal or the interface between metal and a dielectric medium, form a surface plasmon.

In the case of infinite half space metal, the oscillating electrons can interact, under specific conditions, with the incident electromagnetic wave and give rise to a maintaining surface wave propagating along the metal surface, which is called surface plasmon polariton (SPP). It is a transverse magnetic field, the charge oscillations are mainly orthogonal to the surface plane, and the induced evanescent electromagnetic field strength decays exponentially on both sides of the medium and metal.

In the case of metallic nanoparticles (MNPs), when an incident electromagnetic wave interacts with MNPs much smaller than the visible wavelengths, the oscillating electrons are confined in the three dimensions and localized surface plasmons (LSPs) get excited. A localized surface plasmon is a non-propagative wave, and the electromagnetic field can be confined in the three dimensions at the nanoscale. This enhanced near-field can be used to design highly sensitive biochemical sensors with specific plasmon resonances tailored by the nanoparticle geometry.

Because the size of MNPs is small compared to the wavelength, the electromagnetic field can penetrate into the entire metal nanoparticles and causes the redistribution of electrons, resulting in the displacement of the charges at both ends of the metal nanoparticles relative to the metal ion lattice. Negative charge will be accumulated in one side and positive charge in the opposite one, creating an electric dipole which produces a local recovery electric field opposite to the external electric field. The free electrons form a collective oscillation under the action of this recovery electric field with external electric field (Figure1.1), which allows for confining light much smaller than diffraction limitation.

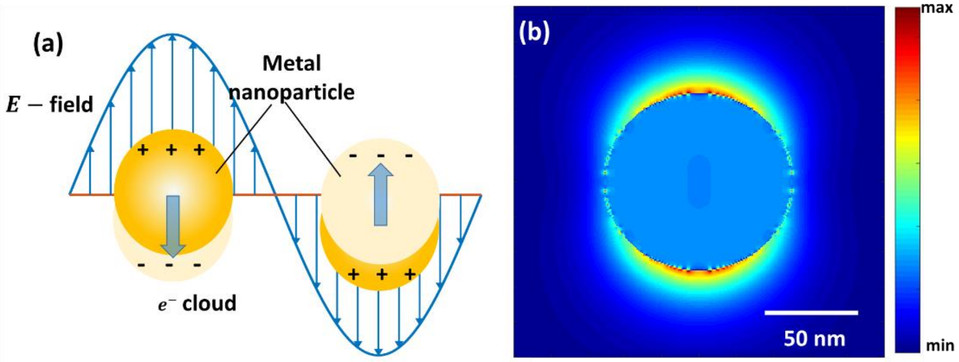

Figure 1.1 Schematic diagram of localized surface plasmon, shows the electron charge relative displacement in a metal nanoparticle. (b) Schematic diagram of localized field distribution of a metallic nanoparticle.

When the frequency of collective oscillation and the frequency of external excitation field are the same, resonance occurs, which is the localized surface plasmon resonance (LSPR). This resonance causes a significant enhancement of the local field around the MNPs that can easily exceed the exciting fields by a factor on the order of 10 or more. As it will be seen in section 1.5, section 3.1.2, and section 4.3 this field enhancement is the key property for our near-field polymerization, and it is commonly used for surface-enhanced Raman scattering (SERS)[33,67] and for modification of the local photonic density of states.

The LSP spectral resonance and the shape of the extinction spectrum is essentially dependent on the nanoparticle composition, size and shape as well as on the local dielectric environment[68,69]. In the case the resonance peak is within the visible region, due to the resonantly enhanced selective absorption and scattering, the nanoparticles show bright colors. For noble metals like gold and silver, it is easy to manipulate the LSPR peak of their nanoparticles fall in the visible and near-infrared bands.

1.2.2 Factors influencing the LSPR of Metal nanoparticles

In the previous section, we introduced the bulk plasmon frequency $\omega_p^2 = \frac{Ne^2}{\varepsilon_0 m}$, which is defined by the intrinsic property of metallic material. In order to understand the mechanism of LSPR in MNPs and analyze the influencing factors, let's firstly consider a metallic nanosphere whose size is even smaller than the penetration depth of the electromagnetic field. Then the electromagnetic phase can be considered as constant throughout the whole region. In that case, the quasi-static approximation[70]can be applied. Assume this metal nanosphere is in a uniform static electric field and the surrounding medium with dielectric constant ε_d. Then the spatial field distribution can be calculated from the Laplace equation describing the potential,

$$\nabla^2 \varphi = 0 \qquad (1.6)$$

φ represents the potential at any point in this electric field. In spherical coordinates, the Laplace equation can be represented as

$$\frac{1}{r^2 sin\theta}\left[sin\theta\partial_r(r^2\partial_r)+\partial_\theta(sin\theta\partial_\theta)+\frac{1}{sin\theta}\partial_\emptyset^2\right]\varphi(r,\theta,\emptyset)=0 \quad (1.7)$$

Considering the boundary condition, the solution of this equation was obtained as

$$\varphi_{in}=-\frac{3\varepsilon_d}{\varepsilon_m+2\varepsilon_d}E_0 rcos\theta \quad (1.8a)$$

$$\varphi_{out}=-E_0 rcos\theta+\frac{\varepsilon_m-\varepsilon_d}{\varepsilon_m+2\varepsilon_d}\frac{E_0R^3cos\theta}{r^2} \quad (1.8b)$$

φ_{in} and φ_{out} represent the potential inside and outside metal sphere. And $\varepsilon_m=\varepsilon_r+i\varepsilon_i$ is the dielectric permittivity of the sphere, same as ε_d, it is a function the excitation frequency. E_0 is the external electric field, r is the distance from the center of sphere, R is the radius of the sphere. Because the electric field can be calculated as $E=-\nabla\varphi$, from (1.8a), the near field can be represented as

$$E_{nf}=-\nabla\varphi_{in}=\frac{3\varepsilon_d}{\varepsilon_m+2\varepsilon_d}E_0 \quad (1.9)$$

Therefore, the near-field enhancement factor can be calculated as

$$EF=\frac{|E_{nf}|^2}{|E_0|^2}=|\frac{3\varepsilon_d}{\varepsilon_m+2\varepsilon_d}|^2 \quad (1.10)$$

The polarizability α introduced by external field in a small sphere using electrostatic approximation, can be written as：

$$\alpha=4\pi\varepsilon_0R^3\frac{\varepsilon_m-\varepsilon_d}{\varepsilon_m+2\varepsilon_d} \quad (1.11)$$

From equation (1.10), when $|\varepsilon_m+2\varepsilon_d|$ is minimum, resonance condition is satisfied and α becomes very large, leading to a maximum electric dipole moment and consequent maximum near-field enhancement and strongest absorption, scattering of incident light. It is also called the Fröhlich condition associated dipole surface plasmon of nanosphere.

- **Dielectric index of the surrounding environment**

Both resonance frequency and associated intensity of the LSP are known to be sensitive to the dielectric properties of the environment and in particular, to the refractive index of the matter surrounding the particle[71]. For example, if we increase the refractive index ε_d of the medium surrounding a gold nanocube with side length of 127 nm, its localized plasmon resonance peak gets red-shifted as shown in Figure 1.2. That was calculated using FDTD solution and the detailed calculation of this kind of cube can be seen in section 3.1.1.

The LSPR of each metal particle is highly sensitive to even a small change in surrounding refractive index and that the shape of nanoparticle affects the sensitivity[72]. The sensitivity of peak wavelength in the measured extinction spectrum or scattering spectrum to environmental changes in the nanometer range around it can be used to develop high spatial resolution biosensor.

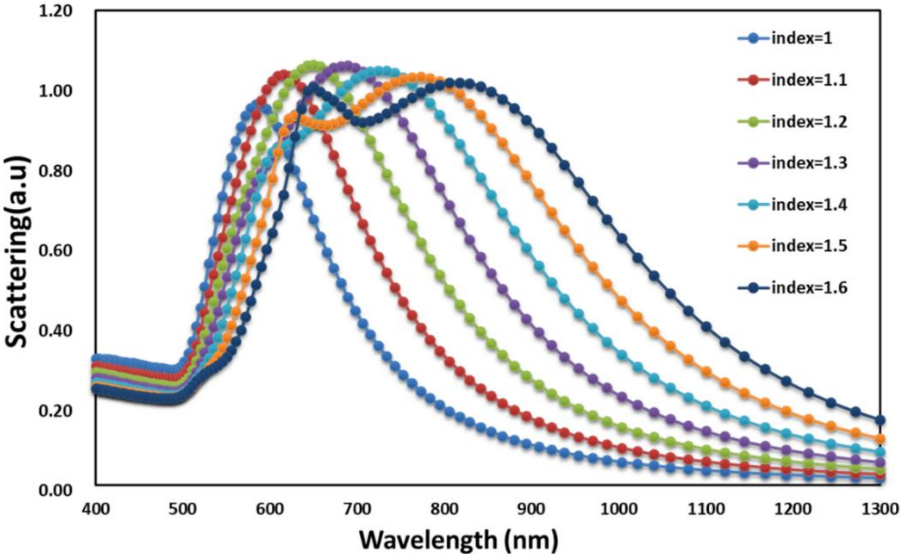

Figure 1.2 The scattering spectra of single gold nanocube (side length=127 nm) in a dielectric medium with different refractive indexes, as calculated by finite-difference time-domain (FDTD).

◆ Size of particle

From the quasi-static limitation, the corresponding scattering and absorption extinction cross sections can be expressed as a function of the ratio R/λ,

$$C_{scat} = \frac{k_0^4}{6\pi}|\alpha|^2 \propto \frac{R^6}{\lambda^4} \tag{1.12a}$$

$$C_{abs} = k_0 Im(\alpha) \propto \frac{R^3}{\lambda} \tag{1.12b}$$

Here k_0 is the wavenumber in vacuum. Therefore, one can find that when the size of particle is small, absorption dominates in the extinction spectrum. On the contrary, when the size become larger, scattering dominates. But it is also clear, for metal particles whose particle size is much smaller than the incident wavelength (for example, 25 nm Au sphere illuminated in the visible), the LSPR peak depends mainly on the dielectric constant of the particles and medium and it poorly changes with the size.

For larger nanoparticles, whose size are compared to incident wavelength (typically larger than 50 nm), multipolar plasmon oscillation can occurs. In that case, Mie theory[73] replaces the quasi-static approximation that is no longer appropriate and is used to solve this problem. The dispersion relation of multipolar modes of local surface plasmon resonance is

$$\frac{\varepsilon_m(\omega)}{\varepsilon_d} + \frac{l+1}{l} = 0, l = 1,2,3 \dots \qquad (1.13)$$

l is the order of multipole. Substitute the relation of $\varepsilon(\omega) = 1 - \frac{\omega_p^2}{\omega^2}$ to Equation (1.13), the multipolar resonance can be calculated as

$$\varepsilon_m(\omega_l) = \omega_p [\frac{1}{\varepsilon_d\left(1+\frac{1}{l}\right)+1}]^{\frac{1}{2}} \qquad (1.14)$$

In case of l=1, the dipolar mode dominates, and when the size of particle increases, the contribution of the multipole modes increases, the corresponding plasmon resonance peaks get red shifted to longer wavelengths and the spectrum get broader. When $l \rightarrow \infty$, the situation becomes similar to the delocalized SPR, that is, the large sphere can be regarded as a smooth infinite metal plane.

◆ Shape

The spatial extent of the LSP fields is strongly dominated by the geometry of the metallic nanostructures rather than by the wavelength of the light. Since the restoring force for SP is related to the charge accumulated at the particle surface, it will be influenced by the particle geometry. If the particle size is much smaller than the incident light wavelength, according to the quasi-static approximation theory, for any shape of metal nanoparticles, the extinction cross-section C_{ext} can be expressed as

$$C_{ext} = 4\pi k Im(\alpha) \tag{1.15}$$

where $k = \sqrt{\varepsilon_d}\omega/c$. According to dipole theory, the polarizability of nanoparticles of any shape can be expressed as[74]:

$$\alpha = \frac{3V}{4\pi}\frac{\varepsilon_m - \varepsilon_d}{\varepsilon_m + L(\varepsilon_m - \varepsilon_d)} \tag{1.16}$$

L is a quantity that represents the shape, V is the volume of the MNPs. Combined with Drude model, an equation of LSPR frequency can calculated as

$$\omega_0^2\left(1 + \frac{1-L}{L}\varepsilon_d\right)^2 = \frac{\omega_p^4}{\omega_0^2} \tag{1.17}$$

Hence, for the same material of the MNPs and same dielectric environment, the resonance wavelength in is only dependent on shape. Figure 1.3 shows an example of three different gold nanoparticles and their absorption spectra[68].

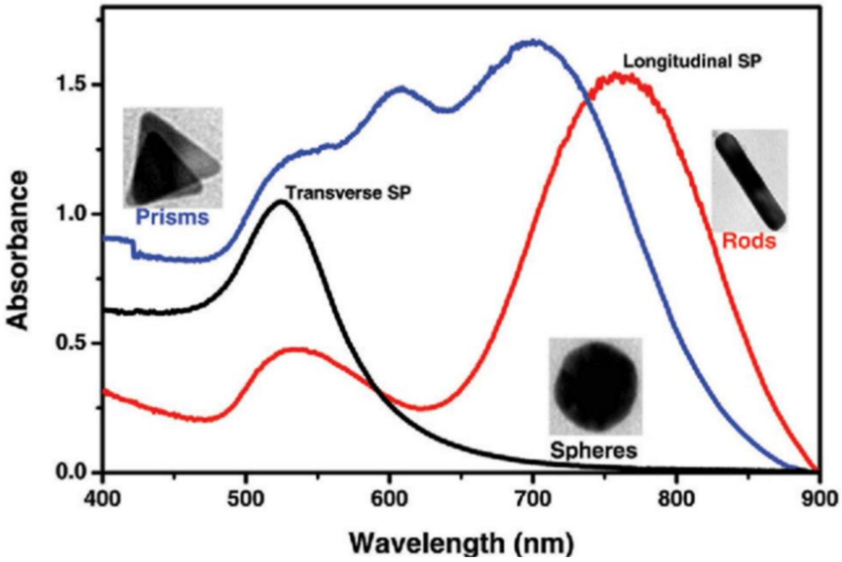

Figure 1.3 Typical absorption spectra of gold nanoparticles with different shapes[68].

In recent years, various numerical methods have been successively proposed for numerically describing the interaction between light and metal particles of arbitrary shapes and to simulate the optical properties of the particles, especially their LSPR and near-field properties. For example, let's cite the discrete dipole approximation (DDA) method and the finite-difference time-domain (FDTD) method which are the most mature two methods. The more complex the metal structure is, the more resonance peaks will appear, and the maximum near-field strength is distributed on the surface and tip because of electrons accumulation.

◆ **Quality factor of plasmonic resonance**

At the resonance frequency ω_{Lsp}, the metallic nanoparticle confines the electric field to its surface leading to a largely enhanced electric field, effectively turning the particle into a "cavity" or a resonator. However, for nanostructures, the damping including radiative and ohmic losses, strongly affects the spectral position and broadens the linewidth of the plasmonic resonances[75].

From Equation (1.12a) and (1.15), the dipolar response can be described by the scattering efficiency, proportional to the polarizability $|\alpha|^2$,

$$C_{scat} \propto \frac{1}{(\omega-\omega_1)^2+({}^{\Gamma_1}/_{2})^2} \tag{1.18}$$

The damping rate Γ_1 in Equation (1.18)[76], indicates loss in particles determines the width of the resonance. Here, an important parameter which is called quality factor Q is intrinsically linked to the ratio of energy stored to the energy lost by an oscillator, can be estimated as $\mathrm{Q} = \lambda_{Lsp}/\Delta\lambda$ (λ_{Lsp} is the resonance wavelength, and $\Delta\lambda$ is the width of the resonance)[75]. The Q factor of a metal nanosphere decreases with the particle size[77].

Plasmonic Nanoparticles are not ideal resonators as they exhibit high ohmic losses, particularly in optical wavelengths. For plasmonic application, such as nanosensing, nanolabeling, or surface-enhanced fluorescence and Raman spectroscopies, the key point is to realize low loss or high-quality factor resonances, especially for the metal-emitter coupling hybrid system.

1.2.3 Gap plasmon in dimer geometry

As we said in section 1.1 when localized surface plasmon resonance of a nanoparticle happens, the electromagnetic near-field of the nanoparticle get spatially enhanced and confined the to its surface and sharp corners, resulting in a so-called "hot-spots". Hot-spots play a crucial role for various applications of surface plasmons. The enhancement factor of a single MNP is subject to its own shape and size characteristics.

When the NPs are adjacent to each other, the interaction between the multi-particles create new plasmon resonance hybrid modes and lead to complex spectral responses resulting from the coupling between the individual LSPR of single particles. The localization field in the region of gap is caused by the suppression of scattering into the far-field via excitation of plasmon mode along the chain direction. The localized field within the gap is greatly enhanced leading a strong 'hot-spots', whose intensity is much higher than it would be for a single particle. In addition, this coupling contributes to high intensity-to-mode volume ratio, boosting the coupling between plasmons and emitters that would be located within the gap. Figure 1.4 shows an example of the near-field amplitudes of a single gold sphere and its dimer with a gap of 10 nm, where the maximum intensity in the gap of dimer is more than 10 times larger than the localized field intensity of single sphere[78].

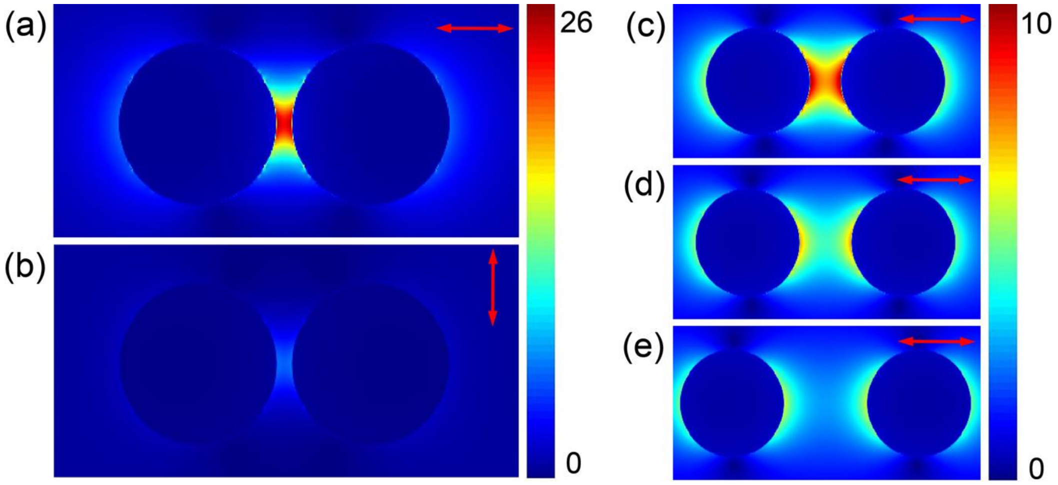

Figure 1.4 Near-field magnitude (|E|, λ = 800 nm) of a gold nanosphere dimer structure with incident polarization[78] *(a) parallel and (b) perpendicular to the interparticle axis and a 10 nm gap, (c–f) parallel to the interparticle axis and a gap of (c) 30 nm, (d) 50 nm, and (e) 80 nm, respectively. Arrows indicate incident light polarizations.*

In particular, the resonant modes of the dimer system consisting of two metallic particles separated by a narrow gap can be analyzed by bonding/anti-bonding state from the coupling of two dipoles, which is in a similar fashion to atomic orbital hybridization[79]. The bonding resonance is most important in this framework: it concentrates the field distribution at the gap and result in a red-shifted resonance peak. Besides, the gap plasmon mode has significant sensitivity to some key parameters such as distance between the NPs, geometry, and light polarization.

1.3 Hybrid plasmon-emitter system

The ability of surface plasmons to spatially squeeze light to nanoscale dimensions results in a strong field enhancement. The intense local field subsequently enhances the interaction between plasmon and nano-emitters that is beneficial for many applications[23,80–83]. In this section, theoretical description of a hybrid system comprising plasmonic nanostructures and nano-emitters will be briefly overviewed.

1.3.1 Interaction between plasmons and emitters

The light-matter interaction[84] can take several forms:

- ✓ fluorescence enhancement/quenching and lifetime modification of emitter
- ✓ strong energy-transfer between emitters and metal nanostructure, leading to the Rabi-splitting of the emission spectrum[56],
- ✓ electromagnetic-induced transparency[85],
- ✓ spaser effect[47,86–88],
- ✓ narrowing of the linewidth of spontaneous emission[89].
- ✓ Etc...

The interaction between plasmon and nano-emitters can be described by the coupling strength[53,90,91]

$$\mathbf{g} \propto \boldsymbol{\mu} \cdot \sqrt{N/V_{eff}} \tag{1.19}$$

$\boldsymbol{\mu}$ is emitter's transition dipole moment, N is the number of emitters coherently coupled to plasmonic cavity, V_{eff} is the corresponding effective mode volume. In particular, the optical coupling between two oscillators (whatever they are: molecules, plasmons) can be divided to weak-coupling regime and strong-coupling regime depending on the coupling strength. The surface-plasmon enhanced fluorescence and Raman scattering both are in the former regime. The interaction between emitters and metal nanostructures is dependent on both the properties of metal nanostructures and the nature of the emitters.

- ◆ **Weak coupling regime**

Emission results from the relaxation of a molecule from the excited state to the ground state. From quantum mechanical treatment, there are actually two possible processes. In the presence of incident photons, excited high-energy electrons are stimulated by incident photon, and jump to low energy levels, releasing one photon that is identical to the incident photon (The frequency is the same as the frequency of external exposure light). Here the number of emitted photons is directly proportional to the number of incident photons. This effect corresponds to the stimulated emission. In the case of the other process, which is called spontaneous emission, after excitation (whatever the pumping process) the photons are emitted in the absence of any incident photons and it is a stochastic process.

The excited electrons at high states can go back to ground state by emitting photons or other energy conversion process. The relaxation process from high energy level to low energy level can be divided into radiative transition and nonradiative transition depending on whether there is photon emission. The Jablonski diagram[92] shown in Figure 1.5 illustrates the electronic states of a molecule and the transitions between them. Fluorescence is a two-step process consisting in the absorption of a photon, followed by spontaneous emission a spontaneous emission. Phosphorescence is another related type of luminescence. In this case, the excited state is a triplet state that is different from the singlet-excited state of fluorescence.

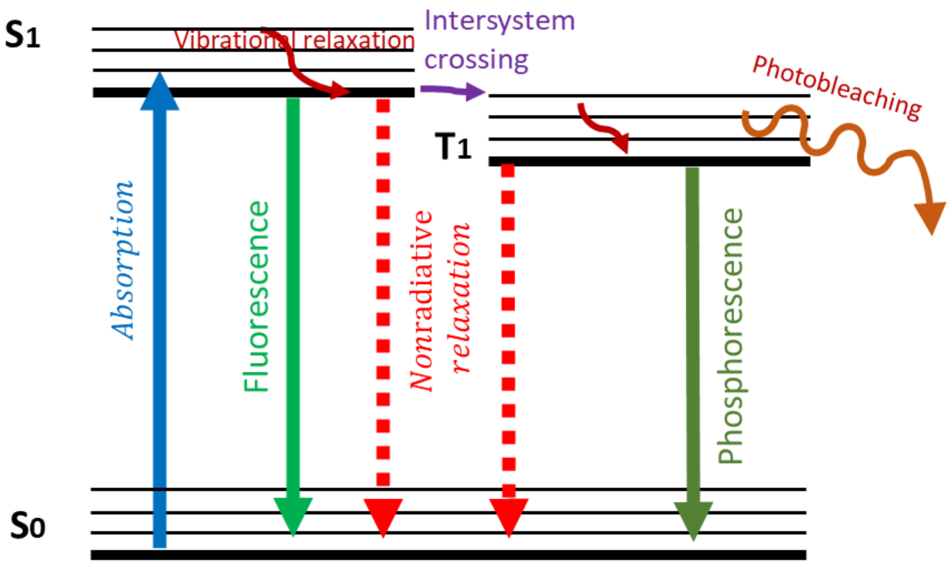

Figure 1.5 Simplified Jablonski diagram presenting the major radiative and nonradiative processes[92]

In general, after absorption a photon, the electron is excited to high vibrational state of S1, and it relaxes, quickly returning to the lowest energy state of S_1 by vibration relaxing. Then it can go back to ground state of S_0 directly and radiate fluorescence spontaneously or by other nonradiative transition processes. The fluorescence process is characterized probability of decay per time unit, called radiative decay rate γ_{rad}. For all nonradiative transitions, for example, internal conversion or quenching, they can be described by a single nonradiative decay rate γ_{nr}. Then the total decay rate that includes all the relaxation channels of relaxing from S_1 to S_0 can be presented as

$$\gamma_{tot} = \gamma_{rad} + \gamma_{nr} \tag{1.20}$$

Because the total relaxation is a random selection process, and radiative decay and nonradiative decay are two competing channels. The fluorescence lifetime refers to the statistical average time that fluorescent molecules stay in the excited state before returning to the ground state and can also be represented as the time required for the fluorescence intensity to decrease from the strongest intensity I_{max} to the intensity of $\frac{I_{max}}{e}$. $\tau_{tot} = \gamma_{tot}^{-1}$ presents the excited state lifetime, and $\tau_{rad} = \gamma_{rad}^{-1}$ is the radiative lifetime which cannot be measured directly. Fluorescence quantum yield Y is defined as the ratio of radiative decay rate to total decay rate,

$$Y_0 = \frac{\gamma_{rad}^0}{\gamma_{rad}^0 + \gamma_{nr}^0} \tag{1.21}$$

Y_0 represents the intrinsic quantum yield of the fluorophore in free space, symbol '0' indicate the situation of free space. It is a fundamental parameter used to describe the fluorescence efficiency of a given fluorophore. In our case, mostly for semiconducting quantum dots, they have a high quantum yield $\mathrm{Y}_0 \approx 1$. It should be stressed that the quantum yield is the probability of light emission once the nano-emitter gets excited. Therefore, the probability of excitation has to be considered too. For excitation below saturation, the emission (fluorescence) rate γ_{em} is a two-step process as what we show in Figure 1.5 which involves the excitation rate γ_{ex}. Then the emission probability can be represented as[24,93]

$$\gamma_{em} = \gamma_{ex} \cdot Y \tag{1.22}$$

The excitation rate, according to Fermi's gold rule[94], is given by

$$\gamma_{ex} = \frac{2\pi}{\hbar} |\langle S_0 | \boldsymbol{E}(\boldsymbol{r},\omega) \cdot \boldsymbol{p} | S_1 \rangle|^2 \rho(E_{S_1}) \tag{1.23}$$

$\boldsymbol{p}$ is the transition dipole moment, $\langle S_0 \, | \boldsymbol{E}(\boldsymbol{r},\omega) \cdot \boldsymbol{p} | \, S_1 \rangle$ represents state transition from S_0 to S_1, $\boldsymbol{E}(\boldsymbol{r},\omega)$ is the local field, $\rho(E_{S_1})$ is the excited state density. Hence, $\gamma_{ex} \propto |\, \boldsymbol{E}(\boldsymbol{r},\omega) \cdot \boldsymbol{p}|^2$, that means excitation rate depending on the local excitation field. In case of CdSe/ZnS QDs, because of their isotropic excitation transition dipole moment, $\boldsymbol{p}$ become a constant, QDs' excitation rate $\gamma_{ex} \propto |\, \boldsymbol{E}(\boldsymbol{r},\omega)|^2$, only associated to local field[95].

Besides, it should be pointed out that most dyes such as Eosin Y, under relatively strong resonant excitation, tend to photo-bleach, which is a type of nonradiative decay will stop fluorescence in a more and less definitive way. For an excited electron in S_1, there is small probability compared to total decay rate for transition to a triplet state T_1 by intersystem crossing. In addition, the triplet state T_1 is highly chemically reactive, especially in oxygen environment. That is why for a fluorophore, its stability is also important for our hybrid system.

The fluorescence of a nano-emitter like QDs depends on both the properties of the emitter itself and the interaction with its environment. When a nano-emitter is located close enough to a metallic nanostructure, because of LSPR, the local field change, which directly affects the excitation rate and thus influences the emission properties. In addition, the radiative and nonradiative decay rates can be modified, both in amplitude and angular dependence, which induce a change of fluorescence lifetime and quantum yield, in particular via the LDOS of the metal nanostructures which acts as possible channels of deesexcition of the emitters. In general, the interplay between MNPs and emitters lead to two major direct phenomena: one is the fluorescence enhancement[93], and the other one is the fluorescence quenching[96]. These two different phenomena depend, in particular, on the original spontaneous property of the fluorophore itself, the distance between the metal nanoparticles and the emitters and the relative polarization direction of the dipole emitter.

The fluorescence enhancement effect in the presence of the metal nanostructure mainly results from two contributions: improvement of the excitation efficiency and emission rate modification (Purcell effect)[97]. Besides, excitation wavelength should be also taken into account[98]. Lastly, at the maximum fluorescence enhancement where the fluorescence excitation rate and radiative decay rate have already been well balanced, far-field fluorescence collection methods should also be considered.

The first mechanism is related the local field enhancement generated near metallic structures. From Equation (1.23), we derived that $\gamma_{ex} \propto |\boldsymbol{E}(\boldsymbol{r},\omega) \cdot \boldsymbol{p}|^2$, excitation rate directly relates to the local near-field intensity. In the presence of MNPs, plasmon generated by the regular movement of free electrons of metal particles under the action of external electromagnetic fields can greatly enhance the electromagnetic field around the particles, when the excitation light wavelength overlaps with the extinction spectrum of the MNPs. In case the frequency of the incident light is consistent with the LSPR frequency, LSPR occurs, and a maximum near-field enhancement factor F is reached.

$$\frac{\gamma_{em}}{\gamma_{em}^{0}} = \frac{\gamma_{ex}}{\gamma_{ex}^{0}} \cdot \frac{Y}{Y_0} = \frac{|\boldsymbol{E}(\boldsymbol{r},\omega)|^2}{|\,\boldsymbol{E_0}(\boldsymbol{r},\omega)|^2 \cdot} \frac{Y}{Y_0} = EF \cdot \frac{Y}{Y_0} \qquad (1.24)$$

Moreover, the enhanced localized near-field intensity directly contributes to improvement of excitation rate, resulting to the fluorescence enhancement.

The other contribute is the increase in the radiative emission rate, which is caused by the increased local densities of photonic states (LDOS) around MNPs[21,90,99]. LDOS quantifies the number of states available to an emitter. A physical picture generally used is that the LDOS of the metal nanostructure acts as channels of deexcitation of the nano-emitters' excited states, resulting in an increase of the deexcitation rate and a decrease of lifetime. In free space situation, in absence of MNPs, the total decay rate from excited state to ground state is $\gamma_{tot}^0 = \gamma_{rad}^0 + \gamma_{nr}^0$, where γ_{rad}^0 and γ_{nr}^0 represent intrinsic radiative decay rate and nonradiative decay rate of the emitter.

In the presence of MNPs, in addition to the intrinsic nonradiative decay, there is another nonradiative decay from energy transfer contributed by the fluorophore molecules in excited states into the MNPs. We use γ_{mnr} to denote this nonradiative decay part. Besides, electromagnetic coupling occurs between the emitter and the nanoparticle plasmon, causing an increase in the radiative decay rate γ_{rad} of the molecule at the emission wavelength via a Purcell factor[81,97] F_p: $\gamma_{rad} = F_p \cdot \gamma_{rad}^0$. The nonradiative decay γ_{nr}^0 accounting for instinct nonradiative losses inside the molecule only is independent to the presence of MNPs. Now the lifetime is

$$\tau = \frac{1}{\gamma_{rad} + \gamma_{nr}^0 + \gamma_{mnr}} \tag{1.25}$$

A decreased lifetime of fluorescence occurs. The modified quantum yield become:

$$Y = \frac{\gamma_{rad}}{\gamma_{rad} + \gamma_{nr}^0 + \gamma_{mnr}} = \frac{F_p}{F_p + \frac{1 - Y_0}{Y_0} + \frac{\gamma_{mnr}}{\gamma_{rad}^0}} \tag{1.26}$$

The Purcell factor defined as the ratio of the increased emission rate of emitter in cavity (a MNP can regarded as a nanocavity) compared to its emission rate in free space. For a dipole emitter on resonance, located at the maximum of the optical field and aligned with the polarization of the field, the Purcell factor is proportional to the ratio between quality factor and effective mode volume of the plasmon mode[100,91,101] $F_p \propto \mathrm{Q}/\mathrm{V}_{eff}$ (Q is the quality factor and $\mathrm{V}_{\mathrm{eff}}$ is the mode volume). According to equation (1.25), the increased radiative decay rate can also contribute to fluorescence enhancement. However, take the induced γ_{mnr} consideration, the energy transfer rate between emitter and MNPs, which is equivalent to the conventional photobleaching mechanism in pure fluorophore, opens another channel of nonradiative decay and will cause fluorescence quenching. The result is the compromise of the two effects that lead to enhancement and quenching.

For larger distance from molecule to metal surface, the interaction between them can be ignored, then we have $\gamma_{mnr} \to 0$ and $F_p \to 0, Y \to Y_0$. In case of some QDs, the original quantum yield $Y_0 \approx 1$, then $Y = \frac{\gamma_{rad}}{\gamma_{rad}+\gamma_{mnr}}$, the energy transfer between molecule and plasmon dominate the whole nonradiative decay that is all most negligeable. In the very near-field, fluorophore is at very close proximity (< 5 nm) or through direct contact with the surface of metals, in which the main mechanism is nonradiative energy transfer from excited state to the metal and thus kept from emitting the photon, leading to fluorescence quenching.

It is complicated to investigate how the radiative decay rate, lifetime and the quantum yield change. In general, the calculation model simplifies the combined system of emitter and MNPs into single dipole emitter and a regular metal nanosphere. The Multipole (MMP)[19] method and the dipole approximation method have been used for calculating both the decay rate and the quantum yield for different particle-emitter configurations. Pascal Anger et al. theoretically calculated the fluorescence rate of a single molecule as a function of its distance between a gold nanosphere[23], shown in Figure 1.6 (from ref 22).

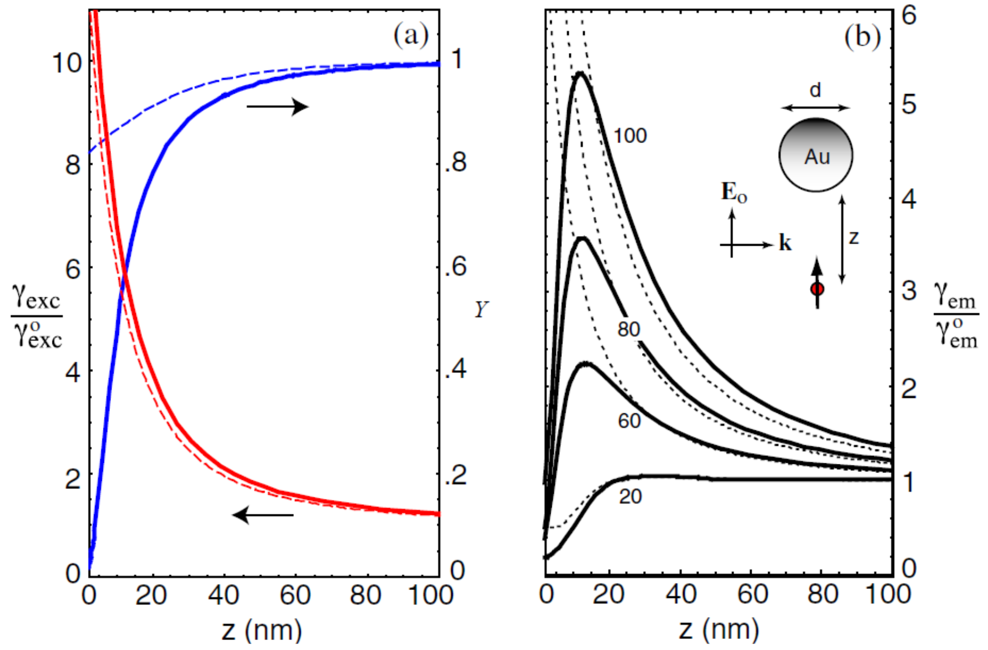

Figure 1.6 Theoretical calculated quantum yield Y, excitation rate γ_{ex}, and fluorescence rate γ_{em} as a function of molecule-particle separation z. The solid curves are the result of MMP calculations, and the dashed curves correspond to the dipole approximation which fails for short distances z. In (a) the particle diameter is 80 nm and in (b) different diameters of Au nanosphere (20,60,80,100 nm)[23].

The weak interaction between emitters and metal nanostructures makes it possible to modify the emission behavior not only the intensity, but also the emission spectrum[102], directivity properties[103], polarization and the angular emission pattern[104]. The mentioned Purcell factor is a parameter used to quantify the spontaneous emission, which scales as the inverse of the electromagnetic confinement volume provided by the plasmonic structure.

◆ Strong coupling regime

For weak coupling, there is not reversible energy transfer, while strong coupling is a two-direction energy exchange between emitter and plasmon leading to a mixed light-matter states where it no longer possible to make the difference between the two entities forming the coupled system. For emitters in a plasmonic cavity, only when the interaction rate exceeds the cavity loss rate and the total emitter decay rate, strong coupling appears. The Jaynes-Cummings (JC) system describing the interaction between plasmon modes from optical cavity and a two-level quantum emitter[105] is the simplest model used for analyzing the plasmon-emitter interactions, especially in strong coupling regime. Figure 1.7 shows a simple illustration of strong coupling occurred between a two-level exciton and a metal nanoparticle.

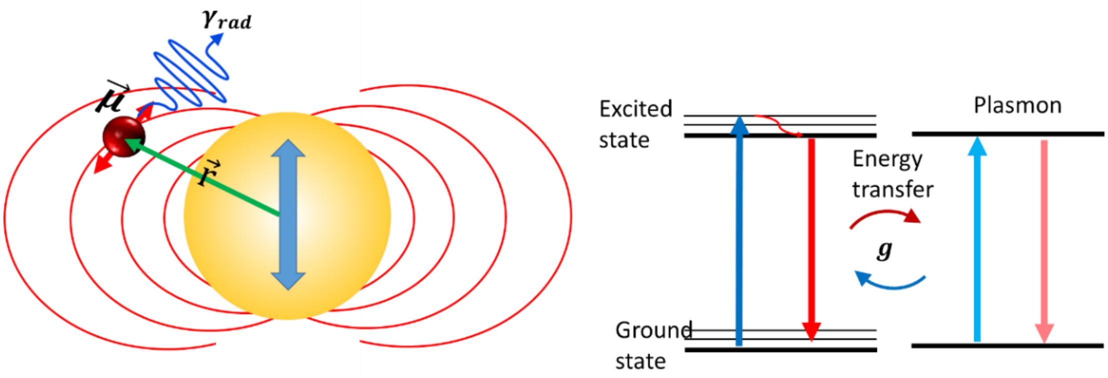

Figure 1.7 Illustration of a strongly coupled plasmon-exciton system composited by a MNP and dipole emitter.

A lot of research groups have reported strong coupling in hybrid emitter plasmon system by using various types of emitters including dye molecule, quantum dots and J-aggregates[106–108]. Doping the nano-gap between gold nanocube and gold film with J-aggregate dye molecules show not only spectral Rabi splitting but also significant modifications of far-field scattering patterns[109]. Strong coupling leading to an enormous Rabi splitting up to 110 meV is achieved by the hybrid system of a PNR probe and single QDs[3]. QDs trapped in the gap of a gold bowtie plasmonic cavity also allowed for obvious strong coupling phenomenon[110,111]. These configurations depending on their special geometry, localized plasmons contribute to ultrasmall effective volume of the resonance modes and give rise to enhanced field intensity, which provide an excellent interface between plasmonic modes and emitters.

The coupling strength is a useful quantity as it can be compared to the other energy transfer rates in the system, most importantly, the excited state lifetime of the emitter (γ^0) and the cavity loss rate (Γ). Then the two coupling regimes can be discussed through the comparison between the respective coupling strengths, emitter decay rates and damping rates of the involved cavities[90,112]. When the coupling strength can overcome the loss of cavity and relaxation decay rate ($g \gg \Gamma, \gamma^0$), reversible energy exchange happen and strong coupling occurs leading to Rabi splitting[100], which is regarded as a classic signature of strong coupling. This effect is associated to Rabi oscillations which illustrate the time period of the energy exchanges between the two systems in interaction. When the coupling strength cannot surpass the loss of the system ($g < \Gamma$), system is in weak coupling regime. In case of plasmonic nanoparticles, the requirement for strong coupling can be simplified[108], as typically $\Gamma \gg \gamma^0$, and so it is enough to satisfy $2g \gg \Gamma$. Increasing the coupling strength g or decreasing the total loss of the hybrid system can help to achieving stronger coupling. Higher g can be obtained by increasing the dipole moment $\boldsymbol{\mu}$, enhancing the field intensity in cavity, or decreasing the mode volume. Decreasing the loss Γ can be achieved by placing this coupling system in low temperature, using emitters with narrow spectra, increasing the quality factor of plasmonic cavity.

When strong coupling is achieved, both scattering and emission of the hybrid system will show Rabi splitting, and larger splitting can be observed in the former one[53,85]. The Rabi splitting and anticrossing in spectra and dispersion functions are characteristic fingerprints of strong coupling[50].

1.3.2 Single-photon emitter coupled to plasmon

According to the Pauli exclusion principle, for an ideal two-level system, when an electron is excited to occupy the excited state and has not yet generated spontaneous radiation, the next electron cannot be excited to this same state. That is to say, the system can only emit one photon during the lifetime period of spontaneous radiation under external pulsed excitation. Many kinds of schemes have already been proposed to work in the single photon regime based on, for instance, the semiconductor quantum dots(QDs)[113,114], nitrogen-vacancy center((NV center)[115,116], single organic molecules[117,118]. The focus on single emitter coupled plasmon system has brought many experimental studies, as we said at the beginning of this chapter. It is well known that the emission properties including the radiative rate, spatial distribution[119,120], spectrum[121], and polarization[31] can be engineered by the interaction between emitter and plasmon, providing an idea for making controllable single-photon light sources. For example, with the coupling between SPP and single QDs on a silver nanowire, remote excitation, and detection of the single QDs is available, which is promising for the application in quantum information[80]. However, for strong coupling in single emitter level, from Equation (1.26), considering strong radiative damping of surface plasmons and other dephasing mechanisms present in emitter it requires ultra-small mode volume. Strong coupling between single emitter and plasmonic nanostructures at room temperature have recently realized using QDs[52,56,122], dye molecule[123] and J-aggregate[124], who were positioned in different gap plasmon cavities.

1.3.3 QDs coupled plasmon system

The currently reported QDs are mainly composed of II-VI, III-V and IV-VI elements. Due to the small size of QDs (general, 2 nm~10 nm), they have discrete energy structure. In addition, QDs can be dispersed in optically transparent materials such as glass or polymer films and can be dissolved in organic solvents such as toluene and hexane.

The most standard QDs used here have core-shell structure. The more representative ones are CdSe/ZnS, CdTe/CdS, etc. QDs of this structure have the advantages of anti-agglomeration, photostability, and high fluorescence efficiency[125]. QDs have broad absorption and symmetrical, narrow half-width emission and their emission wavelength can be easily adjustable with the size of the quantum dots. These characteristics make QDs very promising emitters for wide applications such as biological labelling, quantum cryptography and conductive polymers composite to prepare narrow-band electroluminescent devices. Besides, QDs possess relatively larger transition dipole moment compare to fluorescent molecule leading to strong oscillator strengths and high emission stability[126], also making them appropriate as a single-photo source and a good candidate for researching light-matter interaction.

Reported studies of QD-plasmon composite systems in the weak and strong coupling regime are numerous. Control the emission of ensemble QDs was achieved by coupling them to various metallic structures, such as metal−dielectric−metal (MDM) waveguide[127], Nanowire Antenna[128], nanoparticles[129]. Additionally, coupling between plasmonic structure can lead to Blinking suppression of QDs[129,130]. Strong coupling between single QDs and plasmonic structures with obvious emission splitting has also been achieved in Ag bowtie[56], metal film-coupled Au nanoparticle[85], tip - film composited nanocavity[131].

1.4 Realization method

The crucial point for realizing the Plasmon nano-emitters composite hybrid system is the precise spatial integration of nano-emitters with plasmonic nanostructures. The current methods can be mainly divided into three typical types.

In most reported cases, emitters were directly spin coated on plasmonic structures or dissolved in PMMA solution then spin coated on structures. This simplest method disperses emitters randomly on the plasmonic structures, without any control of the position relative to the metal nanostructures. As a result, many samples must be made before obtaining a satisfactory one where the emitter location is suitable for physical studies of interest. For example, in ref. 35, the authors used the gap mode of a bowtie antenna. They deposited active molecules everywhere. Only a few of them, falling within the bowtie gap, allowed one to randomly demonstrate a strong fluorescence enhancement based on weak coupling (Figure 1.8 (b))[35]. Using homogeneous low concentration of QD-containing solution, a single QD was successfully placed in the gap between gold film and single silver cube (Figure 1.8 (c))[132]. However, the repeatability is uncontrolled.

To address this issue, some reported studies tried to restrict the distribution of emitters in one direction. With the help of a spacer layer such as PMMA, the emitters were trapped in a spacer layer. Using this type of method, related studies have achieved large fluorescence enhancement and strong coupling in single emitter level. For instance, it has been possible to design a nanocavity based on surface plasmon coupling between a silver substrate and a silver nanowire lying parallel to the substrate and to integrate spacer layers with dyes in the gap (Figure 1.8 (d))[38]. Special host–guest chemistry of macrocyclic cucurbit[n]uril molecules layer used for trapping emitters can confirm homogeneous dispersion of emitters and decrease the size of gap to 0.9nm (Figure 1.8(e))[53]. They ensured the repeatability and stability of the experiment while achieving strong coupling between the single molecule and the nanocavity. Some examples demonstrate that the coating layer covered nanoparticles can also be used as spacer layer to build the hybrid system[132,133]. These methods allow one to control the distance between the emitter and the metal structure. It is only suitable for positioning the emitter in the gap region between the two-dimensional film structure and the nanoparticles, while cannot be realized for other structures.

A special lithography method has been used for controlling emitters' relative position in three dimensions. Some reported studies used homogeneous nano-emitters deposition as a first step followed by subsequent steps to fabricate the plasmonic structure to localize them at strategic positions: optical lithography[5], electron beam lithography[134], or atomic force microscopy[4]. Such an approach is powerful but does not permit a high flexibility in the nano-emitters positioning in the sense that still only gaps between metal nanoparticles can be functionalized.

DNA based approaches were also used for linking nano-emitters to metallic nanostructures with confirming distance. For example, Figure 1.8 (g) shows a dimer with emitter trapped in the gap using DNA link[1]. However, this kind of method usually needs special surface functionalization treatment and for the entire nanoparticle surface, no specificity is selected. In another method, the emitters are trapped in the shell covering the whole metallic nanoparticles[20,32].Although this method traps the emitter near the metal nanoparticle in three directions, the distribution of the emitter relative to the particle is still isotropic.

Another kind of method used the metallic nanostructures to scan the randomly dispersed emitters on the platform[3]. The distance between emitters and metallic probe changes during the scanning. This method is useful for studying the spectra, radiative decay rate and coupling changing while not suitable for building a stable integrated light source.

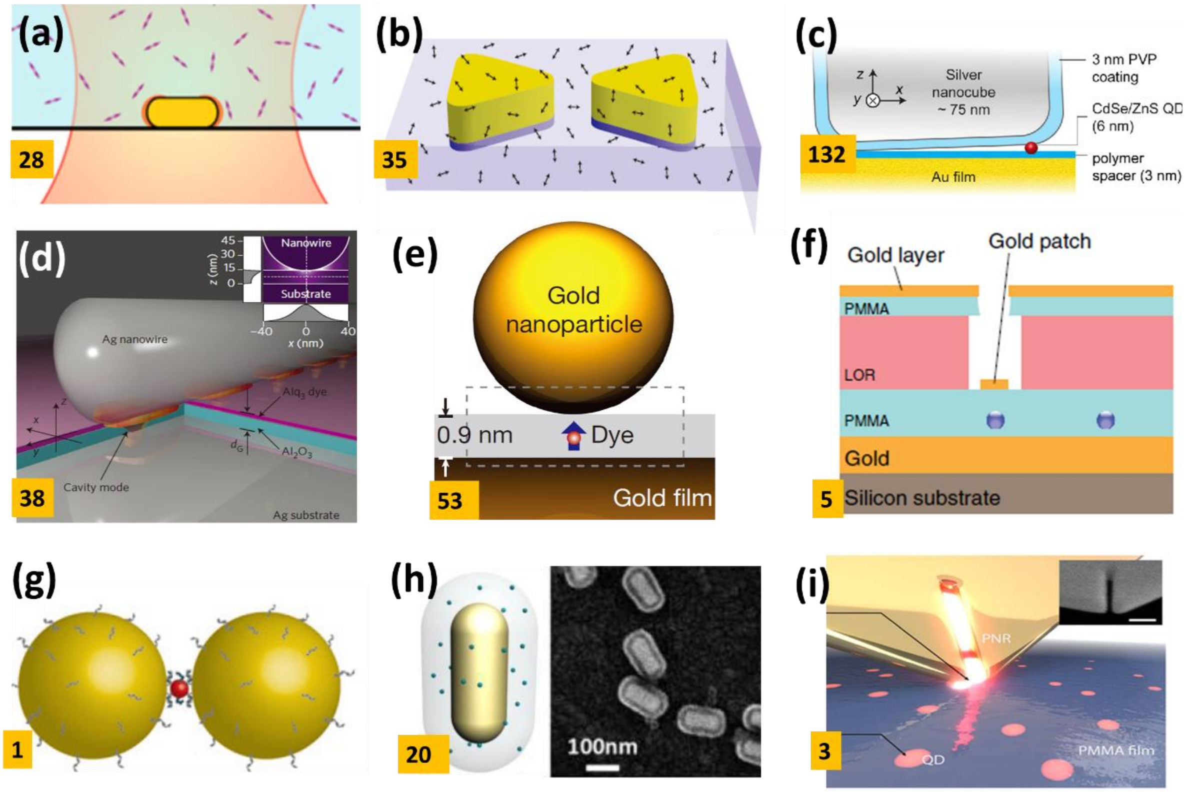

Figure 1.8 Different methods used for integration of emitters with plasmonic nanostructures. The number in yellow squares represent the reference number.

1.5 Our Approach

Different from all the methods introduced before, our method is based on localized near-field nano-photo-polymerization triggered by surface plasmons, allowing us to achieve controllable anisotropic emitter-containing polymer distribution near metal nanoparticles. It consists of a polymer printing of specific pre-selected local plasmonic modes supported by the metal nanoparticles.

The plasmon-triggered photopolymerization method developed by our group has achieved many previous studies including nanoscale imprinting the near-field distribution of nanorods[135], nanospheres[136], nanodisks[137] and small nanocubes[6]. This method has also achieved fixing QDs in the vicinity of EBL (electron-beam lithography) fabricated nanodisks[7]. Our group has also studied the plasmon-enhanced Raman spectra with methylene blue molecules trapped in the gap of dimer structure by this fabrication method[138]. Previous research mostly focused on near-field imprinting and although some works have trapped emitters in polymer, the success rate and repeatability are not high enough, we have never achieved the trapping of single emitters before. Besides, even the former work has realized plasmon-triggered photopolymerization on single nanocube, it was based on one-photon polymerization. In this thesis, we achieved plasmon-triggered two-photon polymerization on a single gold nanocube and study the polarization sensitivity of the emission from our hybrid system by building a link to the spatial overlapping ratio of polymer distribution and exciting field. Benefit from better nanoscale controlling of polymer distribution, we successfully decrease the number of nano-emitters to a single-photon regime. In addition, we develop another emitters-polymer combination method based on surface functionalization that is useful for selectively placing nano-emitters at 'hot-spots' of metal nanoparticles.

Generally speaking, our method is based on different steps (see illustration Figure 1.9). Plasmonic MNPs are covered by a liquid photopolymerizable formulation containing nano-emitters to be integrated. Localized field enhancement of MNPs is excited by a low-intensity laser irradiation with wavelengths overlapping with both the polymerizable formulation absorption spectrum and the MNPs' Plasmon resonance. The resulting local plasmon-enhanced energy density exceeds the threshold for two-photon polymerization (TPP). Then, the photopolymerization reaction is triggered in localized area resulting in a trapping of the nanoemitters inside the cured polymer. The threshold dose of the polymerizable formulation is previously assessed. Using an incident dose below of threshold will not bring out polymer dots. The polymerization is restricted to occur only in the localized plasmonic near-field region.

As we said in section 1.2 , the near-field distribution is dependent on the shape of metallic nanostructure, parameters of the excitation light. By using different geometries of gold nanoparticles and different modes of Plasmon excitation, nano-emitter-containing active medium can be structured selectively with different degrees of symmetry in the close vicinity of the metal nanostructures.

More precisely (see Figure 1.9) dispersed MNP are deposited on ITO coated glass substrate, and then covered by of homogenous homemade formulation used for TPP on the substrate to let the MNPs immersed in it. Then, the incident laser with appropriate wavelength is focused on the MNPs using a dose below the threshold: $D_{in} < D_{th}$. The near-field intensity of the MNPs is enhanced from LSPR and gives rise to an effective energy density that exceeds the threshold. Here, the polymerization is triggered at the near-field region around MNPs. After removing the remaining liquid formulation by rinsing, we get a hybrid nanostructure containing nano-emitters surrounded/trapped by polymer.

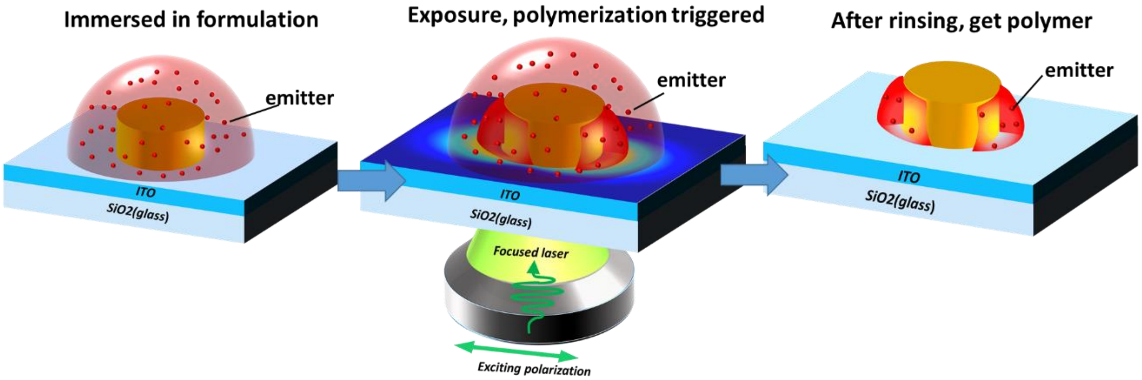

Figure 1.9 Schematic diagram of plasmonic triggered Two-photo polymerization method for fabrication hybrid structure.

For metal nanoparticles of different shapes excited by different polarized modes, different near-field distributions will be obtained, corresponding to different polymer distributions. The anisotropy of the hybrid nanostructures and the subsequent polarization dependence is the most important point in our project. For instance, as it is illustrated in Figure 1.9, linearly-polarized incident laser excites the dipolar plasmon mode of a nanodisk. The spatial anisotropy of the near-field distribution leads to the spatial anisotropy of the photopolymerization process. It helps us selectively trap the nano-emitters to produce a controllable plasmonic nano-emitters.

1.6 Summary

In this chapter, we introduced the development of Plasmonic hybrid nano-emitters. The basic theory of localized surface plasmon was introduced the influencing factors parameters for MNPs'

LSPR were discussed. The different interaction between plasmons and emitters have been overviewed in this chapter. The special properties of QDs as a single-photon light source which was mainly used in our thesis have also been briefly introduced. Finally, we discussed current methods used for the integration of nano-emitters in the vicinity of plasmonic and introduced our method based on plasmons-triggered near-field photopolymerization.

Chapter 2 Experimental methods

For hybrid plasmonic nano-emitters based on the combination of quantum emitters and localized plasmonic nanostructures, the nanoscale control of the quantum emitters' position helps to control the light emission. As we introduced in section 1.5, our method is based on surface plasmon-triggered two-photon polymerization of a photosensitive formulation containing nano-emitters, which has the most prominent advantage of the selective anisotropic distribution of the emitters. In this chapter, we will introduce all the experimental procedures used for fabricating our hybrid nano-emitters. We will start from metal nanostructure fabrication, characterization. Then, a brief introduction about two-photon polymerization will be made and the optical set-ups will be described. Finally, we will present the methods used for analyzing the fabricated hybrid nanosystems, including the analysis of the light emission and the assessment of size and geometry of the polymer nano-parts.

2.1 Metal nanostructures fabrication

To carry out surface plasmon-triggered two-photon polymerization on metal nanostructures, we need to comprehensively consider the absorption spectrum of our photochemical formulations, the wavelength of the exciting laser source, the LSPR properties of the metal nanostructures, and the emission wavelengths of our QDs. So, as a first step, it is imperative to produce suitable metal nanostructures. There are two basic methods for producing size-controlled metal nanostructures. One is based on the electron beam lithography (EBL), which is suitable for the fabrication of, e. g., nanodisks and nanodimers. The other is the chemical synthesis method, which is easy for producing a lot of 3D nanoparticles of special shapes, such as nanorods[139], nanocubes and nanopyramids[140]. This section will introduce these two methods in detail.

2.1.1 Top-down approach: Electron beam lithography

EBL is a mature and widely used Micro / Nanomanufacturing technology, whose basic idea is transferring any particular pattern written on resist by scanning ebeam to another layer of specific materials by etching or lift-off process. It is possible to generate any confined shape of metal nanostructures whose feature size is larger than the resolution of EBL. Compared to the chemical synthesis method, EBL is more suitable for controlling the shape of the nanostructures. Moreover, regular arrangements allow for precise positioning, which is very convenient to localize the metal structures for plasmon-triggered polymerization.

For our experiment, we need a transparent substrate to avoid reflection. Generally, glass or indium-tin-oxide (ITO) coated glass is selected as a substrate according to our different needs. ITO- coated glass is better for SEM observation, and pure glass substrate is easy for keeping clean surface. We uniformly use 22x22 mm^2 square in shape glass cover slit with a thickness of 0.17 mm and the commercial ITO coated glass with 40 nm ITO layer on the former mentioned thin glass substrate[141].

The EBL process basically consists of 6 steps, shown is Figure 2.1. The first step is to clean the substrate. Then the electron sensitive resist is spin-coated on the clean substrate. Depending on its different chemical reactions to electron exposure, the resist is divided into positive and negative. A Positive resist becomes soluble after electron exposure because of the breaking of its chemical structure: exposed matter is removed by the development step. In contrast, the exposure area of the negative photoresist polymerizes and get retained after the development step. In this thesis, we use Polymethylmethacrylate (PMMA) as a positive resist. Hence, after exposure, we get the opposite pattern on the substrate. The next step is depositing needed metal material on the patterned substrate. For example, we use the evaporation-based coating to deposit a layer of Au. The final step is to remove the resist and the extra metal layer on it. This step is named the “lift-off” step. The aimed metal nanostructures laying on the substrate can thus be obtained.

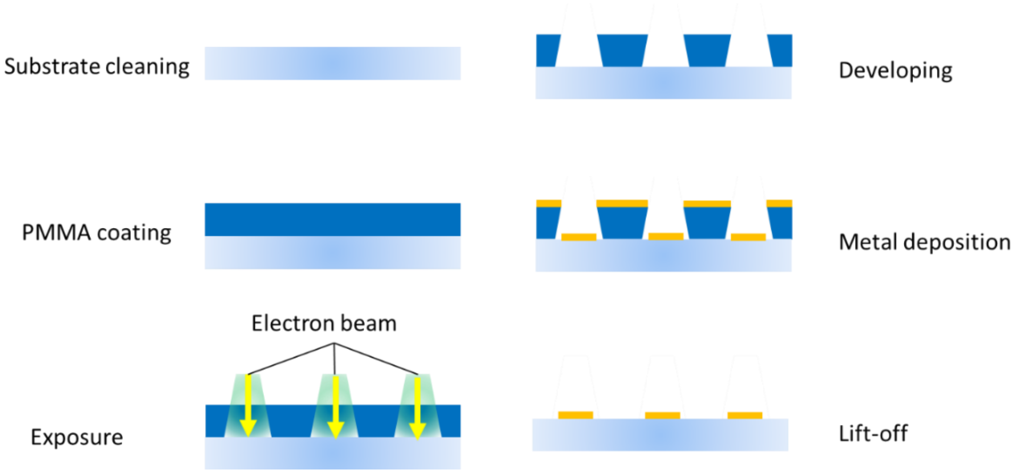

Figure 2.1 Schematic image of the metal nanostructure fabrication process by electron beam lithography.

◆ **Substrate cleaning**

The substrates must be cleaned totally before using them. Universally, the substrates are sonicated by Decon 90 solution (5%, v/v), acetone, Isopropanol (IPA) in succession. Then, the substrates are sonicated in deionized water 10 minutes for 3 times, and finally dried with air.

◆ **PMMA spin-coating**

The polymeric resist PMMA is dissolved at a concentration of 30g/L in methyl isobutyl ketone (MIBK). To fabricate a structure of 50 nm height after lift-off, the thickness of the resist should be at least three-fold or more, typically 150 nm. The PMMA is spin-coated on the substrate using the following parameters: 4000 rmp/s acceleration, 3000 rmp speed, and 30 s duration

After spin-coating, an essential heating step is taken in order to reduce the PMMA layer's unevenness due to centrifugal forces, viscosity of PMMA, etc. Unflat layer would cause focus deviation in the subsequent exposure process leading to shape distortion of the final structure. So, we put the PMMA-coated substrate in an oven at 160℃ for 3 hours This heating process allows for the evaporation of the residual MIBK and make the PMMA soft with a high mobility, contributing to a flat PMMA layer.

For most of our experiments, we use ITO-coated glass. Since the ITO layer will reduce the transmittance of the fluorescence, and will bring a rougher surface, and will make the QD more difficult to remove in the subsequent "development" process, sometimes for cleaner backgrounds and larger fluorescence signals, we use pure glass. For pure glass substrate, before the step of EBL, a thin aluminum layer (normally less 10 nm) is coated on the PMMA layer as a conductive layer for electron exposure.

◆ **Exposure by electron beam**

We use an SEM microscope (SE3500N Hitachi), and an e-beam lithography system (eLine Raith) to combine an EBL nanofabrication system. CAD designs the nanostructure pattern which is transferred to the nanometer pattern generation system (NPGS) to control the irradiation. The pattern's feature size is limited by the size of the e-beam focusing spot. So, before e-beam exposure, it is essential to adjust the focus spot to a round spot with the highest quality, avoiding the aberration's influence. Normally, it is better to test several energy doses until one finds the one that produces the best nanostructures. It is easy to reproduce identical arrays of nanostructures by the same dose. We usually use 20 kV voltage, 40 pA intensity current for fabrication of gold nanostructures.

◆ **Development**

After e-beam exposure, in the illuminated area, the chemical chain of PMMA is broken and becomes dissolvable. Then, the substrate is immersed in methyl isobutyl ketone (MIBK): isopropyl alcohol (IPA) (1:3) solution for 60 s for dissolving the exposed part totally. Afterwards, IPA directly rinsed the sample for about 20 s to remove the residual MIBK: IPA solution. After drying the sample, the designed pattern is finally achieved on the substrate.

◆ **Evaporation of Au layer**

After the development process, the sample with PMMA as a mask can be used for the evaporation of metals. Here, because gold is not easy to adhere on the substrate, a 3 nm layer of Cr is coated firstly, and then a 50 nm layer of gold is deposited on the Cr layer. Then the Au film is deposited onto the substrate by electron-beam evaporation.

◆ **Lift-off**

Lift-off is last step to remove the resist mask and the extra metal layer by immersing the sample in acetone solution for about 12 hrs. After rinsing by IPA for about 2 min, the aimed metal nanostructures are obtained on the substrate.

Figure 2.2 gives two examples of gold nanostructures fabricated by EBL. The left one is the AFM image of an array of gold dimers of disks. The right one is the SEM image of an array of gold bowties. Obviously, by EBL, we can fabricate any shape of metal nanostructures. Just like the gap of dimers and the corners of the bowties, the feature size can achieve sub-10nm resolution corresponding to the electron beam's smallest focused spot size and limited by the electron's scattering in both resist and substrate. Although the gap size below 10 nm can be achieved, it is difficult to accurately control and the repetition rate is not high.

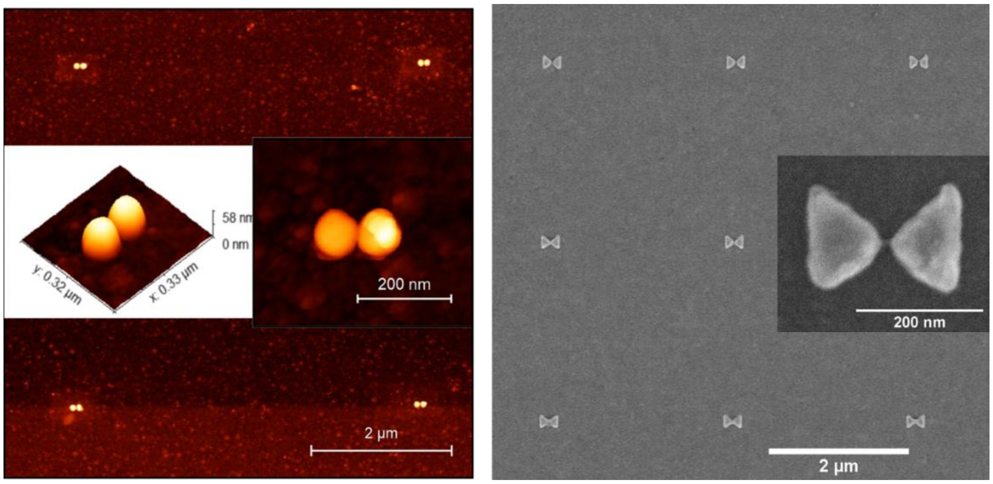

Figure 2.2 Left: AFM images of an array of gold disks; Right: SEM image of an array of gold bowties

2.1.2 Chemically synthesized colloids

Unlike the EBL method, chemically synthesizing colloids is a better way to fabricate some special metal nanoparticles having a high-quality crystal structure. This method can achieve efficient and stable nanoparticles. More importantly, it is less expensive than EBL and allows one to fabricate thousands of metal nanoparticles with relatively uniform shape and controllable size at the same time. The particles' shape is controlled by the type and concentration of the surfactant, the synthesis time, the temperature, and other key chemical parameters. Surfactant such as cetyltrimethylammonium bromide (CTAB) and cetyltrimethylammonium tosylate (CTAT) is a class of material that is surface active and has the ability to control the shape and size of crystal growth[142,143]. Besides, surfactant also helps to avoid the aggregation of nanoparticles. For different shapes and materials of nanoparticles, the synthesis and deposition methods are different. In this thesis, the synthesis of gold nano-cubes and gold nano-bipyramids is mainly involved.

◆ Gold nanocubes

Gold nanocubes synthesis

Here, we use 127 nm Au nanocubes for plasmon-triggered two-photon polymerization. The cubes were fabricated by Sylvie Marguet from CEA Saclay. The Au-cubes are synthesized in aqueous solution in presence of the cetyltrimethylammonium bromide (CTAB) surfactant, following the seed mediated growth protocol described in details in ref-144, Small nanocubes of 40-nm are synthesized first, and then used as “seed” in a second step of growth. The growth solution (5ml) is prepared by successively mixing 3.6 ml of a 22 mM CTAB solution with 100 µl of HAuCL4 (0.01 M) and 1.3 ml of ascorbic acid (0.01 M). Adding the seeds (100 µl) initiates the growth of the cubes. Sharp edges and corners are obtained by adjusting the ratio of ascorbic acid to HAuCl4 to a value of 13. After one night at 30°C, 127 nm nanocubes roughly purified (~60%) are obtained, through selective sedimentation at the bottom of the reaction vessel owing to a depletion-induced interaction. The solution is then centrifuged twice and dispersed in water to remove excess CTAB down to about 1 mM. The chemicals used are cetyltrimethylammonium bromide (CTAB ≧ 98%), chloroauric acid ($HAuCl_4 \cdot 3H_2O$), sodium borohydride ($NaBH_4$, 99%), ascorbic acid (99%). Deionized water is used for all experiments.

Deposition of gold nanocubes

The gold nanocubes are deposited is on the glass substrate coated by a 40 nm thick ITO layer. After being exposed by UV-ozone for 15-min, the ITO-coated substrate is activated in a typical experiment and can make the sample adhere to the substrate. And then, the substrate is drop-casted immediately by 2ul of that CTAB/nanocubes-containing solution. To make the cubes' distribution homogenously during the dry process, we put a cover glass on the drop and let the drop dry slowly by itself. After evaporation, we expose the substrate in UV-ozone for 5-min and rinse it by ethanol for 5-min to remove the CTAB totally. Figure 2.3 gives an example of the resulting colloidal gold nanocubes deposited on glass.

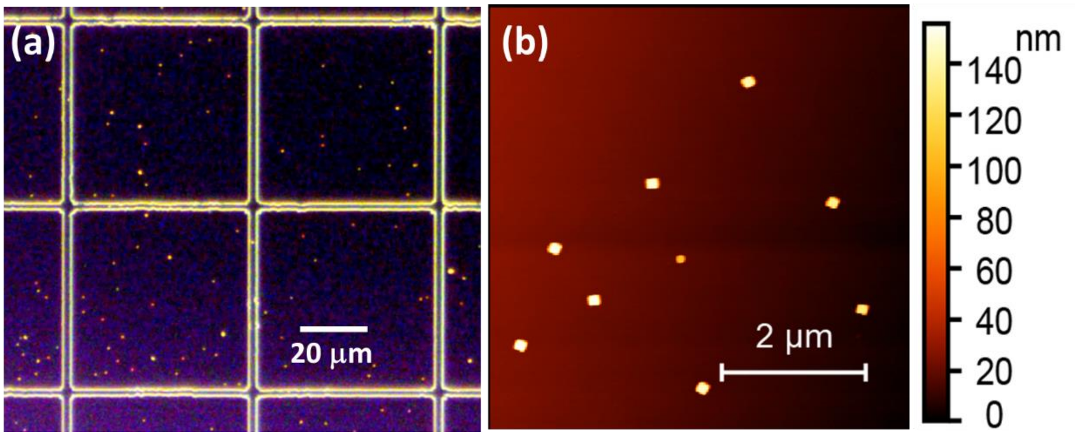

Figure 2.3 An example of the colloidal gold nanocubes deposited on glass. (a) The dark-field optical image of the nanocubes dispersed on a grid-engraved glass. Every square covers an area of 50x 50 μm^2; (b) AFM images of the dispersed nanocubes.

- **Gold nanobipyramids**

Bipyramids synthesis

Gold bipyramids (AuBPs) used in this thesis is produced by M. S. Kirschner and R. D. Schaller from Northwestern University, USA. The AuBPs are also synthesized using a seed-mediated growth approach. The main steps can be divided into two parts. Firstly, to synthesize gold bipyramids, gold seeds are created by reacting HAuCl4 with NaBH4 solution in the presence of sodium citrate. The seed solution is aged for 2 hrs before use. Then, for growth of the bipyramids, HAuCl4 solution with trace amount of AgNO3 added are mixed with CTAB solution, acidified by a small amount of HCl, and reduced by L-ascorbic acid. Right after the reduction, small amounts of seeds are added, and the reaction can proceed in a 30 °C bath for 2hrs. Then the bipyramids solution with defined LSPR peak are prepared. This AuBPs colloid solution can be stored stably for several months.

In our case, we need gold bipyramids who have a LSPR peak within the 680-780 nm range. Compared to nanorods, the bipyramids behave in a similar way: the higher the aspect ratio, the bigger LSP resonance wavelength. We can control the LSPR wavelength by controlling the aspect-ratio of the bipyramids. More interesting, in the case of bipyramids, their truncation and aspect-ratio are linked together since truncation reduces aspect ratio. By varying the truncation or the aspect-ratio of gold bipyramids, it is possible to modify the tips' sharpness and play on the

LSPR[145,146]. The way to control the bipyramid aspect ratio consists in adding different amounts of seed, as shown in Figure 2.4.

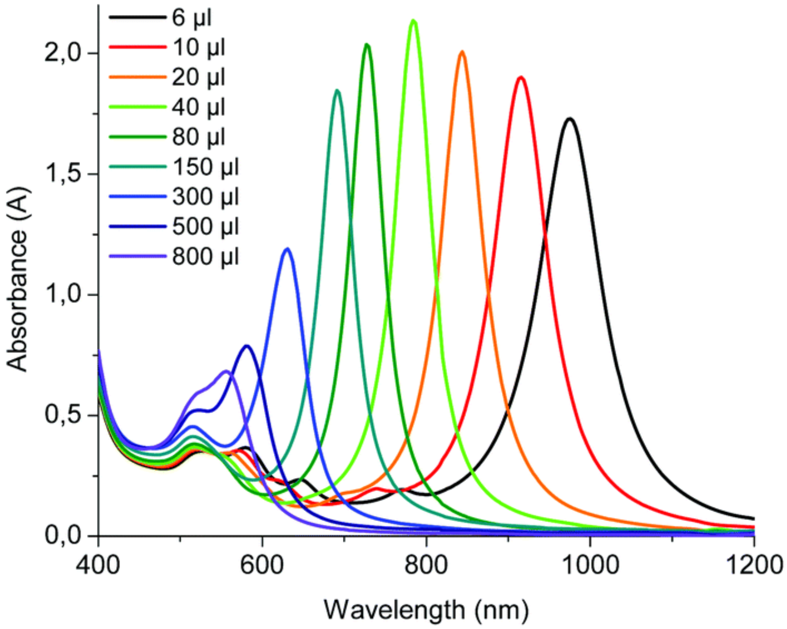

Figure 2.4 Absorption spectra of the synthesized bipyramids versus the volume of Seeds solution added[145].

Deposition of gold bipyramids

Compared to nanocube, the bipyramid is much more challenging to adhere on the glass substrate. The shape of its cross-section shows that the face that can contact the substrate's flat surface is smaller. For fixing the bipyramids tightly on the substrate, we need to functionalize the surface of the glass. In brief, the glass slides are cleaned using the same steps mentioned in the previous section and then immersed in ethanol solution with the presence of APTMS (1%, v/v). After 30 min, each glass slide is washed with ethanol and pure water. After drying the glass by air-gun, the surface-functionalized glass has been prepared for AuBPs' deposition.

Before deposition, the bipyramids solution should be diluted, and extra surfactants should be removed. 20 µl of the original bipyramids' solution is added into 580 µl deionized water to form 600 µl of dilution. The diluted solution is then sonicated for 10 minutes in room temperature. The homogenous diluted solution is centrifuged at 8000 rpm for 10 minutes. Afterward, we remove 400 µl of the supernatant and re-add 400 µl deionized water to form new diluted solution. After 15 minutes of sonication in a water bath, 3 µl of the dilution is drop-casted on the preprocessed glass and keep it for 15 minutes. Then the glass substrate is washed by ethanol and water gently for several times.

When we use ITO-coated glass as a substrate, we use the same process as what we performed for cube deposition. After UV-ozone treatment, the diluted bipyramid solution is dropped on ITO, and dried by evaporation. In the middle of the drop, homogenous dispersion of bipyramids is gotten. An example of well-dispersed bipyramids is shown in Figure 2.5.

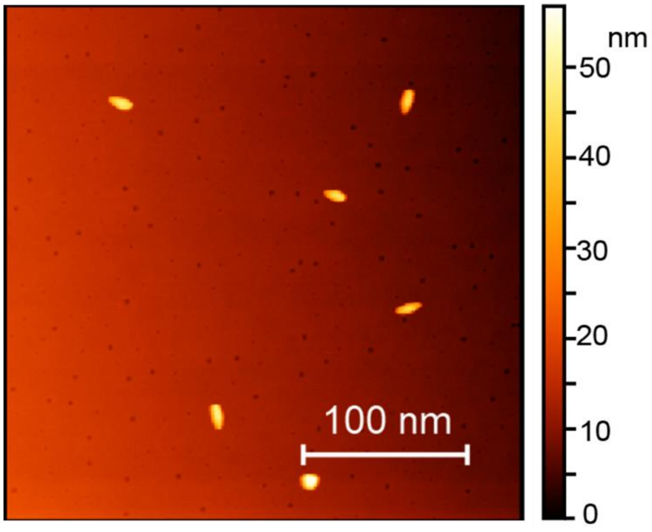

Figure 2.5 AFM image of the colloidal gold bipyramids deposited on glass substrate

◆ **Mark Fabrication**

Thousands of colloids are randomly distributed on the substrate. However, in our case, we need to do TPP on single nanoparticles one by one. An accurate alignment is thus necessary. Additionally, for optical characterization of the resulting hybrid nanosources, we need to collect and analyze light emission from pre-identified isolated particles. Producing some marks on the substrate is a convenient and efficient method to help us localize single particles.

There are several methods for making marks. It is easy for the glass substrate to use UV lithography to integrate grids on the substrate (as shown in Figure 2.3) Top-down process to fabricate some gold marks by EBL is also possible. For ITO-coated substrate, making scratches manually can also help us identify particular regions.

Another method that can be used is producing a grid by pure polymer using Nanoscribe, which is a micro-fabrication platform using two photons lithography. (introduction will be found in section 2.2.3). The polymer layer can be designed as a grid of precise shape with well-defined coordinates and be fabricated on a clean substrate. By using this technology, addressing a single particle becomes possible. However, special attention must be paid to avoid these grid marks' impact on subsequent experiments. We can selectively use different methods for different samples and substrates.

2.2 Sample Characterization

We use Atomic Force Microscope (AFM), Scanning electron microscopy (SEM) cooperated with dark-field optical imaging to calibrate single gold nanoparticles. The concentration of colloids particles solution is adjusted to match both AFM scanning area and SEM test region. Moreover, the separation distance between single isolated MNPs should be more than 1um to be entirely appropriate to make dark-field measurements. However, compared to AFM, SEM is a quick and convenient way to observe the particles in marked areas on the ITO coated substrate. After comparing the dark-field image in the same observed area, it is also easy to address every individual particle.

2.2.1 Dark-field imaging and Scattering spectrum measurement

The CARY 100 UV-visible spectrometer is convenient to measure the absorption from solutions including the solution of MNPs. But this spectrum corresponds to big ensemble of particles, which means the result reflects the statistical average. Even two particles in the same solution can have two different plasmon spectra due to their different sizes. In general, despite de high quality of the solutions prepared by S. Marguet, one solution may contain nanoparticles of different shapes and sizes. For example, our solution containing 127-nm nanocubes turned out to contain nano-spheres too. At this point, the absorption spectrum from the solution can just be used as a reference.

For our case, it is better to get the exact spectrum corresponding to the plasmonic resonance from exact individual particles. Scattering is a straightforward way to get the plasmonic resonance characteristics from single MNPs. As shown in Figure 2.6, a dark-field condenser with a numerical aperture (NA) of 0.9 is installed above the sample stage of an inverted microscope (Olympus IX71). The light scattered by a single nanoparticle is collected by an objective of 40X with 0.6 NA (< 0.9) below the sample, after pass through a tube lens, the light is divided by a beam splitter into two light paths. One of the light paths goes into the CCD camera after focusing by this tube lens. In the other light path, another lens is added between the output of the IX71 microscope and the spectrometer to magnify the image and the spectrometer's entrance slit is placed at the second image plane. The Spectroscopic system consists of a Shamrock 303i spectrometer and an iDUs CCD camera. This system allows us to select only one particle by decreasing the slit's width and collecting signal from an exact isolated single cube/bipyramid using the multi-track mode. The scattering spectra are calculated as in equation:

$$S_{scat} = \frac{S_S - S_{dark}}{S_{source} - S_{dark}} \tag{2.1}$$

S_s is the collected light signal from the target particle under dark-field illumination, which contains the scattering signal and the signal from the background. S_{dark} is the background signal without any illumination. S_{source} indicates the light source signal, which is measured from under the same conditions in a blank area without any nanoparticle

In Figure 2.6, the image on the right-bottom is an example of dark field image of gold nanocubes. The top right image is the scattering spectra from a single isolated gold nanocube. Taking such a method, we can abandon the other deformed particles that are not precise cubes and get every addressed cube’s scattering spectrum.

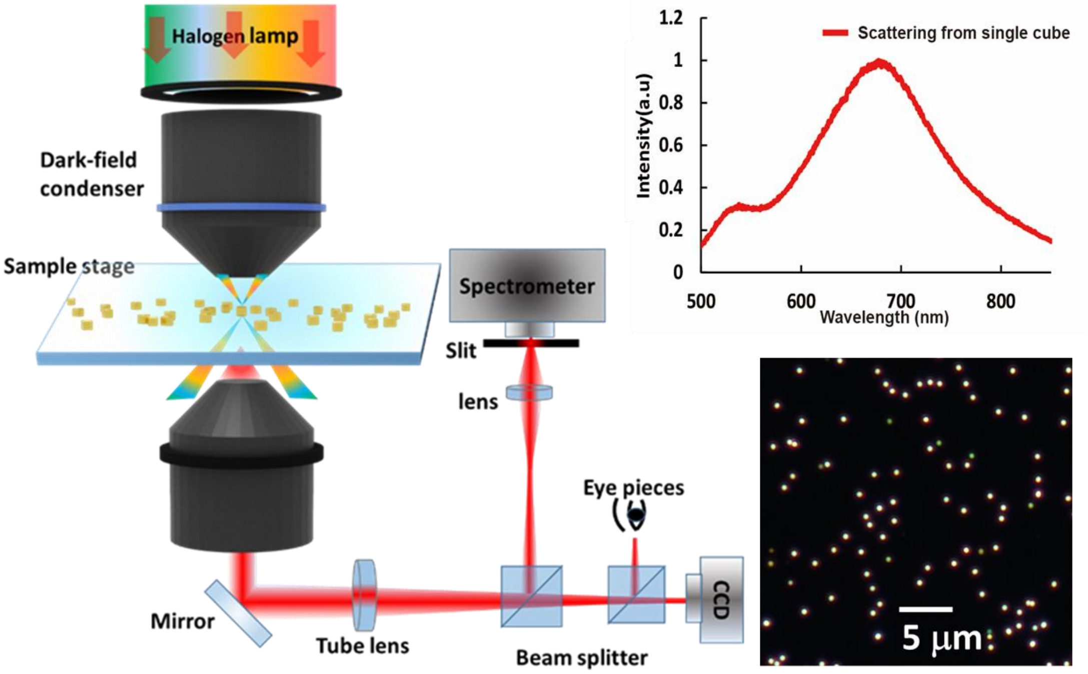

Figure 2.6 The Left image is a schematic representation of the dark field set-up; the right bottom one shows a dark-field image from an area of nanocubes on ITO-coated glass substrate; the right top one is the scattering spectrum from single isolated nanocube.

2.2.2 Topographic characterization by AFM and SEM

The knowledge of both geometry and dimension of the fabricated metal nanostructures is crucial for analyzing the LSPR and the distribution of the electromagnetic field. It is important to know the actual dimension parameters for building numerical simulation models. In the case of nanoparticles of several tens of nanometers, it is impossible to obtain size information through an optical microscope due to the diffraction limit. Atomic Force Microscopy (AFM) and Scanning electron microscopy (SEM) are two predominant technologies to visualize surface features and make spatial measurements at the nanoscale. SEM has excellent high lateral resolution and can give the real in-plane dimension and can image structures that have a strong vertical relief. Besides, SEM scans a sample surface in a much faster way than an AFM does. AFM can routinely measure images with sub-nanometer resolution and accurately measure the height of a sample. We use both SEM and AFM to take advantage of their complementary capabilities.

- **Atomic force microscopy (AFM)**

AFM is used for characterizing almost all the nanostructures used in this thesis, especially the samples developed on the glass. Our polymer is softer than the metal materials, and the process of polymerization may cause some impurities to remain on the surface of the substrate. The used AFM model is ScanAsyst iCON from Bruker and the Peak Force mode[147] is preferably used. The “PeakForce Tapping” mode operates similarly to the Tapping Mode[147] in that it avoids lateral forces by intermittently contacting the sample to protect from hurting the samples. However, it is quite different from the normal tapping mode. The Peak Force Tapping oscillation is performed at frequencies well below the cantilever resonance, thus avoiding a resonating system's filtering effect and dynamics. The PeakForce tapping mode combines the advantages of tapping mode and contact mode simultaneously, which achieves direct control of the force and avoids damage to the sample. The PeakForce tapping mode of this AFM allows us to achieve high resolution while still having a faster scanning speed. Besides, PeakForce mode records PeakForce error information as well as the topographic information. The former is worth highlighting because it often gives prettier picture and clearer edges. Figure 2.7 gives two groups of examples. Compare Figure 2.7(a1) and (b1), (b1) offers a clearer edge signature. Figure 2.7 (a2, b2) show a hybrid gold/polymer particle that was fabricated using the approach similar to the method described on & 1.5, chapter 1, and it will be introduce in & 5.2, chapter 5. Compared to (a2), (b2) gives a more distinguishable image of the hybrid cube, showing quantum dots on the surface of the polymer.

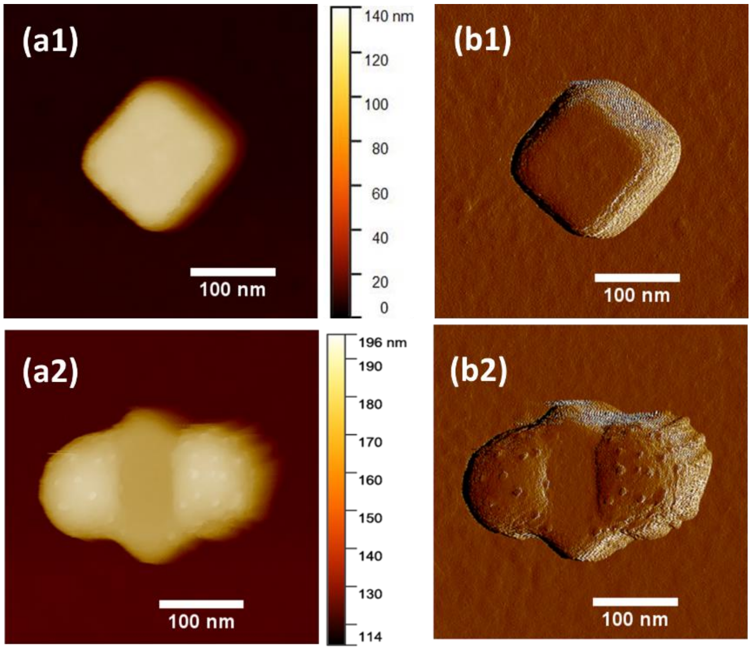

Figure 2.7 AFM images (a1) topographic images and (b1) Peak Force error images of a gold nanocube. (a2) topographic images and (b1) Peak Force error images of a polymer/gold hybrid nanocube with QDs on the surface of polymer.

Using AFM to compare the 3D topography of nanoparticles before and after Plasmon-triggered polymerization is another useful approach. Figure 2.8 shows AFM images of the same nanocube taken before and after the photopolymerization procedure. The Comparison between the original topography and the topography of the hybrid structure is made through the subtracted topography which presents the real distribution of the integrated polymer around the nanocube.

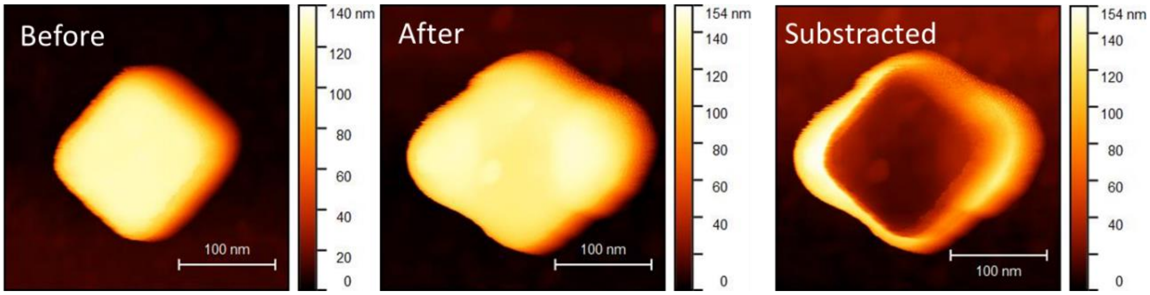

Figure 2.8 AFM images taken before (a) and after (b) Plasmon-triggered polymerization. (c) The subtracted image (after – before).

However, the AFM topography is affected by the convolution between the actual sample shape and the AFM tip geometry. Therefore, the AFM image's effectiveness is limited by the quality of the tip and by the way the tip is installed (including position, tilt angle, etc.). During scanning, the AFM tip inevitably get slowly damaged. Therefore, in addition to the slight deviation of the probe's installation at different times, the actual tip shape before and after exposure cannot be entirely consistent. So, the information about the height of samples measured by the AFM is relatively more reliable than the information about the lateral dimension.

In order to get high resolution image of single nanoparticle by AFM, we need to scan an area bigger than 10um X 10um to distinguish the target area, and then focus on the exact target single particle. After we localize the target single particle, which is normally has a size about 100nm, we use speed rate of 1Hz to scan a 1um x 1um area to get enough high resolution. Generally speaking, it takes more than 30 minutes for the whole characterization process by AFM.

◆ Scanning electron microscopy (SEM)

As mentioned before, SEM can allow one to observe the surface structures of nano-objects directly and quickly. For example, it requires only one image capture to complete the entire area scanning, and it is easy to zoom in the area of interest, while AFM takes more than 30 minutes to obtain a high-resolution image. SEM is convenient for characterizing our nanostructures, especially for the chemically synthesized nanoparticles deposited randomly on an ITO substrate. Thousands of nanoparticles are dispersed on the substrate, and in the chemically synthesized nanoparticle solution, there are many impurities of other shapes that are not needed. SEM can help us to quickly localize each selected nanoparticle with a suitable shape. It is better to use SEM than AFM to get accuracy dimension data to build the simulation model. The to-view SEM images make possible the assessment of the actual size without any image processing requirement.

The Hitachi SU8030 FE-SEM provides secondary electrons (SE), backscattered (BSE) electrons, and diffracted backscattered electron (EBSE) imaging modes. Among them, SE is the most used mode for characterizing samples' morphology and can make the polymer and metal show different contrast under high voltage, which will be useful for our hybrid system. Figure 2.9 (a) and Figure 2.9(b) show, respectively, the SEM image a bare Au nanocube and the SEM image of a hybrid nanocube with polymer, resulting from the plasmon-triggered photopolymerization process. Figure 2.9(c) is a tilted image of the hybrid nanostructure. When we use a voltage above 10 kV, under SE mode, the polymer part becomes transparent compared to metal nanoparticle in Figure 2.9 (b) and (c). From Figure 2.9 (b) the analysis of the elongation of the polymer turns out to be convenient.

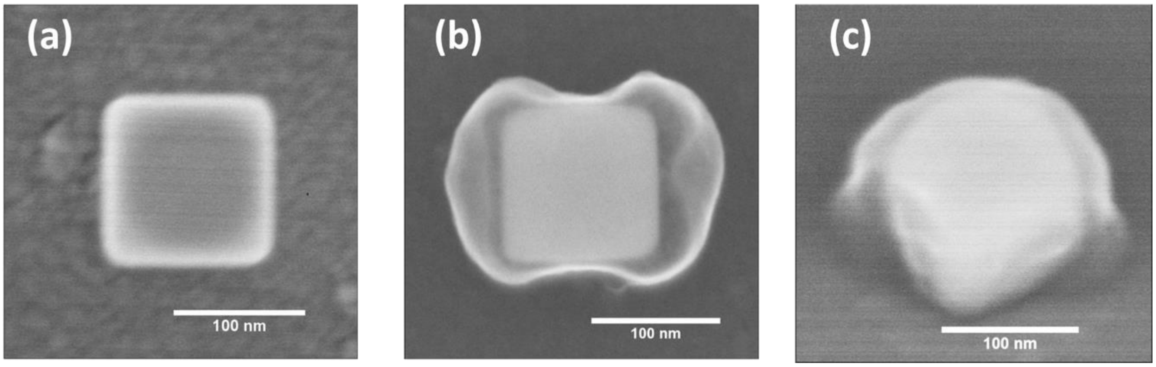

Figure 2.9 SEM image of hybrid-cube before (a) and after polymerization (b). Titled image of (b).

However, SEM has got some restrictions. The sample must be conductive, and size limited. In the case of a non-conductive sample, the deceleration mode of SEM is capable of observing[148]. However, when it comes to a sample of nanoparticles randomly dispersed on glass, it becomes impossible because of hard focusing and difficulty locating. Coating a few nanometers thick conductive layer on the sample surface is the solution. Nevertheless, it also means a change in the sample's performance, which is not allowed in subsequent exposure and emission test process. Besides, SEM cannot give the sample's depth parameter even though it can offer a 3D image by tilting the sample stage, as shown in Figure 2.9.

2.2.3 Finite-difference time-domain (FDTD) used for simulation

The finite-difference time-domain (FDTD) method already has mature commercial calculation software. FDTD was proposed by K.S.Yee and it is a numerical method for calculating electromagnetic field[149]. In FDTD, the electric component E and magnetic component H in the electromagnetic field are discretized. Space is divided into countless grids by alternating sampling in space and time domains. Each E (or H) component is surrounded by H (or E) components, creating a Yee cell. The core idea is to convert the original Maxwells' equations into a set of discretized differential equations in both space and time, then use the given initial values and boundary conditions to iteratively solve the equations in time according to the alternate sampling method of the magnetic field and electric field. A step-by-step method can be used to solve the electromagnetic field distribution in time at each point. The FDTD method is widely used because it can easily and quickly solve many problems related to light propagation, light-matter interaction at different scales, radiation, and scattering. It can also provide near-field and far-field properties for objects of any size or shape and can provide the system's time response. The FDTD method is not an approximation but offers an exact solution of Maxwell's equations limited only by the time step intervals and grid size used in the calculations.

In this thesis, we have used the software of FDTD solutions to calculate the scattering spectra and near-field distributions from nanoparticles. The perfectly matched layer (PML) absorbing boundary condition was used to truncate computational regions for simulating unbounded electromagnetic problems.

2.3 Principle of two-photon polymerization

For either weak coupling or strong coupling, one of the main challenges is the accurate positioning of the photon emitter within the volume of the optical plasmonic hotspot and reproducibility from structure to structure. The most prominent advantage of our method, introduced in chapter 1, section 1.5 , is that QDs can be easily trapped inside the polymer at the position of the hotspot, which is achieved based on the photopolymerization triggered by localized plasmon. In this section, the basic principles of two-photon polymerization are described.

Surface plasmon triggered near-field polymerization uses photopolymerization characteristics to solidify a flowing liquid into a solid to trap emitters within polymer lobes close to metal nanoparticles. The basic process of photopolymerization uses light as an energy source to induce the conversion of small unsaturated molecules in the liquid state to a solid polymer, through polymerization reactions. During the TPP process, the photoinitiator, which is quite sensitive to light irradiation, get excited via two-photon absorption (TPA) and form initiating species of radicals or cations. Radical, also known as free radical, refer to an atoms or iron with unpaired electrons formed by splitting of covalent bonds of compound molecules under external conditions such as light[150]. The radicals react with monomers, producing monomer radicals, which combine with new monomers and finally create a polymerization reaction. This process can be described by several steps[151,152]:

Initiation step: $I \xrightarrow{\text{light}} I^{*} \rightarrow R^{\cdot}$

Chain propagation: $R^{\cdot} + M \rightarrow RM^{\cdot} \rightarrow RMM^{\cdot} \ldots \rightarrow RM_{n}^{\cdot}$

Final step: $RM_{n}^{\cdot} + RM_{m\rightarrow}^{\cdot}R_{m+n}R$

Here I is the photoinitiator, I^{*} is an intermediate state of the photoinitiator after absorbing two photons, $R^{\cdot}$ is a radical, M is the monomer (n, m indicate the number of the monomer in the chain reaction).

Due to the quick development in micro/nano devices, microelectromechanical systems, biosensors, the demand for high-speed and effective nano-manufacturing technique becomes more and more urgent. Under such circumstances, two-photon polymerization (TPP) providing a 3D nanofabrication with a spatial resolution about 100 nm is a highly competitive method[151].

2.3.1 Basic mechanism of TPP

Compared to one-photon polymerization (OPP), the photoinitiator of TPP is excited by its two-photon absorption of light, which is a nonlinear process that helps to achieve smaller polymer volume, leading to precise position controlling of the active medium.

The energy for activating initiators in TPP polymer is provided by absorbing two near-infrared photons simultaneously though a single quantum event whose energy corresponds to the UV region of the spectrum. The basic TPA mechanism is illustrated in Figure 2.10.

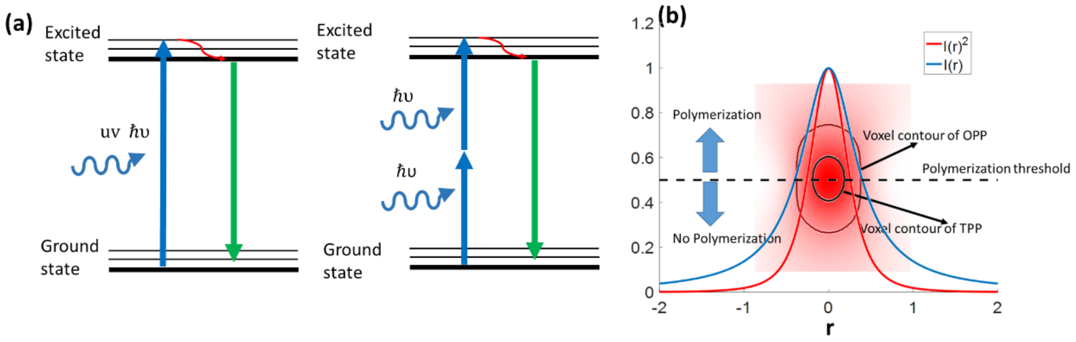

Figure 2.10 Basic schematic representation of the difference between single-photon polymerization and two-photon polymerization. (a) left, the single-photo excitation process, right, the two-photon excitation process. (b) Different polymerization voxel of the resin by OPA and TPA.

Corresponding to the actual situation of the experiment, suppose the laser of Gaussian beam is focused on the sample plane, then the intensity distribution at the focal plane (z=0) can be represented with the following relation

$$I(r) = I_0(\frac{-2r^2}{{w_0}^2}) \tag{2.2}$$

where I_0 is the beam intensity at the central axis in the focus plane, w_0 is the beam waist is and r is the radial distance along the cross-section. The photon intensity at r along the cross section and z in the propagation direction from the center can be expressed as follows[153]:

$$I(r,z) = I_0(\frac{{w_0}^2}{w(z)^2}) \cdot e^{\frac{-2r^2}{w(z)^2}} \tag{ 2.3}$$

$w(z)$ is the radius of the focused beam spot at position z, it is proportional to z. The polymerization rate of TPP is proportional to the square of photon intensity, $p \propto [I(r,z)]^2$ which means the polymerization interaction region is strongly confined at the focus center, both in the axial direction and propagation direction, contributes to a higher 3D spatial accuracy, illustrated in Figure 2.10 (b). However, it also means the sample must be controlled strictly in the effective focal area, otherwise, polymerization will not be triggered, or the polymers will not be fixed on the substrate after rising as what we illustrate in Figure 2.11.

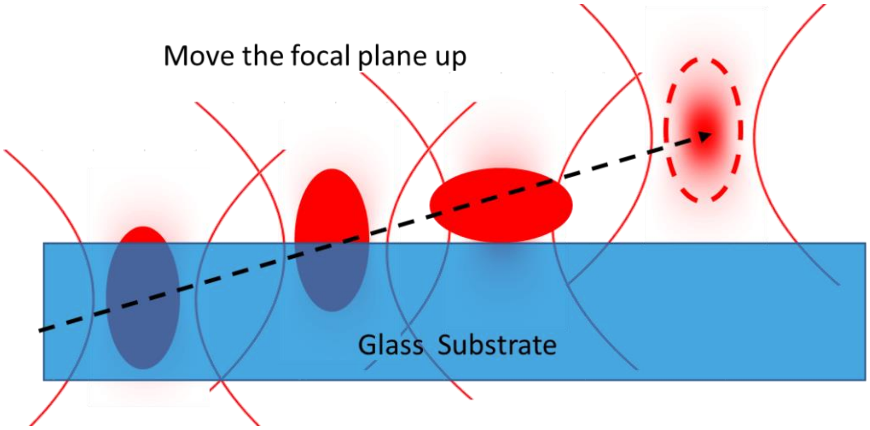

Figure 2.11 Effective voxels of polymer formed at different focusing level.

2.3.2 Threshold of TPP

During polymerization, there are other side reactions[151] that are shown in Figure 2.12. An initiator gets excited from the ground (S0) to the first excited (S1) singlet state by absorbing two photons, whose energy equals to the subtraction of the two energy states. Then, it relaxes by transition to the triplet state (T1) via intersystem crossing, where the co-synergist amine contributes to producing radicals for photopolymerization. The chain propagation reaction finally brings out a polymer 3D network.

The side reactions, such as the deactivation of the molecule and the radical peroxidation by oxygen, lead to competition between the main polymerization and inhibition of the polymerization, resulting in a threshold dose to initiate polymerization, defined as the minimum dose below which no polymerization occurs. Significantly, the effect of radical peroxidation, generating much fewer active radicals, reduces polymerization efficiency. Hence, the two-photon photopolymerization threshold is generally due to the presence of oxygen[152].

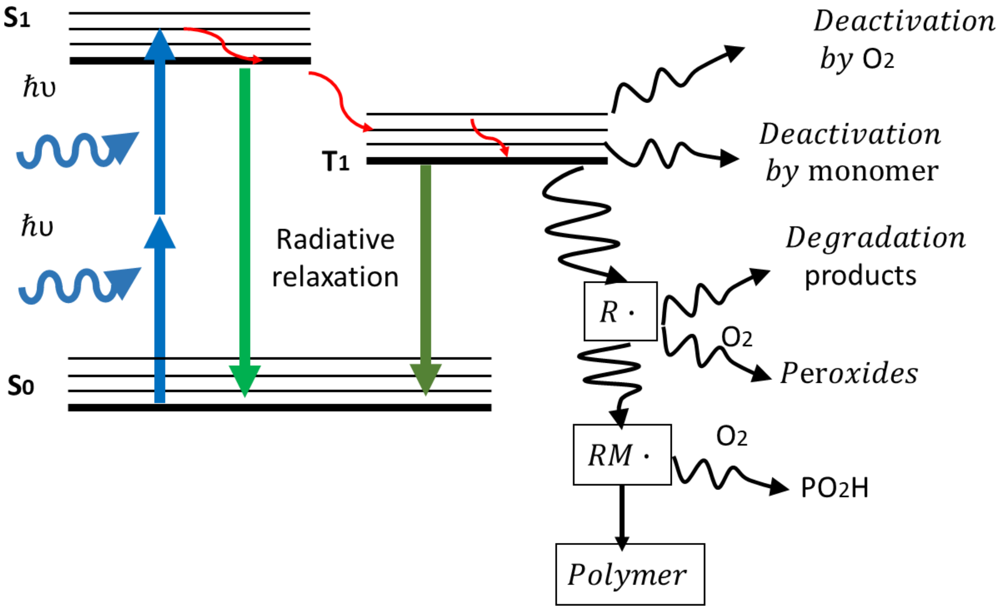

Figure 2.12 Energy diagram for two-photon excitation and processes occurring in the TPP procedure.

In our case, before the fabrication of hybrid nanostructures, the determination of the polymerization threshold is crucial because our approach is based on plasmon-assisted of the threshold dose while the far field incident dose is always smaller than the threshold (see Chapter 1). We measure the threshold dose of our homemade formulation on the same substrate as the one we use for the preparation of the sample and using the same geometry for illumination (focused laser, normal incidence, see section 2.6). According to the process of TPP, for a given formulation, the threshold dose depends on the wavelength of the incident power, the exposure time, and the light intensity[154].

It is crucial to choose the appropriate incident wavelength for efficient plasmonic polymerization on the metal nanoparticles. This wavelength should match the photoinitiator's effective absorption band and be close to the LSPR of the metal nanoparticles within the formulation. Another point to note is the threshold value of a given formulation is subject to changes during storage time, which can be an important issue because TPP is very sensitive to the threshold value. Consequently, the threshold dose determination must be done before every series of exposures. To determine the threshold for a given incident wavelength, we can vary the power and keep the exposure time constant or vary the exposure time and keep the power consistent. We decreased the incident dose step by step and observed polymer dots' changes through the camera simultaneously until the polymer dots disappear. The minimum dose before the polymer dot disappeared is the threshold. The polymer voxel change corresponds to the modification of the transverse and longitudinal dimension of the obtained polymer dot. Figure 2.13 gives an example of the polymer size changes as a function of the incident power with fixed exposure time. The size is represented by the transverse diameters of the polymers dot.

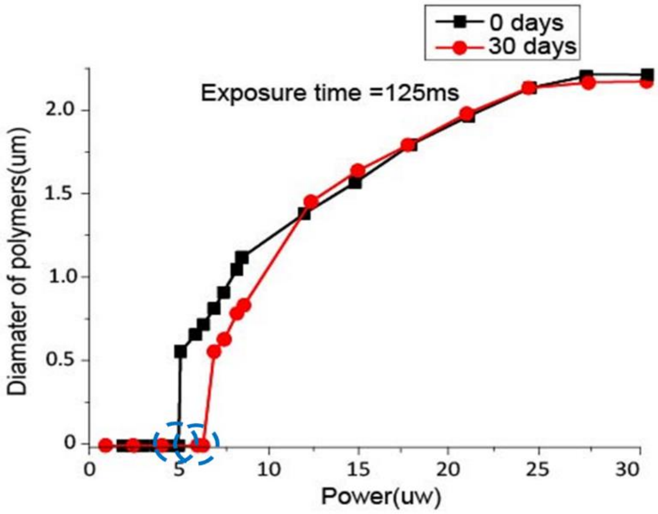

Figure 2.13 Polymer diameter varies when the incident dose increase. The black square represents the fresh formulation; the red round points represent the formulation after 30 days.

From Figure 2.13, based on observation of polymer dot sizes, the fresh formulation has a threshold about 5 μw/cm^2. After 30 days after, this threshold is slightly shifted to 6 μw/cm^{2}bigger than 5 μw/cm^2 with old formulation.

2.3.3 A powerful tool: the Nanoscribe system

TPP has potential use in fields such as photonics, optoelectronics, biology, micro- machines, and MEMS, and so forth. These applications benefit from direct laser writing ability, which allows for the fabrication of computer-generated 3D structures. Nanoscribe GmbH supplies such a commercial system used for multiscale nanoimprinting by TPP. This set-up, shown in Figure 2.14, is combined with the software package. A liquid photopolymerizable formulation is coated on a substrate which is mounted on an XYZ positioning stage. A pulsed Ti: sapphire laser at 780 nm is used as an irradiation source. The laser beam is focused by a microscope objective immersion lens (100×, Zeiss oil lens with N. A=1.4). The substrate is scanned through the volume of the photosensitive material to expose certain areas; the scanning path is designed and driven by the computer. Polymerization occurs only where the laser energy density exceeds a threshold value, which occurs in a small 3D volume near the focal point. Hence, arbitrary 3D complex patterns can be written by this system.

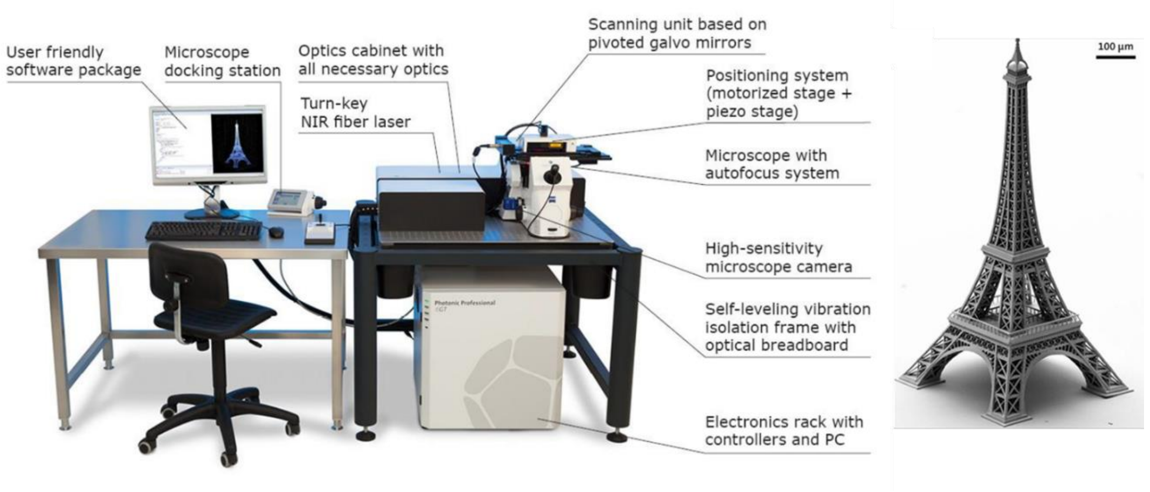

Figure 2.14 Nanoscribe set-up and a 3D print example fabricated by it[155].

2.4 Formulation preparation

As mentioned in Chapter 1, section 1.5 , Plasmon triggered near-field polymerization needs the overlapping between polymer absorption spectrum and the nanoparticle Plasmon resonance. Therefore, in addition to the metal nanoparticle itself, the photopolymerizable formulation is another crucial element. This section aims at describing the details of the formulation and its preparation process.

2.4.1 Chemical components for TPP formulation

According to the theory of photopolymerization described in section 2.3.1 , the primary basic photopolymerizable formulation contains two components: a monomer and a photoinitiator. We mix together PETA (pentaerythritol triacrylate), a well-known multifunctional acrylate as the monomer, and 1%wt Irgacure (IRG) as the photoinitiator to prepare the liquid photopolymerizable formulation. PETA has a transparency in the visible that does not influence the visibility of MNPs under dark-field microscopy that helps us achieve point-to-point exposure for TPP. Iragure819 is a versatile photoinitiator for radical polymerization of unsaturated resins upon UV light exposure, which is suitable for TPP. Figure 2.15 (a) and (b) show the molecular structure of PETA and Iragure819 respectively.

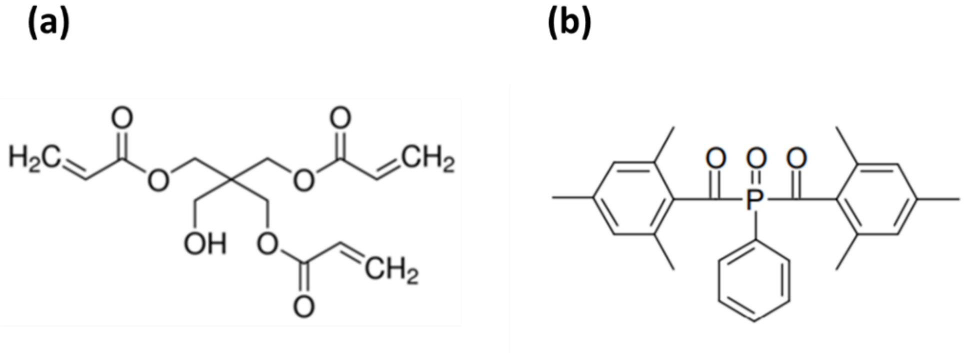

Figure 2.15 Molecular structure of the components of formulation: (a) PETA, (b) Iragure819.

Different QDs will be mixed with this basic formulation for the needs of different emission wavelengths or for matching the LSPR of different samples. Our QDs are synthesized by the colloid chemistry method[156] that has been developed rapidly in recent years. This method is pretty simple, easy (although is requires some experience) and low cost, which makes it a more common way of preparing quantum dots in the laboratory. Size and morphology of quantum dots prepared by colloidal chemistry are easy to control. The surface of quantum dots can be modified according to different needs during the synthesis process. Commonly, for preparation of the photopolymerizable formulation, the prepared QDs are dispersed in PETA with a 5 mg/mL concentration under vigorous magnetic stirring. Then 1% IRG 819 is added into the PETA solution to get the final formulation for making hybrid nano-emitters. The above is the most basic reagent used in this thesis. It changes slightly according to the different needs. For example, the monomer can be associated with particular functional group for attaching QDs or adding radical inhibitor for higher spatial resolution[157].

2.4.2 Formulation characterization

- **Two-photon absorption in formulation**

The absorption spectrum of the mixed formulation varies with different concentrations of IRG819. The absorption of classic formulation (1%Irgacure 819 solved in PETA) was collected by a CARY 100 UV-visible spectrometer shown in Figure 2.16. It has an effective absorption of light from UV to 450 nm, which means the effective spectral range for two-photo absorption falls in the range from 680 nm to 900 nm.

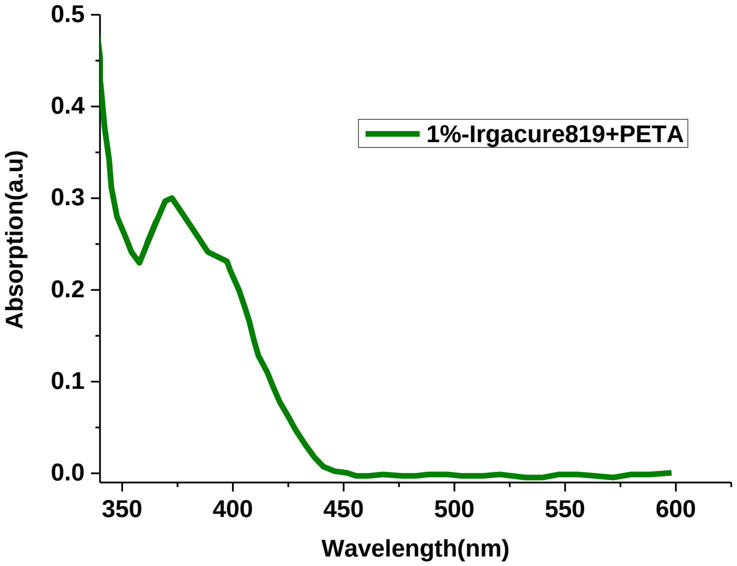

Figure 2.16 Absorption spectrum of 1%Irgacure 819 solved in PETA, measured CARY 100 UV-visible spectrometer.

However, the absorption spectrum measured by UV-visible spectrometer is precisely the spectrum of single-photon absorption. Measuring directly the two-photon absorption spectrum is complicated. To analyze the two-photon absorption of photopolymerizable formulation, we can measure the size of polymer dots under the same exciting power at different incident wavelengths and use the size change trend as a judgment. It also allow us to preliminarily determine the effective excitation wavelength range and rough threshold. Figure 2.17 gives an example of the polymer size changes along the incident wavelength.

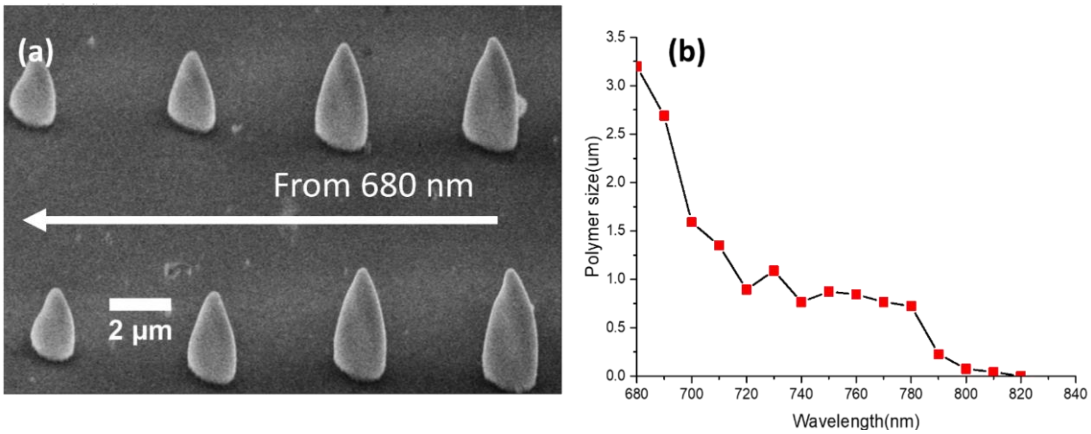

Figure 2.17 Two-photon absorption spectral sensitivity of formulation (1%Irgacure+Red QDs grafted PETA). (a) SEM image of two lines of polymer dots, they are polymerized by same incident dose (25mw 125ms) with exciting laser wavelength varies from 680 nm (right) to 720 nm (left) .(b) Diameter of polymer dots changes as a function of the exciting wavelength varying from 680 nm to 820 nm.

◆ **QDs characterization**

Figure 2.18 (a) shows the absorption and emission spectra from green and red CdSe/ ZnS QDs in toluene solution. Figure 2.18 (b) displays the Photoluminescence image from homemade photosensitive formulations containing these two kinds of QDs under the illumination of a UV LED lamp.

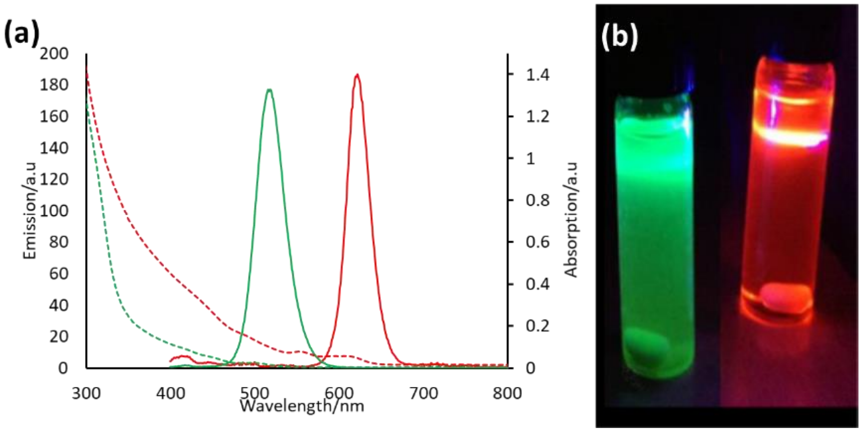

Figure 2.18 (a) Absorption and emission spectra of green and red CdSe/ZnS QDs in the Toluene solution. (b) Photoluminescence images of QDs-containing formulation illuminated by a UV lamp.

We use AFM and SEM in combination to characterize the nanostructures and the hybrid structures. However, neither of these two techniques can observe the QDs inside the polymer. Transmission electron microscopy (TEM) is a technology whereby a beam of electrons is transmitted through a specimen to form an image. It has a higher resolution than SEM and offers valuable information on the sample's inner structure, such as crystal structure, morphology, and stress state information. It can be used to observe the trapped QDs inside the thin polymer layer. Figure 2.19 (a) shows a TEM image of CdSe/ZnS (620 nm) QDs directly on the substrate, and Figure 2.19(b) shows the TEM image when QDs are trapped in a thin layer of polymer.

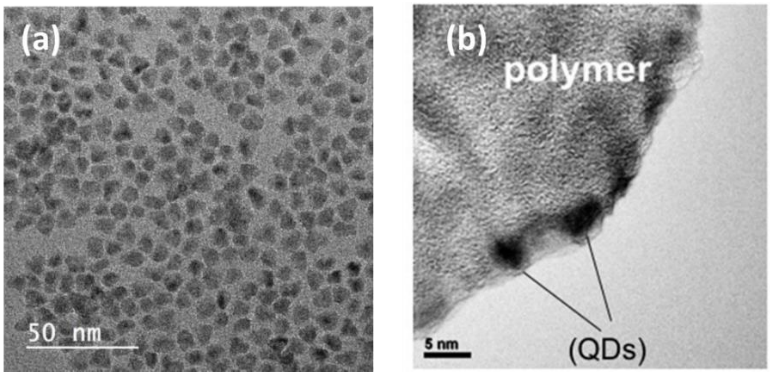

Figure 2.19 TEM images of CdSe QDs (620 nm). (a) Free space QDs deposited on substrate, obtained from our college Dr. Farid Kameche in Mulhouse. (b) QDs inside a thin polymer layer.

For TEM measurement, the samples should be prepared in a special way. Typically, metal nanoparticles should be mounted on a TEM grid for analysis. The standard TEM grid has a 3mm diameter and supported by a 50 nm silicon nitride support film as the transparent window, the small size and easy-broken filmmaking this step more complicated than it is for SEM and AFM. For our hybrid nanostructure, firstly, good distribution is necessary. Besides, the rinsing and drying of the TEM sample is trickier because the TEM grid is fragile. In our case, the QDs' distribution position is critical for analyzing their interaction with metal nanoparticles. TEM provides a direct method of observation of QDs trapped inside the polymer and is currently the only method permitting this obervation. Nevertheless, for polymer material thicknesses > 10 nm, the embedded QDs are hardly discernible on TEM images, the observation of QDs within thin polymer allowed us to roughly access the volume density of QDs within the polymer. This the reason why only the QDs at the edges at the polymer can be observed in Fig. 2.19 (b)

2.5 Optical configuration and Procedure for fabrication

In section 2.3.1 , we have described the mechanism of TPP, which is a non-linear optical process based on the simultaneous absorption of two photons in a photosensitive material and requires high intensities. Several requirements need to be met for initiating surface plasmon-triggered TPP on a single nanoparticle. Firstly, we need sufficient light intensity density; secondly, we have to make sure that the spot's position is consistent with the position of the nanoparticles. Thirdly, the high quality of the focused light spot is required. The optical path of the incident laser used for exciting, localized surface Plasmon is illustrated in Figure 2.20.

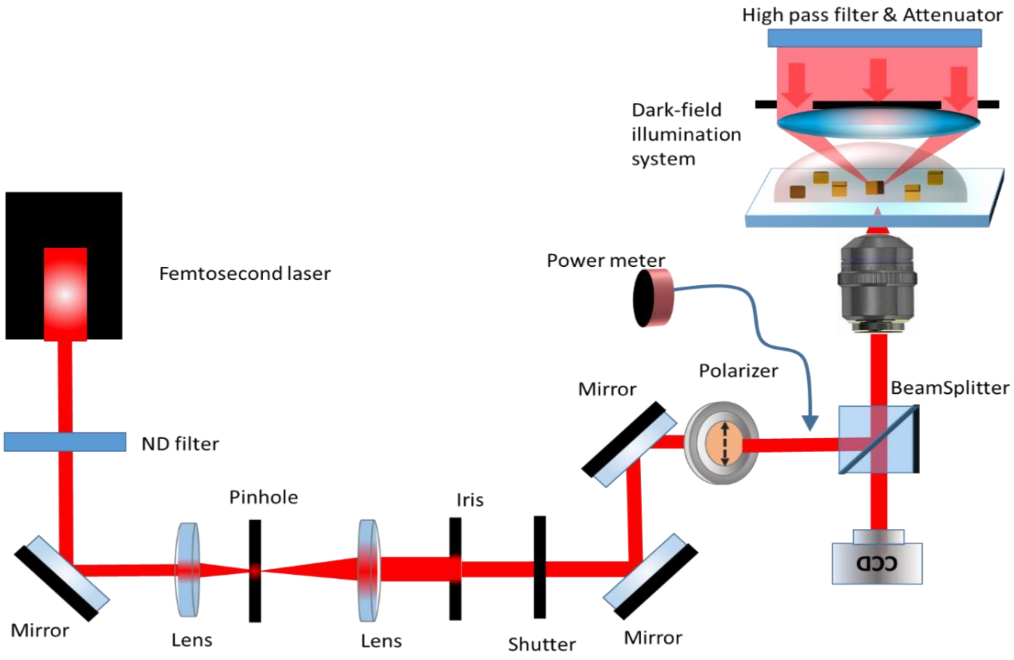

Figure 2.20 Scheme of optical configuration for Plasmon-based Two-photon polymerization on single nanoparticle.

A femtosecond Ti:Sapphire laser is focused by an objective lens(N.A=0.6) at a single nanoparticle observed by dark-field white light illumination. The light illumination source used for dark-field is attenuated by a 540nm high-pass filter to avoid unwanted polymerization from UV/blue light. The available wavelengths of the Ti:Sa laser range from 680 nm to 1080 nm, which match pretty well both the LSPR of the metal nanoparticles (e. g. see Figure 2.6) and two-photon absorption spectral properties of the photopolymerizable formulation (e.g. see Figure 2.17)

The homemade Keplarian beam expanding system composed of two lenses with a pinhole at the intermediate focus plane is used for better spot quality. The laser intensity is controlled by a continuously variable metallic neutral density filter. A linear polarizer is added for modifying the direction of the incident polarization direction. It is easy to add another quarter-wave plate for changing linear-polarization to circular-polarization. An electronic shutter controls the exposure time. The incident laser power is measured before the microscope lens. The threshold dose D_{th}must be identified firstly, and the position by the laser spot should be marked on the CCD camera at the beginning of every experiment. D_{th} is assessed easily by keeping exposure time at 125ms and decreasing the laser intensity step by step. The smallest intensity before the polymer dot disappeared is chosen as the threshold intensity. In the case of the example shown in Figure 2.21, the volume of polymer dots decreases as the incident power decrease, and when the power arrived at 7mw, no polymer dots can be observed. Then 7.5mw with an exposure time of 125mw can be defined as the threshold of this formulation.

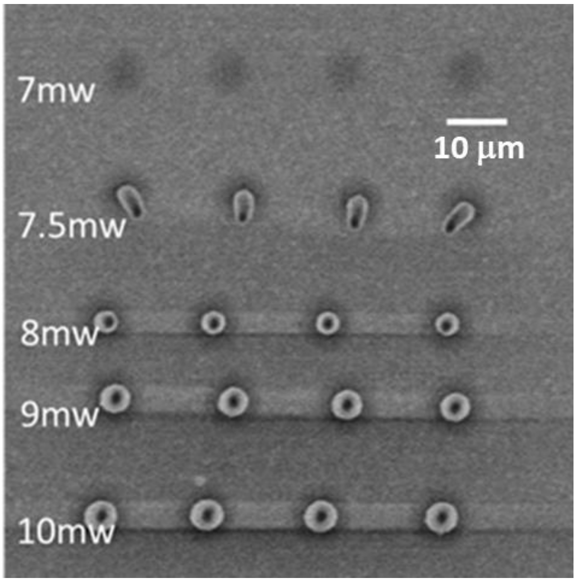

Figure 2.21 SEM image of the polymer dots fabricated using decreasing incident power. The exposure time is kept as 125ms.

In order to avoid any changes in light path and polarization, after threshold energy is found, we replaced the sample to the focus plane directly. Each targeted isolated single particle will be then moved in the laser focus area by a stepper motor stage and exposed at an intensity below the threshold. A drop of photosensitive formulation is deposited on a pre-identified gold nanoparticle. A Ti:Sa pulsed femtosecond laser with adjustable wavelength isused as the excitation light, whose wavelength should be chosen to fit IRG819 two-photon absorption (Irgacure819 presents strong one-photon absorption in the 350-450 nm range, refer to Figure 2.16) and lies inside plasmon resonance in the presence of the polymerizable solution. Incident light is focused (1.6 μm spot, N.A objective lens=0.6) from under the substrate onto the substrate top surface, allowing one to address a single pre-identified gold nanoparticle. Incident power dose is used to adjust the incident dose $D_{in} = p \cdot D_{th}$, where p < 1.

After exposure, the sample should be rinsed with acetone, hydrochloric acid solution, and isopropanol, each process last 10 minutes. Excess of QDs and the liquid formulation was efficiently removed from the substrate by this process. Finally, we get QDs-contained polymers obtained around the particle absolutely indicate the correlation mapping of the Plasmon near-field distribution.

2.6 Results Analysis

2.6.1 Polymer characterization

As we mentioned in section 2.2.2 , SEM and AFM were used as the main tools for characterizing both bare nanoparticles and hybrid nanoparticles. In general, from the AFM images of hybrid nanostructures after exposure, we cannot obtain the polymer elongations directly. The AFM topography of the hybrid structure after exposure minus the one before exposure. The resulting image represents the three-dimensional distribution of the polymer obtained by surface plasmon triggered polymerization. Similarly, we can also get the difference image through the SEM images before and after exposure. In addition, the simplest method is to use the difference in contrast between polymer and metal materials under high voltage to obtain the elongation length of the polymer directly, see Figure 2.9 (b). However, this method needs to avoid the interference of structural collapse caused by long-term electron beam exposure and the complete destruction of QDs.

2.6.2 Photoluminescence measurement

The photoluminescence signal from the hybrid structure was analyzed by a spectrometer coupled to an inverted optical microscope (Olympus IX71); a similar system indicated in Figure 2.6. We used a 405 nm continuous laser to excite fluorescence. A 50× objective lens then collected the signal (N. A=0.8). It was also used to focus the 405-nm excitation light onto single hybrid nano-emitters and separated from the laser excitation using a 514 nm long-pass filter. For single hybrid nano-emitter measurements, image mode is used with the slit fully open, and the laser spot was first modified to the center and marked on the CCD image. After aligning the targeted single nanoparticle to the mark, spatial filtering is made by adjusting the slit size to detect an area less than 1µm × 1µm, ensuring single object signal measurements. A half-wave plate cooperated with a linear polarizer controlled the polarization direction. The emission spectrum must be measured from a single isolated hybrid structure. Usually, the integration time of measuring a fluorescence spectrum was set to 50 s to eliminate data errors caused by instability and other influences from the environment. Its intensity was decided by the QDs' concentration, the polarization direction of the exciting laser, coupling effect between QDs and nanostructures (See details in Chapter 3).

2.6.3 Time-resolved Photoluminescence measurement

When the number of QDs captured in the hybrid structure is reduced to a few or even one, the resulting single-photon source can be characterized by the second-order autocorrelation function $g^{(2)}(0)$, which can be measured using the Hanbury Brown and Twiss experiment[158]. As Figure 2.22 indicates, the light emitted by a single-photon source is sent to a beam-splitter and is evenly divided into two beams connected to two single-photon detectors APD1 and APD2, separately. The two APDs' outputs are sent to correlation electronics for measuring the coincident probability of detecting the arrival of a photon in channel 1 at time T and another photon in channel 2 at time $\mathrm{T}+\mathrm{t}$. Every pair of photons has an arrival delay time t. After many pairs of photons, a histogram of number of photon pairs with the time difference of arrival can be obtained. For an ideal single-photon source, at every period, only one of the APD detector record a photon, which means there is no pair of photons with no arrival time difference. The second-order correlation function gives the distribution of infinite pairs of photons. The normalized second order correlation function is defined as[159]

$$g^{(2)}(t) = \frac{\langle n_1(T) n_2(T+t)\rangle}{\langle n_1(T)\rangle\langle n_2(T+t\rangle} \tag{2.4}$$

where $n_i(T)$ is the number of photons recorded by APD_i at time T.

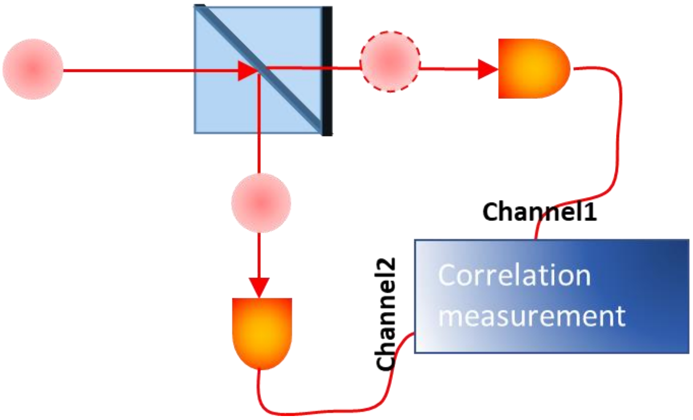

Figure 2.22 The schematic of Hanbury Brown and Twiss experiment

For an ideal antibunched single photon, $g^{(2)}(0) = 0$. However, for actual experiment, because of background, perfect $g^{(2)}(0) = 0$ cannot be obtained. Normally, the $g^{(2)}(0) < 0.5$ implies single photon[160].

Fluorescence lifetime is an inherent characteristic of fluorescent molecular clusters. It is extremely sensitive to the microenvironment where the molecules are located, such as PH, oxygen saturation degree, ion concentration, protein interaction, etc. Plasmon-emitter interaction, as we discussed in section 1.3.1 , causes the modification of the decay rate, corresponding to the lifetime change. Fluorescence characteristics of the hybrid polymer particle hybrid system including its emission intensity, spectral shape, and fluorescence lifetime, are an essential means to analyze the interaction between metal nanoparticles and QDs.

Time-correlated single-photon counting(TCSPC)[161] is a very broad technique for single-photon detection. It measures the Time-correlated counting of photons and can reflect the distribution characteristics of target photons in time, which is an indispensable method for characterizing emitter's decay. The basic scheme for TCSPC to measure fluorescence lifetime is illustrated in

Figure 2.23. High repetitive pulse laser (normally picosecond laser femtosecond laser) is used to excite the sample. In each pulse period, up to one photon is emitted by the sample, so at most one photon can be detected in each period. Timing is started from the moment of the trigger pulse and stops when a photon is detected, then the arrival time from 'start' and to 'stop' is recorded. After multiple periods, a large amount of data is accumulated; finally, the photon count distribution with a time of arrival can be obtained, equivalent to the decay profile of fluorescence. The lifetime can be calculated afterward by fitting the attenuation profile or other forms of data analysis.

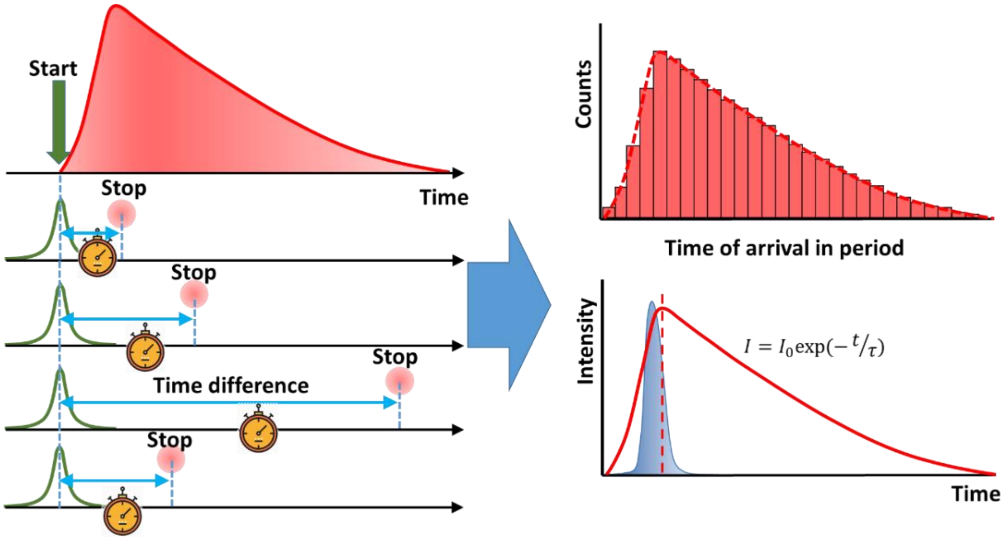

Figure 2.23 TCSPC technique for fluorescence lifetime analysis.

Generally, this distribution exhibits a single-exponential or multi-exponential decay depending on the amount of fluorescence lifetime components[162,163]. For a fluorophore excited by a pulse of light, in actual calculations, its fluorescence intensity decay characteristics can be defined as:

$$I(t) = \sum a_i \exp(-t/\tau_i) \qquad \sum a_i = 1 \qquad (2.5)$$

where a_i is the contribution of different fluorescence lifetimes, and τ_i is the lifetime of the species i. For most of the QDs, its fluorescence intensity changes as a single exponential decay $I(t) = \exp(-t/\tau)$. In actual experiments, the detected intensity is characterized by the interaction with the fluorescent background and the convolution with the system[161,164], so it can be expressed as

$$D(t) = [I(t) + background] \otimes IRF \qquad (2.6)$$

The total Instrument Response Function (IRF) contains all the time-spreading component from the pulsed excitation source and timing jitter of the electronic components, which characterize the time resolution of the TCSPC system. When a population of fluorophores is excited by an ultrashort or delta pulse of light and no time-spread effect from the system, the IRF also has a delta-function of $\delta(t)$, the time-resolved fluorescence will decay exponentially. The lifetime can be calculated very well by fitting the intensity decay profile using a single exponential function. In most cases, the fluorescence lifetime can be obtained by the least-squares fitting method, which minimizes the difference between the detected fluorescence decay curve and the theoretical intensity characteristics. However, when the signal curve decrease more quickly or the width of IRF is compared to the fluorescence decay curve, the lifetime of the decay function is then obtained by iterative re-convolution method.[165]

In this thesis, the Hanbury Brown & Twiss system using TCSPC was coupled with a confocal scanning imaging system built with the help from Professor Chiristophe Couteau and his team. Figure 2.24 shows the schematic diagram of this system.

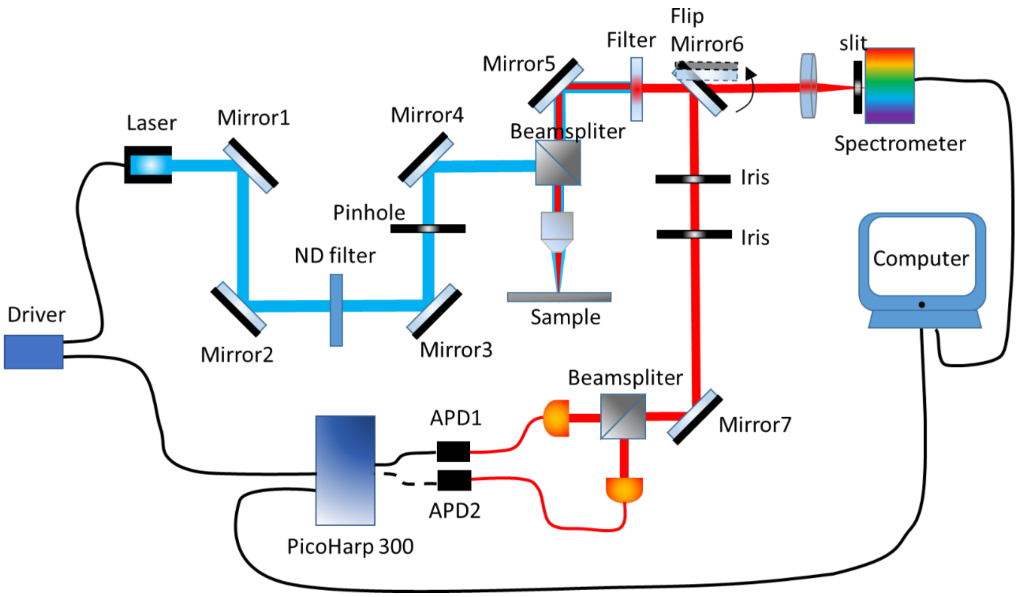

Figure 2.24 Schematic diagram of the whole Hanbury Brown & Twiss system, using TCSPC coupled confocal scanning imaging system

A pulsed laser (Picoquant LDH-P-C-405) connected with an extra driver box (PDL 800-B), whose repetition frequency can be modified from 80 MHz to 2.5 MHz. The laser beam is focused on the scanning sample hold stage by an objective lens of 100 x 0.95. Our sample of hybrid emitters is then excited to emit light its fluorescence wavelength. The fluorescence is collected by reflection, and then after removing noisy signals by an appropriate filter, the collected light is directed by a fiber towards an APD (Picoquant PMA- 182). The signal is sent to the stand-alone TCSPC Module (TimeHarp-300), which is linked to the laser driver. Then this system will record the fluorescence decay signal by a reverse start-stop mode, as we mentioned.

For single photon autocorrelation $g^{(2)}$ measurement, as we show in Figure 2.22we just need to divide the fluorescence signal to another path to work as a reference instead of the electric driver signal to perform the Hanbury Brown and Twiss experiment.

2.7 Summary

Chapter 2 introduces and describe all the experimental methods used during the thesis, including the sample and formulation preparation before exposure, the fabrication process of the hybrid nano-emitters, and the optical system used for two-photon polymerization whose principle is also briefly introduced in this chapter. These will help us realize hybrid nano-emitters based on specific nanoparticles in the following chapters. Finally, the methods of optical characterization of the fabricated hybrid nanosources have been presented. They include single-photon analysis and lifetime measurement.

Chapter 3 Polarization sensitive hybrid nano-emitters based on gold nanocubes and nanodisks

As already stressed in 0, although some methods have been proposed for localizing nano-emitters at strategic positions of plasmonic nanosystems, our method, in general, is a simpler approach to get on-demand, integrated hybrid plasmonic nano-sources with the controlled position of the active medium. Our team has completed many previous studies, and plasmon-triggered near-field one-photon or two-photon photopolymerization was used for imprinting near-field distribution firstly[135,136,166]. Recently, some groups have developed other near-field polymerization methods, where polymerization can be triggered via hot electrons directly[167], and more kinds of monomer materials can be used, such as aryl diazonium salts[168] and divinylbenzene[169].

In this chapter, using gold nanocubes and gold nanodisks and different modes of plasmon excitation, we report on the fabrication of advanced nano-emitters that are based on structured active medium with different degrees of symmetry in the vicinity of the metal nanoparticles. Figure 3.1 gives the corresponding schematic diagram of those hybrid nano-emitters. We will see that, due to the controlled spatial anisotropy of the active medium, the hybrid plasmonic nano-emitters are highly sensitive to the direction of polarization used for exciting the system. In addition, most importantly, after comparing the polarization sensitivity of different hybrid nano-emitters structured by gold nanocube and gold nanodisk, we proposed a concept of nanoscale spatial overlap between the active medium and the local excitation field order to interpret the photoluminescence properties of the hybrid nano-emitters.

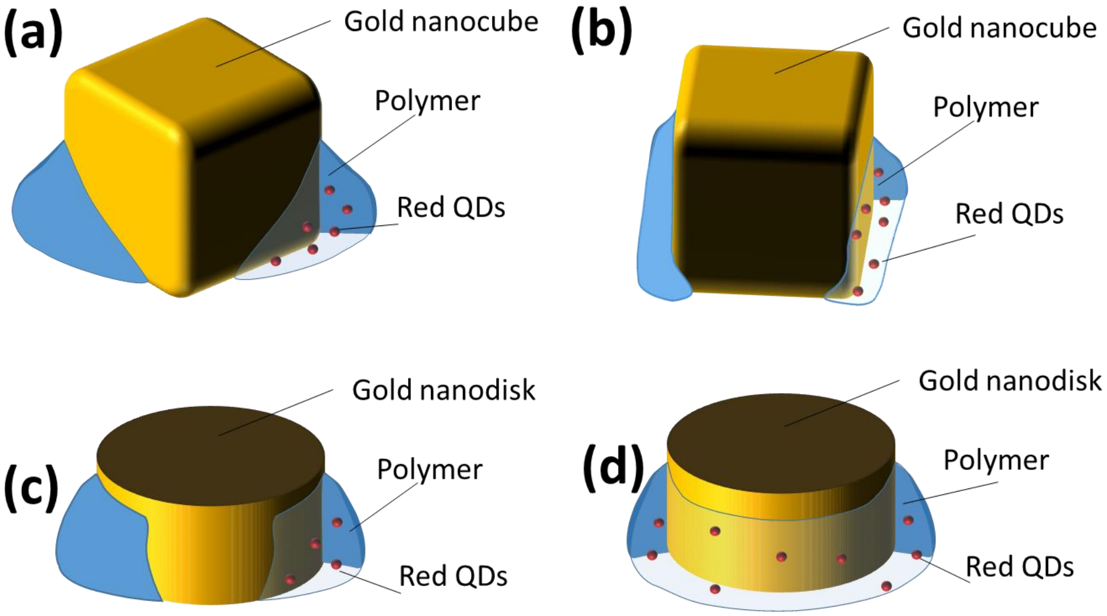

Figure 3.1 Schematic diagram of a hybrid nano-emitters fabricated based on gold nanocube and gold nanodisk by using different modes of plasmon excitation.

3.1 Anisotropic hybrid nano-emitters based on Au nanocubes

Gold nanocubes deposited on a substrate are nano-objects with a C_{4v} in-plane symmetry. A cube possesses three dipolar plasmon eigenstates of E and A1 symmetry respectively. The two degenerated E modes correspond to the two charge combinations (0, 1, 0, -1, 0, 1, 0, -1) and (1, 0, -1, 0, 1, 0, -1, 0), where the number sequences represent the top and bottom corner positions. These orthogonal eigenvectors correspond to the diagonals of the top and bottom faces. The A1 dipolar mode corresponds to a unique eigenstate vector. Its polarization is aligned along the z vertical axis and can be described by the charged corner sequence (1, 1, 1, 1, -1, -1, -1, -1). All these resonance states can be selectively excited via a proper choice of the polarization of the incident light field[144].

Our plasmonic samples consist of gold nanocubes deposited on an Indium Tin Oxide (ITO)-coated glass substrate. The surfactant of CTAB used during the synthesis of the Au cubes is totally removed before TPP. And all the cubes used for fabrication are selected with perfect shape and clean surrounding, checking by AFM and SEM. During TPP process, these randomly dispersed selected cubes were exposed one by one in a certain order. Due to their different orientations, the plasmon mode excited by each cube is different, resulting in different hybrid structures.

3.1.1 Characterization of Au nanocube

In order to characterize the gold nanocubes and the resulting hybrid nano-emitters, SEM, AFM, dark-field white light imaging/spectroscopy, and micro-photoluminescence techniques were used (see Chapter 2). Controlling the cube solution's concentration within an appropriate range allowed us to address single nano-objects (averaged density of 0.1 nanocube/µm²). Figure 3.2shows a typical set of AFM, SEM images, and the size distribution histogram of 100 randomly selected cubes, showing an average side length of 127 nm±3nm. By AFM and SEM, the orientation of a nanocube can be characterized clearly.

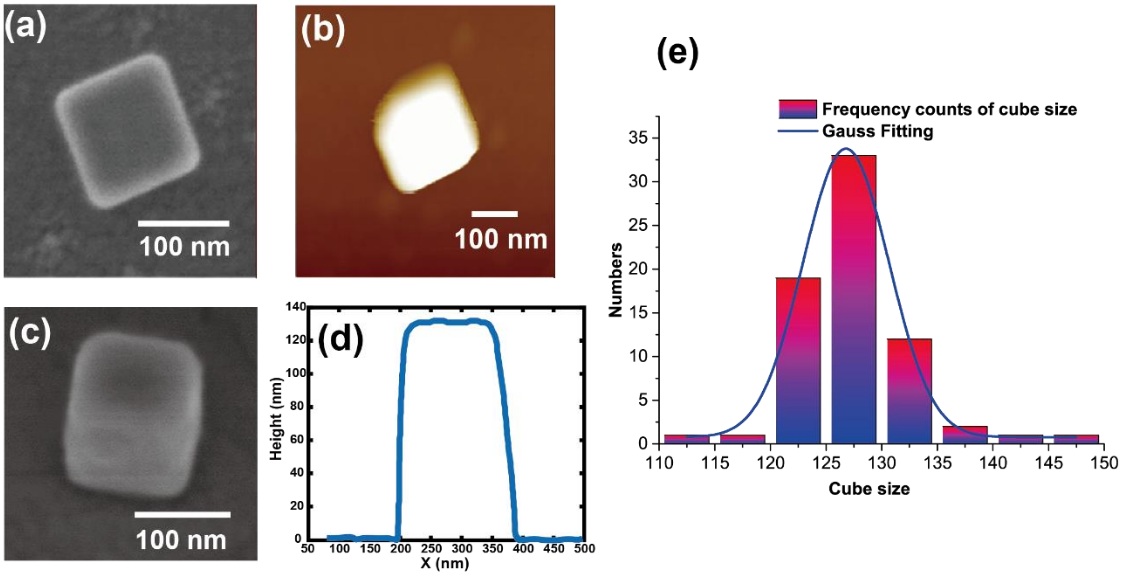

Figure 3.2 Characterization of the morphology of gold nanocubes deposited on a glass substrate. (a) SEM image of a representative single gold nanocube. (b) AFM image of the same nanocube. (c) Tilted SEM image under 3D view. (d) AFM height profile along the axis marked by a black dashed line in (b). (e) Size (edge length) histogram obtained from a set of 100 nanocubes (SEM analysis).

As discussed in section 2.2.2 (chapter 2), the morphology image obtained via AFM has errors due to the tip convolution effect, while the actual height can be precisely measured. Conversely, SEM can allow one to get more accurate two-dimensional size information but not height, unless the sample is tilted. Figure 3.2(c) and (d) show SEM and AFM images reflecting the height information. In particular, Figure 3.2(d) shows the accurate height of 130 nm of this nanocube.

Au nanocubes present LSP resonance wavelengths λ_{Lsp} at which the electromagnetic field can be locally enhanced. Moreover, considering photopolymerization, there is an optimal excitation wavelengthλ_{exc} corresponding to the photopolymer's one-photon absorption peak wavelength λ_{abs} . Our near-field two-photon polymerization based on Au cubes, needs to make these several wavelengths as consistent as possible, which means $\lambda_{Lsp} \approx \lambda_{exc} \approx 2 \cdot \lambda_{abs}$. It makes importance for measuring and simulating cube's scattering spectrum to check its resonance wavelength. Numerical simulations of scattering spectra and field distribution were carried out using the finite difference-time domain-method (FDTD Solutions, Lumbrical). We build the cube model using the size parameters measured from AFM and SEM, and the gold refractive index is set using the Johnson & Christy data[170]. Figure 3.3(a) illustrates the configuration of the model used for FDTD calculations.

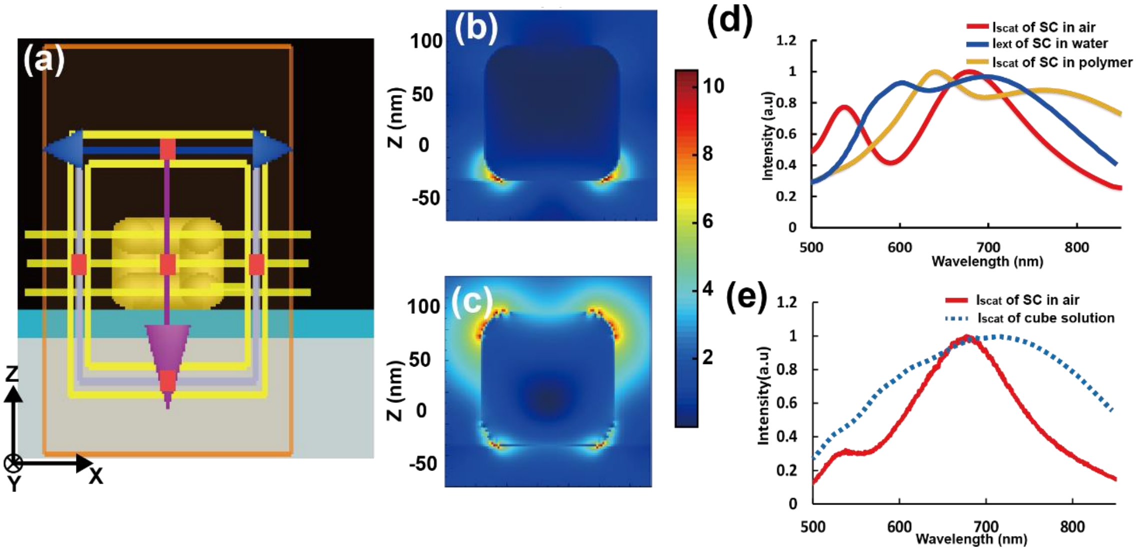

Figure 3.3 FDTD Calculation of the optical properties of an Au cube deposited on ITO-coated glass substrate. The thickness of the ITO layer is 40 nm, with refractive index of 2. (a) Illustration of the Model (b)(c) Field modulus map at the middle cross-section parallel to yz plane to of the cube excited by wavelength λ=670 nm and λ=540 nm, respectively. (d) Normalized calculated scattering spectrum of a single nanocube (SC) in air (red curve) or in polymer (index=1.48, orange curve) and the normalized extinction of a SC in water (blue curve) (e) Normalized experimental scattering spectrum of a single gold nanocube in air on ITO-

coated glass substrate (red curve) and measured extinction spectrum from cube solution (water solvent, blue dotted line)

According to Figure 3.3(b) (c), gold nanocubes presenting an in-plane dipolar plasmonic mode at 680 nm in the air mainly from the bottom face towards the substrate, and another plasmonic mode at 540 nm mainly from its top face towards the air. Besides, the 680 nm mode gives higher near-field enhancement. The top and bottom face's different performances can be explained through the mode-mixing coming from symmetry-breaking induced by the substrate[171,172]. In our case, we focus on the resonance position and the field enhancement at the peak wavelength. In Figure 3.3 (d) and (e), when the cube is immersed in air, the simulation model leads to a scattering spectrum that is in good agreement with our experimental. In addition, the calculated extinction spectrum from a single cube immersed in water also in agreement with the real extinction spectrum from cube solution reflecting the ensemble results of all the particles in water including gold nanocubes and spherical impurities. If the polymer formulation is taken into consideration, its higher refractive index has to be considered. From ellipsometry measurements its value is in the 1.48−1.52 range, depending on the rate of reticulation. According to the calculation, the scattering peak corresponding to the dipolar plasmon mode shifts to 780 nm when the cube is immersed in a material with a refractive index of 1.5 (Figure 3.3(d), blue curve). This situation corresponds to the experimental one during TPP.

3.1.2 Near-field imprinting via TPP on single nanocube

After characterization of single Au nanocube on substrate, a drop of the photopolymerizable formulation is deposited on the sample. Here we use a formulation prepared by 1 %wt Irgacure 819 and 0.1%wt QDs with an emission wavelength of 620 nm solved in PETA. For exposure, a femtosecond laser with a wavelength of 780 nm is used. This whose wavelength is in the effective spectral range for two-photon absorption from 680 nm to 900 nm and lies inside the nanocube in-plane dipolar plasmon resonance in the presence of the polymerizable solution (see Fig. 3.3(d), blue curve). Here, different incident doses are used for exciting, the exposure time was kept at 125ms, and average incident power at the sample plane is in the 40-400 μW range, resp. [0.5 – 5.0 kW / cm²], allowing us to adjust the incident dose $D_{in} = p \cdot D_{th}$ where p is from 10% to 90%, changed by 10% as a step, *D_{th}* is the threshold dose of TPP, it has been predefined using the method described in section 2.3.2 , chapter 2.

The polarization state of the 780 nm curing light is always linear-polarized along the X-axis. It is worth to be noted that the bottom edge of the substrate is defined as the X-direction, which is also the reference for calibration of the orientation of each isolated single cube. Figure 3.4 shows the AFM images of several Au nanocubes with different orientations before and after exposure under incident dose $D_{in} = 40\% \cdot D_{th}$.

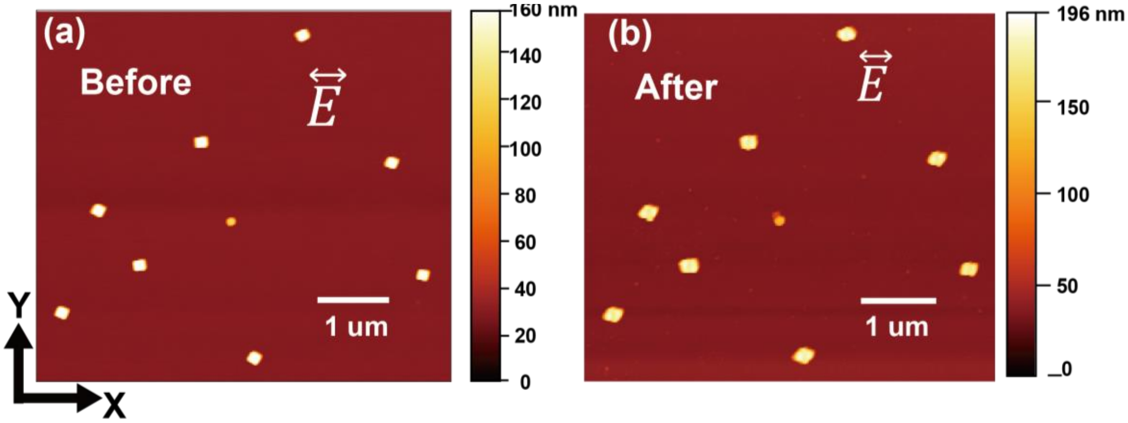

Figure 3.4 AFM images of the same region (a) before (b) after polymerization on the same sample of these 127 nm Au nanocubes. Incident light was linearly polarized parallel to the bottom side of images, along the X axis

Because our approach is based on the photopolymerization triggered by enhanced localized near-field, the polymer lobe obtained are expected to imprint the spatial distribution of the enhanced near-field of MNPs. Figure 3.5(a,c) exhibits SEM images of resulting Au/polymer hybrid nanostructure fabricated on nanocubes with two typical orientations of the incident polarization used for TPP. The corresponding computed near-field distributions are also shown (Figure 3.5(b,d)). The presence of QDs inside the polymer does not prevent the two-photon polymerization process[157]. The SEM images in Figure 3.5are obtained with an accelerating voltage of 10 kV leading to significantly different contrast between gold and polymer, where the polymer part appears more transparent.

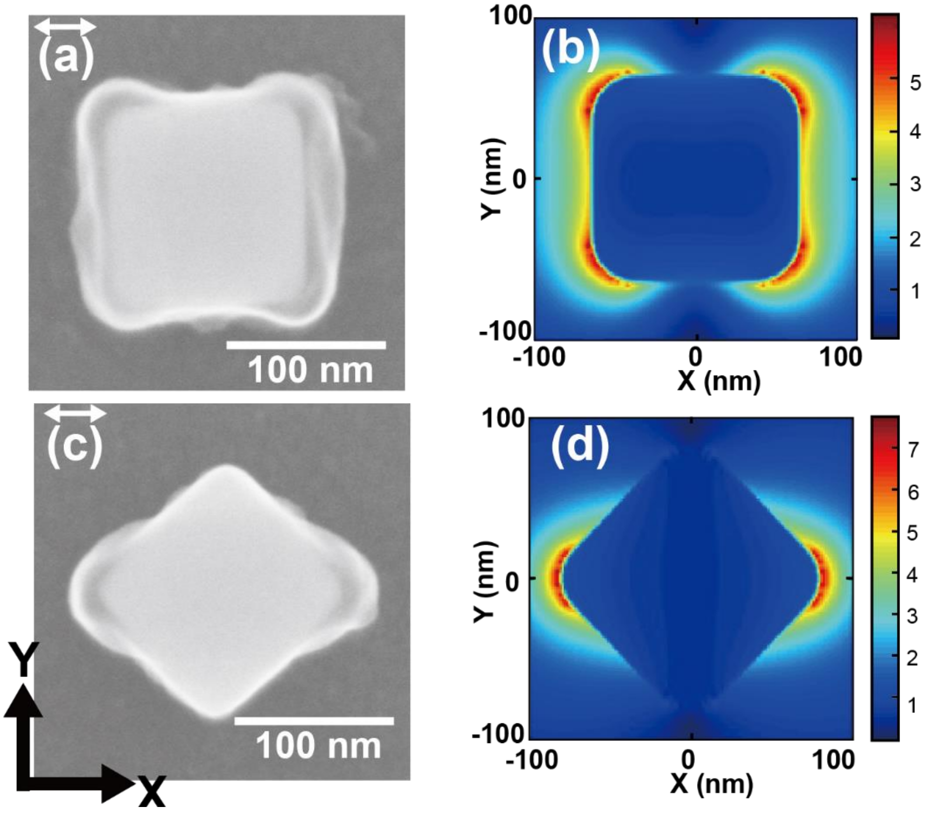

Figure 3.5 Gold nanocube-based hybrid nanostructure made by plasmonic two-photon polymerization ($\lambda = 780nm$). SEM images of the hybrid structures obtained with incident polarization along the x-direction (see white arrow (a) top side edge parallel to the incident light and (c) diagonal parallel to the incident light. (b), (d) FDTD maps (at 25 nm distance from the substrate) of field the modulus ($\lambda = 780nm$) in the vicinity of the gold nanocube within polymer, in the case of (a) and (c) respectively.

3.1.3 Polymer elongation measurement

The polymer elongation, in other words polymer thickness, is the distance from the metal surface to the edge of the integrated polymer lobe. It can be measured by SEM or AFM. As we introduced in section 2.2.2 , the difference topography AFM images subtracting the original cube from the hybrid polymer-coated nanocube, provide an image of the polymer spatial distribution. Examples are shown in Figure 3.6. The cross-section profile of the polymer region is shown in Figure 3.6(b) and (d), giving the polymer height information along the white dotted line indicated in Figure 3.6(a) and (b), respectively. From these figures, the cube's right side and left side are slightly asymmetric which may be caused by the tip's tilt angle or non-perfect shape. This asymmetry is not real information of the cube's profile.

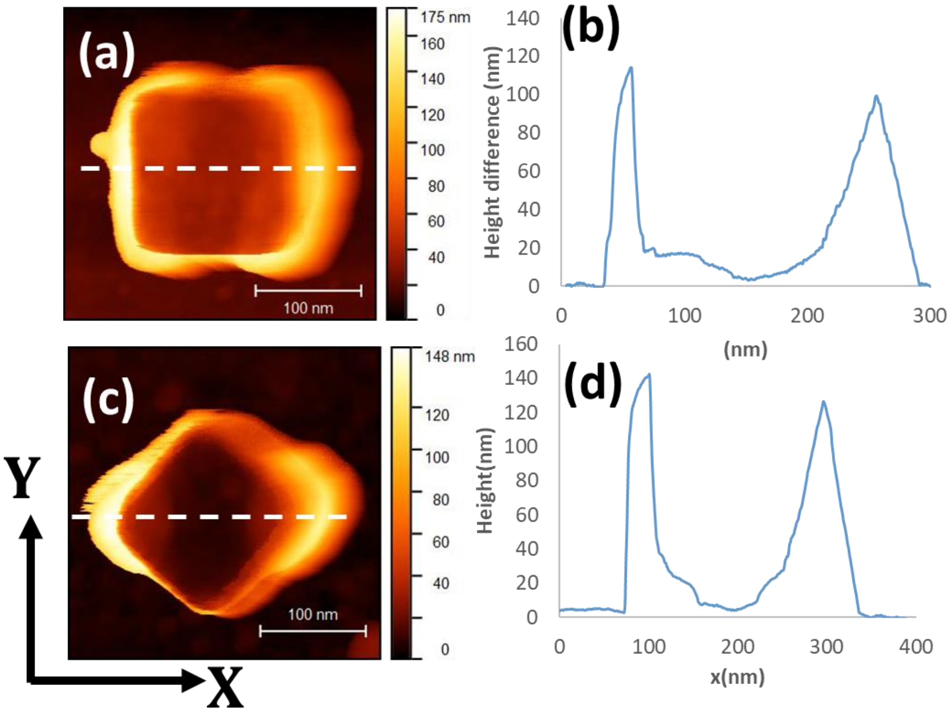

Figure 3.6 (a) (c) are subtracted topographic AFM images of single nanocubes. (b) and (d) Show the cross-section profile of polymer height along incident polarization at the position marked with white dashed line in (a) and (c) respectively.

Here, we can get average polymer heights about 110 nm and 130 nm in the case of (b) and (d) respectively. The thickness of polymer lobes can also be estimated at about 24 nm and 30 nm. As we discussed in section 2.2.2 , before and after exposure, due to the scanning damage and the slight movement of probe position, the shape and tilt angle of the AFM tip may change, so that the polymer thickness value cannot be measured accurately. SEM images can also provide polymer thickness information thanks to the contrast between metal and polymer at high accelerating voltage, as shown in Figure 3.5. Superimposed SEM images can also be used to highlight the integrated polymer parts (e.g. see Figure 3.7)

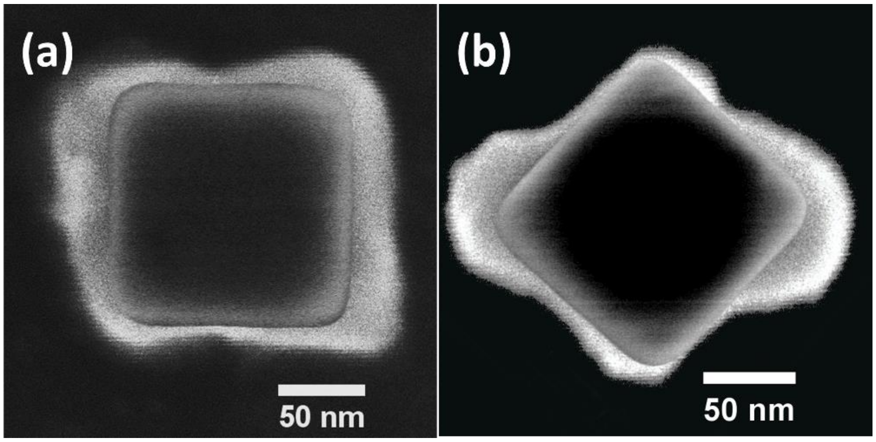

Figure 3.7 SEM images of hybrid nanocubes after polymerization at low accelerating voltage of 2KV, with original bare same cube superimposed in the middle, allowing for the highlight of the polymer resulting from the plasmonic TPP.

3.1.4 Polymer elongation as a function of the incident dose

In the case of TPP, when the exposure time is defined, the probability of two-photon absorption and resulting polymerization depends quadratically on the local light irradiance I (intensity per surface unit).

$$P = F(I^2) \qquad (3.1)$$

Function F contains all of the processes related to the two-photon polymerization and is a monotonically increasing function. The incident dose threshold D_{th} transfers to a threshold power I_{th}, below which no polymerization can occur. I_{th} is firstly experimentally accessed by far-field experiments (see section 2.3.2 and section 2.4.2). Photopolymerization depends on the effective local light intensity that results from both the incident light intensity I_{in} ($I_{in} = p \cdot I_{th}, where\ p < 1$) and the local near-field enhancement. As a result, higher incident dose leads to a larger polymerized region. Figure 3.8shows a group of polymerized nanocubes whose diagonals along the x axis are parallel to the incident light polarization direction, as for Figure 3.5(c) and Figure 3.7(b), with different incident doses controlled via the incident intensity. It turns out that a decrease of the dose leads to a decrease of polymer volume adhering the cube surface.

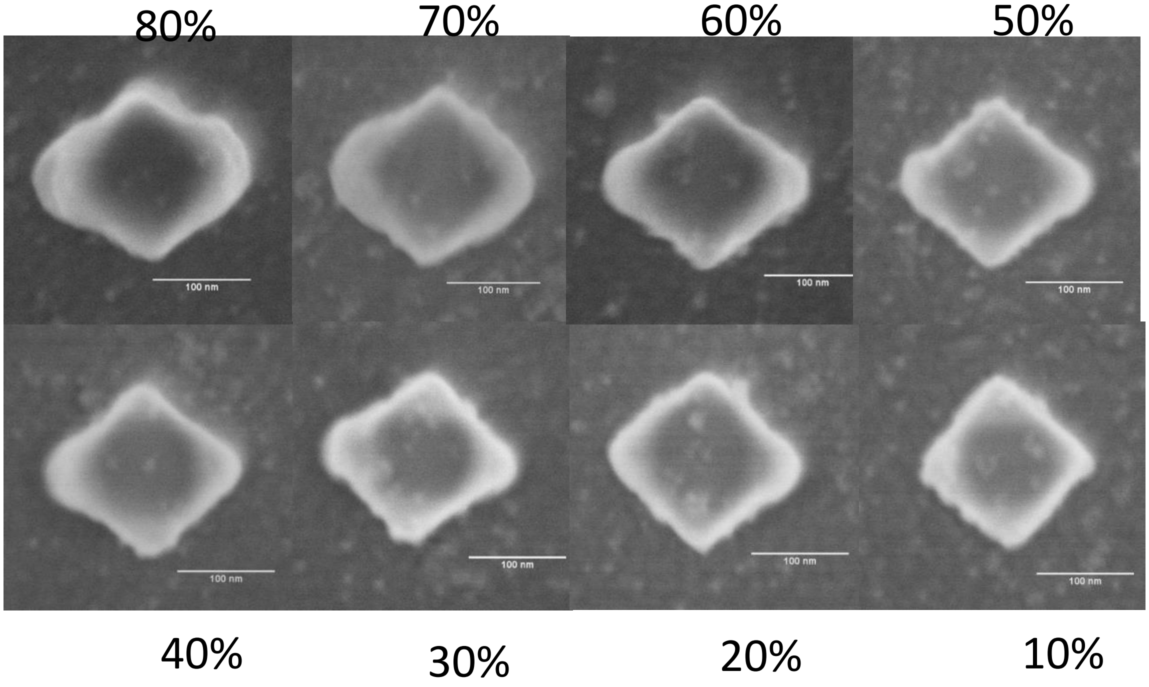

Figure 3.8 SEM raw images of hybrid nanosystems based on height gold nanocubes, whose diagonals along the x axis are parallel the incident light polarization direction. The hybrid nano-objects were obtained by plasmon-induced two-photon polymerization with different incident doses, from 10 to 80 % (=p) of the bulk energy polymerization threshold. Nano-Objects used are different from one image to the other one, but the height nanocubes are statistically identical to each other. The scale bars represent 100 nm.

In order to establish a quantitative link between the spatial in-plane extension of the polymerized lobes (i.e., the polymer elongation along the x-diagonal here), and the experienced local electromagnetic field, we carried out a parameter study. The polymer elongation along the nanocube diagonal was measured for different values of p ranging from 0.1 to 0.9. Figure 3.9(a) shows the result of the study. Polymer thickness increases as the dose increased in a nonlinear way. The apparent log-like function is the signature of the plasmonic field's evanescent nature. This result can be understood by considering the near-exponential decay of the near-field of the excited nanocube. In the vicinity of the gold nanocube, the effective local irradiance for polymerization is:

$$I_{eff} = f_{max}\, I_{in} exp(-x/\delta) \tag{3.2}$$

Where f_{max} is the maximum intensity enhancement factor inside the LSPR triggered polymerized area, δ represents the LSPR's characteristic intensity decay length, and x is the distance from the nanocube surface along the diagonal direction. Polymerization is achieved only where $I_{eff} > I_{th}$, resulting in the following condition

$$x < \delta\,.\ln\left(f_{max} \times \frac{I_{in}}{I_{th}}\right) = x_{max} = \ \delta\,.\ \ln(p \times f_{max}) \tag{3.3}$$

x_{max} is the observable parameter that can be accessed by SEM or AFM. It corresponds to the polymer elongation represented in Figure 3.9. Equation (3.3) can be rewritten:

$$\frac{1}{p} = f_{max} \times \exp\left(-x_{max}/\delta\right) \tag{3.4}$$

It should be stressed that 1/p represents the plasmon-induced intensity gain. For example, the fact that the polymer was obtained for p=0.1 demonstrates an intensity enhancement of, at least, 10. Equation (3.4) explains the exponential-like function shown in Figure 3.9(b). Analytical fitting from the experimental data leads to the determination of f_{max} and δ.

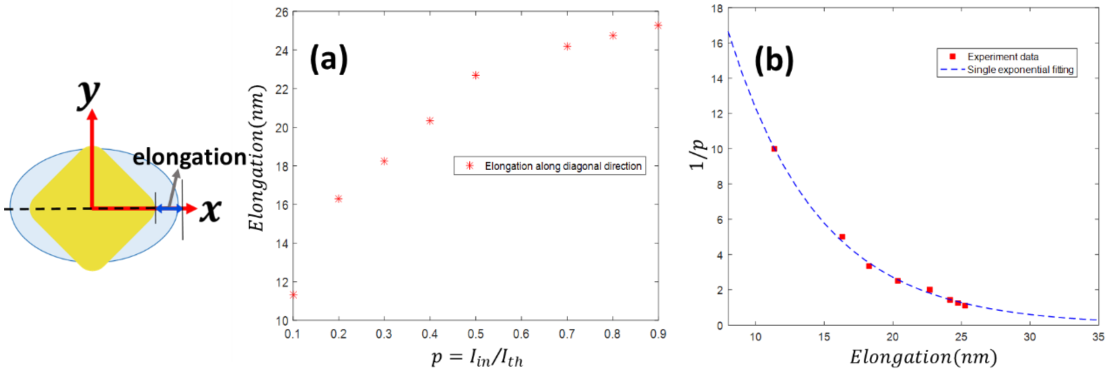

Figure 3.9 Quantitative analysis of polymers' elongation as a function of the incident laser intensity. (a) Effect of the relative exposure power $p = I_{in}/I_{th}$ on the measured elongation of the polymerized volume along the cube x-diagonal. (b) Experimental data points (red square) of the $1/p$ ratio plotted as a function of the resulting measured polymer elongation and exponential fit with a single exponential decay according to Equation (3.4).

In the case of Figure 3.9 (b), we find f_{max}= 56 and δ = 7 nm. Thus, this method constitutes a unique way of measuring the evanescent decay, the size of the optical nanostructure, and the plasmon intensity enhancement factor[6].

For comparison, by FDTD calculation, we got numerical values: f_{max} = 59 and δ = 10 nm respectively, shown in Figure 3.10. These values compare well with those extracted from the experimental data fit (Figure 3.9), indicating that the photochemical method is suitable for the quantification of the plasmonic near-field properties single gold nanocubes. More precisely, the FDTD simulation leads to a slightly longer decay length δ along with the x-diagonal. This difference can be explained by the fact we consider a stable and uniform dielectric environment around the cube for FDTD simulation. During polymerization, the surrounding refractive index is expected to change, resulting in a slightly different decay length.

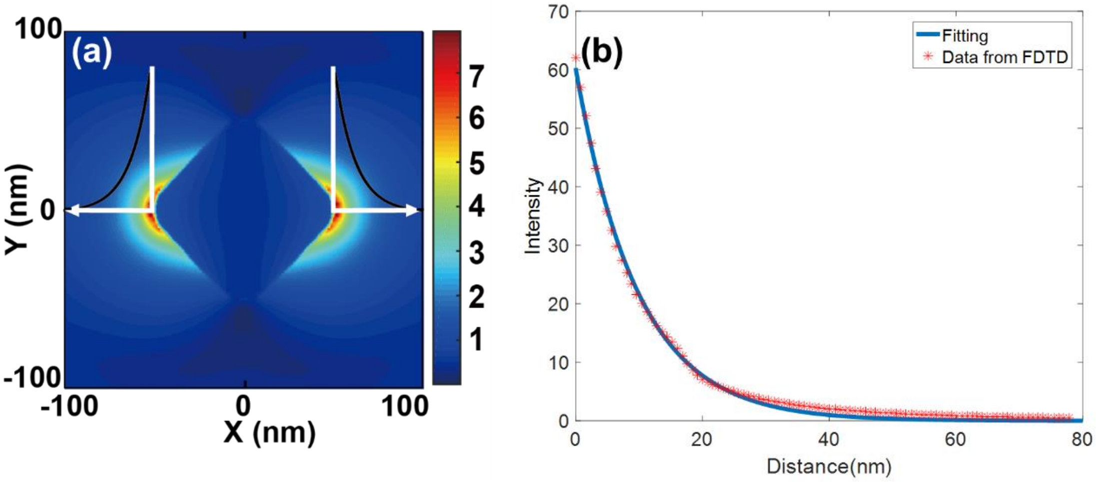

Figure 3.10 (a) Near-field intensity calculated by FDTD (b) Near-field intensity decay as a function of the distance from the metal surface (red dots represent data simulated by FDTD) and exponential fit with a single exponential function according to (a).

3.1.5 Controllable anisotropic polymer distribution of hybrid nanocube

For a given incident dose of light with polarization along the x-direction, nanocubes with different orientations get different polymer distribution (refer to Figure 3.6 and Figure 3.7, and more details will be shown in Figure 3.11). This is due to the anisotropy of localized surface plasmon energy on nanocube, who is a C_{4v} in-plane symmetry system. The orientation angle θ of a nanocube is defined as the angle between the fixed incident x-polarization and the side of nanocube (see Figure 3.11(a)). When θ equals to 0°, incident polarization parallel to the side of nanocube, hot-spots at the side of the cube are excited. When θ equals to 45°, incident light is polarized along the diagonal of nanocube, hot-spots at the corner are mainly excited. In this case, there is almost no polymerization reaction at the two corners perpendicular to the polarization direction of the incident light, while corners along the polarized direction have the most extended polymer elongation, which means higher localized polymer distribution. Figure 3.11(b) displays a set of hybrid nanocubes fabricated from various nanocubes' orientation using a fixed x-polarized incident light with a dose of 50% D_{th}.

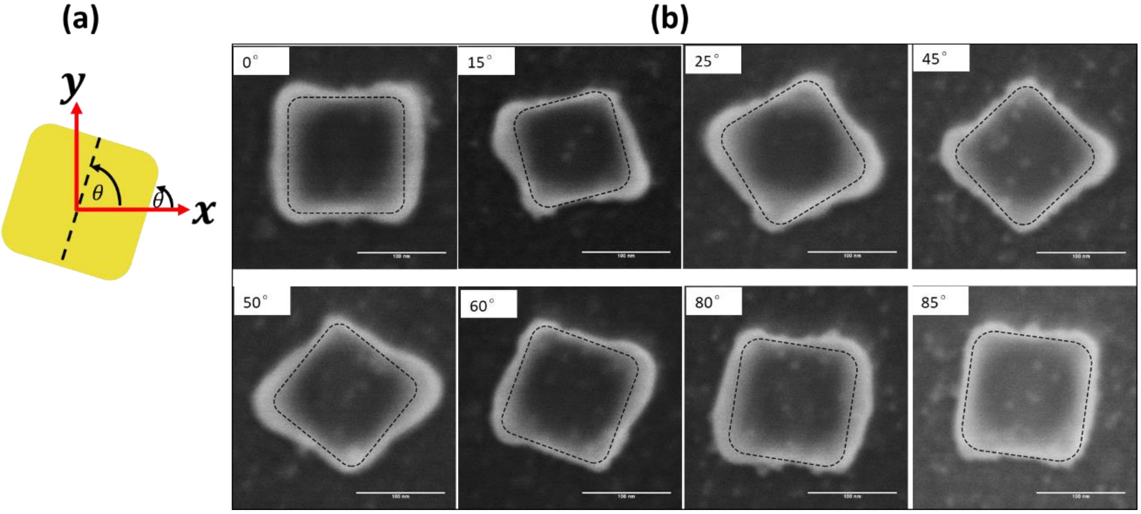

Figure 3.11 (a) Definition of the orientation angle of nanocube. (b) SEM images of hybrid nanostructures fabricated from nanocubes having different orientations (exposed by light polarized along x-direction). The dashed line marks the contour of the bare nanocubes. The scale bar represents 100 nm.

To analyze the relation between elongation at a specific cube’s corner and the cube's orientation angle θ, the SEM images of the hybrid structures fabricated using cubes with varying orientation should be studied, as shown in Figure 3.12. It is clear that the elongation of the polymer at the pointed cube's corner gets a maximum value of 25 nm when $\theta = 45^{o}$, at which time cube's diagonal has consistent direction as the polarization of incident curing light. More deviation of the diagonal from the incident light's polarization direction leads to shorter elongation, and when θ arrives at 135^{o}, elongation tends to 0 nm. Statistically, the polymer distribution follows the particle dipolar near field distribution imposed and controlled by the incident polarization and incident dose. Consider the ideal situation, QDs are evenly distributed inside the polymer, which means the number of fixed QDs is positively related to the volume of the polymer. Although the presence of QDs in a nanocube vicinity is challenging to detect by direct SEM imaging, their distribution will exhibit anisotropy consistent with the polymer.

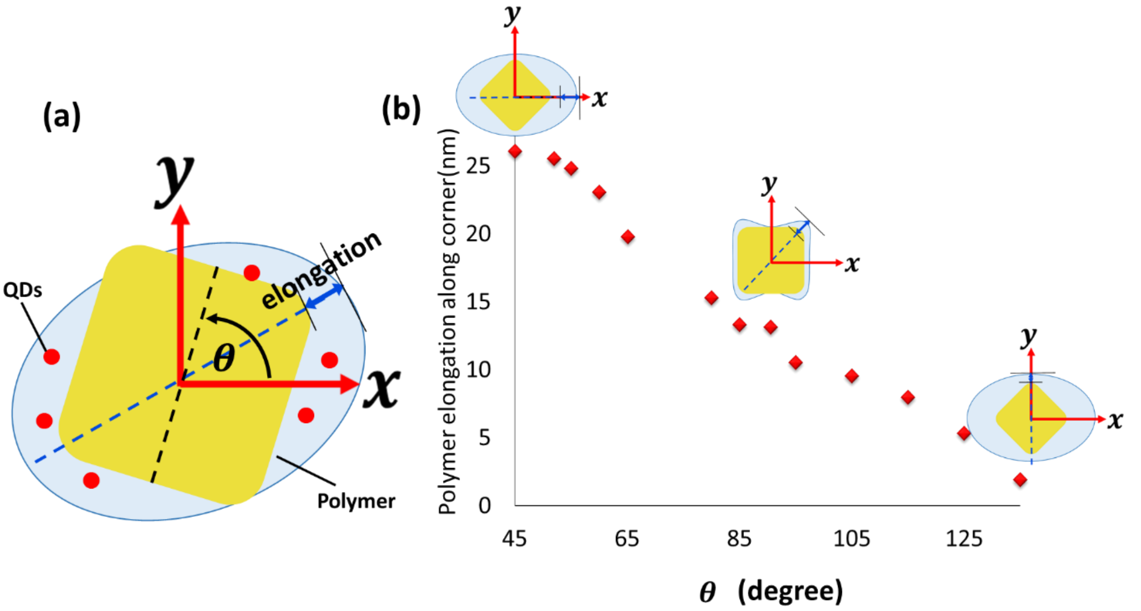

Figure 3.12 (a) Schematic diagram describes the definition of polymer elongation along the identified corner of nanocube. (b) Polymer elongation along with corner as a function of the nanocube's orientation

3.1.6 Photoluminescence (PL) Emission of hybrid nanocube

The far-field red PL image can allow us to check the presence of QDs trapped within the polymer. A 405 nm CW laser is used for exciting the hybrid nanocubes according to QDs' absorption spectrum shown in Figure 2.18 (b) (the red dotted line). Furthermore, the Photoluminescence (PL) from every single hybrid structure is measured following the steps described in 2.6.2 . Figure 3.13 displays normalized PL spectra from two isolated hybrid nanocubes and the original QDs-containing formulation.

Figure 3.13shows spectral analysis of the hybrid nanocubes. In Figure 3.13(a), the PL spectra from hybrid structures are slightly narrower than that from formulation, and there are slight fluctuations in their peak positions. This is because there is a large number of QDs in formulation excited, where its PL spectrum reflects the envelope of PL spectra from lots of QDs (inhomogeneous spectral broadening). The hybrid structure with polymer size smaller than the diffraction limit contains a limited number of quantum dots. This reveals the feasibility of manufacturing hybrid emitters containing very few or even single QDs using this method.

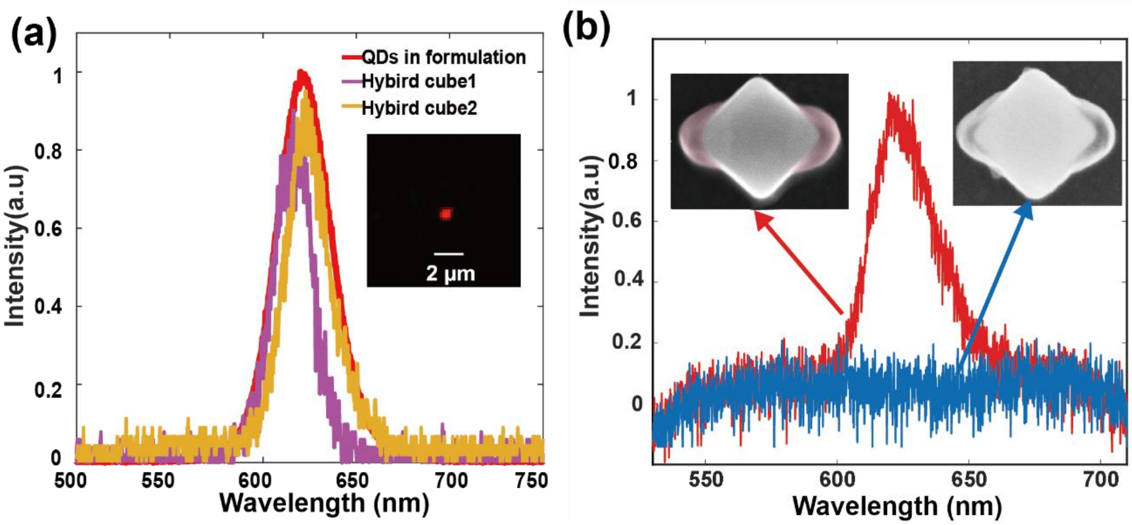

Figure 3.13 (a) Orange and pink line are normalized PL spectra of two isolated hybrid nanocubes (excited by 405 nm laser), and the small image inserted in the upper right corner is a far-field PL image of a single hybrid nanocube. The Red curve represents the PL spectrum from the polymerizable formulation. (b) Compare the PL signal from hybrid polymer/cube with QDs trapped in the polymer (red line) and the reference signal from hybrid polymer/cube without QDs (blue line). The left-side image is artificially colored in red for illustrating the fact the polymer lobes contain red QDs.

For comparison, the hybrid polymer/gold nanocubes structure without any QDs were produced and spectrally analyzed. In other words, the plasmonic near-polymerization was carried out with a photochemical formulation which does not contain any QDs. In that case, no red PL emission was observed from the resulting hybrid nanocube, as Figure Figure 3.13(b) shows (blue curve). The two hybrid nanostructures shown in Figure Figure 3.13(b) were produced using the same parameters. The only difference between the one shown in the left small subgraph and the right small subgraph is that no QDs were added into the photosensitive formulation to produce the second one, resulting in hybrid polymer/gold nanocubes not contain any nano-emitters. Photoluminescence spectra were measured on the two kinds of hybrid nanoparticles. The first kind shows a clear red spectrum from the CdSe/ZnS QDs (see Figure 3.13 (b), red curve). This spectral signature is not visible on the second kind (see Figure 3.13(b), blue curve), proving that the red spectrum corresponds to the photoluminescence of the QDs trapped with the polymer nano-volumes in the close vicinity of the gold nanocube.

3.1.7 Time stability of the PL emission from hybrid nanocubes

Four nanocube-based hybrid plasmonic nanosources, identical to that of Figure 3.14, are fabricated to access the time stability of the PL emission. The PL emission intensity is regularly monitored from 1 day to 22 days. Every time they were continuously excited for 30ss and the PL spectrum is measured. The results are shown in Figure 3.14. 405-nm wavelength with 25 µW/cm2 incident power was used (polarization parallel to the QD-containing polymer lobes) except for the fourth one (70 µW/cm2). Except for the first set of data recorded during 4h, the PL data (intensity and spectrum) are randomly got in one day. According to Figure 3.14(a), for 25 µW/cm2, in continuous 4 hours, it is hard to distinguish any attenuation of PL intensity. According to Figure 3.14(b), the PL emission still stays reasonably stable for 7 days but has a noticeable decrease on the ninth day. The two spectra shown in Figure 3.14 (c) are collected 22 days apart. The intensity –turns out to be maintained at an acceptable level after 22 days. For a power density of 70 µW/cm^2, PL intensity quickly drops to 65% of the initial intensity and stays pretty stable for 10 days. Observed time stability turns out to vary depending on the incident power and the considered hybrid nano-sources. More studies need to be made to investigate photodegradation's origin and process for the most fragile hybrid nanosources. Based on the current results, it can be considered that our hybrid nanosources' PL intensity keeps stable for one day, especially when we use a relatively modest exciting power. It makes our study about polarization sensitivity of PL reasonable, which lasts less than 4 hours for one hybrid nanosource.

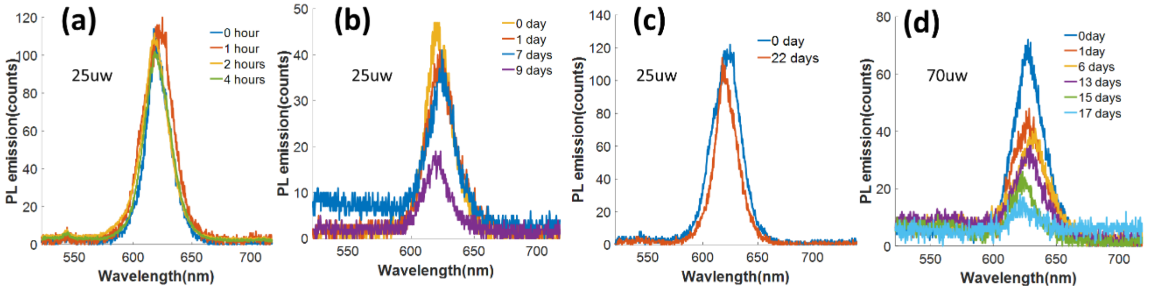

Figure 3.14 Study of time stability of the photoluminescence from four different hybrid nano-emitters. Each time, the hybrid cube-based nanostructures was shined for 30 s for one spectrum collection (405 nm incident wavelength) with an incident power of 25 µW/cm^2, except for the last one (70 µW/cm^2).

3.2 Hybrid nanostructures based on nanodisk

For comparison, hybrid nanostructure is made from gold nanodisks. Nanodisks fabricated by EBL have diameters of 90 nm and height of 50 nm, whose scattering spectra show similar LSPR peak as the 130 nm-nanocubes. A set of SEM images and experimental scattering spectra of Au nanodisks on glass substrate (diameters = 70, 80, 90 nm) are shown in Figure 3.15. Spectra were measured either in air on in PETA, after the deposition of a drop. PETA induces a clear red-shift of about 30 nm. The nanodisk surrounded by PETA present an effective resonant in-plane dipolar plasmon response in the 600-800 nm range, permitting resonant plasmonic two-photon polymerization under the same condition as the nanocubes.

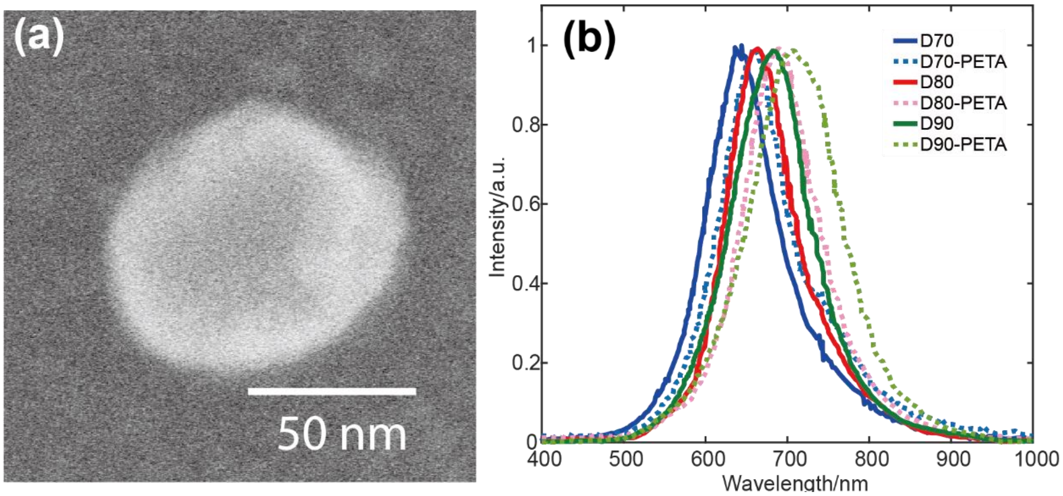

Figure 3.15 (a) SEM image of 90 nm-diameter Au disk. (b)Scattering spectra of Au nanodisks with

diameters of 70 nm, 80 nm, and 90 nm, fabricated by EBL on ITO-coated glass substrate.

Unlike cubes, the $C_{\infty v}$ in-plane symmetry generates a dipolar near field distribution with no sharp hot spots (no apexes), contributing to lower light confinement, which can be reflected from its calculated near-field distribution shown in Figure 3.16 (a). This distribution is characterized by two lobes parallel to the incident linear polarization (C_{2v} symmetry, where patterns are retrieved after a π rotation). Besides, Figure 3.16(b) indicates a ring-like near-field distribution of nanodisk excited by circular-polarized light, indicating a $C_{\infty v}$ in-plane symmetry of the field distribution.

In the case of nanodisk, whose diameter is around 90nm, we use the same near-field photopolymerization method as what we used for fabricating the cube-base hybrid structure. Except for linear-polarized, an additional was used for plasmon-induced two-photon polymerization. The resulting nanostructure, shown in Figure 3.16(c) and (d), are characterized by active medium exhibiting either two polymer lobes (linearly-polarized excitation) or a homogenous ring having a $C_{\infty v}$ symmetry (circularly polarized excitation) respectively, which are in keeping with the near field distribution calculated by FDTD. In the following sections, we will see that the different polymer distributions correspond to different distribution of active medium (QDs), resulting in different polarization sensitivity of the photoluminescence from these hybrid structures.

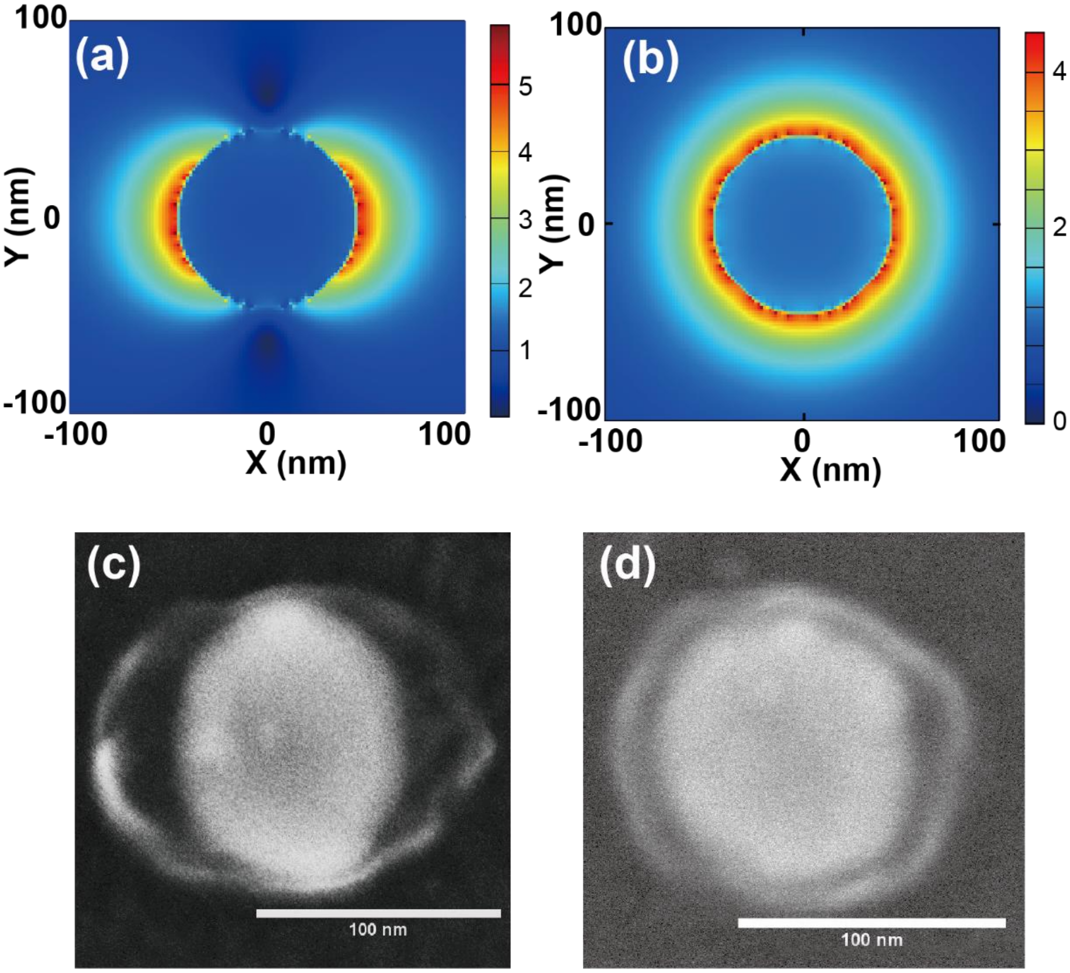

Figure 3.16 FDTD calculated near-field amplitude distribution of nanodisk (90nm diameter, 50nm height) using an exciting wavelength of 780nm. (a) using linear-polarized exciting light, and (b) using circular-polarized exciting light. SEM images of nanodisks after TPP, wavelength of the curing laser is set to 780nm. The small "grains" observed on the calculated maps of (a) and (b) correspond to numerical artifacts due to the square-in-shape meshing (c) disk-based hybrid nanostructure polymerized by a linear-polarized light, (d) disk-based hybrid nanostructure polymerized by a circular-polarized light.

3.3 Photoluminescence properties of the hybrid nanosystems

By using gold nanoparticles with different geometric shapes and different plasmon excitation modes, the active medium containing nano-emitters can be selectively constructed with different symmetry near the metal nanoparticles, thereby forming a polarization-sensitive hybrid nano-emitter. In the previous sections, we used the same method for fabricating cube-base and disk-based hybrid nano-emitters. In this section, we analyze the photoluminescence (PL) properties of the hybrid nano-emitters. In particular the polarization dependence of the PL is discussed in terms of spatial overlapping between the active medium and the exciting local field

3.3.1 Basic mechanism of polarization controllable photoluminescence

Our hybrid structure contains gold nanoparticle providing near-field manipulation ability, and QDs dispersed in polymer close to the metal nanoparticle. Besides, we have shown that the QDs' spatial distribution is controllable by the polarization state of the excitation light used for polymerization. This layout would allow one to use the incident polarization also as a fast and efficient remote optical control of light emission from the hybrid emitter. Let us describe analytically this point.

According to the discussion about plasmon-emitters interaction in chapter 1, section 1.3.1, we can derive another equation from Equation (1.22)and Equation (1.23):

$$\gamma_{em}(v_{em}) = \gamma_{exc}(x, y, z, v_{exc}) \times Y(v_{em}) \times \rho(x, y, z)dV \qquad (3.5)$$

where γ_{em} is the rate of emission of the QDs, γ_{exc} is the rate of excitation, *Y* is the nano-emitter quantum yield, and $\rho(x, y, z)dv$ is the probability of the presence of emitters around the metal nanoparticle within an elementary volume $dV(= dxdydz)$ at position (x,y,z). $\rho(x, y, z)$ is thus the volume density of probability of the presence of QDs. It should be pointed out that $\rho(x, y, z)$ can also be considered as the volume density of QDs. v_{em} is the frequency of the emitted light. v_{exc} is the frequency of the exciting field that is absorbed by the QDs. v_{exc} should be within the absorption band of the emitter. $v_{em} - v_{exc}\,(< 0)$ represents the stoke shift. It should be reminded that *Y* is related to the probability of light emission once the nano-emitter is excited and that it also depends on (x,y,z)[21]. This dependence will be discussed further. For the moment, let us focus our attention on the spatial dependencies of γ_{em} and ρ. For increasing the final PL signal, emitted light can be amplified by a good match with the plasmon resonance of the metal nanoparticle or, in the more practical point of view, by optimizing the geometry of light collection matches it to the far-field radiation diagram of the hybrid nanostructure.

γ_{exc} related to the metal nanoparticle plasmonic near-field, whose spatial distribution can be controlled through incident polarization for given nanoparticle size and geometry. When it comes to the nano-emitter spatial distribution, described by ρ(x,y,z), in most reported cases we have introduced in section 1.4 , it is not controlled.

According to Equation (3.5), the control of the nano-emitters spatial distribution $\rho(x,y,z)$ would allow one to control light emission through control of the active medium/exciting field overlapping. This general concept is not new in micro-optoelectronics. For example, Equation (3.6) expresses the overlap integral that accesses the way a specific waveguide mode can be excited:

$$\eta = \frac{|\iint E_1 \cdot E_2 dxdy|^2}{\iint |E_1|^2 dxdy \cdot \iint |E_2|^2 dxdy} \tag{3.6}$$

where η is the coupling efficiency between E_1 and E_2 which are, respectively, the complex amplitude of the mode to be coupled and the complex amplitude of the incident exciting field.

In nano-optics, especially for our hybrid system, this concept is worth developing because the nanoscale control of $\rho(x,y,z)$ would allow one to exploit $\gamma_{exc}(\mathrm{x,y,z})$ fully.

3.3.2 Experimental study of the polarization sensitivity of the photoluminescence

Our approach of plasmon-based photopolymerization to integrate polymer nanostructures containing QDs in the close vicinity of metal nanoparticles can control the dispersion of nano-emitters, as shown in sections 3.1 and 3.2 . We use this method to discuss spatial overlapping between the active medium and the local exciting field on advanced hybrid nano-emitters based on gold nanocubes and nanodisks.

For small thicknesses of the polymer matrix, QDs can be observed at the periphery of the polymerized drops by transmission electron microscopy, see Figure 2.19(b). For polymer material thicknesses > 10 nm, the QDs are hardly discernible on TEM images. This observation allows us to roughly access the volume density of QDs within the polymer. Figure 2.19(b) reveals that the QDs are separated from each other with a distance of about 7 nm. Each 6.7-nm size QDs would thus occupy a sphere of about 14 nm in diameter, resulting in a maximum volume density of QDs ~ 7x105/μm^3 = 7x10^{-4} QD/nm3. A typical integrated polymer nanolobe has a volume of about 70x25x50 nm^3(e. g. Figure 3.6 (c) and Figure 3.17 (a)) corresponding to a few tens of QDs per lobe. Since the polymer contains QDs (~ a few tens of QDs for the biggest polymer lobes), the control of the polymer distribution shown in Figure 3.7 and Figure 3.16 offers a way to control $\rho(x, y, z)$, the spatial distribution probability in equation (3.5), making the hybrid system an anisotropic nano-emitter. We study the relationship between PL intensity and spatial overlapping between the polymer and near-field distribution under different excitation polarization from our nanocube-based and nanodisk-base hybrid structures described in section 3.1 and section 3.2 .

Firstly, for systematic analysis, an angle ϕ in polar coordinates is defined as the polarization angle of the excitation light (see Figure 3.17 (a)). Figure 3.17 shows photoluminescence (PL) data ($\lambda_{PL} = 625nm$) from a single nanocube-based emitter ($\lambda_{exc} = 405$ nm) fabricated by TPP with X-polarized 780 nm laser beam, where cube's orientation angle $\theta = 45^o$ (see Fig. 3.12(a)). It should be pointed out that the 405-nm excitation wavelength has been chosen for efficient light absorption by the QDs. With regards to the plasmonic gold nanostructures, this wavelength permits an off-resonant excitation (gold 5d-6sp interband transition for wavelengths < 520 nm[173]). However, as it will be seen in Figure 3.17, gold nanocube still makes possible spatial confinement of the local field that excites the hybrid nanosource. Figure 3.17(a) shows the SEM image of the considered hybrid nano-object. Figure 3.17(b) and Figure 3.17(c) show, respectively, the far-field PL image from a single hybrid nanosource and the corresponding PL spectrum. Under the same condition of excitation at 405 nm, no measurable emission at 625 nm was observed on bare nanocubes, bare polymer matrix or nanocubes exposed to a photosensitive formulation without any QDs (Figure 3.13(b)). Additionally, a similar PL spectrum was measured from a micronic pattern made of the same QD-containing polymer[157].

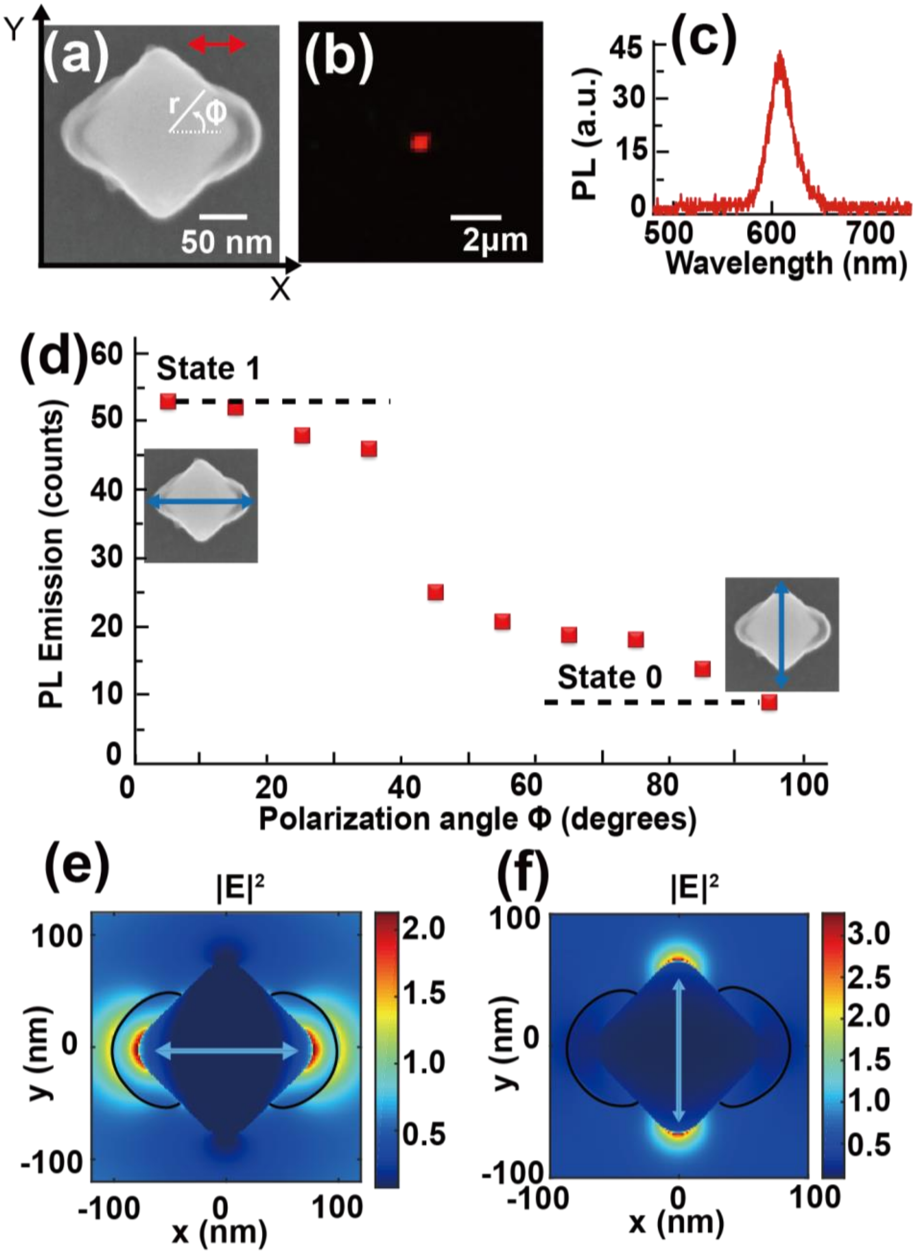

Figure 3.17 Photoluminescence (PL) from single hybrid nanosource based on gold nanocube and red QDs embedded within the polymer lobes along one cube diagonal. (a) SEM image of the hybrid plasmonic nanosource. Red arrow indicates the polarization used for fabrication of the hybrid system based on plasmonic two-photon polymerization. The polar coordinate defines the polarization angle ϕ of the incident laser used for exciting the nanosystem at 405 nm. The raw image is superimposed with the image of same bare nanocube. (b) Far-field PL of the nanosystem shown in (a) excited with a 405 nm laser, ϕ = 0^o. (c) Corresponding PL spectrum. (d) PL intensity as a function of the polarization angle ϕ of the excitation light. The blue arrows indicate two perpendicular polarizations corresponding to $\phi = 0^o$ and $\phi = 90^o$. (e) and

(f) Simulated near-field intensity (at the middle sectional x-y plane of the cube, λ = 405 nm) in the vicinity of a realistic hybrid nanocube. Blue arrows indicate two perpendicular polarizations corresponding to ϕ = $0^o$and ϕ = 90^o. Black lines represent the contours of the polymer lobes as deduced from the SEM image in (a).

Figure 3.17(a) shows an apparent anisotropy of the active medium presenting a C2v in-plane symmetry with highly confined distribution, suggesting a significant polarization sensitivity of the emitter. In other words, we can define $\rho(r,\phi)$ the probability of presence of the nano-emitters as the function of polar coordinates (r,ϕ) represented in Figure 3.17(a). From SEM images, ρ is high for $(r\in([65\text{ nm}-100\text{ nm}])\cap(\phi\in[335°-25°]\cup[155°-205°])$ and nil elsewhere (very thin polymer layers, of thickness small compared to the QD size, are neglected because they are unlikely to contain QDs). As far as the azimuthal angular distribution of nano-emitter is concerned, we define the angular filling factor, named β, which quantifies the angular occupancy of the active medium in the vicinity of the metal nanoparticle. In Figure 3.17 (a), the active medium occupies less than 30% (~27%) of the space. For comparison, a *spaser* made of a spherical core-shell plasmonic structure surrounded by a homogeneous layer of QDs[87] exhibits an active medium in the region $(r\in[20\text{ nm}-25\text{ nm}])\cap(\phi\in[0°-360°])$, i.e an angular filling factor of β = 100%. The control of $\rho(r,\phi)$ constitutes a strong feature of this new type of hybrid nano-emitter. Figure 3.17(d) shows the PL intensity of single hybrid nanosource as a function of the incident polarization direction (λ = 405 nm). The PL level varies quickly depending on the polarization direction. This effect results from the spatial overlapping variation between the local near-field excitation and the distribution of active medium. To illustrate this important point, the near-field intensity at 405 nm was calculated by FDTD on a realistic nanocube-based hybrid system presenting polymer lobes at two cube corners.

Figure 3.17(e) shows the exciting near-field for incident polarization parallel to the polymer lobes, $\phi = 0^o$. Although the gold nanocube is not resonant at this wavelength, it acts as a nano concentrator that confines light along the cube diagonal where the QD presence probability $\rho(x,y,z)$ is high, resulting in a high level of PL, named "state 1" in Figure 3.17(d). In Figure 3.17 (e), apparent field enhancement at the extremity of the polymer lobes is due to the field component's discontinuity perpendicular to the polymer-air interface. For the case of a perpendicular polarization (Figure 3.17(f)) the near field/active medium overlap is weak, which causes the PL to decrease, resulting in “state 0” in Figure 3.17(d). In this perpendicular case, the nanosource gets almost turned off, as shown in Figure 3.18 that presents far-field PL images as a function of incident polarization angles.

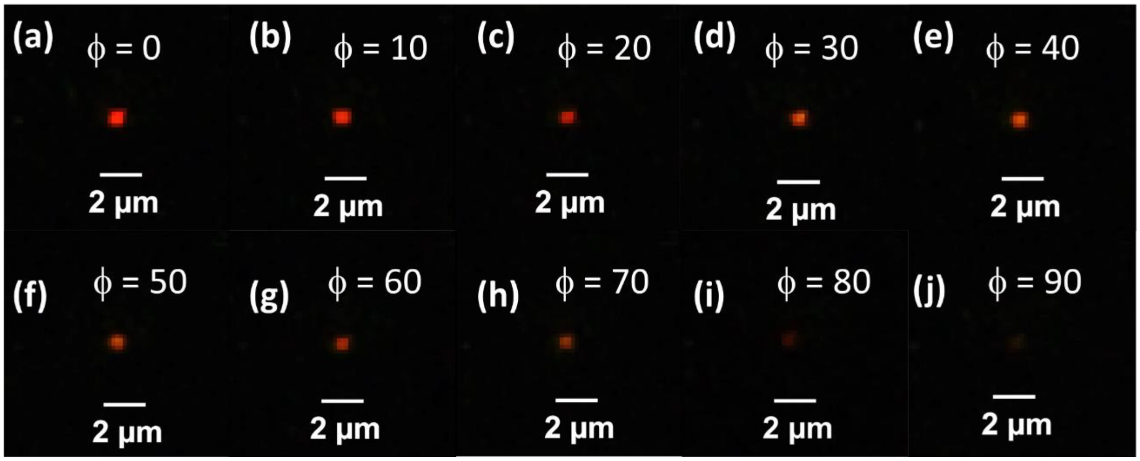

Figure 3.18 Far field PL images indicate that emission intensity of the hybrid nanocube shown in Figure 3.17 (a) decrease as polarization angle of the exciting light ϕ *varies from 0 degree in (a) to 90 degrees in (j).* ϕ *changes 10 degrees between two continues images.*

It should be pointed out that quantum yield *Y* is actually the effective quantum yield in the presence of the metal nanoparticle. It is generally different from the free space quantum yield and also depends on position (x,y,z)[21]. In general, *Y* decreases in the very close vicinity (< 10 nm) of the particle due to non-radiative relaxation (quenching) and can get strongly increased in the near-field of the plasmonic nanoparticles[23]. In Figure 3.17(e), QDs are expected to be efficiently excited within the polymer (black line marked contour) but quenching can occur at the nanocube surface. Only QDs laying on this surface (if there are any) are expected to be perturbed. In Figure 3.17(f), light is confined at two nanocube corners. The main QDs excitation would be at the nanocube surface (highest intensity) where quenching is expected. However, this point is of no consequence for the emission since the probability of the presence of QDs at this specific location is low (no polymer or negligible polymer thickness).

PL polarization sensitivity can be discussed through a polarization contrast:

$$\delta_{PL} = \frac{IPL_{max} - IPL_{min}}{IPL_{max} + IPL_{min}} \tag{3.7}$$

where IPL_{max} and IPL_{min} are the maximum and minimum PL intensities (that we name IPL), respectively. From Figure 3.17(d), we get $\delta_{PL} \sim 0.7$. We fabricated another 5 hybrid structures in the same case of Figure 3.17(a) and totally get 6 groups of data about PL intensity as a function of polarization angle ϕ shown in Figure 3.19. All of them have a $\delta_{PL} \sim 0.7$, proving the repeatability of our method and the reliability of δ_{PL}. Besides, in Figure 3.19(e), (f), when ϕ = 180° the PL intensity goes back to the same high level as ϕ = 0° presenting the C2v in-plane symmetry of this kind of hybrid nanostructures.

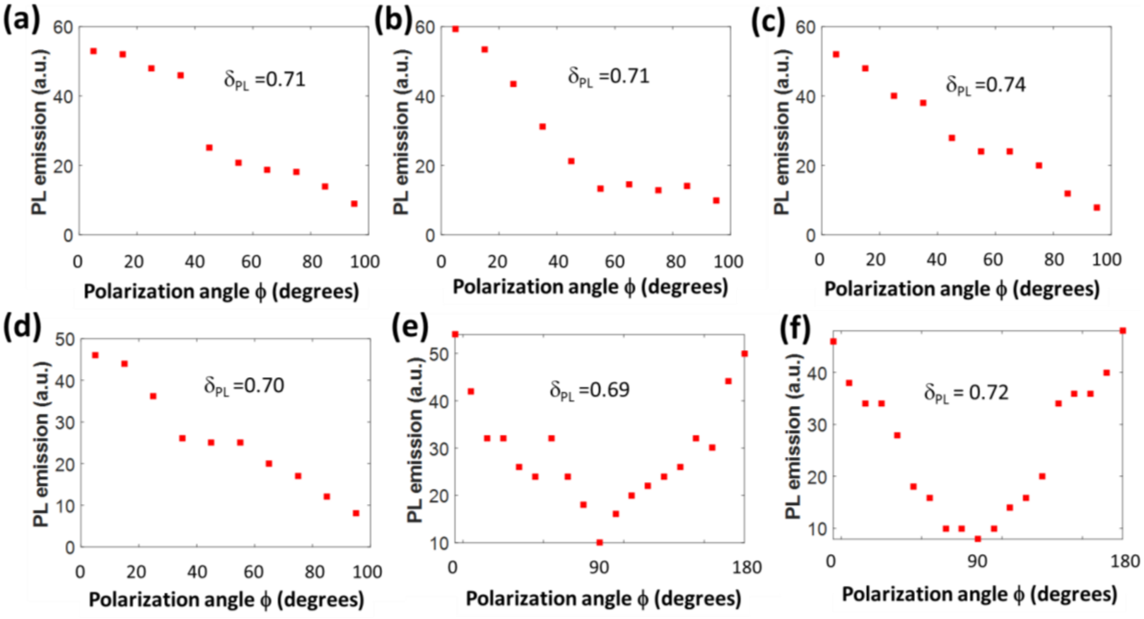

Figure 3.19 PL intensity as a function of the polarization angle ϕ of the excitation measured from 6 different hybrid nanocubes similar to that of Figure 4.17(a).

However, this high value is limited by the PL background from the incident far-field, whatever the polarization. In particular, in Figure 3.17(f), the calculated intensity of the excitation field is not nil within the black line contour representing the emitter-containing polymer, letting us expect a non-zero resulting PL.

δ_{PL} depends on the hybrid emitter structure that is controlled through proper choice of the metal nanoparticle geometry and the selection of plasmonic mode used for near-field polymerization. In order to illustrate this critical possibility, different kinds of hybrid plasmonic nanosources were fabricated. Figure 3.20 shows the PL data from a single nanosource fabricated by a nanocube whose orientation angle $\theta = 0$, in which case, the exciting field parallel to the cube edges, then both diagonal plasmonic eigenmodes are symmetrically excited and all of the cube's four corners exhibit near-field enhancement (Figure 3.5(b)).

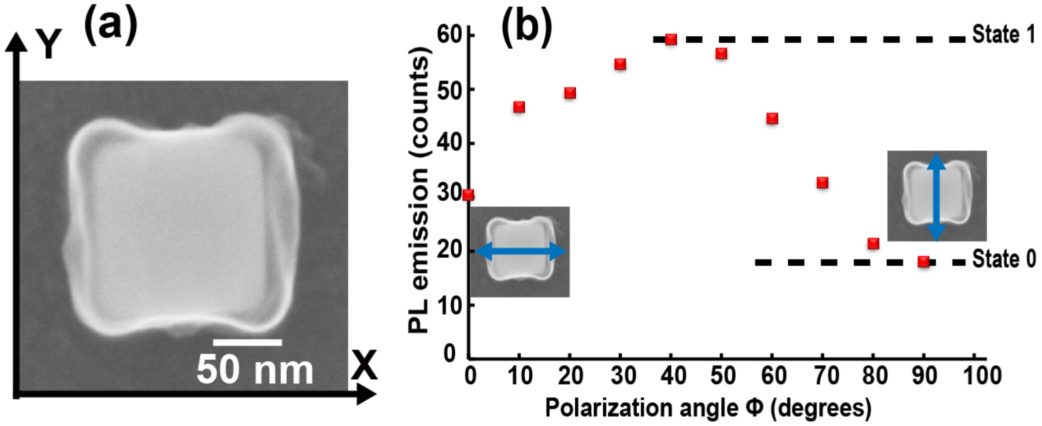

Figure 3.20 Photoluminescence (PL) of a single hybrid nanosource based on a gold nanocube and red QDs embedded in the polymerized volume that was integrated along the cube sides. (a) SEM image of the hybrid nanostructure observed under 10Kv. (b) PL intensity as a function of the angle of polarization of the excitation light, the incident electric field is represented as blue arrows.

According to Figure 3.20(a), the resulting nanostructure also presents a C_{2v} in-plane symmetry. This symmetry results from the C_{4v} symmetry of the four hot spots shown in Figure 3.5(b). Compared to Figure 3.5(d), although weaker field was excited at the cube sides, it still led to local polymerization at these sides, resulting in a final C_{2v} symmetry of the hybrid nano-object. This interesting example shows that nanoscale plasmonic photopolymerization can allow for the control of the local degree of symmetry[137]. Compared to Figure 3.17(a), Figure 3.20(a) presents a less confined polar distribution: ρ is likely to be high for $(r\in([65\text{ nm}-100\text{ nm}])\cap(\phi\in[0\text{-}65°]\cup[115°\text{-}245°]\cup[295°\text{-}0°])$, corresponding to more than 70% of the angular space around the nanocube ($\beta\sim72\%$). Figure 3.20(b) indicates the PL polarization dependence, which shows much weaker signal fluctuation compared to Figure 3.17(d). The highest PL level around 45° (225°) corresponds to thicker polymer volumes at the cube corners that results from electromagnetic singularity at the cube corners as shown in Figure 3.5(b). PL contrast is measured to be $\delta_{PL} \sim 0.3$, which is due to higher homogeneity (weaker polar confinement) of QD-containing polymer in the vicinity of the gold nanocube.

The hybrid nanostructure presented in Figure 3.17 and Figure 3.20 were made from a cube with sharp corners and edges. For comparison, the initial $C_{\infty v}$ symmetric gold nanodisks made by EBL were used for producing hybrid nanosources. They have a 90-nm diameter and are 50 nm thick. They present an in-plane dipolar plasmon resonance in air and polymer at 700 nm and 730 nm respectively (see Figure 3.15(b)), permitting resonant plasmonic TPP under the same condition as those used for the nanocubes. An X-polarized curing light is still used for TPP on nanodisks, and dipolar near-field enhancement was used to get a two-lobe hybrid nanostructure shown in Figure 3.21(a).

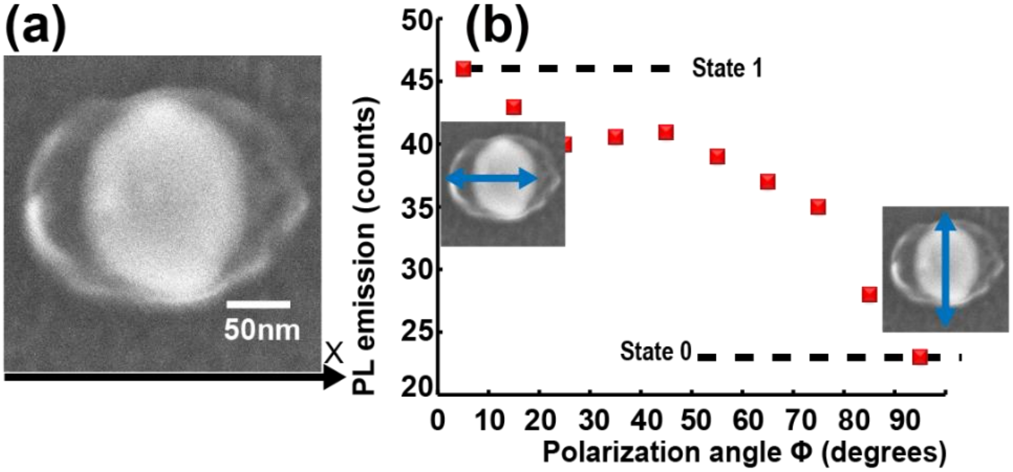

Figure 3.21 Photoluminescence (PL) from a single hybrid nanostructure based on a gold nanodisk and red QDs embedded within the two polymer lobes. The hybrid nanostructure was obtained by plasmonic TPP using linear polarization along the X-axis. (a) SEM image of the nanostructure (raw image). (b) PL intensity as function of the angle ϕ of polarization of the excitation light at 450 nm. The direction of the incident electric field is represented by blue arrows.

The obtained structure presents two lobes along X axis, corresponding to the direction of polarization used during TPP. The resulting active medium distribution is of C_{2v} point group symmetry and presents a pretty weak polar confinement: $(r\in([45\text{ nm}-80\text{ nm}])\cap(\phi\in[310°-50°]\cup[130°-230°])$ corresponding to $\beta\sim 55\%$. Its PL polarization dependence (Figure 3.21(b)) presents weak fluctuation with $\delta_{PL} \sim 0.3$. Compared to the nanocube case, the dipolar near-field distribution yields of photopolymerization process with reduced control over the spatial confinement. In contrast to the nanocube case, here the $C_{\infty v}$ in-plane symmetry of the nanodisk generates a dipolar near field distribution with no sharp hot spots yielding a low asymmetry of the final polymerized deposit. It should also be pointed out that metal nanoparticles made by EBL can present, compared to chemically grown particles, local roughness and crystal defects that can result in lower light confinement.

From the same gold nanodisk, an additional type of hybrid nanosource was made by using circular polarization at 780 nm for plasmon-induced two-photon polymerization. The resulting nanostructure, shown in Figure 3.22(a), is characterized by an active medium exhibiting a ring-like distribution of $C_{\infty v}$ symmetry, i.e., occupying 100% (=β) of the angular space, consistent with the near-field distribution shown in Figure 3.16(b). Accordingly, the resulting PL varies poorly with the polarization angle of the exciting field at 405 nm. A PL low contrast $\delta_{PL} \sim 0.1$ is obtained from the experimental data in Figure 3.22(b). This slightly positive value may come from the imperfection of the circular pattern, the inhomogeneous distribution of QDs within the polymer volume or slight direction deviation when rotate polarization.

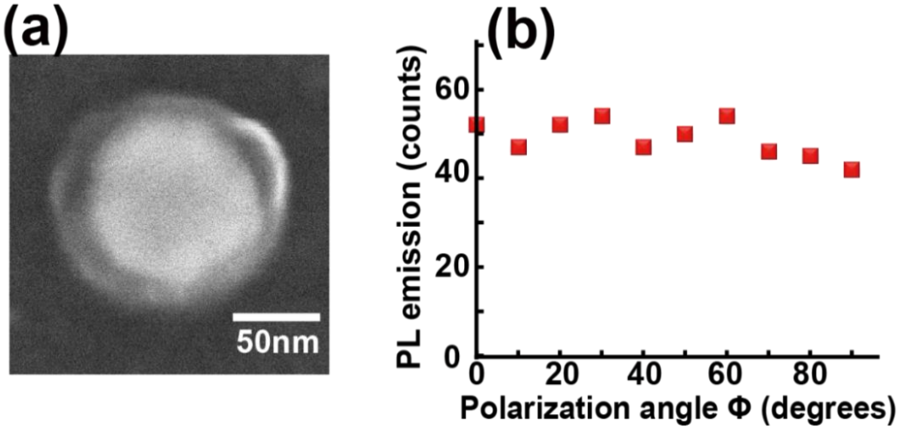

Figure 3.22 Photoluminescence (PL) from a single hybrid nanosource based on a gold nanodisk and red QDs embedded in a polymer shell obtained by plasmon-induced two-photon polymerization using circular polarization. (a) SEM image of the hybrid nanosource. (b) PL intensity as a function of the angle ϕ of polarization of the excitation light at 450 nm.

3.3.3 Discussion on the origin of the observed polarization dependence of the photoluminescence

Experimental data obtained on the previous four kinds of plasmonic hybrid nanosources can be discussed in terms of nanoscale spatial overlap integral between QDs' spatial distribution and local near-field configuration.

Inspired by Equation (3.6), we define a normalized spatial overlapping ratio, named $\eta_{nf/em}$, between the off-resonant exciting plasmonic near-field intensity and the distribution of QDs:

$$\eta_{nf/em(\theta)} = \frac{V \iiint E_{exc}{}^{2} \times \rho dV}{\iiint E_{exc}{}^{2} dv \times \iiint \rho dV} \qquad (3.8)$$

where $E_{exc}(x,y,z)$ is the modulus of the local plasmonic field that excites the QDs at the 405 nm wavelength. It is calculated by FDTD. $\rho(x,y,z)$ is the volume density of probability of presence of the QDs, as defined in Equation (3.5). It can be assessed experimentally from SEM and AFM images. V is an arbitrary constant that can be considered as the total volume of integration.

$\eta_{nf/em}$ quantifies the way the exciting field intensity and QDs' spatial distribution overlap with each other for a given situation, with a given excitation polarization direction (e.g., Figure 3.17(e)). For example, $\eta_{nf/em}$=0 would mean that overlap is nil: QDs do not get excited and PL is expected to be negligible. On the other hand, $\eta_{nf/em}$=1 is expected to lead to the highest possible PL. The most important part of Equation (3.8), in terms of physical meaning for describing the overlap, is the numerator. The denominator is only used for normalization. For any given hybrid nanostructure excited with a given polarization direction this denominator has a constant positive value and never goes to zero (the integral $\iiint \rho dV$ is always strictly positive, although some elements ρdV within the integral, corresponding to an absence of polymer, can be locally nil).

Figure 3.23 shows calculated $\eta_{nf/em}$ as a function of the polarization direction of the incident field at 405 nm, for three different types of hybrid nanostructures. All the nanostructures were fabricated by TPP using X-polarized curing light. It should be reminded that a given polarization direction working on a given nanoparticle corresponds to a specific $E_{exc}(x,y,z)$ spatial distribution while $\rho(x,y,y)$ is fixed for a given hybrid nanostructure. For this calculation, we considered that both orientation and spatial distribution of QDs within the polymer matrix are random and do not change during excitation. For simplicity, we defined $\rho=1$ with the presence of a polymer and $\rho=0$ with the absence of polymer. In other words, the $\rho(x,y,z)$ map is a homogeneous reproduction of the polymer nanostructure in the vicinity of the metal nano-object and it is assumed that QD distribution within the polymer is homogeneous.

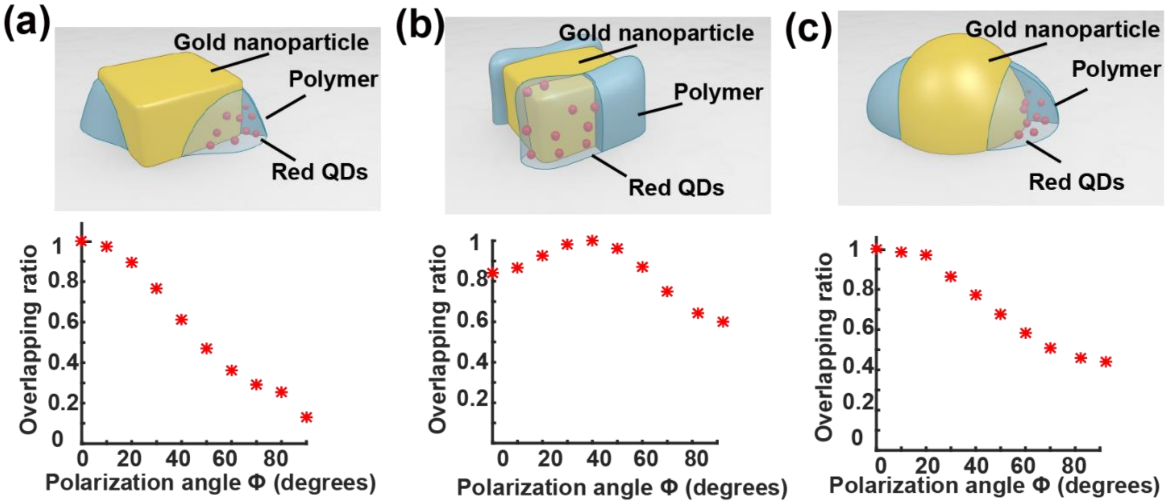

Figure 3.23 Computed spatial overlap integral $\eta_{nf/em}$, defined in equation (3.8), between the local excitation field and the active medium as a function of the incident polarization angle ϕ for three different hybrid nanosources. The incident field (λ_{exc} = 405 nm) is X-polarized. (a) Gold nanocube with polymer lobes integrated along the diagonal direction (cube orientation angle θ = 45°). (b) Gold nanocube with polymerization at two cube faces (cube orientation angle θ = 0°). (c) Hybrid gold nanodisk with two polymer lobes along X axis.

From Figure Figure 3.23, it turns out that $\eta_{nf/em}$varies like the PL intensity (Figure 3.17 , 20-21), showing that the PL level directly depends on $\eta_{nf/em}$. It is thus important to control this parameter. Figure 3.23(b) is worth noting the maximum at 45°, which corresponds to a higher polymer thickness along with the cube diagonal, as observed experimentally in Figure 3.20.

Each value of $\eta_{nf/em}$ is thus associated to a PL intensity value. In order to precisely establish the link between $\eta_{nf/em}$ and IPL, we consider that IPL results from the PL issue from an ensemble of nanovolumes *dv* in the vicinity of the metal each nanovolume, positioned at x,y,z, emits a PL intensity d_{IPL} that is defined as:

$$d_{IPL} = \alpha \times \gamma_{exc}(x, y, z, \nu_{exc}) \times Q(\nu_{em}) \times \rho(x, y, z)dv \qquad (3.9)$$

where α is a constant including the incident intensity and the efficiency of light collection (setup geometry, numerical apertures of lenses…). $\rho(x,y,z)dv$ is the probability of presence of emitters inside dV.

For a given hybrid metal particle, we assume that α and $Q(\nu_{em})$ are constant. In particular, it is supposed that the PL results from an average constant effective quantum yield, ruling out quenched nano-emitters touching the metal surface.

As we discussed in section 1.3.1 , for QDs, γ_{ex} is proportional to $|\mathbf{E_{exc}}|^2 \cdot |\boldsymbol{\mu}|^2$. By considering a statically constant dipole moment, γ_{ex} becomes proportional to $\mathrm{E_{exc}}^2$ and $d_{IPL} \propto E_{exc}{}^2 \times \rho dV$. The resulting IPL signal can thus be expressed as:

$$\mathrm{IPL}(\theta) = \iiint d_{IPL} = \alpha \iiint \boldsymbol{E_{exc}}^2 \times \rho dv \qquad (3.10)$$

From equations (3.8) and (3.10), it turns out that IPL is proportional to $\eta_{nf/em}$.

As a result, equation (3.7) becomes

$$\delta_{PL} = \frac{IPL_{max} - IPL_{min}}{IPL_{max} + IPL_{min}} = \frac{\eta_{nf/em}^{max} - \eta_{nf/em}^{min}}{\eta_{nf/em}^{max} + \eta_{nf/em}^{min}} = \delta_{nf/em} \qquad (3.11)$$

where $\eta_{nf/em}^{max}$ and $\eta_{nf/em}^{min}$ are, respectively, the maximum and minimum value of $\eta_{nf/em}$ in Figure 3.23.

The term of $\delta_{nf/em}$ in Equation (3.11) was calculated from Figure 3.23 data. We found 0.74 (Figure 3.23(a)), 0.25 (Figure 3.23(b)), and 0.35 (Figure 3.23(c)). These values can be compared with those of δ_{PL} that were experimentally determined: 0.7, 0.3 and 0.3, respectively. As predicted by Equation (3.11), it turns out that $\delta_{nf/em}$ and δ_{PL} are equal. This important result validates the proportionality link between $\eta_{nf/em}$ and IPL, although local QDs inhomogeneity could explain some unexpected fluctuation in the PL plot.

3.4 Towards a single photon switch

Optical switch operating at single–photon level always plays a key role in quantum circuits[174] and quantum information science[175,176]. Our hybrid nanosources have exhibited their polarization-driven controllability of PL intensity and their limited numbers of fixed QDs make them of high possibility for operating at single-photon regime.

3.4.1 Single QD characterization

In our method, QDs are used as the active medium. When it comes to a single QD level, it is necessary to characterize QDs' features, especially their PL emission and lifetime. In order to compare the emission properties of QDs in polymer with emission from QDs inside the polymer lobes of hybrid plasmonic nano-emitters (i.e. in the vicinity of gold nanostructures), single CdSe/ZnS QDs embedded in polymer dots on glass substrate (see Figure 2.17 chapt. 2) were analyzed.

Figure 3.24 shows the time evolutions of the PL spectrum from three different QDs embedded polymer dots. Here, we use CdSe/ZnS QDs that emit at 620 nm. Clear Blinking is seen in Figure 3.24, which is characteristic to single QD emission,[177,178] proving that only single or few QDs are contained in these polymer dots. We used a pulsed 405-nm diode laser with a repetition frequency of 20 MHz for PL measurement.

Let us explain how we got these polymer dots containing single QDs. Polymer dots were fabricated on a clean glass substrate by two-photon polymerization with an incident dose above the threshold using the same methods described in section 2.4 . They are same as the polymer dots shown in Figure 2.21. In order to achieve single QD level, we decreased the QDs' concentration in the photosensitive formulation. The original photosensitive formulation was prepared according to the conventional composition ratio (PETA+QDs+1%IRG819). 4 mg IRG819 was added into 396 mg pure PETA to prepare diluent formulation without QDs was prepared at the same time. We mixed a certain proportion of original formulation and diluent together and stirred to obtain a low QD concentration of formulation. In that way, we got a low concentration (20% of the original) formulation. Quantitatively, the original formulation contains 1 mg QDs in 1 g polymer while the low concentration formulation contains 0.2 mg QDs in 1 g polymer.

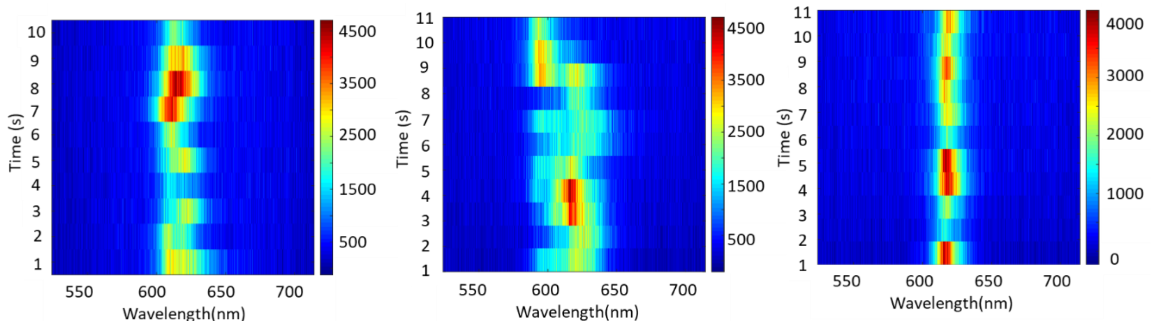

Figure 3.24 Emission properties of single QDs embedded in polymer dots on glass substrate. a time evolution of the PL spectrum from six different QDs. They are excited by a 405 nm pulsed laser in frequency of 20MHz and exciting power density of 2.5uW/um2.

As explained in section 2.6.3 , chapter 2, the definitive evidence of a single photon relies on the corresponding autocorrelation function ($g^{(2)}$) measurement, where $g^{(2)} < 1/2$ implies single-photon projection[160]. Figure 3.25 shows three groups of lifetimes and from three different single QDs embedded within sub-micronic polymer dots on glass substrate. It shows the signature of single photon emission ($g^{(2)}(0)$ in the 0.2-0.35 range) with a stable lifetime in the 17.5 ns-17.9 ns range.

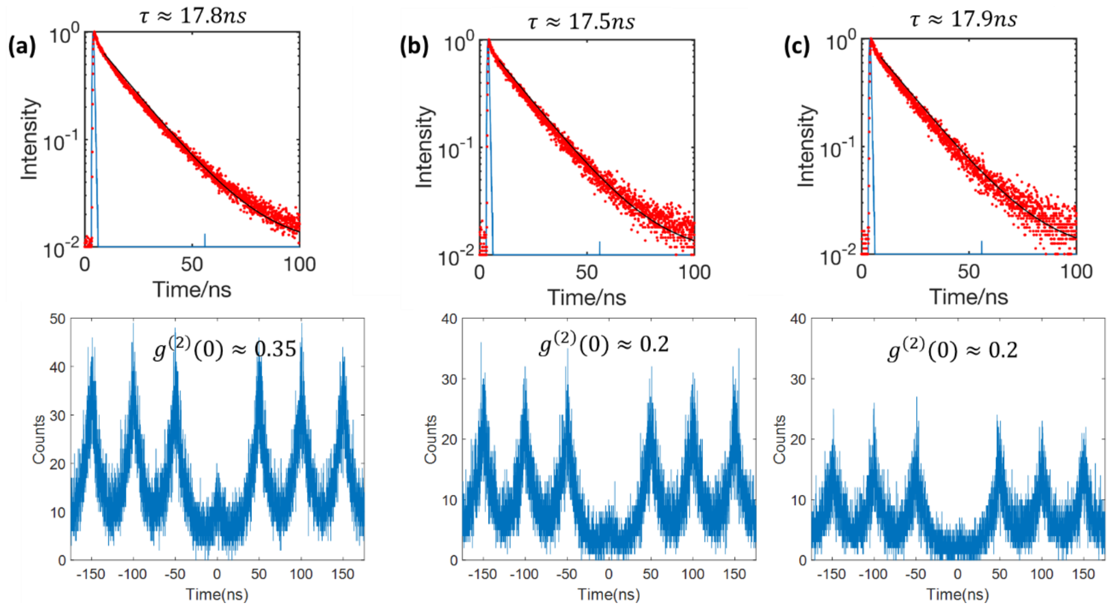

Figure 3.25 lifetime (top, 0.62 $\mu W/\mu m^2$ incident power, 5 MHz repetition rate, the blue plot corresponds to the IRF: instrument response function) and $g^{(2)}$ autocorrelation function (bottom, 2.5 $\mu W/\mu m^2$ incident power, 20 MHz repetition rate) measured from three different single QDs.

3.4.2 Towards single-photon plasmonic hybrid nano-source

The possibility of controlling the nanoscale spatial overlap between an exciting field and the active medium was extended to the single-photon regime with a single QD. The decreased concentration of QDs within the photopolymerizable formulation allows us to trap a small number of QDs (a single QD or a few ones) inside the polymer nano-lobes of a nanocube-based hybrid nano-emitter. Figure 3.26(a) shows an AFM image of such a hybrid nano-emitter. This nanocube-based hybrid nano-emitter is chosen because its original nanocube has a classic orientation angle $\theta = 0^o$ leading to polymer lobes along X-axis after polymerization using X-polarized curing light. A pulsed laser of 405 nm with incident polarization angle ϕ = 0^o (parallel to the polymer lobe along the X-axis) was used for PL exciting. The corresponding PL spectrum was obtained using the same Hanbury Brown-Twiss system coupled with the confocal scanning system described in Figure 2.24(see section 2.6.3) that is sensitive to single quantum emitter emission, by which both single-photon counting and spectral measurement can be achieved. We can see a clear blinking from Figures Figure 3.26(b) and Figure 3.26(c), which is the signature of a single (or few) QDs emission (time traced 50 s). More interestingly, in Figure 3.26(b), this emission gets switched off when the incident polarization is rotated to $\phi = 90°$ (using a half-wave plate) due to the sudden lack of overlap between the exciting near-field and the single QD. Autocorrelation function $g^{(2)}$ measurement was performed in order to determine the photon emission regime. We found that at a zero delay, $g^{(2)}(0) \sim 0.35$ (Figure 4.26(d)), which is below 0.5, illustrating there is only single-photon emitted at the same time. This result was equally obtained on single QDs in polymer without gold nanocubes. This represents a first demonstration of a polarization-driven switchable single photon emission. We also measured the Purcell effect owing to the weak coupling between the trapped single QD and the gold nanocube, which turns out to be significant. The instrument response function (IRF) of the system was measured every time before the lifetime measurement of the hybrid nano-emitter. We used a 5 MHz repetition rate pulsed laser for IRF and lifetime measurement and obtained an IRF of about 0.63 ns. With the same set-up, we measured the lifetime of several typical hybrid nano-emitters, presented by black, red, and green curve lines in Figure 3.26(e). The typic lifetime of hybrid nano-emitter is 0.725ns, while the lifetime of single QDs in polymer was measured to be around 17.5 ns (Figure

3.25and Figure 3.26(f)). These measures correspond to an averaged Purcell factor of 17.5/0.725~23. Statistically, several hybrid nanosources revealed smaller lifetimes, close or probably smaller than the IRF (see for example yellow curve in Figure 3.26(f)), suggesting higher Purcell factors larger than 28 (=17.5/0.63). This variation of lifetime is believed to be related to the random position of the QDs within the polymer lobes in the vicinity of the gold nanocube: farthest QDs present a lifetime of ~0.8 ns while closest ones have a lifetime close and even below the resolution of our system (~0.63 ns). Here, the measurement of lifetime of QDs trapped in hybrid nanostructure is restricted by our TCSPC system's time resolution.

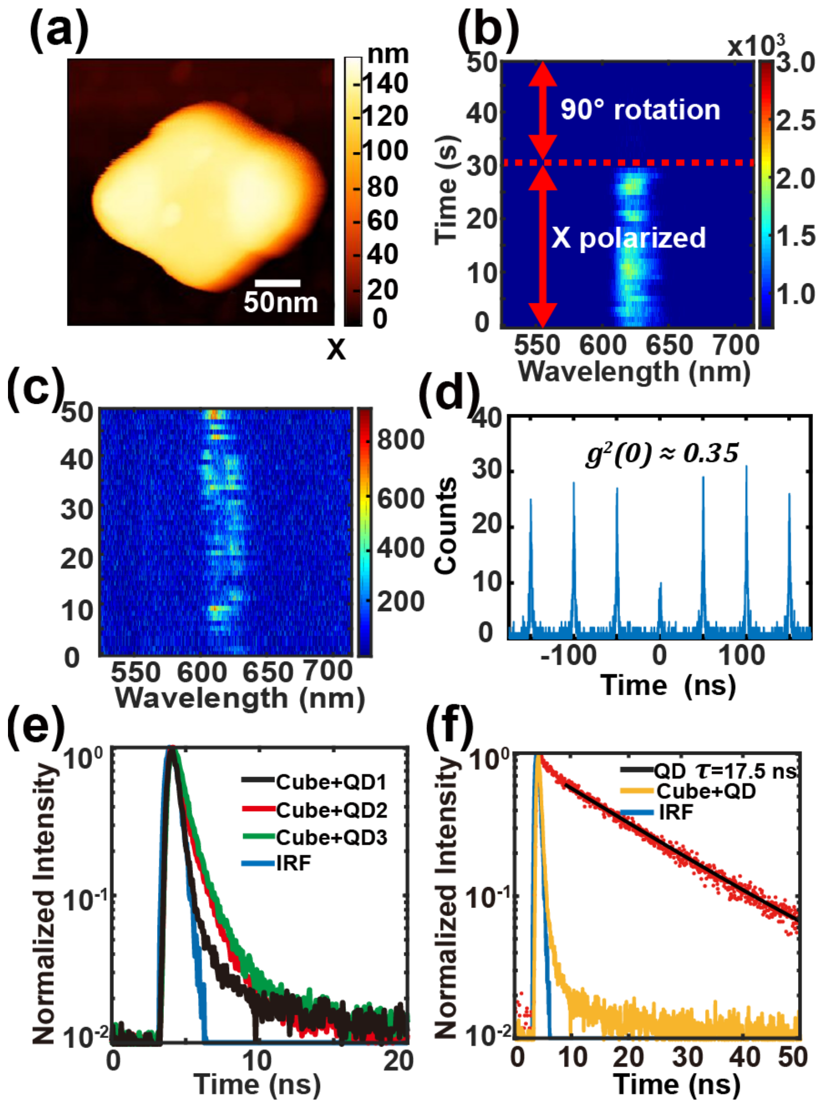

Figure 3.26 Hybrid nano-emitters in the single photon regime. (a) AFM image of a nanocube-based hybrid nano-emitters. The polymer lobes, fabricated in the same way as Figure 3.17(a), contain a single QD or a

few QDs. (b) and (c) PL spectrum time trace of t=50 s with an incident X linear polarization at 405 nm. In (b) at time t=32 s., the polarization direction was 90° rotated. (d) $g^{(2)}$ measurement showing $g^{(2)}(0) = 0.35$. (e) Lifetimes from three different nanocube-based hybrid nano-emitters containing single QDs (0.62 μW/μm2 incident power, 5 MHz repetition rate). A typical lifetime measurement on single-QD hybrid nano-emitter ~0.725 ns. The blue curve represents the instrumentation response function (IRF) of 0.63 ns. (f) Lifetime measurement: comparison between single QD in polymer without gold nanocube (red curve, 17.5 ns) and single QD in the vicinity of a gold nanocube (hybrid nano-emitter: the yellow curve shows the smallest observed.

The hybrid nano-source fabric based on nano-cubes prepared by TPP can thus reach the single-photon regime. Besides, by analyzing the change in fluorescence lifetime of quantum dots at the single-photon scale, we can estimate the Purcell factor to determine the strength of the coupling effect between quantum dots and gold nanocubes, laying the foundation for further exploring the possibility of achieving higher strength coupling between metal nanoparticles and QDs based on this method.

3.5 Summary

Different hybrid plasmonic nano-emitters fabricated by plasmon-based two-photon nanoscale polymerization have been introduced in this chapter. The hybrid emitters present anisotropic spatial distribution of the active medium with different controllable degrees of symmetry. The resulting polarization dependence of the photoluminescence has been analyzed and quantified on the basis of new specific parameters whose definition and use are made possible for the first time: i) spatial distribution of nano-emitters including angular distribution of the active medium, ii) nanoscale spatial overlap integral between active medium and exciting near-field, and iii) associated photoluminescence polarization contrast. We also demonstrated the ability to make such hybrid systems down to the single-photon level. A preliminary result of a polarization-driven single-photon switch was reported.

This new class of anisotropic plasmonic nano-emitters opens up the avenue for polarization-driven tunable nano-emitters, including even single-photon emitters. Polarization could thus command the associated color in the case of anisotropic nanoscale distribution of differently colored nano-emitters.

Chapter 4 Hybrid nanostructure based on special shape of MNPs: Gold bipyramids

Au nano-bipyramid (AuBP) is quite different from other shapes of MNPs such as cube and disk that we have discussed in the previous chapters. It is a kind of anisotropic structure similar to nanorod with two major localized dipolar surface plasmon resonance (LSPR) modes, where the traversal one corresponds to the short-axis mode, and the longitudinal one corresponds to the long-axis mode. Besides, compared to gold nanorod, AuBPs can get stronger near-field enhancement leading to bigger Photoluminescence quantum yield[179] because of the sharp ends. In this chapter, we will study the properties of AuBPs and AuBP-based hybrid structures that result from plasmonic nanophotopolymerization. This part of the work was done in collaboration with Ph.D. student Quan Liu, who is a dual Ph.D. student of Université Eberhard Karl de Tübingen and Université de Technologie de Troyes. The Argonne National Laboratory and Northwestern University (USA) have been involved too.

4.1 Characterization of Au bipyramids

The Au nano-bipyramids are provided by our colleague Matthew S. Kirschner, who is directed by Prof. Richard D. Schaller in Northwestern University (USA). They used a seed-mediated growth approach to synthesize altered-size AuBPs with LSPR peaks ranging from 680 nm to 900 nm, which match well with the absorption spectrum of our photosensitive formulation used for TPP. The deposition method of AuBPs has been introduced in section 2.1.2 (Chapter 2 , and the good dispersion of AuNPs ensures that the following experiments that need isolated single AuBP can be carried out.

Figure 4.1(a) illustrates the SEM image of several aggregated AuBPs. Obviously, due to the presence of unwanted spherical nanoparticles in the solution of AuBPs, not all the nanoparticles dispersed on the substrate are effective. Figure 4.1(b) displays a dark-field optical image of the dispersed particles on ITO-coated glass. The different colors correspond to different nanoparticles, which can help distinguish the effective AuBPs. The red dots correspond to AuBPs, and green dots correspond to spheres, dots appearing blue generally correspond to residual surfactant. Figure 4.1(c) and (d) show the size distribution of 100 effective AuBPs analyzed from

SEM images: we can deduce a AuBPs' average length of 115.6±4.45 nm for the long axis and 45.8±4.10 nm for the short axis. These dimensions were used as input parameters for FDTD simulations to calculate the scattering spectrum. Figure 4.1(e) displays the calculated scattering spectrum (dashed curves) of single bare AuBP placed on ITO-coated glass (40 nm thick ITO layer) in air or in PETA. It is in keeping with the measured dark-field scattering spectrum (solid line curves) from single AuBP. The prominent peak around 700 nm is related to AuBPs' long-axis mode, and the weaker peak around 570 nm is assigned to short-axis mode, they are the so-called longitude plasmon resonance mode (LPRM) and transverse surface plasmon resonance mode (TPRM).

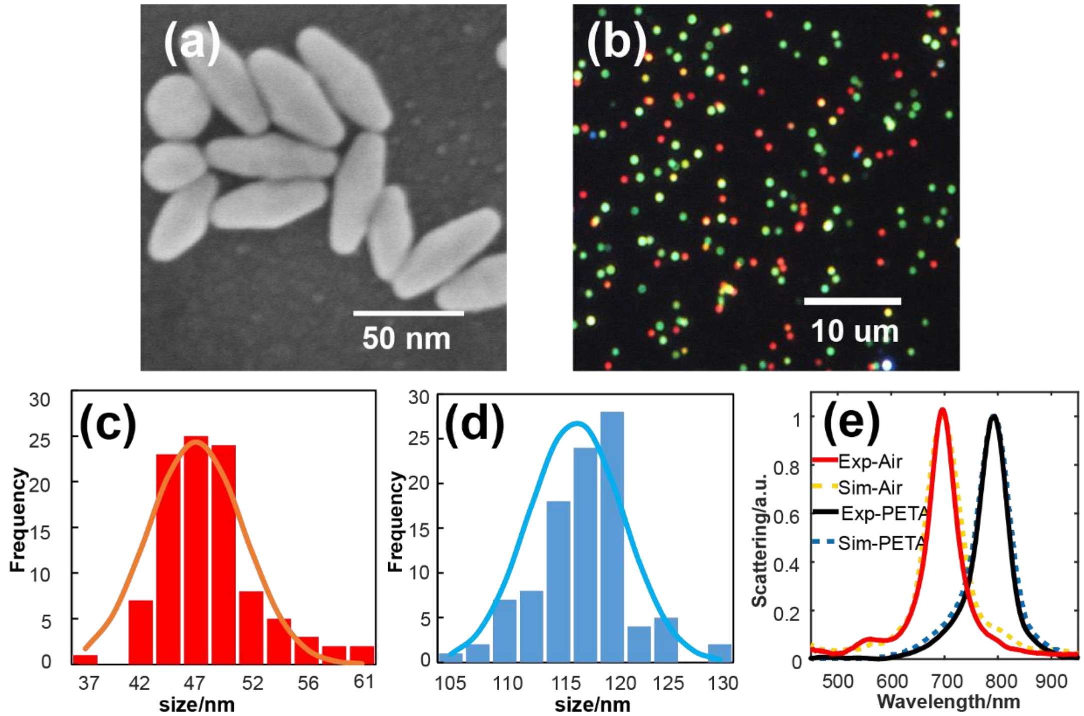

Figure 4.1 Properties of AuBPs. (a) Typical SEM images of several aggregated AuBPs. (b) Dark-field image of dispersed AuBPs. Different colors correspond to different kind of particles. The size distribution of (c) short axis and (d) long axis of 100 random AuBPs, analyzed by SEM images. (e) Red and black solid lines show the measured scattering spectrum from a single AuBP immersed in air and PETA; orange and blue dashed lines show the FDTD-calculated scattering spectra from a single AuBP deposited on ITO-coated glass substrate, immersed in air and polymer (PETA) respectively. Size parameters used in the FDTD simulation were obtained from the SEM image.

AuBPs are different from cubes; they cannot have a flat surface touching the substrate. That is why there will be a slope angle between the long axis of AuBPs and the surface of substrate. Figure 4.2(a) and (b) show a typical SEM image and AFM image of a deposited AuBP. The topography image with height information observed by AFM reflects the tilt of AuBP. The topography cross-section profile shown in Figure 4.2(c) corresponds to the white dotted line in Figure 4.2(b). From Figure 4.2(c), we can determine that corner 1 of AuBP is above. Besides, according to the contour map obtained by SEM and the height information obtained by AFM, the tilt angle between AuBPs and the substrate can be estimated at less than 10 degrees (calculated method according to ref. 144)

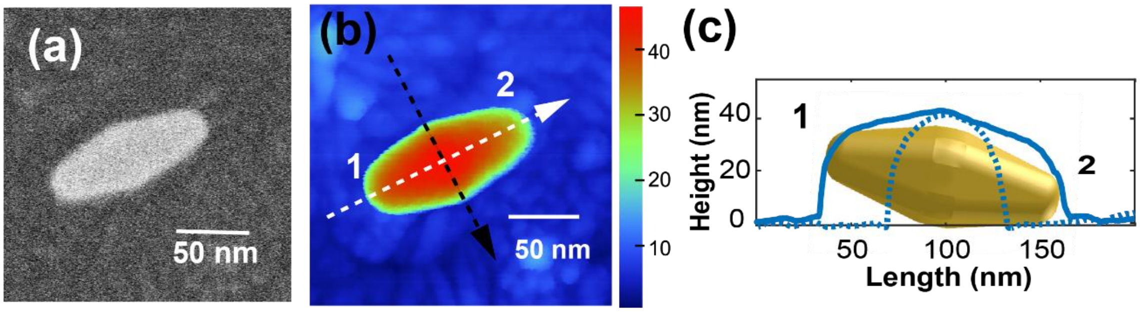

Figure 4.2 Typical SEM and AFM image of a single Au nano-bipyramid (AUBP). (a) SEM image and (b) AFM image of the same single AuBP. (c) Blue solid line and blue dotted line show the cross-section profiles of the position marked by the white dotted line and black dotted line in (b) respectively, number 1 and 2 marks the two corners along AuBP's long axis and we can distinguish that corner 1 is above.

4.2 Orientation measurement by direct Photoluminescence pattern imaging

AuBP has sharp ends and exhibit notably narrower LSPR resonance than other shapes of MNPs such as nano-cubes and nano-spheres, which helps it to work as a more sensitive plasmon probe. SEM and AFM can be used for characterizing the orientation of AuBPs. However, using AFM is incredibly time-consuming and using SEM may cause damage or contamination to the AuBPs. The non-contact method, such as defocused dark-field imaging[180], back-focal plane imaging[181], differential interference contrast (DIC)[182], and scattering-based total internal reflection (TIR)[183] , have been used for characterizing the orientations of anisotropic gold nanoparticles, especially for gold nanorods. Confocal scanning microscopy cooperated with higher-order laser mode exciting has been proven to be used for dipole orientation detection at single-molecule level[184] and has also been used for single gold nanorod detection[185,186]. Different from the former methods, this method provides information about the excitation transition dipole moment (TDM) instead of emission DM. Let us introduce these high-order modes in the following section.

4.2.1 Azimuthally and radially polarized doughnut modes

A specific field distribution with unique electric field components can be created by the tightly focused azimuthally and radially polarized beam. Figure 4.3 shows the field intensity and polarization characteristics of these two modes. The spatial distribution of the polarized directions of radially polarized and azimuthally polarized light has center-symmetric characteristics. The electric field vectors' direction at both ends of the optical axis is precisely the opposite (i.e., there is a π phase difference), forming a hollow ring-like intensity distribution. Therefore, they are also known as azimuthally polarized doughnut mode (APDM) and radially polarized doughnut mode (RPDM). These two modes have only in-plane vector electric components in the input plane perpendicular to propagation direction z, while their behavior becomes different when they are focused. There are only in-plane polarization components of the electric field for azimuthally polarized mode. In contrast, for radially polarized mode, there are both in-plane and longitudinal (out of plane) components and the longitudinal components at the focal plane.

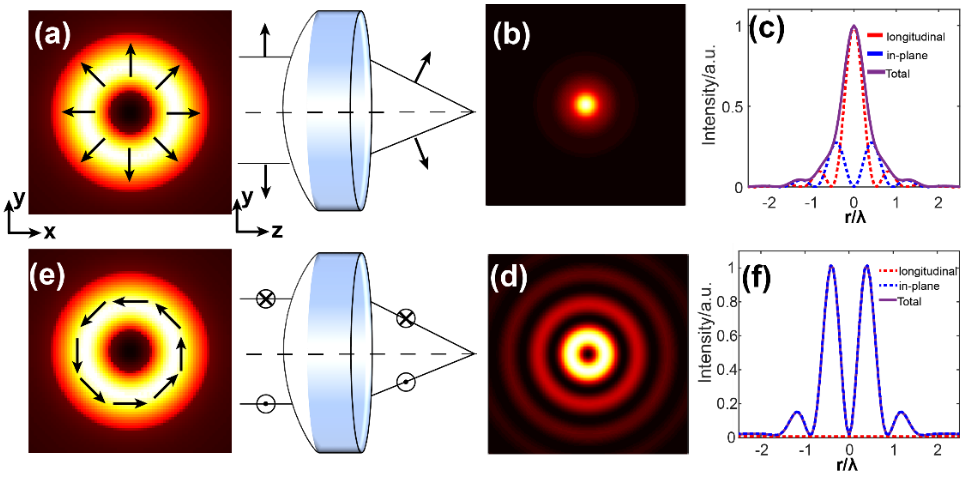

Figure 4.3 Schematic diagram of the electrical field formation of a radially polarized mode (a) and an

azimuthally polarized mode (e). (b) and (d) show the examples of their respective focused field intensity distribution (focused by a lens NA=0.95, calculated by Matlab according to vector diffraction theory from Richards-Wolf[187,188]). (c) and (f) represent the comparison of longitudinal component, in-plane field component, and total intensity distribution of the focal spot of the radially polarized beam and azimuthally polarized beam.

During the interaction of this kind of field with a single dipole, a given electric field component selectively excites the single electric dipole parallel to its polarization. Normally, a single molecule is much smaller than the laser beam's focal spot, during scanning, the molecule works like a scanning probe, and it can only be excited when its transmission dipole moment has projected component in the polarization direction of the excitation beam. The excitation intensity satisfies the equation of

$$I \propto |\boldsymbol{E}_{exc} \cdot \boldsymbol{\mu}|^2 \tag{4.1}$$

$\boldsymbol{E}_{exc}$ represents the spatial position-dependent complex electric field vector of the focused laser beam, $\boldsymbol{\mu}$ is the fluorescence molecular excited transition dipole vector. That means the transition dipole of the molecule maps the local electric field at different positions of the focal spot leading to a specific spatial intensity distribution pattern. Conversely, the three-dimensional spatial orientations of dipole can be judged by comparing the different excitation imaging patterns. Figure 4.4 shows the different imaging patterns when a dipole with different orientations interacts with a focal spot of APDM and RPDM. Because the focus spot of APDM has only in-plane polarization components of the field, as a consequence, a molecule orientates with its transition dipole moment perpendicular to the focus plane cannot be excited by the mode of APDM (Figure

4.4 (b), $\theta = 0^{o}$). Once if the transition dipole moment has a lateral component, the excitation pattern becomes double-lobe shaped (Figure 4.4 *(b),* $\theta = 30^{o}, \theta = 60^{o}, \theta = 90^{o}$).

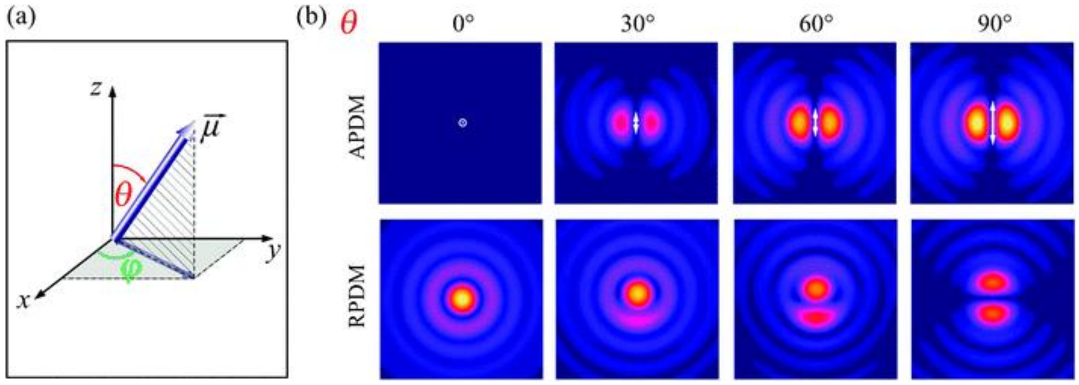

Figure 4.4 Interaction of an APDM and a RPDM in the focal spot with a dipole of a quantum emitter: (a) coordinate system of the dipole moment, (b) calculated patterns for different θ *angles (*$\varphi = 0^{o}$ *is a constant). The arrows drawn in the patterns resulting from APDM excitation indicate the lengths of the dipole moment's projection onto the x/y-plane*[189]*.*

4.2.2 PL imaging pattern of bare bipyramid

For metal nanoparticles, which also have the excitation and emission characteristics of electric dipoles, such as AuBPs, their 3D orientation can be distinguished by its photoluminescence (PL) [190] imaging pattern excited by azimuthally and radially polarized doughnut modes. In the case of single AuBP, the excitation patterns are obtained by scanning it through the APDM and RPDM laser beam area. According to equation (4.1), the photoluminescence intensity of AuBPs can be described as below [190]

$$I_{lum} \propto \left|\boldsymbol{E_{exc}} \cdot \widehat{\boldsymbol{P}}\right|^2 \qquad (4.2)$$

where $\widehat{\boldsymbol{P}}$ is the unit vector of polarizability tensor. For any 3D orientations of AuBPs, $\widehat{\boldsymbol{P}}$ can be decomposed into three orthogonal dipoles Pa, Pb and Pc, which are consistent with the main axis of AuBPs, shown in Figure 4.5(a). Since the short axis of AuBP is relatively shorter to its long axis (Figure 4.2), and the cross-section perpendicular to the long axis has round corners, the modulus of Pb and Pc is approximately consistent. Similar to what they did for nanorods in ref [191], simulated photoluminescence pattern of AuBPs excited by either an APDM or an RPDM can be calculated, results are shown in *Figure 4.5*(b). The interband transition[192] can be also included by introducing an extra term into diagonal elements of $\hat{\boldsymbol{P}}$.

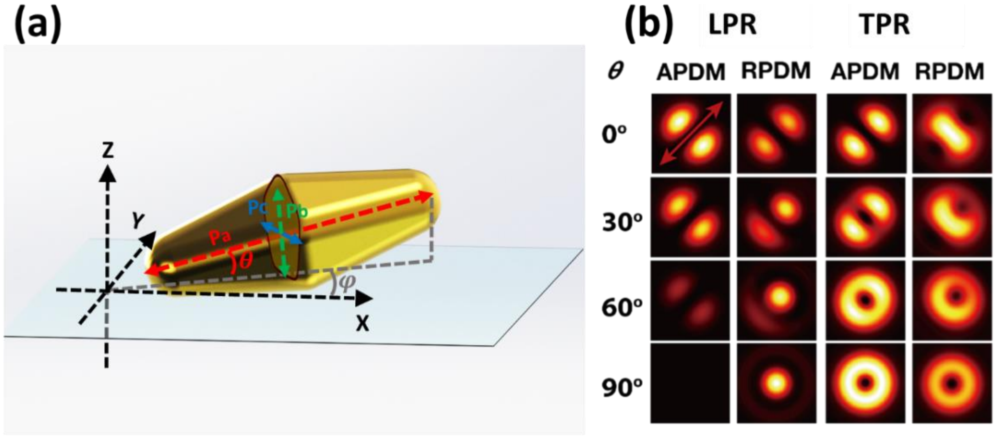

Figure 4.5 (a) 3D schematic diagram of a single AuBP deposited on the substrate. The Blue and green arrows indicate the orientation of transversal plasmon resonance mode (TPRM) and longitudinal plasmon resonance mode (LPRM). φ *and* θ *are the in-plane angle and out-plane angle, respectively. (b) Simulated photoluminescence patterns of gold AuBPs using an APDM mode and RPDM mode respectively, for both longitudinal plasmon resonance (LPR) and transverse plasmons resonance (TPR). The red arrow indicates the projection of the long-axis of AuBP on sample plane.*

Figure 4.6 shows a group of experiment results, including AuBPs' PL spectra and the correlated PL patterns obtained by APDM and RPDM using different exciting wavelengths. The double-lobe-shaped patterns resulting from 632 nm excitation (Figure 4.6 (b) bottom row) prove that this wavelength can excite AuBPs' longitudinal plasmon resonance mode (LPR mode: LPRM) and leading it works like a dipole with transition moment along the long axis. Asymmetric patterns excited with RPDM in Figure 4.6 (b) (bottom right image) reveals an out-of-plane tilt. The orientation indicated from the double-lobes entirely agrees with AuBPs' SEM image in Figure 4.6 (a). While the excitation laser changed to 530 nm, perfect ring-shape patterns were obtained under APDM and spot-like patterns were obtained under RPDM, shown in Figure 4.6 (b) (top row). So, the PL patterns under both APDM and RPDM show no directionality. We note that the out-of-plane orientation of a single bipyramid can ambiguously be determined via RPDM excitation under 632nm excitation. In Figure 4.6 (c), the PL patterns were transferred to polar images; the polar image behaves circular symmetry excited by 530 nm and behaves obvious anisotropy under 632 nm excitation. Figure 4.6(d) shows the PL spectra excited by different wavelengths. By comparing Figure 4.6(d) and Figure 4.1(e), the PL spectra roughly follow the dark-field scattering, namely the LPR mode spectra. However, PL peaks have a blue-shifter with respect to the scattering peaks that are related to the aspect ratio[193,194], which may originate from high electron density[195]. PL spectrum has no blinking phenomena, as shown in Figure 4.6(e), which is generally quite different from the PL emission of single QDs. This can help distinguish and exclude QDs ’fluorescence signals from AuBP PL after introducing QDs around AuBPs in subsequent experiments.

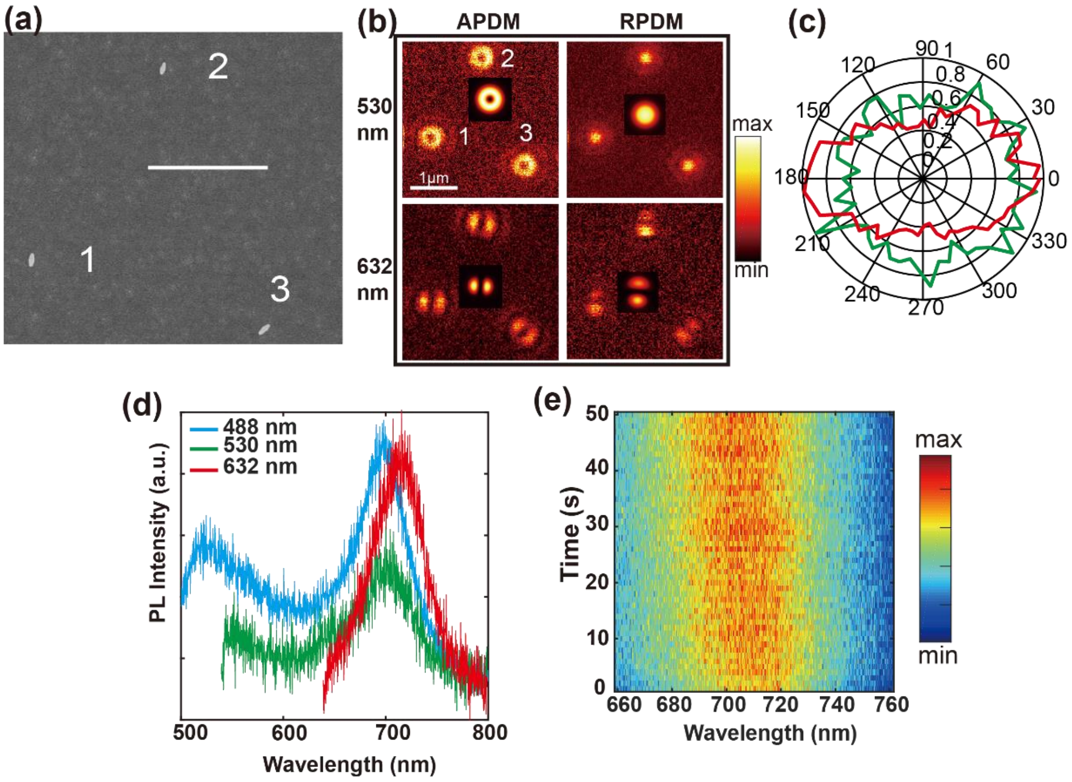

Figure 4.6 (a) SEM image of three separated single AuBPs. (b) Photoluminescence (PL) excitation patterns of AuBPs are shown in (a) excited by 530 nm (top row) and 632 nm (bottom row) using APDM and RPDM modes. The inserted small images give out the simulated PL patterns of AuBP No.1. (c) The corresponding Polar plot of normalized extinction value from PL patterns of AuBP No.1 in (b) using APDM mode, green and red lines represent the exciting wavelength of 530 nm and 632 nm respectively. (d) PL spectra of single AuBP No.1 in (a) that were obtained using different excitation wavelengths. The excitation laser's power

was set to 25 uW. (e) Time trace of PL spectra of AuBP No.1 acquired under 530 nm excitation.

According to Figure 4.6 (d), all the PL emission spectra under different exciting wavelengths have a main peak around 700nm assigned to LPRM's plasmonic emission. When excited at 488nm/530nm, a weak peak shows up as a shoulder around 570nm that coincides with the transverse plasmon resonance mode, but too weak compared to the peak from longitudinal plasmon resonance mode. Besides, under 488nm excitation, the PL spectrum has another obvious peak around 522nm caused by interband transition. Under 530nm, it is unavailable to observe this peak because of the high-pass filter presence at 532nm. *Figure 4.7* tries to explain the mechanism for plasmon luminescence of AuBPs. After excitation, the electron-hole pairs created either directly through interband excitation or generated by plasmon excitation can recombine and relax very efficiently through non-radiative pathways and emit a photon, or take part in plasmonic oscillation after a fast dephasing (~1 ps) process, which can subsequently relax through radiation process[196–198]. At 488nm, interband transition is excited, and generate electron-hole pairs, then the hot electrons lose their energy nonradiatively and interconvert to TPRM or LPRM, following with plasmonic emission. At 530 nm, both the TPRM and interband transitions can be excited and generate hot electron-hole pairs that subsequently decay into LPRM, which emits photons and displays a peak around 700nm. Here, the interconversion between the TPRM and LPRM is achieved with the involvement of electron-hole pairs[199]. The interband transition has isotropy of polarizability tensor. Hence, under 530 nm excitation, the centrosymmetric PL patterns in Figure 4.6 (b) directly reflect the focus's field distribution due to isotropic excitations indicate that the interband transition plays the major role for PL. Even though TPRM mode can be excited by 530 nm, it did not contribute to PL. At a wavelength of 633 nm, the low energy is impossible to excite interband absorption, direct excitation of the longitudinal surface plasmon resonance occurs. In general, the pattern shape allows one to distinguish photoluminescence caused by the plasmon or interband transitions.

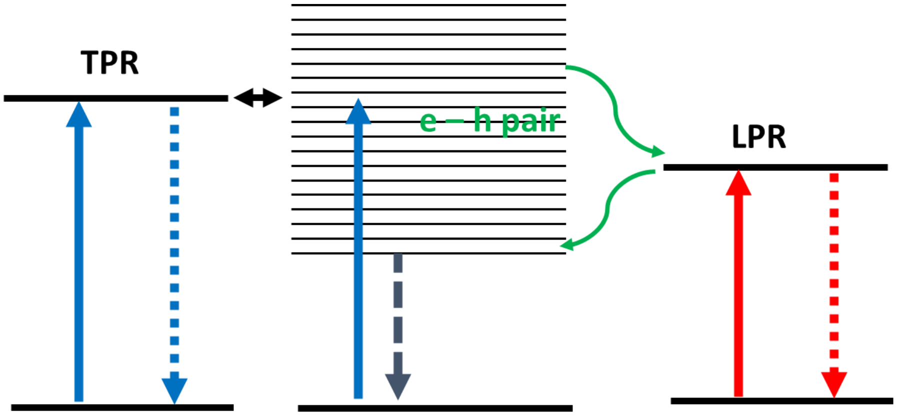

Figure 4.7 Schematic diagram of the mechanism for plasmon luminescence of AuBPs. The blue lines represent excitation under 530 nm, which excites both interband transitions creating electron hole (e-h) pairs and the transverse plasmon resonance mode (TPRM). The red line pictures the excitation of the longitudinal plasmon resonance mode (LPRM) under 632 nm laser. The blue and red dashed lines represent emission from TPRM and LPR, respectively. The gray dashed line presents the nonradiative relaxation by recombination of e-h pairs. Energies used for exciting interband transition and TSPR are similar because of their spectra overlap and are bigger than LSPR.

In order to tell whether there is a preference between different relaxation paths when excitation polarization varies. We use different filters (634 nm long-pass filter, 633 nm short-pass filter) to separate the emission from LPRM and TPRM into green channel and red channel. If the relaxation path is related to specified excitation polarization, emission intensity will vary with the polarization. At 488 nm or 530 nm, both interband transitions and the transversal plasmon resonance (TPRM) can be excited. As shown in Figure 4.8, excitation patterns of AuBPs that are labeled 4,5,6 remain isotropic for both green and red channel implying the contribution of certain free electrons relaxation path is not related to excitation polarization. Hence, we can conclude that 530 nm excitation gives rise to mainly longitudinal surface plasmon emission, which does not depend on the excitation polarization. This result is consistent with previous similar reports[191,196].

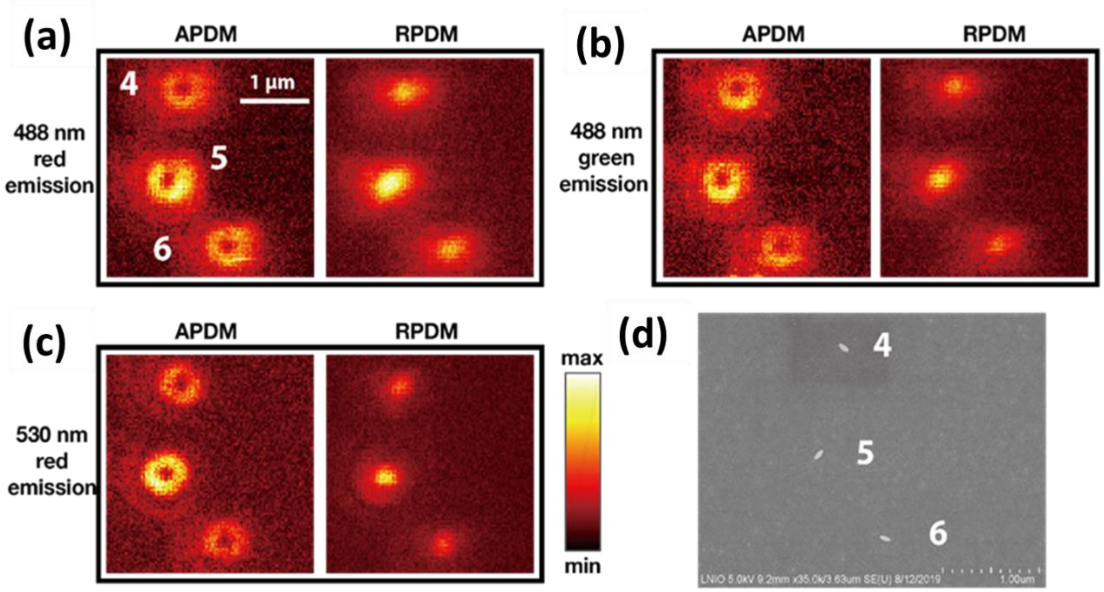

Figure 4.8 (a)-(c) Photoluminescence excitation patterns of single AuBP excited at 488 nm and 530 nm using APDM and RPDM laser beam. Emission was separated into green and red channel at 633 nm to distinguish the emission from LPRM, and TPRM and interband transition. SEM image of the same area is shown in d). Laser power used for excitation is set to 25uw.

4.3 Anisotropic emission pattern of AuBPs-based hybrid nanostructures

As what we did on gold nanocubes in previous chapters, plasmon-triggered near-field TPP was also applied on AuBPs. Considering the LSPR peaks of AuBPs with the inevitable red-shift within polymer, we chose 800 nm as the wavelength used for TPP. A typical group of results is shown in *Figure 4.9*.

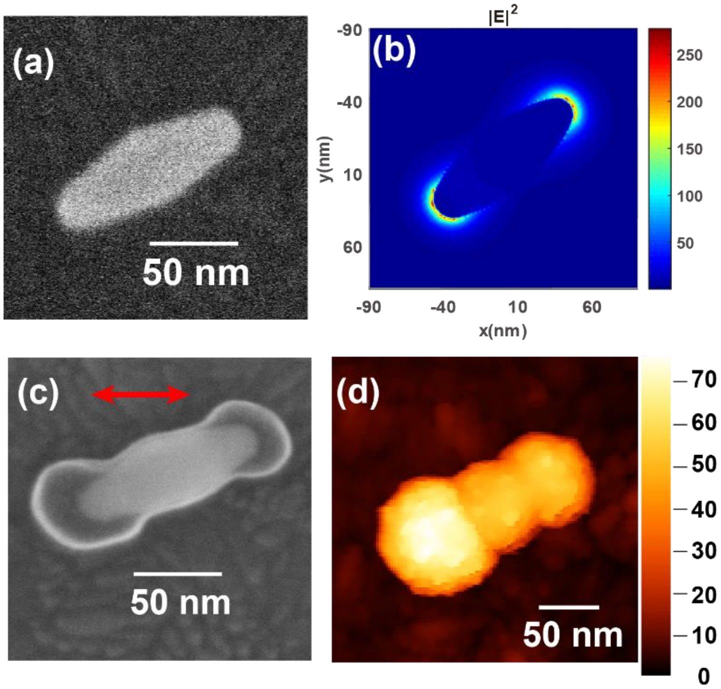

Figure 4.9 Hybrid structure based on AuBPs fabricated by Near-field TPP. (a) SEM image of bare single AuBP. (b) Simulated near-field distribution around AuBP excited by 800 nm. SEM image (c) and AFM image (d) of the hybrid structure fabricated on the AuBP in (a) by linear-polarized laser. The red arrow in (c) indicates the polarization direction of the curing laser used for TPP.

The near-field distribution of AuBPs is more localized than it is for gold nano-cubes; and the enhancement factor is higher. With Au nanocubes, we have found the plasmon-triggered near-field distribution is dependent on the orientation of cubes. With AuBPs, even when the polarization direction of the incident light used for polymerization is not parallel to the long axis of AuBP, most of the integrated polymer is located at the two tips of the AuBP. No polymerization occurs only when the long axis of AuBP is orthogonal to the polarization direction of the excitation light. *Figure 4.10* displays six examples of the hybrid AuBPs with different orientations; all of them were fabricated using a linear-polarized laser whose polarization direction was represented by the red arrow. Because for each two AuBPs, the sizes and sharpness of tips, are slightly different, that will lead to different volume of the generated polymer lobes caused from different localized field intensity.

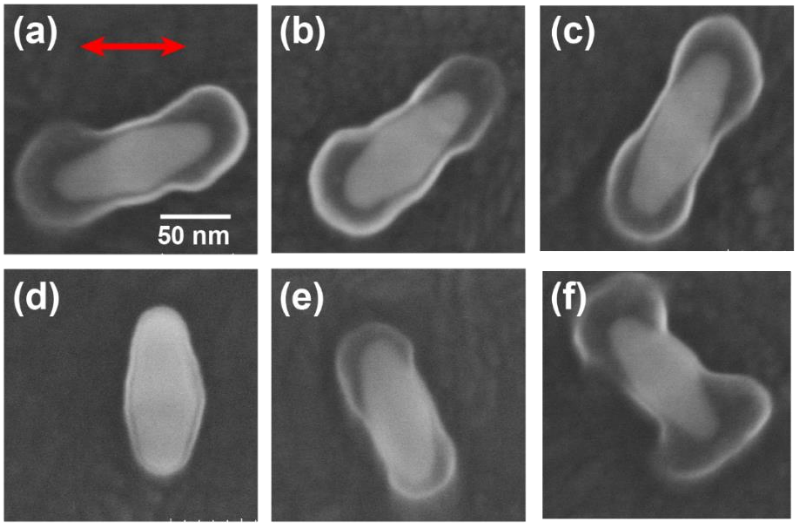

Figure 4.10 Several examples of hybrid AuBPs fabricated by near-field TPP. The red arrow indicates the polarization direction of the incident light used for polymerization. All of these six hybrid AuBPs were fabricated using same conditions.

The photosensitive formulation used for AuBPs is similar to the former one used for nanocubes. It also consists of three components: the PETA, 1%wt IRG 819 and QDs. In order to increase the coupling between QDs and AuBPs, we chose red QDs with an emission wavelength of 670 nm instead of 620 nm. Considering the absorption spectrum of QDs (see figure 4.11(a)), the lowest energy optical transition of the QDs around 720 nm is close to the longitudinal plasmon excitation of Hybrid AuBP (see in Figure 4.11(b)). The good overlap between both the absorption and emission of the QDs and the AuBPs is achieved, which means good coupling between QDs and AuBPs is expected.

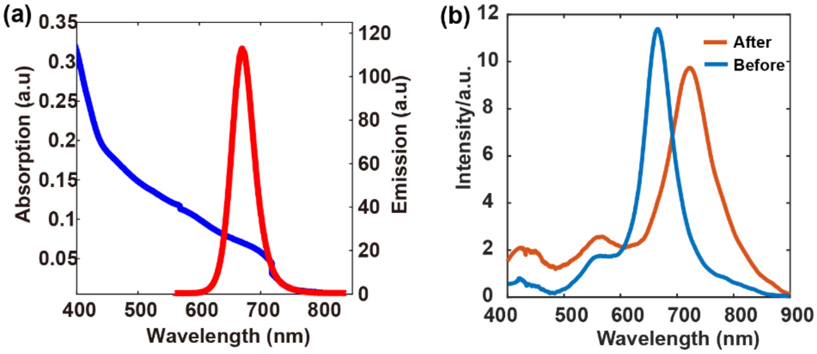

Figure 4.11 (a) Absorption and emission spectra of red QDs (in Toluene) used for hybrid AuBPs. (b) Dark-

field scattering plasmons spectra from a same AuBP before and after TPP polymerization. In (b), the formulation only contains PETA and photoinitiator, which means the hybrid AuBP has no QDs.

After polymerization, the resulting hybrid AuBPs/polymer/QDs nanosystems were scanned by the same set-up using APDM and RPMD mode; their fluorescence emission patterns are shown in

Figure *4.12*. The PL signal from AuBP is much weaker than the fluorescence emission signal from QDs. We use 1.4uw for exciting hybrid AuBP-based nanostructures instead of 25uw that was used for getting the same level of PL signal from pure AuBPS. Besides, the fluorescence emission signals from QDs in a hybrid system show obvious blinking (see Figure 4.16) while the PL signal has not this phenomenon (see Figure4.6). Compare the PL patterns from pure AuBPs and hybrid AuBPs (QDs-contained). We find that the emission patterns of hybrid AuBPs excited by 532nm using APDM show directionality instead of isotropic ring patterns in pure AuBPs. It can be seen more clearly in the corresponding polar images in *Figure 4.12* (c) and (d).

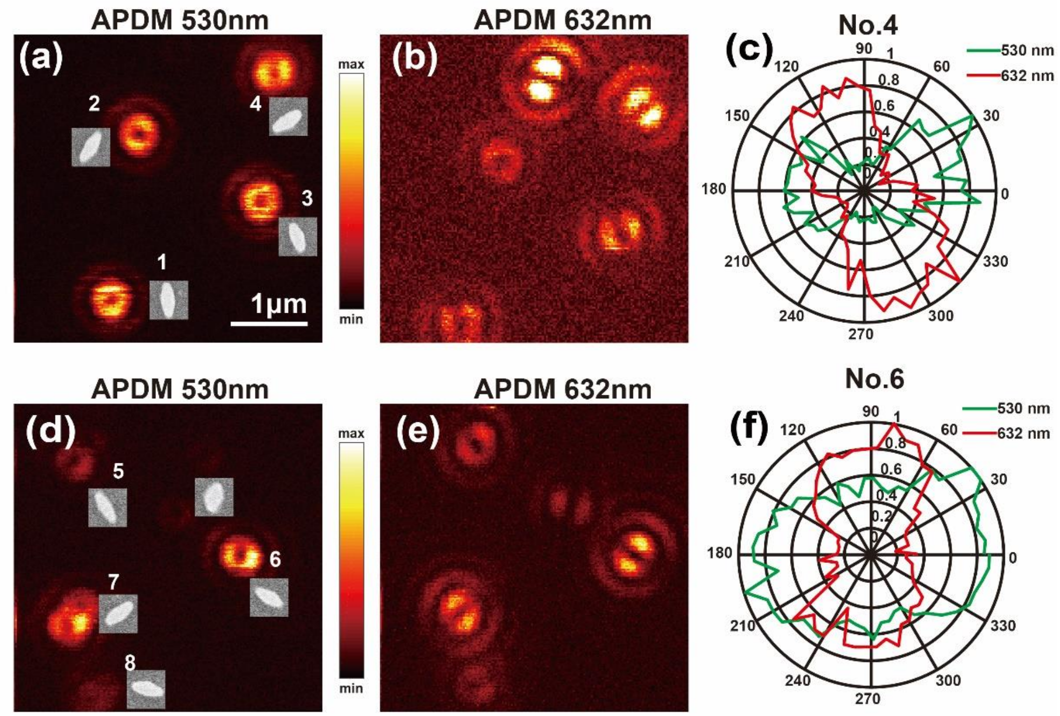

Figure 4.12 (a) (b) are the PL images measured from the first group of hybrid AuBPs (No.1 ~No.4) with APDM excited using 530 nm and 632 nm respectively; inserted small images show the original SEM images

of the corresponding AuBPs. (c) The corresponding polar image of emission patterns from No.4 hybrid AuBP in (a) (b). (d) (e) are the PL images from the second group of hybrid AuBPs (No.5 ~No.8) excited 530 nm and 632 nm, respectively. (f) Shows the corresponding polar image of emission patterns from No.6 hybrid AuBP in (d) (e). The laser power used for excitation is about 1.4uw.

Taking QDs' properties into consideration, as we discussed in section 1.3.1 , $\gamma_{ex} \propto |\boldsymbol{E}(\boldsymbol{r},\omega)\cdot\boldsymbol{\mu}|^2$($\boldsymbol{\mu}$ is QDs' excitation TDM). The excitation transition dipole moment (TDM) of a single CdSe/ZnS QDs has been proved to be isotropic and non-directional in 3D dimension by measuring its excitation pattern[200]. The bare "excitation patterns" of our QDs can be obtained through the PL image obtained by scanning the dispersed QDs on glass with APDM and RPDM using 530nm, the results were shown in Figure 4.13(a) (b), and they are isotropic (non-directional) as we expected. The excitation patterns demonstrate clear blinking phenomena implying high possibility of single QDs. The g^2 measurement from single QDs in Figure 4.13(c) further proves the existence of single QDs emitting single photons. The excitation patterns created by APDM and RPDM shows standard ring and spot shapes indicating isotropic symmetry.

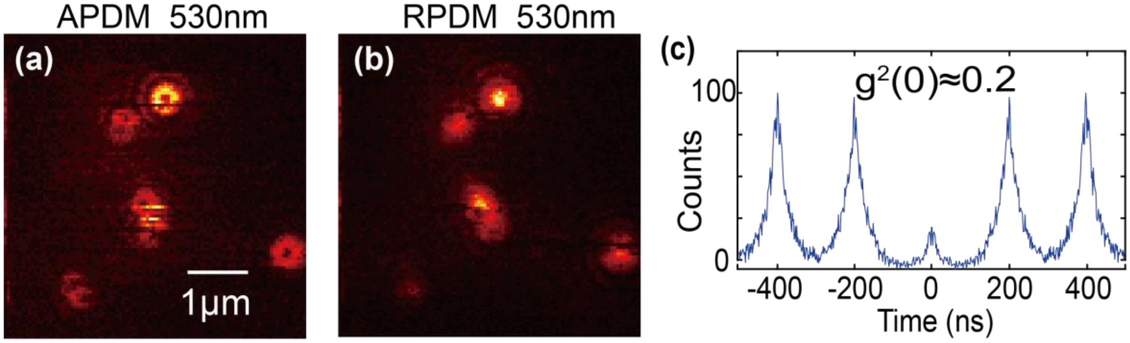

Figure 4.13 670 nm QDs' PL image scanned by APDM (a) and RPDM (b) excited using 530 nm. (c) g (2) measurement from the position of one spot in (b) showing a data smaller than 0.5. The laser power of 530nm is set about 0.4uw.

Compare the patterns excited by 530 nm using APDM in Figure 4.6 (b), Figure 4.12, and the patterns in Figure 4.13, independent QDs and AuBPs both have isotropic excitation PL patterns, while the fluorescence emission patterns from hybrid AuBPs with QDs in vicinity show anisotropy or another saying directionality.

In order to figure out the reason of changing of symmetry state in the “excitation patterns”, “non-active” hybrid AuBPs were fabricated using photosensitive formulation only containing PETA and photoinitiator without QDs. The second kind of hybrid AuBPs was measured using the same process and their excitation patterns were shown in *Figure 4.14*.

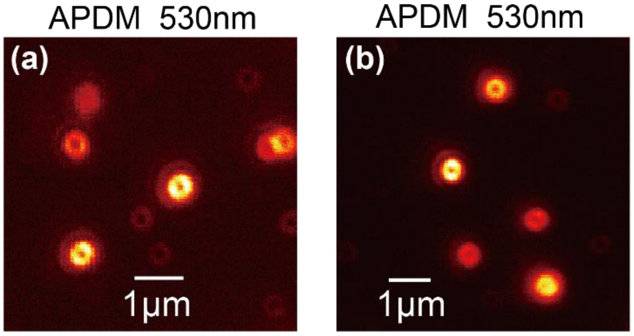

Figure 4.14 Several examples of the PL patterns measured from hybrid AuBPs without QDs contained in polymer using APDM excited at 530 nm. The laser power used here is set to 25uw.

The PL patterns in Figure 4.14 do not give out clear directionality. That means the anisotropy in the PL patterns from hybrid AuBPs with QDs results from the interaction between QDs and AuBPs. According to Figure 4.6(b) and

Figure *4.12*(b) (e), for both pure AuBPs and Hybrid AuBPs containing QDs, their PL patterns and fluorescence emission patterns show the brightest when exciting polarizations were along the long axis of AuBPs under exciting of 632nm. Under 530 nm excitation, the emission patterns of hybrid AuBPs display the biggest signal when the excitation polarization is along the short axis of AuBPs. However, most of the QDs are placed around bipyramids' tips, whose connect lines are along the long-axis. In addition, if we compare the PL patterns from pure AuBPs under 632nm excitation using APDM (where the AuBP works like a dipole), and the emission patterns from hybrid AuBP, both images show anisotropy, while the PL patterns from pure AuBP show higher anisotropy because its PL patterns are clear unconnected two-lobe patterns instead of having a weak connected part in the middle.

According to Figure 4.7, in presence of QDs, we have a hybrid AuBP-QDs energy system shown in Figure 4.15. When a bare AuNB was excited by 530nm, both interband transition and TPR mode was excited and the generated electron-hole pairs after a fast-dephasing process, finally leads to LPR emission. When QDs in present, using 530nm for excitation, it turns out that polarization along the short-axis obtain a brighter signal than polarization along the long-axis.

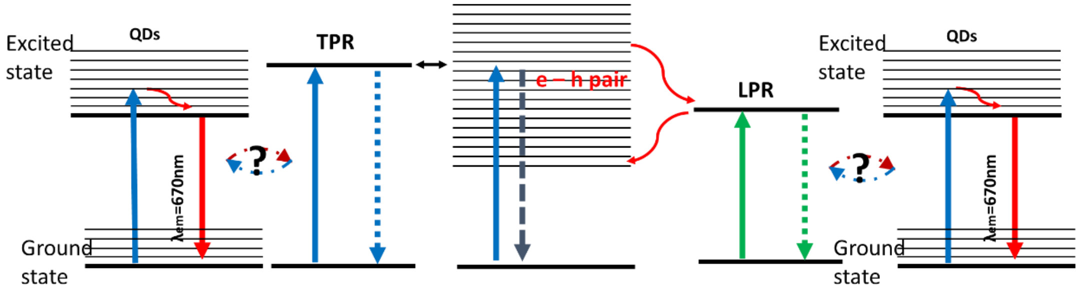

Figure 4.15 Schematic diagram of the emission mechanism of the hybrid AuBPths with QDs in the vicinity.

One possibility is that excitation along AuBP' short-axis attributes to higher emission from QDs. It may because in presence of QDs, under 530nm excitation (TRRM is excited and the interband transition is exciting), the quick dissipation of TPRM is converted to QDs' emission. Another possibility is that, when exciting the hybrid AuBP-QDs along the long-axis, the QDs' emission is suppressed that may come from the quenching effect. In any case, there must be interactions between QDs and AuBP's TPRM or LPRM. At present, we have not a clear idea about these results, more discussion and study are needed for understanding. Emission spectra study from Bipyramid-based hybrid structure

For hybrid AuBPs, another property we concern about is their emission spectra. The confocal scanning system is easy to couple to the spectrometer and constructs the Hanbury Brown & Twiss system as illustrated in Figure 2.24. 6(a) shows the time trace spectra from bulk QDs, showing stable emission. After diluting the QDs' solution and dispersing it well on the substrate, with the help of $g^{(2)}$ measurement, we found single QDs and recorded the time trace spectra from single QDs shown in 6(b). All the active hybrid AuBPs were fabricated using the formulation composited by PETA+1%IRG+670 nm QDs. Although QDs' distribution follows the polymer's distribution, the exact position of every QD is random, their position relative to the AuBP is also random. Besides, for our AuBPs, there are differences in the size of individual AuBPs leading to different localized plasmon resonance peaks. All these parameters will contribute to different strengths of coupling between QDs and AuBPs. Figure 4.16 (c), (d) and (e) display the time trace spectra from three different active hybrid AuBPs. The fluorescence spectrum from the first hybrid AuBP has clear one main peak, while the other two hybrid AuBPs exhibit obvious or less obvious two emission peaks. Figure 4.16 (f), that shows the fluorescence spectra of bulk QDs, single QD, and active hybrid AuBPs, clearly reveals these different regimes of light emission. Bulk QDs' fluorescence spectrum results from the ensemble of all the excited QDs' emission, and it has an FWHM (Full-Width Half Maximum) about 36 nm. The spectrum from isolated single QD (dashed grey line) and the spectrum from the first example of hybrid AuBP (red line) are narrower with an FWHM about 25 nm. Besides, the emission spectra from single QD and first hybrid AuBP are within the spectral envelope of the spectrum from bulk QDs. However, for the other two hybrid AuBPs (e.g. 2 and e.g.3), their fluorescence spectra display two peaks and a broader spectrum envelope. Additionally, hybrid AuBP e.g. 2, shows a bigger separate between two peaks than hybrid AuBP e.g.3. These special fluorescence spectra are quite different from the emission of whether bulk QDs or single isolated QD. AuBPs can be regarded as nanocavity because of its high near-field confinement ability and relatively larger quality factors (about 13) compared to gold nanocube. Hence, we have some reason to suppose that this two-peak phenomenon is due to the Rabi spectral splitting, which might result from the strong coupling between AuBPs and QDs. However, so far, there is not enough evidence to confirm this speculation. More experimental data and calculation data need to be obtained in the near future. Precise evidence, including dark-field scattering with clear spectrum splitting and anti-cross dispersion curves, needs to be observed to prove it.

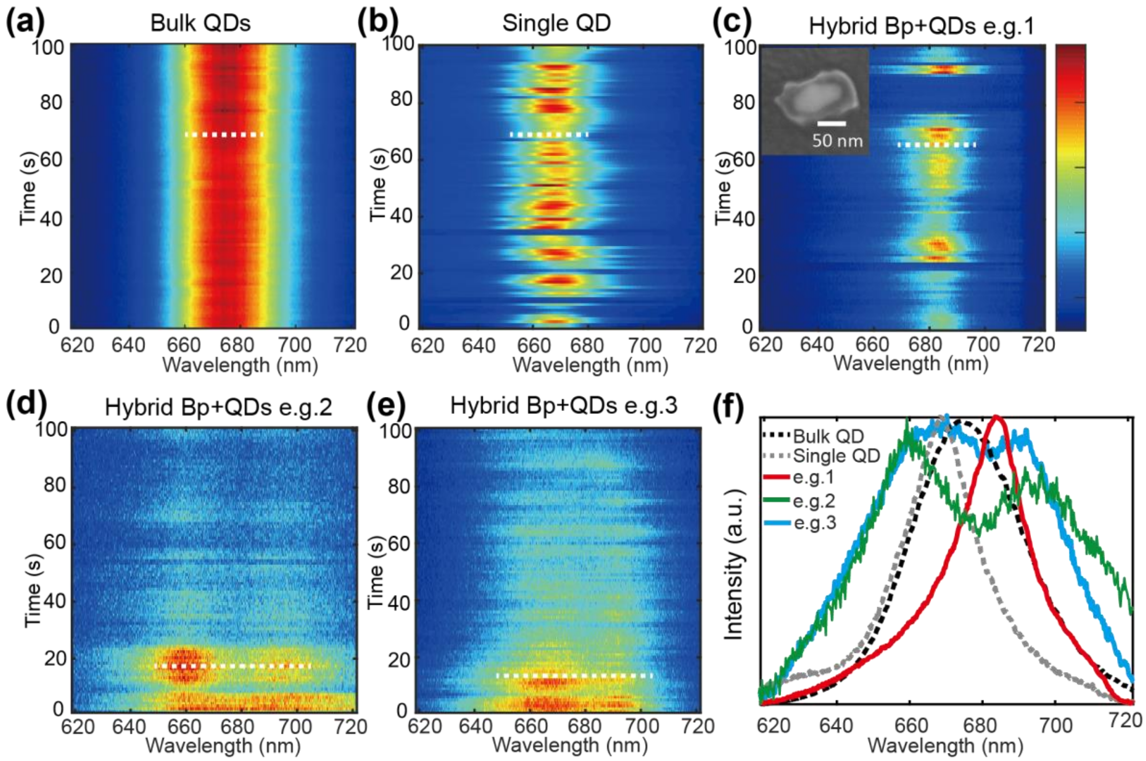

Figure 4.16 Spectra from pure QDs (bulk of many QDs) and hybrid AuBPs containing QDs. (a) Time trace of fluorescence spectra of bulk QDs. (b) Time trace of fluorescence spectra of single QD. (c) (d) (e) three examples of the time trace fluorescence spectra from hybrid AuBPs with QDs inside the polymer. (f) Pick up one moment of spectra from previous images (a) ~ (e), time position indicated by dashed white line.

The autocorrelation g^2 function measured from the hybrid AuBP, e.g.3, is shown in Figure 4.17. It worth noticing that $g^2(0) = 0.45 < 0.5$, revealing that there are only a few QDs (close to a single QD emitting single photons). From the lifetime change between the isolated QDs (about 8ns) and QDs in hybrid AuBPs (less than 0.23ns can be obtained), a high Purcell factor (more than 30) is revealed, suggesting a significant modification of the QDs' radiation characters by coupling between AuBPs.

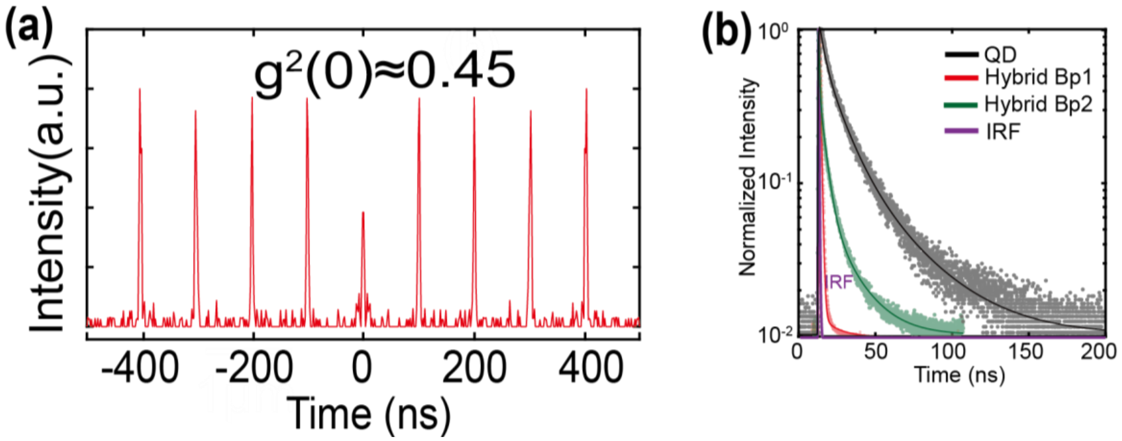

Figure 4.17 g$^{(2)}$ autocorrelation function measurement of hybrid QDs-contained AuBPs in Figure 4.16 (e) (incident power of 15uw with a laser of 530nm, 10 MHz repetition rate). (b) Lifetime measurement: comparison between single QD without AuBPs (black curve, 8 ns), hybrid AuBPs with single QD inside its polymer (red curve, about 0.98ns) and another example of hybrid AuBPs with few QDs in polymer (green curve, about 0.23ns).

4.4 Summary

Different from nanocubes, bipyramids with significantly anisotropic shapes have two different localized surface plasmon resonance modes, corresponding to its long-axis and short-axis respectively. In this chapter, we have measured the photoluminescence of a single gold bipyramid deposited on a glass substrate. The PL patterns of AuBPs obtained using Raster-scanning confocal microscopy combined with APDM and RPDM can help us figure out the 3D orientations of AuBPs. Near-field TPP was used again for fabricating the AuBPs-based hybrid light emitting systems. When 530 nm is used as the excitation wavelength, the PL mode of the pure bare AuBPs and the isolated QD is circularly symmetrical and non-directional, while the hybrid AuBPs with QDs in vicinity exhibit apparent anisotropy and directionality. We fabricated hybrid AuBPs as nano-emitters with number of the trapped QDs reduced to a single level. Additionally, we got some unusual fluorescence spectra from hybrid AuBPs. Some of them display two emission peaks, which must be investigated deeply for a better explanation.

Chapter 5 Perspectives and outlooks

This chapter introduce some perspectives of the thesis and show associated preliminary results.

In chapter 3, we assessed the number of QDs inside polymer lobes. In order to be more accurate, direct observation of the QDs inside the polymer in the vicinity of metal nanoparticles should be done. We succeeded to fabricate several hybrid cubes containing QDs on a TEM grid, which would allow us to observe the QDs in the thin area of polymer lobes.

According to the discussion in section 3.3, chapt.3, the emission from cube-based hybrid nanoemitters have high polarization sensitivity, based on which, it is highly feasible to develop a two-color system, and it is expected to get a higher polarization-sensitivity compared to the work published in ref-7. Furthermore, we can consider a three-color hybrid nano-emitter based on nano-triangles, nano-tripods, etc.

In the previous chapters (chapter 3 and chapter 4), hybrid cube-based nanostructures and hybrid bipyramid-based nanostructures have been introduced. These gold nanoparticles confine the light field to a nanoscale volume at the resonance frequency and cause near-field enhancement. However, their field confinement ability, field enhancement ability and plasmon mode damping limit the interaction strength between single metal nanoparticles and emitters. Dimer structures made of two adjacent metal nanoparticles with tunable gap size can achieve much higher field enhancement with smaller mode volume and lead to stronger interaction between emitters[201]. The near-field plasmon triggered photopolymerization method will also be used on dimer structures, for example, gold disk dimers and gold bowties.

Besides, previous hybrid structures were fabricated using emitters (QDs) initially contained within the photo polymerizable formulation. The incident light used for polymerization can perturb the emitters at the same time. Additionally, it is not easy to predict/control the exact position of the QDs within the polymer lobes. Another approach based on surface functionalization may be used to address these potential limits. This approach is based on 2 steps Near-field photopolymerization is first carried out, while the emitters are then attached, in second step, to the polymer surface after polymerization instead of being contained in the formulation during polymerization. With this method, we can integrate emitters on the polymer's surface in metal nanoparticles' vicinity.

In this chapter, the above points will be discussed separately.

5.1 Multi-color hybrid nano-emitters

The anisotropic cube-based hybrid nano-emitter shown in Figure 3.5 (c) was fabricated using one-step exposure permitting the trapping of one kind of QDs within two polymer lobes on the corners along cube' one diagonal. Since the gold nanocube has a C4v in-plane symmetry, the two LSPR modes excited along its two orthogonal diagonals are the same.

The integration of two colors is possible.[7] After generating a same hybrid structure shown in Figure 3.5 (c), the polarization of the curing laser is rotated from X-direction to Y-direction, and a second plasmonic TPP is carried out, as described in section 3.1.2 chapt.3, with another formulation containing the second kind of QDs, keeping the other parameters unchanged, resulting in two other polymer lobes along the other diagonal. In that way, an hybrid cube/polymer nanostructure with two different kinds of QDs can be obtained, as shown in Figure 5.1 (a) and (b). Figure 5.1 displays a set of preliminary results of a two-color hybrid nanostructure with QDs-1 (emission at 620nm) and QDs-2 (emission at 670nm) trapped in four polymer lobes.

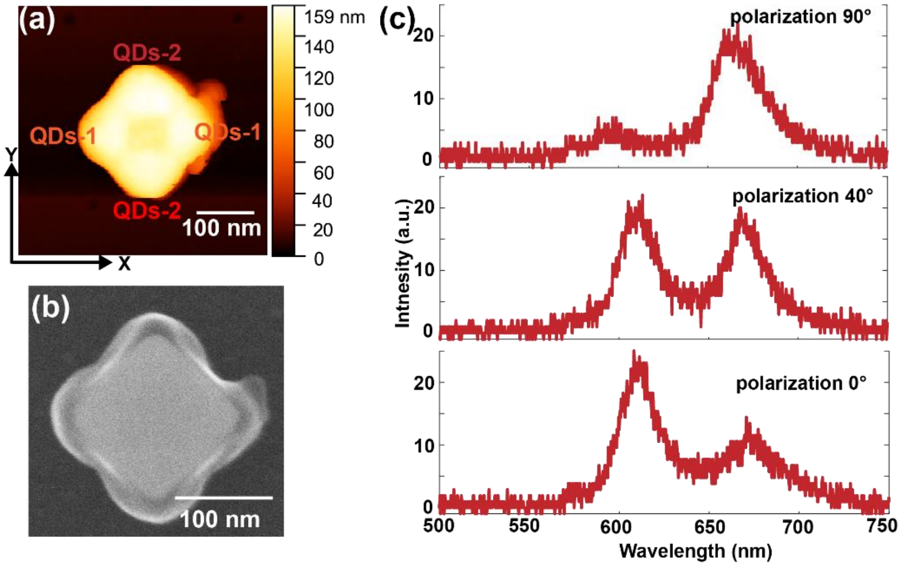

Figure 5.1 Two color hybrid cube-based nano-emitter.(a) AFM image. (b) SEM image. (c) Emission spectra

of the hybrid nanostructure in (a), excited by a 405nm linear-polarized laser. The polarization direction of the exciting laser rotated counterclockwise from x-polarized (0o) to Y-polarized (90o), from bottom to top.

In Figure 5.1 (c), the two emission peaks correspond to two kinds of QDs. When the excitation polarization is along X-direction, more of QDs-1 are excited and the emission intensity of peak (620nm) from QDs-1 is much bigger than the emission peak from QDs-2. And when the excitation polarization is along the bisector of the angle between X and Y, the two peaks are well-matched in strength. When the polarization is along Y-direction, the peak of 670nm dominates. Obviously, this cube-based two-color hybrid nano-emitter can realize the switching between two emission wavelengths with different intensities.

In the future a very ambitious perspective is to fabricate three-color hybrid nano-emitters. For a gold nano-triangle presenting a C3v symmetry, if we use an excitation laser whose wavelength matches the triangle's LSPR, by rotating the polarization direction of the laser, we could control the integration of the polymer lobes only at the triangle's corners, as shown in Figure 5.2(a) which illustrates this capability. By using three steps of exposure, it is potentially possible to trap three kinds of QDs with different emission wavelengths in the vicinity of the triangle's three corners, respectively. Figure 5.2(b) shows the schematic representation of this idea.

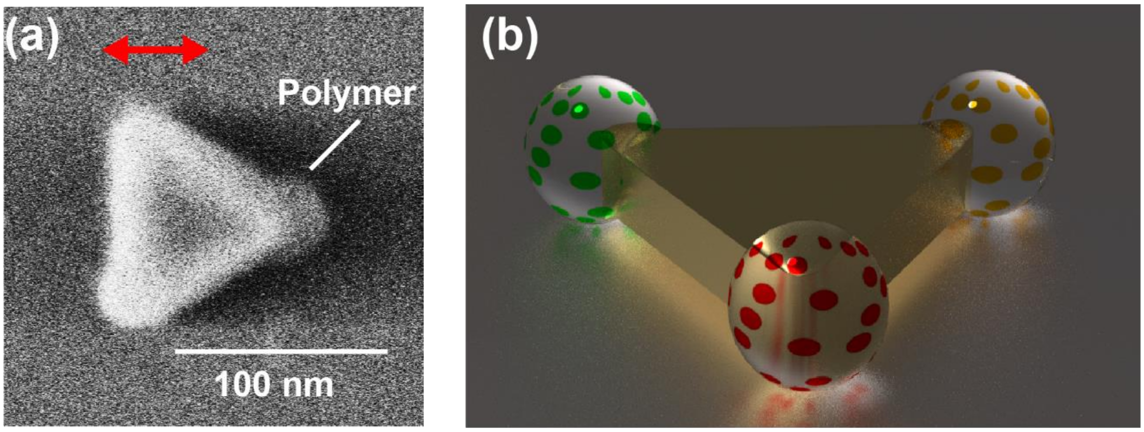

Figure 5.2 Three-color hybrid nano-emitter based on triangle. (a) A SEM image of a hybrid Au triangle with a polymer dot on one of its corners, fabricated by near-field TPP using a linear-polarized laser, the polarization direction is shown by the red arrow. (b) Schematic diagram of a three-color hybrid nano-emitter based on a gold triangle.

5.2 Hybrid plasmonic nanostructures based on dimers

As multi-particles structures, disk dimers and bowties are first considered due to their relative simplicity and ease of manufacture by top-down EBL. Here, we use gold disk dimers with height of 50 nm and diameter of 80 nm, and bowties having a length of 80 nm and a thickness of 50 nm. The gap size of all the dimer structures changes from 0 nm to 30 nm. The round corners of bowties have a radius of about 15 nm that is much smaller than the radius of disks, contributing to better field confinement. Figure 5.3 shows a typical group data of Au disk dimers with a gap of about 20nm. It is worth noting that the topography AFM image cannot reflect the real gap size as SEM can do. Figure 5.3(c) displays the scattering spectra of this dimer with different incident polarization directions of the incident white light. We can see LSPR peak corresponding to the mode of long-axis (gap mode) is switched to another peak corresponding to the short-axis mode. Long-axis is defined as the connecting line between two disks' centers, and the short-axis is orthogonal to it. When the gap mode is excited, the light will be confined in the gap with a much larger intensity as what we have shown in Figure 5.3 (d) calculated by the FDTD solution. Meanwhile, even for the two disks themselves, weaker field enhancement will appear on the opposite side of the gap along the long-axis by off-resonant exciting because the resonant peak of mode given by the short-axis is not too far away from gap mode. Following near-field polymerization results will reflect this more clearly.

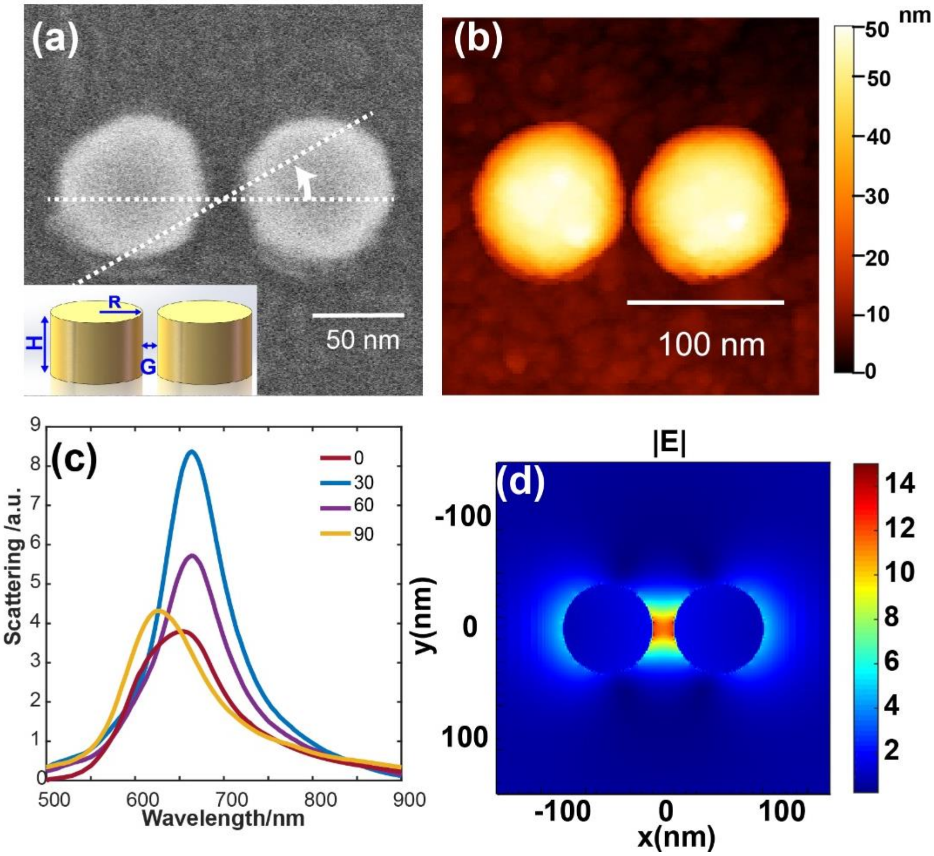

Figure 5.3 Characterization of the Au disk dimers. (a) SEM image of an Au disk dimer with a gap size around 20nm. (b) The topography image obtained by AFM. (c) Measured dark-field scattering spectra of the dimer with different polarization angles. Polarization angles are defined in (a). (d) Local electric field enhancement $|E/E_0|$ amplitude profile for gap size of 20 nm at XY slice. The XY slice is calculated at the center of dimer.

Au bowties, with a gap around 20 nm, were also characterized by AFM and SEM, as shown in Figure 5.4(a) and (b). The scattering spectra measured under different polarization direction was listed in Figure 5.4(c). Figure 5.4 (d) shows a higher field enhancement amplitude in the gap of bowtie than disks dimer with the same gap size.

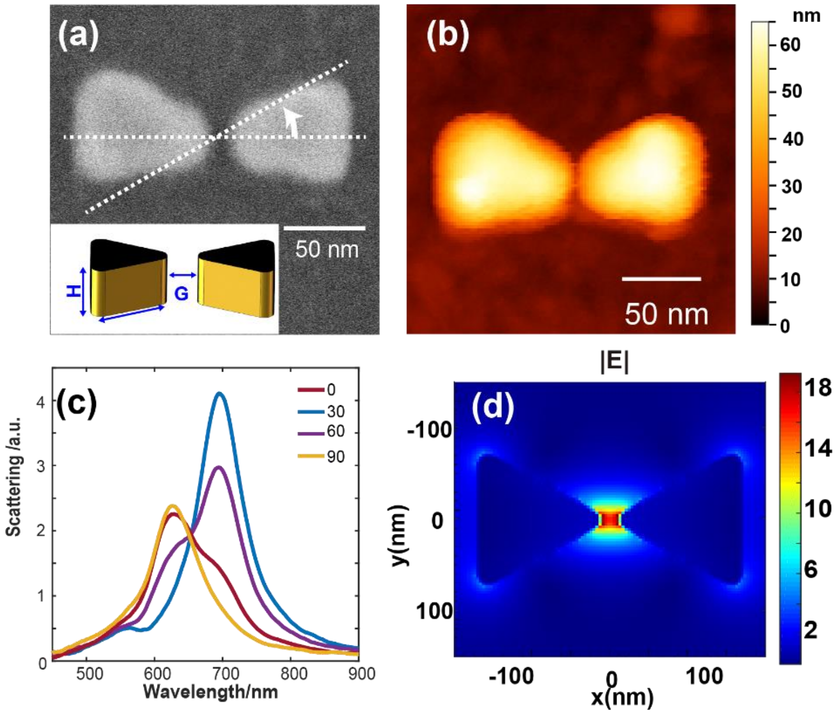

Figure 5.4 Characterization of the Au bowties. (a) SEM image of an Au bowtie with a gap size around 20 nm. (b) The topography image of the same bow tie obtained by AFM. (c) Measured dark-field scattering spectra of the dimer with different polarization angles for the incident white light. Polarization angles are defined in (a). (d) Local electric field enhancement |E/E₀| amplitude profile for gap size of 20 nm at XY slice. The XY map is calculated at the center of bowtie.

Figure 5 shows the effect of the gap size. The long-axis LSPR blue shifters as the gap size increases, shown in Figure 5.5(a) for the situation of bowties and Figure 5.5(b) for the situation of dimers of disks. For both bowties and dimers, when the gap size reaches the 30 nm value, increasing the gap size will not influence the LSPR peak position, which suggests that the plasmon coupling between two monomers start to disappear. Especially for dimer, the long-axis mode has the same peak with short-axis mode, which further confirms the coupling effect's disappearance. Taking the size of QDs into consideration (~10 nm); it is reasonable to use gap size from 15 nm to 30 nm for our QDs-trapping experiment. Besides, as we generally recognize from former experience, the LSPR peak's red-shift with the presence of polymer needs to be considered. However, it is not easy to calibrate the amount of redshift precisely. During polymerization, all the dimer structures are supposed to be immersed in the liquid formulation, while only part of the structure will be covered by polymer after polymerization and rinsing.

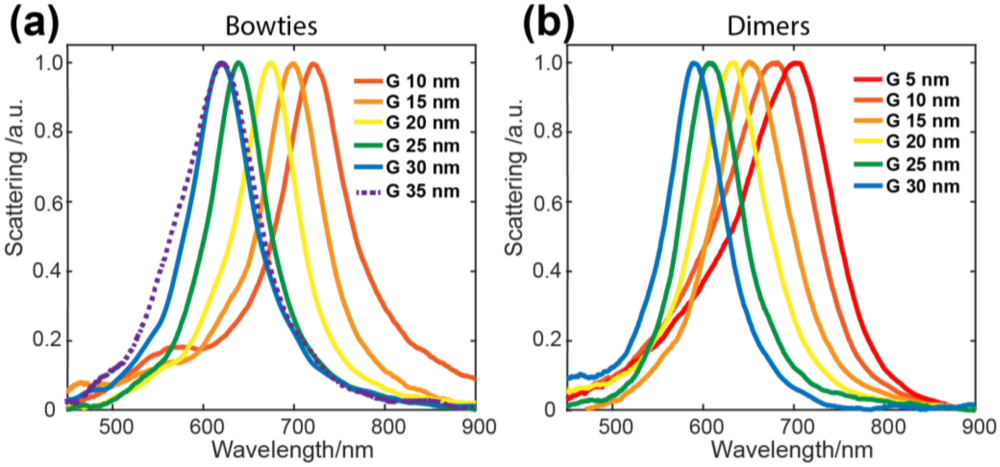

Figure 5.5 Scattering spectra of Au bowties (a) and Au disks dimers (b) with incident polarization along long axis when the gap size changes.

Figure 5.6 and Figure 5.7 show typical results of plasmonic TPP based on dimer and bowtie, respectively. Before exposure, the Au dimer in Figure 5.6(a) has a gap size of about 20 nm, after exposure, the most part of the polymer in the gap region indicates a good localization of polymer distribution. The same convincing result is also achieved on the bowtie shown in Figure 5.7 (b). As we discussed in section 3.3.1 chapt.3, the distribution of polymers can be related to the distribution of QDs that are grafted to the polymer chains. The control of the exciting dose used for photopolymerization makes possible the integration of the polymer only in the gap region. It can be expected that we get better polarization sensitivity and stronger coupling efficiency of hybrid structures based on dimer/bowtie. Especially, the hybrid structure based on bowtie has the potential to achieve strong coupling at a single QD regime.

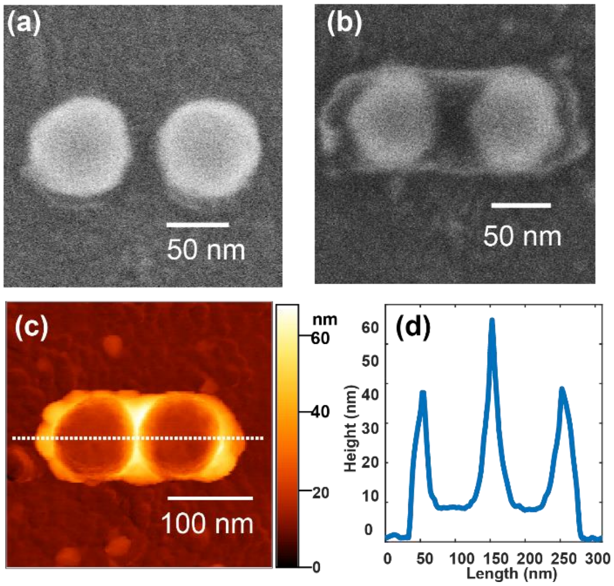

Figure 5.6 SEM images of Au disk-shaped dimer (a) before and (b) after exposure. (c) Subtracted AFM topography image after exposure. (d) Cross-section height profile of the position marked by dashed line in (c).

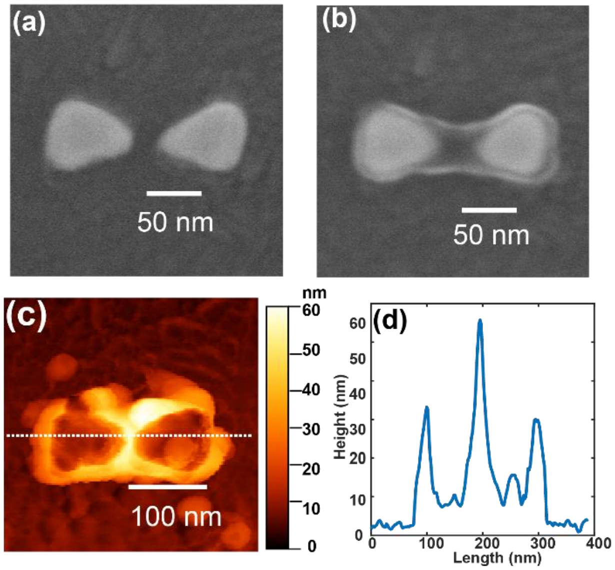

Figure 5.7 SEM images of Au bowtie (a) before and (b) after exposure. (c) Subtracted AFM topography image after exposure. (d) Cross-section height profile of the position marked by dashed line in (c).

Although the limited gap size potentially allows only a very small number of quantum dots to be fixed, which is very beneficial to achieve a single quantum dot, the limited polymer volume may also prevent one from efficiently trapping quantum dots. The limited gap size may also cause a small distance between the QDs and metal surface and consequently induce fluorescence quenching.

Near-field plasmonic TPP has been successful on dimers and bowties. By adjusting the concentration of QDs in the formulation and controlling the incident energy, in the near future, we are likely to obtain a single QD trapped in the gap of these structures.

5.3 Functionalization method used for attaching emitters

As we discussed in Chapter 3 and chapter 4, our common hybrid nanostructure manufacturing method uses a formulation containing nano-emitters (QDs). After polymerization is initiated, the QDs are trapped inside the polymer volume making their exact position unclear. Alternatively, it can be interesting to attach the QDs at the surface of the polymer nanolobes. The functionalization method is able to assemble plasmonic nanoparticles and QDs in a controlled way[202]. Some reports have discussed functionalization methods for building a hybrid metal-emitters system. For example, through ethyldimethylaminocarbodiimide (EDC) coupling, the AuNPs functionalized with thioctic acid can get linked to the QDs functionalized with cysteamine[85]. Metal nanoparticle surface functionalization can occur by means of noncovalent modifications such as electrostatic interactions, hydrophobic entrapment, and van der Waals forces, in addition to covalent modifications through a variety of chemistries. The functionalized surface makes the nanoparticle available to connect to other nanoparticles with corresponding surfaces. We can use this method to perform specific functionalization of polymers and quantum dots to achieve their assembly. Functionalization is specific to polymer only, maintaining the advantages of polymer anisotropy distribution.

Figure 5.8 shows the images of hybrid nanocube with QDs attached at the surface of the functionalized polymer. The QDs are anchored at the surface of polymer and can be distinguished in SEM and AFM images.

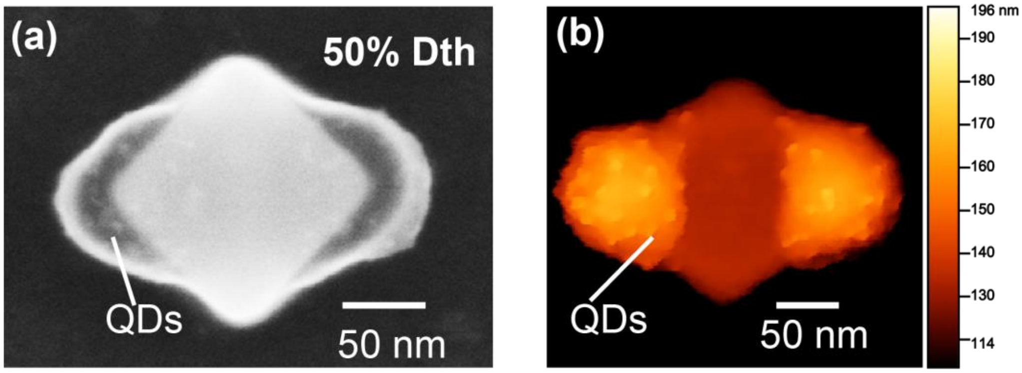

Figure 5.8 (a) SEM image of hybrid nanocube with QDs (white dots) attached at the surface of the polymer. (b) AFM topography image of the same hybrid cube in (a). The 620nm QDs are functionalized by specific chemical treatment. Incident light dose was set to 50% of the threshold.

This method mainly has two steps. Firstly, we fabricate a hybrid cube with surface functionalized polymer lobes by the same procedures as we described in chapter 3, using a photopolymerizable formulation including specific chemical components like amine molecules. Then the obtained hybrid cubes are immersed in a solution of pre-functionalized QDs for a period of time resulting in the attachment of these nanoparticles on the polymer surface due to the high attraction towards the functionalized structures. For a fixed-size polymer, the number of attached QDs on the polymer surface can be conveniently adjusted by controlling the concentration of QDs' solution and immersion time. Another example of hybrid nanocubes with fluorescent polystyrene nanoparticles attached on the surface of the polymer is shown in Figure 5.9.

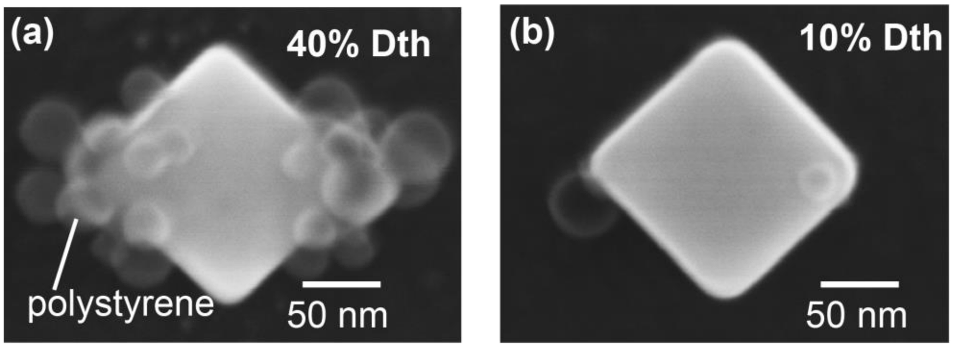

Figure 5.9 SEM images of hybrid nanocubes with fluorescent polystyrene nanoparticles attached on the surface of the polymer nanolobes. Higher incident dose used for TPP (40% of D_{th}) result to more polystyrene nanoparticles in (a); lower dose (10% of D_{th}) results to a few polystyrene nanoparticles in (b).

Because the emitters are attached to the surface of the polymer, the distance between the emitters and the metal surface is exactly the thickness of the polymer. Compared to our previous method which resulted in randomly dispersed QDs inside the polymer nanovolumes, this method leads to better control of the distance between emitters and the metal surface, which will allow us to study the change of emitter's lifetime as a function of its distance to the metal nanoparticles.

5.4 Summary

In this chapter, we briefly showed the feasibility of our plasmon-triggered near field photopolymerization method on dimer plasmonic nanostructures. The use of plasmonic gap modes will contribute to stronger interaction between the trapped QDs in the gap and plasmonic nanostructures.

The surface functionalization method constitutes another way of building a hybrid plasmon-emitter system on the basis of near-field photopolymerization and achieve better emitters' distribution.

Additionally, hybrid polymer-metal structures with a spatial distribution of QDs can be extended to a multicolor system utilizing nanostructures with different symmetry. For example, Xuan Zhou built a two-color hybrid nanodisk fabricated based on this plasmon-triggered near-field photopolymerization method[7]. It is foreseeable that three-color hybrid nanostructures can also be manufactured based on C3c symmetry metal nanostructures such as triangle or tripods.

Finally, my colleague successfully integrated QDs on integrated waveguides[203] which indicate a very promising possibility to integrate our polarization-controlled hybrid nanosources into nanophotonic circuits.

Conclusion

During the thesis, within the frame of a strong international partnership involving France, Singapore, USA and Germany, we have developed and studied anisotropic hybrid plasmonic nano-emitters via near-field two-photon polymerization that is triggered by localized field enhancement from surface plasmon supported by metal nanoparticles.

The key idea is that the active emitters, in particular semiconducting QDs, are contained in the polymer, resulting in an anisotropic distribution of polymer that reflects the anisotropic distribution of nano-emitters.

Using gold nanocubes and nanodisks and different modes of plasmon excitation, and different related near-field distributions, we have successfully fabricated different metal/polymer nanosystems presenting different polymer distributions with different degrees of symmetry in the close vicinity of the metal nanoparticles. The reproducibility of the method allowed us to carry out parameter studies and discuss and quantify the polarization sensitivity photoluminescence of the hybrid nanosources in terms of the spatial overlap between the exciting optical near-field and the nanoscale active medium. In particular, the resulting polarization dependence of the photoluminescence has been analyzed and quantified on the basis of new specific parameters whose definition and use were made possible for the first time: i) spatial distribution of nano-emitters including angular distribution of the active medium, ii) nanoscale spatial overlap integral between active medium and exciting near-field, and iii) associated photoluminescence polarization contrast. The hybrid nanocube-based nanostructure that is fabricated using a linear-polarized laser with a polarization direction along the diagonal of the cube turned out to be most polarization sensitive nanosystem with a PL polarization contrast of 0.7.

In basis of this, we decreased the number of QDs inside polymer lobes by decreasing the concentration of QDs in the photosensitive formulation, and finally reduced the number of QDs to single level. As a result, we demonstrated for the first time the ability to make such hybrid systems down to the single photon level with an associated Purcell Factor of about 30. Thus, a preliminary result of polarization-driven single photon switch was reported.

The same near-field plasmonic TPP method was also used on gold bipyramids who have two sharp extremities. We fist studied the orientations of the bare bipyramids via the imaging of their photoluminescence resulting from an excition presenting either azimuthally or radially polarized doughnut modes. Then, we successfully fabricating for the first time single-QD hybrid bipyramid/polymer nanostructures whose PL characterization has revealed interesting effects suggesting singular polarization contrast and possibility to achieve strong coupling at the single QD level.

Finally, we introduced some promising future routes to be explored and demonstrated their interest through preliminary results we decided to share with the readers. We discussed the feasibility of realizing a two-color hybrid nano-emitter based on a single gold nanocube and a three-color hybrid nano-emitter based on a C3v symmetry single gold triangle. In particular, nanoscale polymerization on gold triangle has been demonstrated and a nanocube-based two-color hybrid nanostructure with QDs-1 (emission at 620nm) and QDs-2 (emission at 670nm) trapped in four polymer lobes has been achieved through two successive near-field exposures. The PL properties of this singular nanostructure was studied. The polarization driven tuning between the two spectral lines turned out to be efficient.

Furthermore, through preliminary strong data, the polymer surface functionalization approach has proved to be promising to connect together metal nanoparticles and nano-emitters with a controlled gap between them. Finally, we demonstrated plasmonic TPP in the gap of gold dimers of disks and bowties, letting us hope the possibility to trap single QDs within the gap of coupled plasmonic nanoparticles.

Chapter 6 French summary

6.1 Introduction

La capacité du plasmon de surface à presser la lumière à des dimensions nanométriques se traduit par une forte amélioration du champ. Le champ local intense renforce par la suite l'interaction entre les plasmons et les nano-émetteurs. Il ouvre de nouvelles applications potentielles telles que le biocapteur[8–10], la photocatalyse[11,12], le circuit micro/nano photonique[13–15] et les règles moléculaires[16,17]. La structure plasmon plasmonique hybride composé de nanostructures métalliques et d'émetteurs fournit une solution pour le développement de nanosources contrôlables intégrées. Cependant, le manque de contrôle de la distribution spatiale à l'échelle nanométrique et les positions relatives des émetteurs et des nanoparticules a toujours été un problème clé au cours de ces expériences. Il existe actuellement plusieurs méthodes pour adresser des émetteurs localisés à des positions stratégiques, telles que l'utilisation de brins d'DNA[1,2], l'utilisation de pointes AFM[3,4], des méthodes de gravure spéciales[5], etc.

Notre méthode est basée sur une nano-photo-polymérisation localisée en champ proche déclenchée par des plasmons de surface[6,7], ce qui nous permet d'obtenir une distribution de polymère anisotrope contenant un émetteur à proximité de nanoparticules métalliques. Il consiste en une impression polymère de modes plasmoniques locaux présélectionnés spécifiques supportés par les nanoparticules métalliques. Dans cette thèse, nous avons fabriqué des nano-émetteurs hybrides anisotropes avancés en utilisant cette méthode. Et étudiez la sensibilité de polarisation d'émission des nano-émetteurs hybrides en fonction de différentes formes de nanoparticules d'or.

6.2 Méthode experimental

Les nanostructures métalliques utilisées dans cette thèse sont fabriquées par deux méthodes de base. L'un est basé sur la lithographie par faisceau d'électrons (EBL), qui convient à la fabrication de, e. g., nanodisques et nanodimères. L'autre est la méthode de synthèse chimique, qui permet de produire facilement de nombreuses nanoparticules 3D de formes spéciales, telles que les nanocubes[144] et les nanopyramides[140]. Dans cette section, nous présenterons toutes les procédures expérimentales utilisées pour fabriquer nos nano-émetteurs hybrides

6.2.1 Polymérisation à deux photons en champ proche

La polymérisation à deux photons (TPP) est un procédé optique non linéaire basé sur l'absorption simultanée de deux photons dans un matériau photosensible. Plusieurs exigences doivent être remplies pour initier un TPP déclenché par plasmon de surface sur une seule nanoparticule. Premièrement, nous avons besoin d'une densité d'intensité lumineuse suffisante ; deuxièmement, nous devons nous assurer que la position du spot est cohérente avec la position des nanoparticules. Troisièmement, la haute qualité du spot lumineux focalisé est requise. Le chemin optique du laser incident utilisé pour exciter le Plasmon de surface localisé est illustré à la Figure 6.1

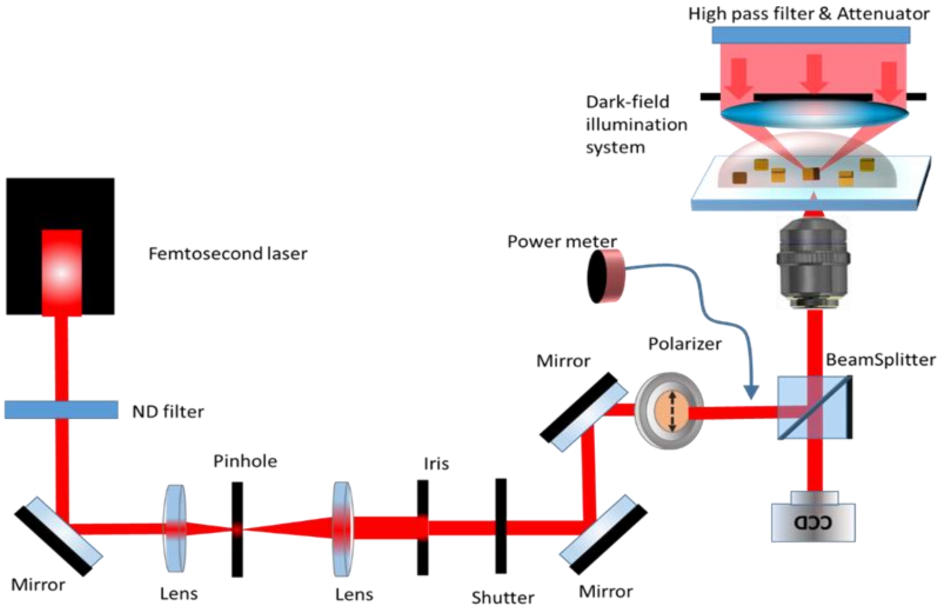

Figure 6.1 Schéma de configuration optique pour la polymérisation à deux photons à base de plasmon sur une seule nanoparticule.

Un laser femtoseconde Ti: Saphir est focalisé par une lentille d'objectif (N.A = 0,6) sur une seule nanoparticule observée par éclairage en lumière blanche sur fond noir. La source d'éclairage utilisée pour le champ sombre est atténuée par un filtre passe-haut de 540 nm pour éviter une polymérisation indésirable due à la lumière UV / bleue. Les longueurs d'onde disponibles du laser Ti: Sa vont de 680 nm à 1080 nm.

La résonance plasmonique de surface localisée (LSPR) a été excitée par un laser focalisé dont la longueur d'onde chevauche l'absorption de la formulation polymérisable et la résonance plasmonique de la nanostructure métallique. La plus grande densité d'énergie résultante dépasse le seuil de TPP. Ensuite, la photopolymérisation n'a été déclenchée que dans la zone localisée et a piégé les émetteurs à l'intérieur du polymère durci. En utilisant différentes géométries de nanoparticules d'or et différents modes d'excitation Plasmon, le milieu actif contenant des nano-émetteurs peut être structuré de manière sélective avec différents degrés de symétrie au voisinage des nanostructures métalliques.

Nous avons déposé du MNPs (nanoparticules métalliques) dispersé sur un substrat en verre enduit d'ITO (Oxyde d'indium-étain), puis déposons une goutte de formulation maison homogène utilisée pour le TPP sur le substrat pour laisser les MNPs immergés dedans. Le laser incident avec la longueur d'onde appropriée a ensuite été focalisé sur les MNPs en utilisant une dose inférieure au seuil $D_{in} < D_{th}$. À ce moment-là, l'intensité du champ proche des MNPs a été améliorée par LSPR et donne lieu à une densité d'énergie effective dépassant le seuil. Ici, la polymérisation est excitée dans la zone de champ proche autour des MNPs. Après élimination de l'excès de formulation par rinçage, on obtient une nanostructure hybride contenant des nano-émetteurs entourés par le polymère. Les principales étapes sont répertoriées dans la Figure 6.2, le laser incident à polarisation linéaire excite le mode dipolaire du nanodisque et finalement nous obtenons deux lobes de polymère à la position de la région améliorée.

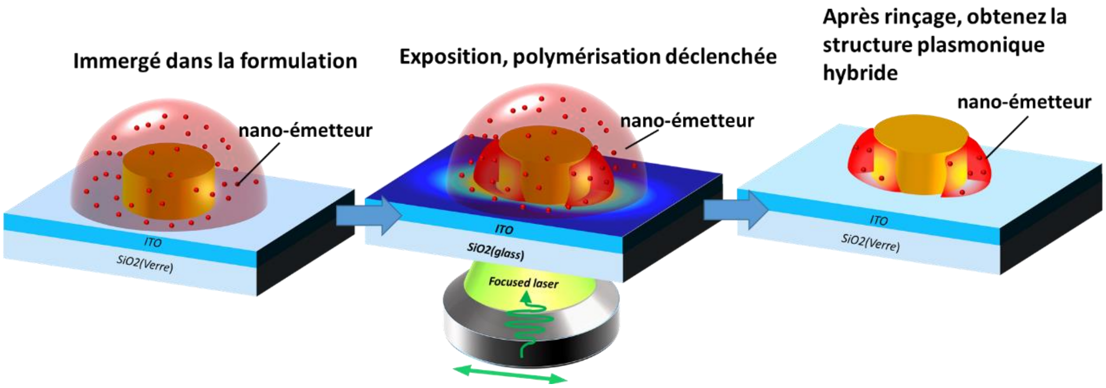

Figure 6.2 The diagramme schématique de la méthode de polymérisation à deux photos déclenchée plasmonique pour la fabrication d'une structure hybride.

6.2.2 Caractérisation topographique

L'AFM permet de caractériser la quasi-totalité des nanostructures utilisées dans cette thèse, en particulier les échantillons développés sur le verre. Le modèle AFM utilisé est ScanAsyst iCON de Bruker et le mode Peak Force est de préférence utilisé. La topographie AFM de la structure hybride après exposition moins celle avant exposition. L'image résultante représente la distribution tridimensionnelle du polymère obtenu par polymérisation déclenchée par plasmon de surface.

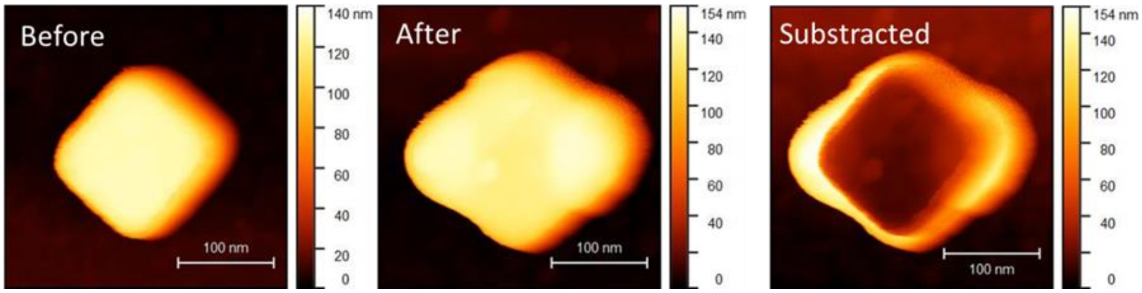

Figure 6.3 Images AFM prises avant (a) et après (b) la polymérisation déclenchée par Plasmon. (c) L'image soustraite (après - avant).

Le Microscopie électronique à balayage (MEB) est pratique pour caractériser nos nanostructures, en particulier pour les nanoparticules synthétisées chimiquement déposées aléatoirement sur un substrat ITO. Les images MEB vues de dessus permettent d'évaluer la taille réelle sans aucune exigence de traitement d'image. Le mode électrons secondaires (SE), est le mode le plus utilisé pour caractériser la morphologie des échantillons et peut donner au polymère et au métal un contraste différent sous haute tension, ce qui sera utile pour notre système hybride. En outre, nous pouvons également obtenir l'image de différence à travers les images MEB avant et après l'exposition. La Figure 6.4 montre les images MEB des deux groupes de cubes avant et après exposition.

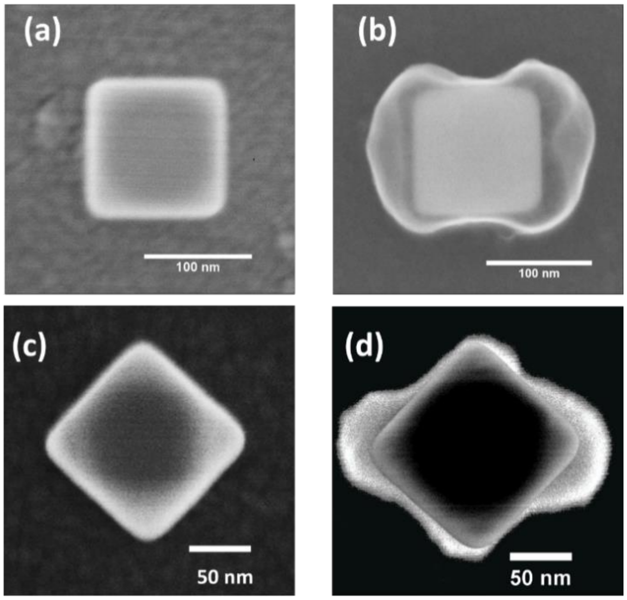

Figure 6.4 Image MEB du cube hybride avant (a) et après polymérisation sous haute tension de 10kv (b). (c) Images MEB de nanocube avant polymérisation. (d) Images MEB de nanocube hybride après polymérisation à basse tension d'accélération de 2KV, avec le même cube (c) nu d'origine superposé au milieu.

6.2.3 Caractérisations optiques

◆ Imagerie en champ noir et mesure du spectre de diffusion

La mesure de diffusion à l'aide de la microscopie à fond noir est un moyen simple d'obtenir les caractéristiques de résonance plasmonique de nanoparticules métalliques individuelles. Comme le montre la Figure 6.5, un condensateur à champ noir avec une ouverture numérique (NA) de 0,9 est installé au-dessus de la platine d'échantillonnage d'un microscope inversé (Olympus IX71). La lumière diffusée par une seule nanoparticule est collectée par un objectif de 40X avec 0,6 NA (<0,9). Une autre lentille est ajoutée entre la sortie du microscope IX71 et le spectromètre pour agrandir l'image et la fente d'entrée du spectromètre est placée au niveau du deuxième plan image. Le système spectroscopique se compose d'un spectromètre Shamrock 303i et d'une caméra CCD iDUs. Ce système nous permet de sélectionner une seule particule en diminuant la largeur de la fente et en collectant le signal d'un seul cube / bipyramide isolé exact en utilisant le mode multipiste

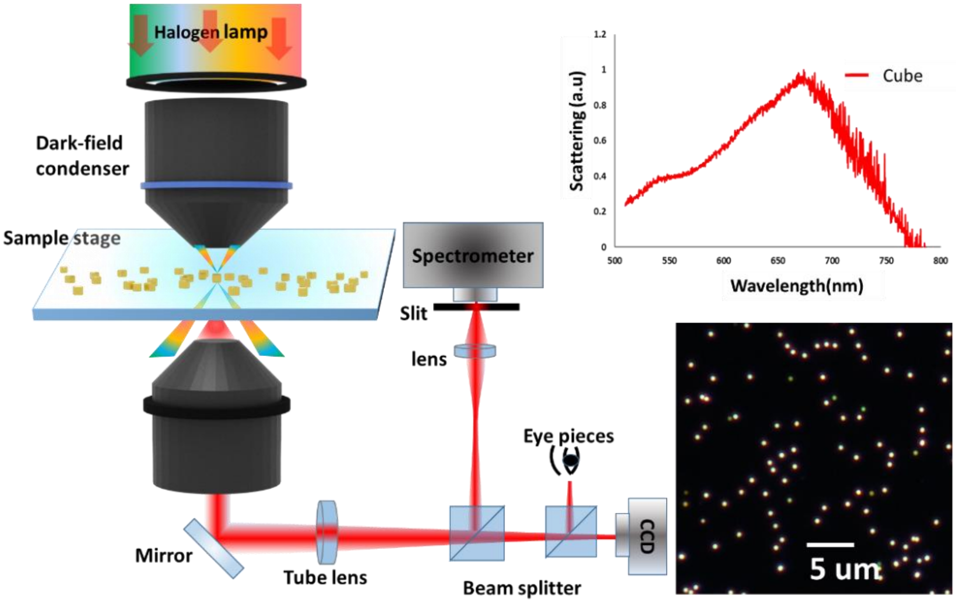

Figure 6.5 L'image de gauche est une représentation schématique de la configuration du champ sombre ; celui du bas à droite montre une image en fond noir d'une zone de nanocubes sur un substrat en verre revêtu d'ITO ; celui du haut à droite est le spectre de diffusion d'un seul nanocube isolé.

◆ Mesure de la photoluminescence

Le signal de photoluminescence de la structure hybride a été analysé par un spectromètre couplé à un microscope optique inversé (Olympus IX71). Nous avons utilisé un laser continu de 405 nm pour exciter la fluorescence. Une lentille d'objectif 50x a ensuite collecté le signal (N.A = 0,8). Il a également été utilisé pour concentrer la lumière d'excitation 405 nm sur des nanoémetteurs hybrides uniques et séparé de l'excitation laser à l'aide d'un filtre passe-long de 514 nm. Pour les mesures de nano-émetteur hybride unique, le mode image est utilisé avec la fente complètement ouverte, et le point laser a été déplacé vers le centre et marqué sur l'image CCD. Après avoir aligné la nanoparticule unique ciblée sur la marque, le filtrage spatial est effectué en ajustant la taille de la fente pour détecter une zone inférieure à 1 µm × 1 µm, assurant des mesures de signal d'objet unique. Une lame demi-onde coopère avec un polariseur linéaire qui contrôle la direction de polarisation. Le temps d'intégration pour mesurer un spectre de fluorescence a été fixé à 50 s pour éliminer les erreurs de données causées par l'instabilité et d'autres influences environnementales.

◆ Mesure de photoluminescence résolue dans le temps

Lorsque le nombre de QD capturés dans la structure hybride est réduit à quelques-uns, voire un, la source de photon unique résultante peut être caractérisée par la fonction d'autocorrélation du second ordre $g^{(2)}(0)$, qui peut être mesurée en utilisant l'expérience de Hanbury Brown et Twiss[158]. Normalement, le $g^{(2)}(0)<0.5$ implique un seul photon[160]. Dans cette thèse, le système Hanbury Brown & Twiss utilisant TCSPC a été couplé à un système d'imagerie à balayage confocal construit. La Figure 6.6 montre le diagramme schématique de ce système. Ce système peut être utilisé pour la mesure de la durée de vie de fluorescence et la mesure de $g^{(2)}(0)$.

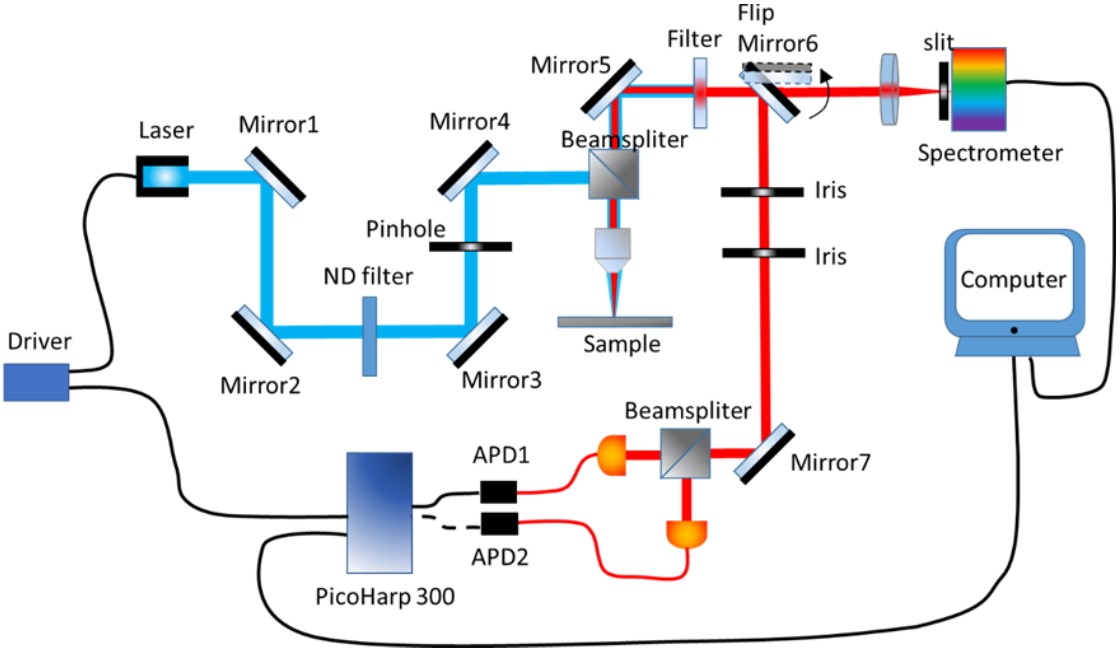

Figure 6.6 Schéma de principe de l'ensemble du système Hanbury Brown & Twiss, utilisant le système d'imagerie à balayage confocal couplé TCSPC.

Un laser pulsé (Picoquant LDH-P-C-405) connecté à un driver box supplémentaire (PDL 800-B), dont la fréquence de répétition peut être modifiée de 80 MHz à 2,5 MHz. Le faisceau laser est focalisé sur l'étage de maintien de l'échantillon à balayage par une lentille d'objectif de 100 x 0,95. Notre échantillon d'émetteurs hybrides est ensuite excité pour émettre de la lumière sur sa longueur d'onde de fluorescence. La fluorescence est collectée par réflexion, puis après élimination des signaux bruyants par un filtre approprié, la lumière collectée est dirigée par une fibre vers un APD (Picoquant PMA-182). Le signal est envoyé au module TCSPC autonome (TimeHarp-300), qui est lié au pilote laser.

6.3 Nano-émetteurs hybrides sensibles à la polarisation à base d’Au nanocubes et d’Au nanodisques

Dans cette section, en utilisant des nanocubes d'or et des nanodisques d'or avec différents modes d'excitation plasmon, nous rapportons la fabrication de nano-émetteurs avancés basés sur un milieu actif structuré avec différents degrés de symétrie au voisinage des nanoparticules métalliques. De plus, nous avons proposé un concept de chevauchement spatial à l'échelle nanométrique entre le milieu actif et le champ d'excitation local afin d'interpréter les propriétés de photoluminescence des nano-émetteurs hybrides.

6.3.1 Nano-émetteurs hybrides anisotropes à base de nanocubes Au

- **Caractérisation du nanocube Au**

La solution colloïdale de nanocubes d’or de taille 127nm a été synthétisés par Sylvie Marguet (CEA Saclay) dans une méthode de croissance chimique de grains. Les nanocubes d'or sont déposés sur le substrat de verre revêtu d'une couche ITO de 40 nm d'épaisseur. La Figure 6.7(a) donne les spectres de diffusion et d'extinction calculés à partir d'un seul nanocube d'or par solution FDTD. La Figure 6.7 (b) montre le spectre de diffusion du champ noir mesuré à partir d'un seul nanocube d'or et également avec le spectre d'extinction de la solution de cube. Les spectres calculés correspondent très bien aux spectres mesurés.

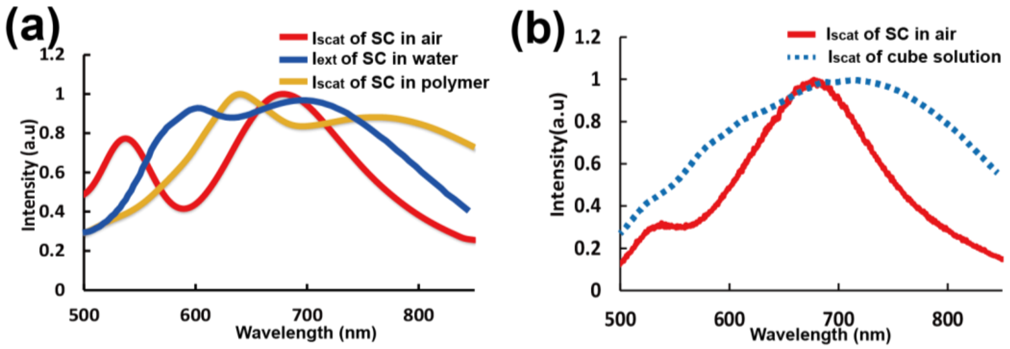

Figure 6.7 (a) Spectre de diffusion calculé normalisé d'un seul nanocube (SC) dans l'air (courbe rouge) ou en polymère (indice = 1,48, courbe jaune) et le spectre d'extinction normalisé d'un SC dans l'eau (courbe bleue). (e) Spectre de diffusion expérimental normalisé d'un seul nanocube d'or dans l'air sur un substrat en verre revêtu d'ITO (courbe rouge) et spectre d'extinction mesuré à partir d'une solution de cube (solvant aqueux, ligne pointillée bleue).

Considérons l'indice de réfraction plus élevé de la formulation, qui se situe entre 1,48 et 1,52, selon le calcul, le pic de diffusion correspondant au mode plasmon dipolaire se déplace à 780 nm lorsque le cube est immergé dans un matériau avec un indice de réfraction de 1,5 (Figure 6.7 (a), courbe jaune). Par conséquent, nous définissons 780 nm comme longueur d'onde d'excitation pour la polymérisation à deux photons

◆ Distribution de polymère anisotrope contrôlable du nanocube hybride

Parce que notre approche est basée sur la photopolymérisation déclenchée par un champ proche localisé amélioré, le lobe polymère obtenu devrait imprimer la distribution spatiale du champ proche amélioré des MNP. La Figure 6.8(a, c) présente des images MEB de nanostructure hybride Au / polymère résultante fabriquée sur des nanocubes avec deux orientations typiques de la polarisation incidente utilisée pour le TPP. Les distributions de champ proche calculées correspondantes sont également présentées (Figure 6.8 (b, d)). La présence de QD à l'intérieur du polymère n'empêche pas le processus de polymérisation à deux photons[157].

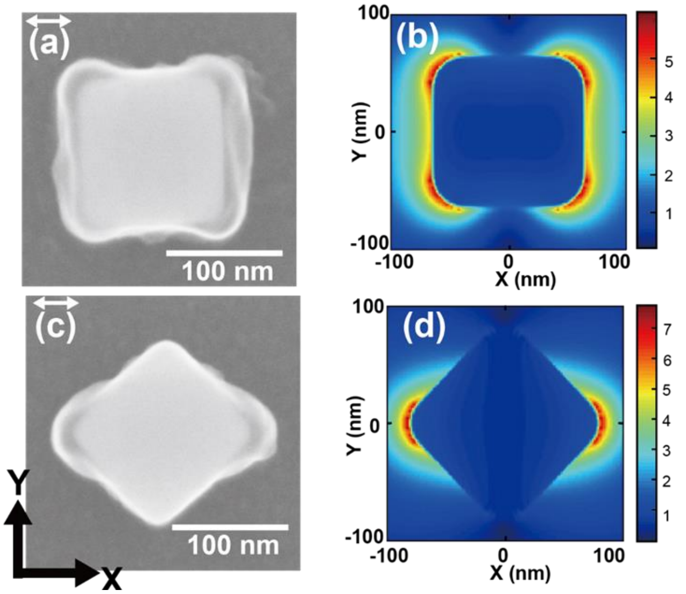

Figure 6.8 Nanostructure hybride à base de nanocube d'or réalisée par polymérisation plasmonique à deux photons (λ = 780 nm). Images MEB des structures hybrides obtenues avec polarisation incidente le long de la direction x (voir flèche blanche (a) bord latéral supérieur parallèle à la lumière incidente et (c) diagonale parallèle à la lumière incidente. (B), (d) Cartes FDTD de champ le module (λ = 780 nm) au voisinage du nanocube d'or à l'intérieur du polymère, dans le cas de (a) et (c) respectivement. Les images MEB sont obtenues avec une tension d'accélération de 10 kV conduisant à un contraste significativement différent entre l'or et le polymère, où la partie polymère apparaît plus transparente.

L'allongement du polymère, c'est-à-dire l'épaisseur du polymère, peut être mesuré par MEB ou AFM. Dans le cas du TPP, lorsque le temps d'exposition est défini, la probabilité d'absorption à deux photons et de polymérisation résultante dépend quadratiquement de l'irradiance lumineuse locale I (intensité par unité de surface).

$$P = F(I^2) \qquad (6.1)$$

La fonction F contient tous les processus liés à la polymérisation à deux photons et est une fonction à croissance monotone. Le seuil de dose incidente D_{th} passe à une puissance seuil I_{th}, en dessous de laquelle aucune polymérisation ne peut se produire. La photopolymérisation dépend de l'intensité lumineuse locale effective qui résulte à la fois de l'intensité lumineuse incidente I_{in} ($I_{in} = p \cdot I_{th}, where\ p < 1$) et de l'amélioration du champ proche local.

L'allongement du polymère le long de la diagonale du nanocube a été mesuré pour différentes valeurs de p allant de 0.1 à 0.9. La fonction logarithmique apparente est caractéristique de la nature évanescente du champ plasmique. Ce résultat peut être compris en considérant la décroissance presque exponentielle du champ proche du nanocube excité. Près du nanocube d'or, l'irradiance locale effective de polymérisation est :

$$I_{eff} = f_{max}\, I_{in} exp(-x/\delta) \qquad (6.2)$$

f_{max} est le facteur d'amélioration de l'intensité maximale à l'intérieur de la zone polymérisée déclenchée par le LSPR, δ représente la longueur de décroissance de l'intensité caractéristique du LSPR, et x est la distance de la surface du nanocube le long de la diagonale. La polymérisation n'est réalisée que là où $I_{eff} > I_{th}$, ce qui entraîne la condition suivante :

$$x < \delta \,.\ln\left(f_{max} \times \frac{I_{in}}{I_{th}}\right) = x_{max} = \delta \,.\ \ln(p \times f_{max}) \qquad (6.3)$$

x_{max} correspond à l'allongement du polymère représenté sur la Figure 6.9. L'équation (7.3) peut être réécrite :

$$\frac{1}{p} = f_{max} \times \exp\left(-x_{max}/\delta\right) \qquad (6.4)$$

1/p représente le gain d'intensité induit par le plasmon. Par exemple, le fait que le polymère a été obtenu pour p = 0,1 démontre une augmentation d'intensité d'au moins 10. L'équation (6.4) explique la fonction de type exponentielle représentée sur la Figure 6.9 (b). L'ajustement analytique à partir des données expérimentales conduit à la détermination de f_{max} et δ.

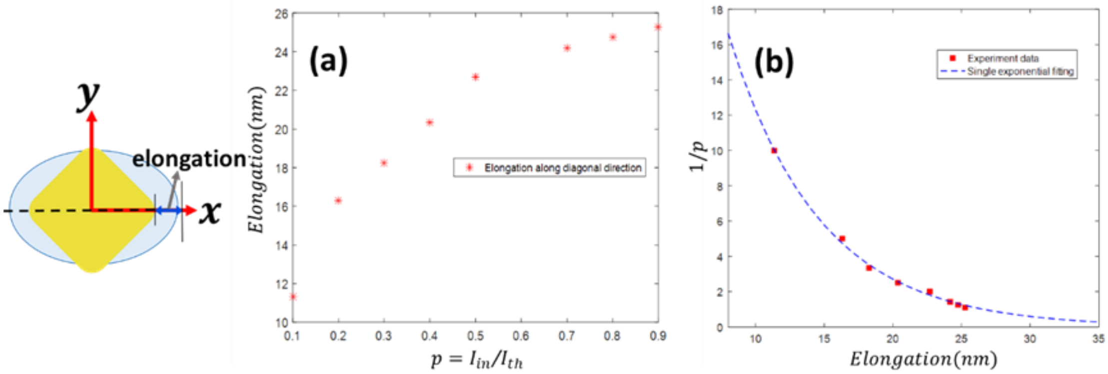

Figure 6.9 Analyse quantitative de l'élongation des polymères en fonction de l'intensité du laser incident. (a) Effet de la puissance d'exposition relative $p = I_{in}/I_{th}$ sur l'allongement mesuré du volume polymérisé le long de la diagonale x du cube. (b) Points de données expérimentales (carré rouge) du rapport 1 / p tracé en fonction de l'allongement du polymère mesuré résultant et de l'ajustement exponentiel avec une seule décroissance exponentielle selon l'équation (3.4).

Dans le cas de la Figure 6.9 (b), nous trouvons f_{max}= 56 et δ= 7 nm. À titre de comparaison, par calcul FDTD, nous avons obtenu des valeurs numériques : f_{max} = 59 et δ = 10 nm respectivement.

◆ Émission de photoluminescence (PL) de nanocube hybride

L'image PL rouge en champ lointain peut nous permettre de vérifier la présence de QD piégés dans le polymère. La *Figure 6.10* affiche les spectres PL normalisés de deux nanocubes hybrides isolés et la formulation originale contenant des QDs.

A titre de comparaison, la structure hybride polymère / nanocubes d'or sans QD a été produite. Dans ce cas, aucune émission de PL rouge n'a été observée à partir du nanocube hybride résultant, comme le montre la Figure 6.10(b) (courbe bleue). Les deux nanostructures hybrides illustrées à la Figure 6.10(b) ont été produites en utilisant les mêmes paramètres. Le polymère dans le petit sous-graphique de gauche contient QDs et le polymère dans le petit sous-graphique de droite ne contient pas des QDs.

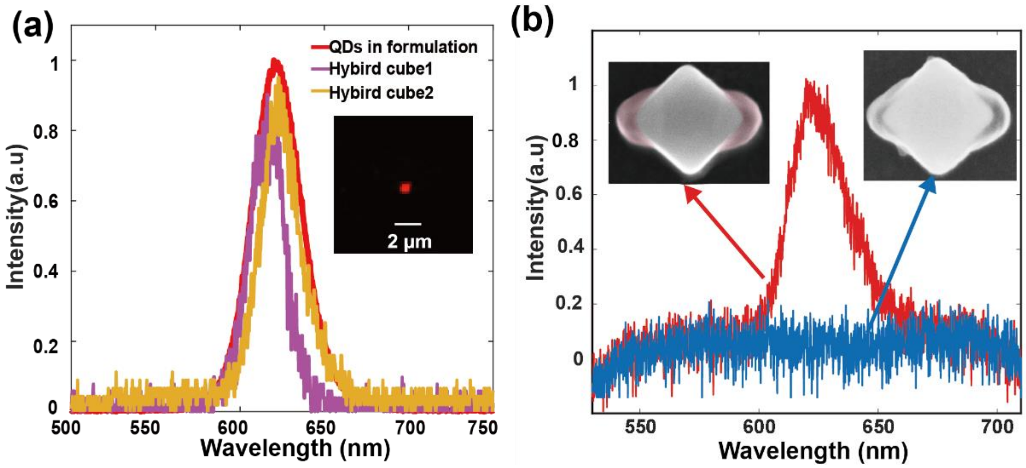

Figure 6.10 (a) Les lignes orange et rose sont des spectres PL normalisés de deux nanocubes hybrides isolés (excités par un laser de 405 nm), et la petite image insérée dans le coin supérieur droit est une image PL en champ lointain d'un seul nanocube hybride. La courbe rouge représente le spectre PL de la formulation polymérisable. (b) Comparer le signal PL du polymère hybride / cube avec les QD piégés dans le polymère (ligne rouge) et le signal de référence du polymère hybride / cube sans QD (ligne bleue). L'image de gauche est colorée artificiellement en rouge pour illustrer le fait que les lobes de polymère contiennent des QD rouges.

6.3.2 Nanostructures hybrides à base de nanodisques

Dans le cas du nanodisque, dont le diamètre est d'environ 90 nm une hauteur de 50 nm, nous utilisons la même méthode de photopolymérisation en champ proche que celle que nous avons utilisée pour fabriquer la structure hybride à base de cube. La nanostructure résultante, représentée sur la Figure 6.11 (c) et (d), est caractérisée par un milieu actif présentant respectivement deux lobes de polymère (excitation à polarisation linéaire) ou un anneau homogène ayant une symétrie C∞v (excitation à polarisation circulaire), qui sont conformes à la distribution de champ proche calculée par FDTD.

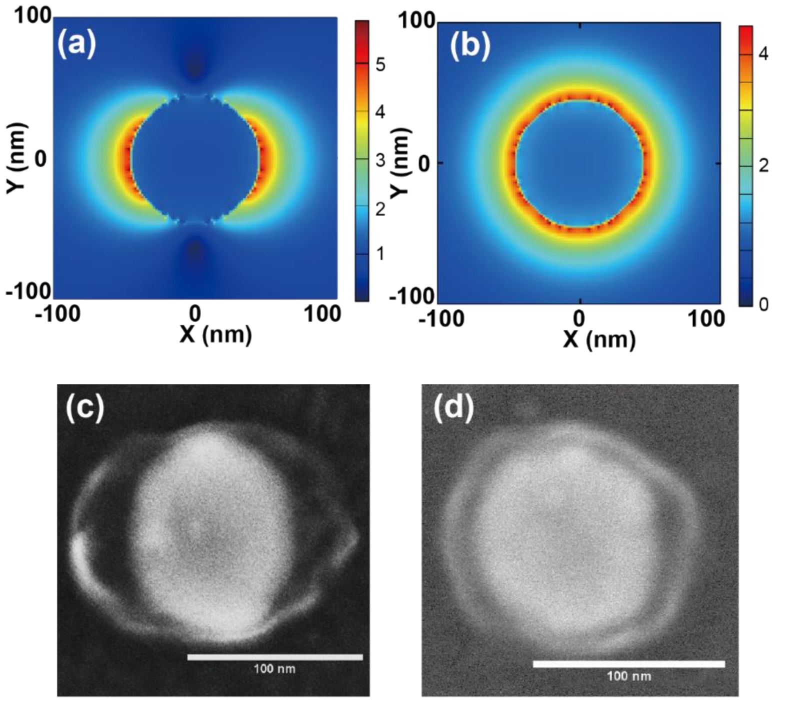

Figure 6.11 Distribution d'amplitude de champ proche calculée du nanodisque (90 nm de diamètre, 50 nm de hauteur) en utilisant une longueur d'onde d'excitation de 780 nm par FDTD. (a) en utilisant une lumière d'excitation à polarisation linéaire, et (b) en utilisant une lumière d'excitation à polarisation circulaire. Images MEB de nanodisques après TPP, la longueur d'onde du laser de durcissement est fixée à 780 nm. (c) nanostructure hybride à base de disque polymérisée par une lumière polarisée linéaire, (d) nanostructure hybride à base de disque polymérisée par une lumière polarisée circulaire.

6.3.3 Sensibilité de polarisation de la photoluminescence

Nous avons montré que la distribution spatiale des QD est contrôlable par l'état de polarisation de la lumière d'excitation utilisée pour la polymérisation. Cette disposition permettrait également d'utiliser la polarisation incidente comme commande optique à distance rapide et efficace de l'émission de lumière de l'émetteur hybride. La probabilité d'émission des QD à l'intérieur du polymère des nanostructures hybrides peut être représentée par[24,93]:

$$\gamma_{em}(\nu_{em}) = \gamma_{exc}(x, y, z, \nu_{exc}) \times Y(\nu_{em}) \times \rho(x, y, z)dV \qquad (6.5)$$

γ_{em} est le taux d'émission des QD, γ_{exc} est le taux d'excitation, Y est le rendement quantique du nano-émetteur, et $\rho(x, y, z)dV$ est la probabilité de la présence d'émetteurs autour de la nanoparticule métallique à l'intérieur un volume élémentaire dV (= dxdydz) à la position (x, y, z).

ρ (x, y, z) est donc la densité volumique de probabilité de présence de QD, il peut également être considéré comme la densité volumique des QD. ν_{em} est la fréquence de la lumièremise. ν_{exc} est la fréquence du champ d'excitation absorbe par les QD. ν_{exc} doit être dans la bande d'absorption de l'émetteur. $\nu_{em} - \nu_{exc}\ (< 0)$ représente le décalage de course. Il faut rappeler que Y Y est lié à la probabilité d'émission lumineuse une fois le nano-émetteur excité et qu'il dépend également de (x, y, z)[21]. γ_{exc} est lié au champ proche plasmonique de nanoparticules métalliques, dont la distribution spatiale peut être contrôlée par polarisation incidente pour une taille et une géométrie de nanoparticules données.

Selon l'équation (6.5), le contrôle de la distribution spatiale des nano-émetteurs $\rho(x, y, z)$ permettrait de contrôler l'émission de lumière en contrôlant le chevauchement milieu actif / champ d'excitation. L'équation (6.6) exprime l'intégrale de chevauchement qui accède à la façon dont un mode de guide d'ondes spécifique peut être excité :

$$\eta = \frac{|\iint E_1 \cdot E_2 dxdy|^2}{\iint |E_1|^2 dxdy \cdot \iint |E_2|^2 dxdy} \qquad (6.6)$$

η est l'efficacité de couplage entre E1 et E2 qui sont respectivement l'amplitude complexe du mode à coupler et l'amplitude complexe du champ d'excitation incident. En nano-optique, spécialement pour notre système hybride, le contrôle à l'échelle nanométrique de $\rho(x, y, z)$ permettrait d'exploiter pleinement $\gamma_{exc}(x, y, z)$.

Étant donné que le polymère contient des QD (~ quelques dizaines de QD pour les plus gros lobes de polymère), le contrôle de la distribution du polymère montré dans la Figure 6.8 et la Figure 6.11 offre un moyen de contrôler $\rho(x, y, z)$, la probabilité de distribution spatiale dans l'équation (6.5), faisant du système hybride un nano-émetteur anisotrope.

Nous étudierons la relation entre l'intensité PL et le chevauchement spatial entre le polymère et la distribution en champ proche sous différentes polarisations d'excitation de nos structures hybrides à base de nanocube et à base de nanodisque.

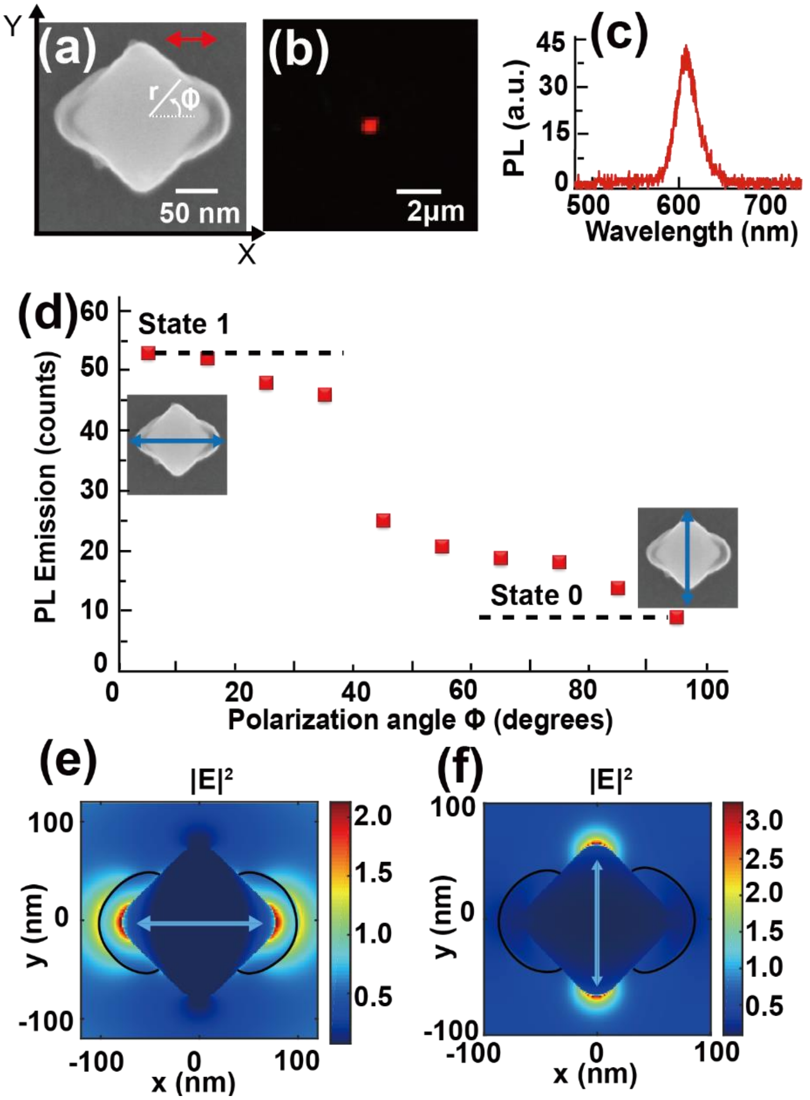

Figure 6.12 Photoluminescence (PL) à partir d'une seule nanosource hybride basée sur un nanocube d'or et des QD rouges intégrés dans les lobes de polymère le long d'une diagonale de cube. (a) imageMEB de la nanosource plasmonique hybride. La flèche rouge indique la polarisation utilisée pour la fabrication du système hybride basé sur la polymérisation plasmonique à deux photons. La coordonnée polaire définit l'angle de polarisation ϕ du laser incident utilisé pour exciter le nanosystème à 405 nm. L'image brute est superposée à l'image du même nanocube nu. (b) PL en champ lointain du nanosystème représenté en (a) excité avec un laser 405 nm, ϕ = 0°. (c) Spectre PL correspondant. (d) intensité PL en fonction de l'angle de polarisation ϕ de la lumière d'excitation. Les flèches bleues indiquent deux polarisations perpendiculaires correspondant à ϕ = 0° et ϕ = 90°. (e) et (f) Intensité de champ proche simulée (au plan x-y de la section médiane du cube, λ = 405 nm) au voisinage d'un nanocube hybride réaliste. Les flèches bleues indiquent

deux polarisations perpendiculaires correspondant à ϕ = 0° et ϕ = 90°. Les lignes noires représentent les contours des lobes de polymère tels que déduits de l'image MEB en (a).

La Figure 6.12(a) montre une anisotropie apparente du milieu actif présentant une symétrie dans le plan C2v avec une distribution très confinée, suggérant une sensibilité de polarisation significative de l'émetteur. On peut définir ρ (r, ϕ) la probabilité de présence des nano-émetteurs en fonction des coordonnées polaires (r, ϕ) représentées sur la Figure 6.12 (a). D'après les images MEB, ρ est élevé pour (r$\in$ ([65 nm-100 nm]) $\cap$ ($\phi\in$[335 ° -25 °]$\cup$[155 ° -205 °]) et nul ailleurs (couches de polymère très minces, de de faible épaisseur par rapport à la taille QD, sont négligés car il est peu probable qu'ils contiennent des QD). En ce qui concerne la distribution angulaire azimutale du nano-émetteur, nous définissons le facteur de remplissage angulaire, nommé β, qui quantifie l'occupation angulaire du milieu actif au voisinage de la nanoparticule métallique. Sur la Figure 6.12 (a), le milieu actif occupe moins de 30% (~27%) de l'espace. A titre de comparaison, un spaser constitué d'une structure plasmonique sphérique cœur-coquille entourée d'une couche homogène de QDs[87] présente un milieu actif dans la région (r$\in$[20 nm-25 nm]) $\cap$ ($\phi\in$[0 ° -360 °]), soit un facteur de remplissage angulaire de β = 100%. ρ (r, ϕ) constitue une caractéristique forte de ce nouveau type de nano-émetteur hybride. La Figure 6.12 (d) montre l'intensité PL d'une seule nanosource hybride en fonction de la direction de polarisation incidente (λ = 405 nm). PL l Le niveau varie rapidement en fonction de la direction de polarisation. Cet effet résulte de la variation de chevauchement spatial entre l'excitation locale en champ proche et la distribution du milieu actif. Pour illustrer ce point important, l'intensité du champ proche à 405 nm a été calculée par FDTD sur un système hybride réaliste à base de nanocube présentant des lobes de polymère à deux coins de cube.

La sensibilité de polarisation PL peut être discutée à travers un contraste de polarisation :

$$\delta_{PL} = \frac{IPL_{max} - IPL_{min}}{IPL_{max} + IPL_{min}} \qquad (6.7)$$

IPL_{max} et IPL_{min} sont respectivement les intensités PL maximum et minimum (que nous appelons IPL). Nous obtenons $\delta_{PL} \sim 0,7$ dans la Figure 6.12(d). Nous avons fabriqué 5 autres structures hybrides dans le même cas de la Figure 6.12(a) et un total de 6 ensembles de résultats ont été obtenus dans la Figure 6.13. Tous ont un $\delta_{PL} \sim 0.7$, prouvant la répétabilité de notre méthode et la fiabilité de δ_{PL}.

Par ailleurs, sur la Figure 6.13 (e), (f), lorsque ϕ = 180° l'intensité PL revient au même niveau élevé que ϕ = 0° présentant la symétrie dans le plan C2v de ce type de nanostructures hybrides.

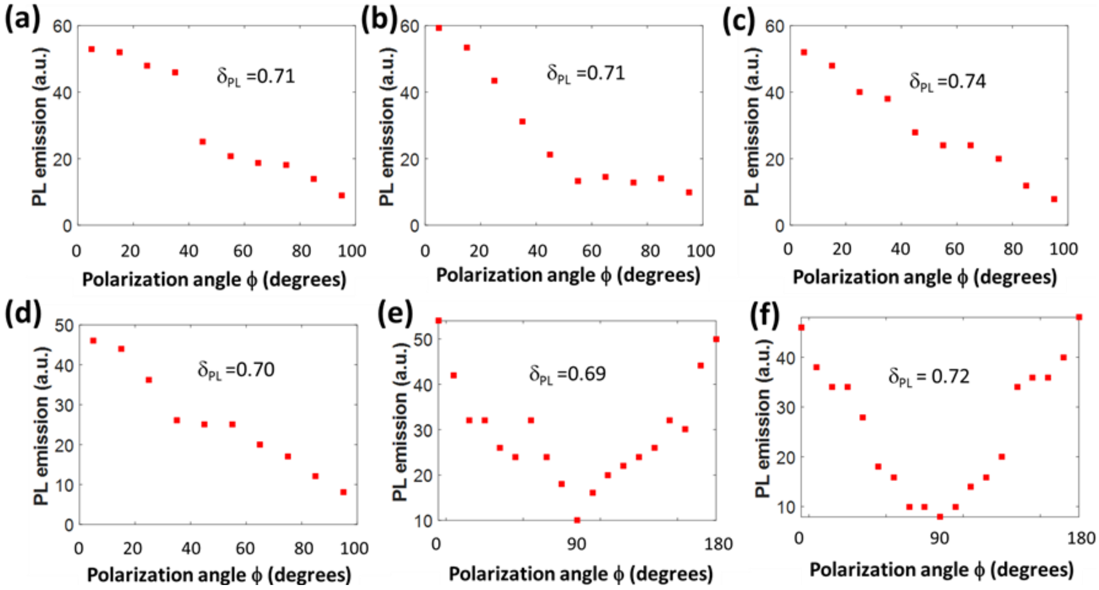

Figure 6.13 Intensité PL en fonction de l'angle de polarisation ϕ de l'excitation mesurée à partir de 6 nanocubes hybrides différents similaires à celui de la Figure 6.12(a).

δ_{PL} dépend de la structure d'émetteur hybride qui est contrôlée par le choix approprié de la géométrie des nanoparticules métalliques et la sélection du mode plasmonique utilisé pour la polymérisation en champ proche. La Figure 6.14 montre les données PL d'une seule nanosource fabriquée par un nanocube dont l'angle d'orientation $\theta = 0$, auquel cas, le champ d'excitation parallèle aux bords du cube, les deux modes propres plasmoniques diagonaux sont excités symétriquement et tous les quatre coins du cube présentent amélioration du champ proche (Figure 6.8(b)).

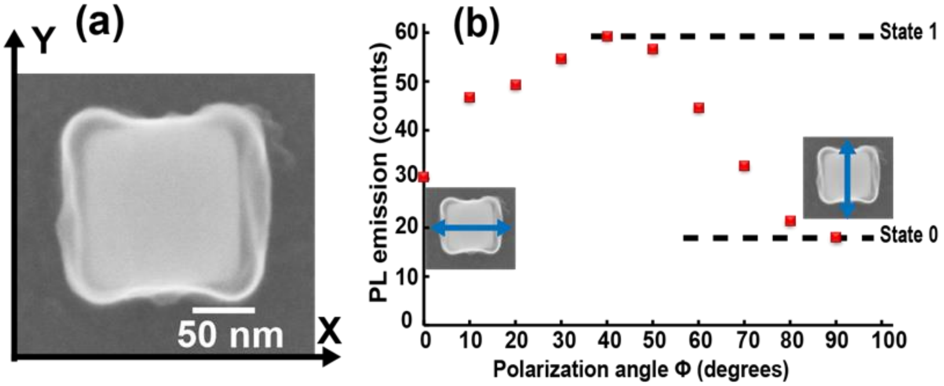

Figure 6.14 Photoluminescence (PL) d'une seule nanosource hybride basée sur un nanocube d'or et des QD rouges intégrés dans le volume polymérisé qui a été intégré le long des côtés du cube. (a) Image MEB de la nanostructure hybride observée sous 10Kv. (b) Intensité PL en fonction de l'angle de polarisation de la lumière d'excitation, le champ électrique incident est représenté par des flèches bleues.

La Figure 6.14 (a) présente une distribution polaire moins confinée et Figure 6.14 (b) montre un champ lointain PL typique de cette nanosource hybride. Sa dépendance de polarisation du PL montre une fluctuation de signal beaucoup plus faible par rapport à la *Figure 6.12* (d). Le contraste PL est mesuré à δPL ~ 0,3, ce qui est dû à une homogénéité plus élevée (confinement polaire plus faible) du polymère contenant du QD au voisinage du nanocube.

À titre de comparaison, les nanodisques d'or symétriques $C\infty v$ initiaux ont été utilisés pour produire des nanosources hybrides. Ils ont un diamètre de 90 nm et une épaisseur de 50 nm. Une lumière de polymérisation polarisée X est toujours utilisée pour TPP sur des nanodisques, et une amélioration du champ proche dipolaire a été utilisée pour obtenir une nanostructure hybride avec deux lobes dans à la *Figure 6.15*.

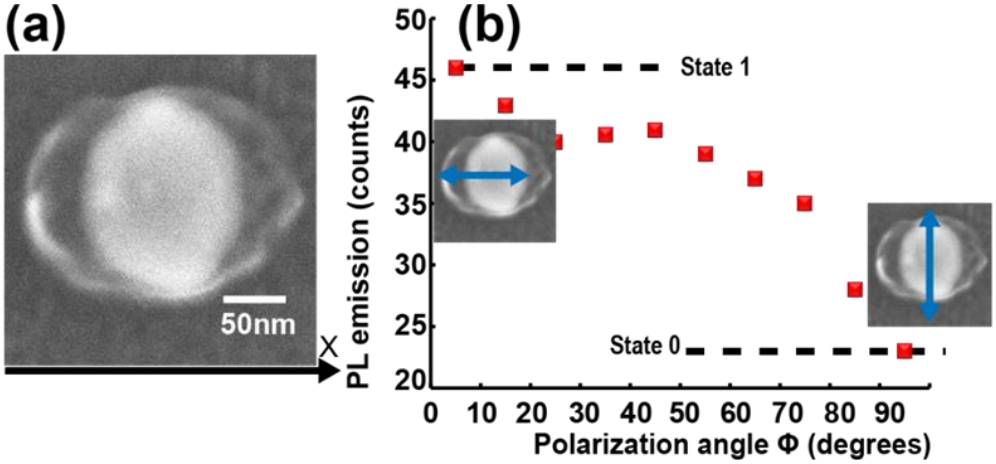

Figure 6.15 PL à partir d'une seule nanostructure hybride basée sur un nanodisque d'or et des QD rouges intégrés dans les deux lobes de polymère. La nanostructure hybride a été obtenue par TPP plasmonique en utilisant une polarisation linéaire le long de l'axe X. (a) image MEB de la nanostructure (image brute). (b) Intensité PL en fonction de l'angle ϕ *de polarisation de la lumière d'excitation à 450 nm. La direction du champ électrique incident est représentée par des flèches bleues.*

La structure obtenue présente deux lobes selon l'axe X, correspondant à la direction de polarisation utilisée lors du TPP. Sa dépendance de polarisation PL (Figure 6.15 (b)) présente une faible fluctuation avec δPL ~ 0,3. Contrairement au cas du nanocube, ici la symétrie dans le plan C∞v du nanodisque génère une distribution de champ proche dipolaire sans points chauds pointus donnant une faible asymétrie du dépôt polymérisé final.

À partir du même nanodisque d'or, un type supplémentaire de nanosource hybride a été fabriqué en utilisant la polarisation circulaire pour la polymérisation. La nanostructure résultante, représentée sur la *Figure 6.16* (a), est caractérisée par un milieu actif présentant une distribution en anneau de symétrie C∞v. Un faible PL contraste δ_{PL}~ 0,1 est obtenu à partir des données expérimentales de la Figure 6.16 (b). La valeur non nulle peut provenir de l'imperfection du motif circulaire, de la distribution non homogène des QD dans le volume du polymère ou d'un léger écart de direction lors de la polarisation de rotation.

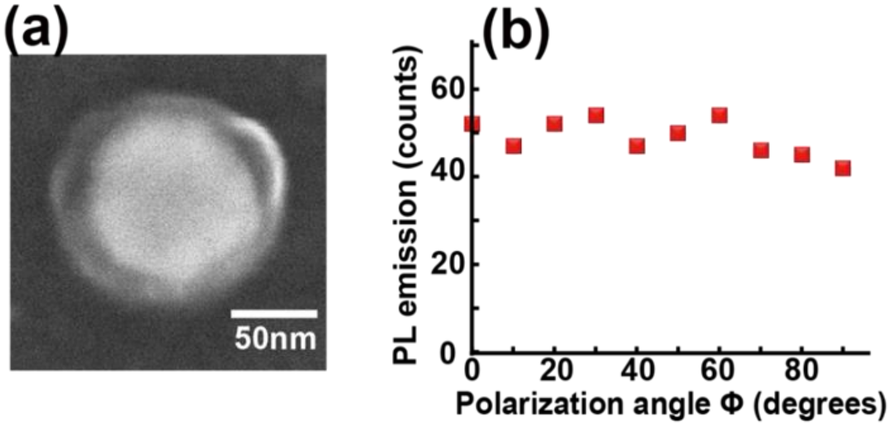

Figure 6.16 PL à partir d'une seule nanosource hybride basée sur un nanodisque d'or et des QD rouges intégrés dans une coque polymère obtenue par polymérisation à deux photons induits par plasmon en utilisant une polarisation circulaire. (a) image MEB de la nanosource hybride. (b) Intensité PL en fonction de l'angle ϕ de polarisation de la lumière d'excitation à 450 nm.

Inspiré de l'équation (6.6), nous définissons un rapport de chevauchement spatial normalisé, $\eta_{nf/em}$ entre l'intensité du champ proche plasmonique excitant hors résonance et la distribution des QDs :

$$\eta_{nf/em(\theta)} = \frac{V \iiint E_{exc}{}^{2} \times \rho dV}{\iiint E_{exc}{}^{2} dv \times \iiint \rho dV} \qquad (6.8)$$

$E_{exc}(x,y,z)$ est le module du champ plasmonique local qui excite les QD à la longueur d'onde de 405 nm. Il est calculé par FDTD. ρ (x, y, z) est la densité volumique de la probabilité de présence des QD. V est une constante arbitraire qui peut être considérée comme le volume total d'intégration. $\eta_{nf/em}$ quantifie la façon dont l'intensité du champ d'excitation et la distribution spatiale des QD se chevauchent pour une situation donnée, avec une direction de polarisation d'excitation donnée (par exemple, Figure 6.12 (e)).

La Figure 6.17 montre le $\eta_{nf/em}$ calculé en fonction de la direction de polarisation du champ incident à 405 nm, pour trois types différents de nanostructures hybrides. Toutes les nanostructures ont été fabriquées par TPP en utilisant une lumière de polymérisation polarisée X. Pour ce calcul, nous avons considéré que l'orientation et la distribution spatiale des QD dans la matrice polymère sont aléatoires et ne changent pas pendant l'excitation. Pour simplifier, nous avons défini ρ = 1 avec la présence d'un polymère et ρ = 0 avec l'absence de polymère.

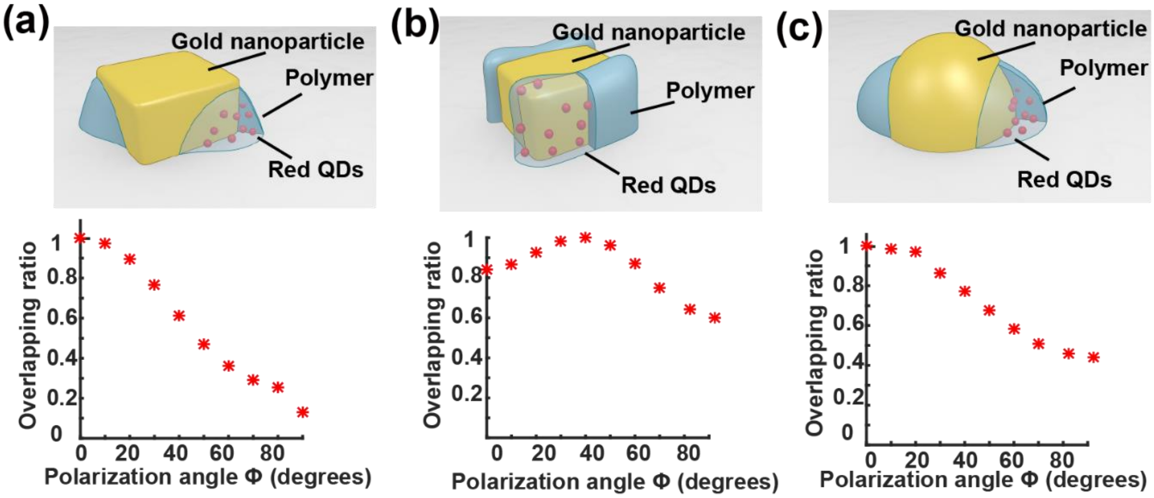

Figure 6.17 Intégrale de recouvrement spatial calculée $\eta_{nf/em}$, définie dans l'équation (7.8), entre le champ d'excitation local et le milieu actif en fonction de l'angle de polarisation incident ϕ pour trois nanosources hybrides différentes. Le champ incident (λexc = 405 nm) est polarisé en X. (a) Nanocube d'or avec des lobes de polymère intégrés le long de la direction diagonale (angle d'orientation du cube θ = 45 °). (b) Nanocube d'or avec polymérisation à deux faces de cube (angle d'orientation du cube θ = 0 °). (c) Nanodisque d'or hybride avec deux lobes de polymère le long de l'axe X.

Il s'avère que $\eta_{nf/em}$ varie comme l'intensité PL, montrant que le niveau PL dépend directement de $\eta_{nf/em}$. Afin d'établir précisément le lien entre $\eta_{nf/em}$ et IPL, nous considérons que l'IPL résulte de l'émission PL d'un ensemble de nanovolumes dv au voisinage du métal que chaque nanovolume, positionné en x, y, z, émet un dIPL d'intensité PL qui est défini comme :

$$d_{IPL} = \alpha \times \gamma_{exc}(x, y, z, \nu_{exc}) \times Q(\nu_{em}) \times \rho(x, y, z)dv$$

(6.9)α est une constante comprenant l'intensité incidente et l'efficacité de la collecte de lumière. ρ (x, y, z) dv est la probabilité de présence d'émetteurs à l'intérieur de dv.On suppose que α et $Q(\nu_{em})$ sont constants et excluant les nano-émetteurs éteints touchant la surface métallique. Le signal IPL résultant peut donc être exprimé comme suit :

$$\mathrm{IPL}(\theta) = \iiint d_{IPL} \; = \alpha \iiint \boldsymbol{E_{exc}}^2 \times \rho dv \qquad (6.10)$$

Il s'avère que IPL est proportionnel à $\eta_{nf/em}$, et en conséquence, l'équation (6.7) devient :

$$\delta_{PL} = \frac{IPL_{max} - IPL_{min}}{IPL_{max} + IPL_{min}} = \frac{\eta_{nf/em}^{max} - \eta_{nf/em}^{min}}{\eta_{nf/em}^{max} + \eta_{nf/em}^{min}} = \delta_{nf/em} \qquad (6.11)$$

Ici, $\eta_{nf/em}^{max}$ et $\eta_{nf/em}^{min}$ sont, respectivement, la valeur maximale et minimale de $\eta_{nf/em}$ sur la *Figure 6.17*. Le terme de $\delta_{nf/em}$ dans l'équation (6.11) a été calculé à partir des données de la *Figure 6.17*. Nous avons trouvé 0.74, 0.25 et 0.35. Ces valeurs peuvent être comparées à celles de δ_{PL} qui ont été déterminées expérimentalement : 0.7, 0.3 et 0.3, respectivement. Il s'avère que $\delta_{nf/em}$ et δ_{PL} sont égaux. Ce résultat important valide le lien de proportionnalité entre $\eta_{nf/em}$ et IPL.

6.3.4 Des QDs uniques dans un nanocube hybride

La diminution de la concentration de QD dans la formulation photopolymérisable nous permet de piéger un petit nombre de QD (un seul QD ou quelques-uns) à l'intérieur des nano-lobes de polymère d'un nano-émetteur hybride à base de nanocube. La *Figure 6.18*(a) montre une image AFM d'un tel nano-émetteur hybride. Un laser pulsé de 405 nm avec un angle de polarisation incident $\phi = 0^{o}$ (parallèle au lobe polymère le long de l'axe X) a été utilisé pour l'excitation PL. Nous pouvons voir un clignotement clair sur les figures *Figure 6.18*(b) et *Figure 6.18*(c), qui est la signature d'une seule (ou quelques) émission de QD (temps tracé 50 s). Plus intéressant encore, sur la *Figure 6.18*(b), cette émission est désactivée lorsque la polarisation incidente est tournée à $\phi = 90°$ (en utilisant une lame demi-onde) en raison du manque soudain de chevauchement entre le champ proche excitant et le seul QD. Nous avons constaté qu'à un retard nul, $g^{(2)}(0) \sim 0.35$ (Figure 6.18 (d)), qui est inférieur à 0.5, illustrant qu'il n'y a qu'un seul photon émis en même temps.

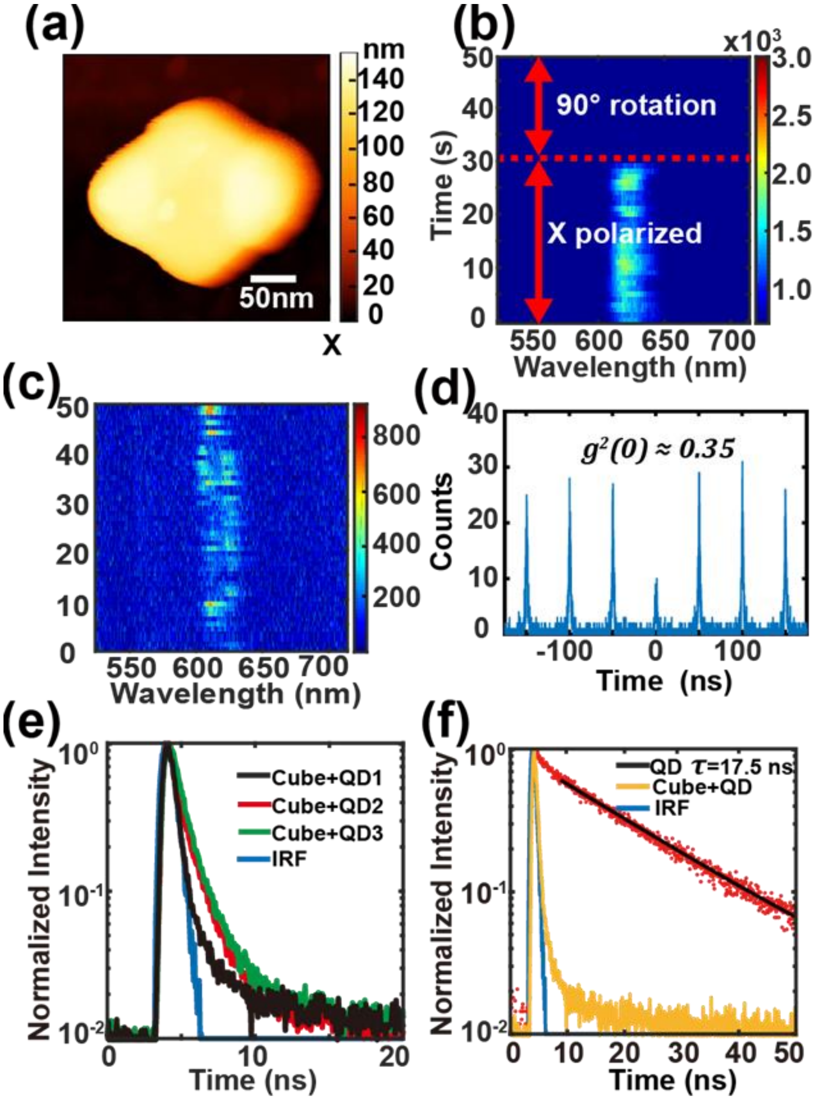

Figure 6.18 Nano-émetteurs hybrides en régime photonique unique. (a) Image AFM d'un nano-émetteur hybride à base de nanocube. Les lobes de polymère, fabriqués de la même manière que la Figure 6.12 (a), contiennent un seul QD ou quelques QD. (b) et (c) trace temporelle du spectre PL de t = 50 s avec une polarisation X linéaire incidente à 405 nm. En (b) au temps t = 32 s, la direction de polarisation a été tournée de 90 °. (d) Mesure de g (2) montrant g (2) (0) = 0.35. (e) Durée de vie de trois nano-émetteurs hybrides à base de nanocubes différents contenant des QD uniques (puissance incidente de 0.62 μW / μm2, taux de répétition de 5 MHz). Une mesure de durée de vie typique sur un nano-émetteur hybride mono-QD ∼0.725 ns. La courbe bleue représente la fonction de réponse d'instrumentation (IRF) de 0,63 ns. (f) Mesure de la durée de vie : comparaison entre un QD unique en polymère sans nanocube d'or (courbe rouge, 17.5 ns) et un seul QD au voisinage d'un nanocube d'or (nano-émetteur hybride : la courbe jaune montre le plus petit observé.

Et plus, nous avons mesuré la durée de vie de plusieurs nano-émetteurs hybrides typiques, présentée par des lignes courbes noires, rouges et vertes sur la Figure 6.18(e). La durée de vie typique du nano-émetteur hybride est de 0.725 ns, tandis que la durée de vie des QD uniques dans le polymère a été mesurée à environ 17.5 ns (Figure 6.18(f)). Ces mesures correspondent à un facteur de Purcell moyen de 17.5 / 0.725 ~ 23. Statistiquement, plusieurs nanosources hybrides ont révélé des durées de vie plus petites, proches ou probablement plus petites que l'IRF (voir par exemple la courbe jaune sur la *Figure 6.18*(f)), suggérant des facteurs de Purcell plus élevés que 28 (= 17.5 / 0.63). On pense que cette variation de durée de vie est liée à la position aléatoire des QD dans les lobes du polymère au voisinage du nanocube d’or.

6.3.5 Hybrides Nanostructure hybride basée sur la forme spéciale des MNP : Au bipyramides

Les Au nano-bipyramides (AuBPs) sont fournis par notre collègue Matthew S. Kirschner (Northwestern University of USA). Ils ont utilisé une approche de croissance médiée par les semences pour synthétiser des AuBP de taille modifiée avec des pics de LSPR allant de 680 nm à 900 nm, ce qui correspond au spectre d'absorption de notre formulation photosensible utilisée pour le TPP.

La Figure 6.19(a) illustre l'image MEB de plusieurs AuBPs. La Figure 6.19(b) affiche une image en champ noir des particules dispersées sur du verre enduit d'ITO. Les points rouges correspondent à des AuBPs et les points verts correspondent à des sphères, les points apparaissant en bleu clair correspondent généralement au tensioactif résiduel. (b) et (c) donnent la distribution de taille de 100 AuBPs, où nous pouvons obtenir la longueur moyenne des AuBPs est de 115,6 ± 4,45 nm pour le grand axe et de 45,8 ± 4,10 nm pour le petit axe séparément.

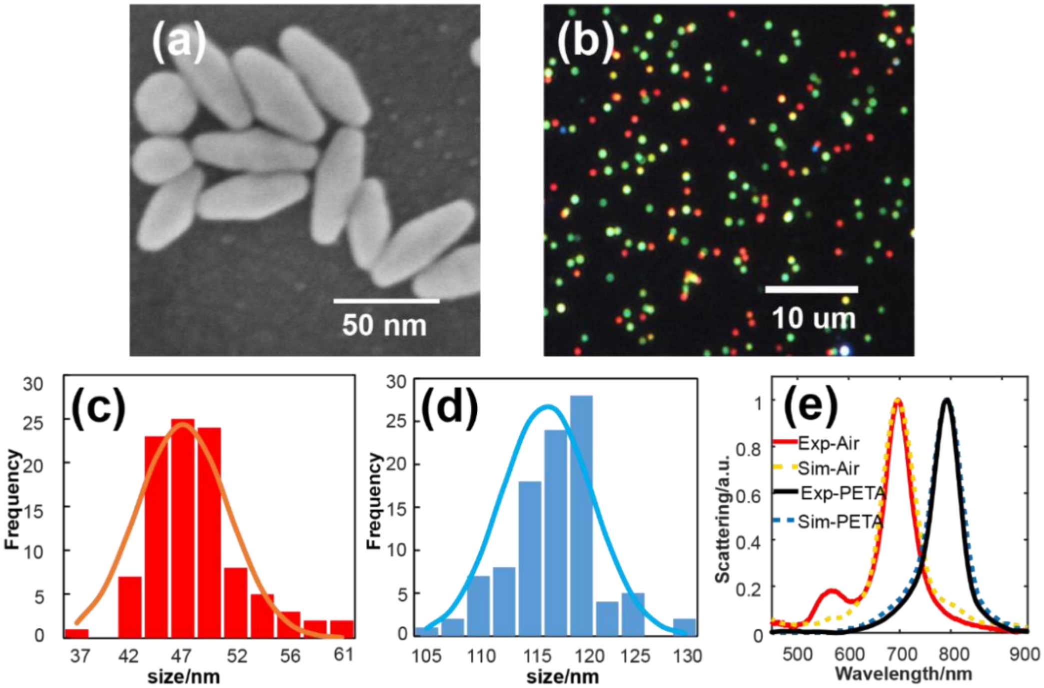

Figure 6.19 L'apparence et la taille des AuBPs. (a) Images MEB typiques de plusieurs AuBPs agrégés. (b) Image en champ noir des AuBPs dispersés. Les points rouges présentent les AuBPs. La distribution de taille de (c) axe court et (d) axe long de 100 AuBPs aléatoires, analysée par des images MEB. (e) Les lignes pleines rouges et noires montrent le spectre de diffusion mesuré à partir d'un seul AuBPs immergé dans l'air et le PETA ; Les lignes pointillées orange et bleu donnent les spectres de diffusion calculés par FDTD à partir d'un seul AuBP déposé sur un substrat de verre revêtu d'ITO, immergé dans l'air et le polymère (PETA). Les paramètres de taille utilisés dans la simulation FDTD ont été obtenus à partir de l'image MEB.

La distribution spatiale des directions polarisées de la lumière polarisée radiale et polarisée azimutale a des caractéristiques symétriques au centre et forme une distribution d'intensité en forme d'anneau creux. Ils sont également connus sous le nom de mode anneau à polarisation azimutale (APDM) et mode anneau à polarisation radiale (RPDM). Ces deux modes n'ont que des composantes électriques vectorielles dans le plan dans le plan d'entrée perpendiculaire à la direction de propagation z, tandis que leur comportement devient différent lorsqu'ils sont focalisés. Il n'y a que des composantes de polarisation dans le plan du champ électrique pour le mode polarisé azimutale. En revanche, pour le mode polarisé radialement, il existe à la fois des composants dans le plan et longitudinal (hors plan) et des composants longitudinaux. La microscopie confocale à balayage coopérant avec ces deux modes s'est avérée être utilisée pour l'orientation de dipôle seul[184] et la détection de l'orientation des nanorod d'or[185,186].

Le modèle de photoluminescence simulé des AuBP excités par un APDM ou un RPDM peut être calculé, les résultats sont présentés sur la Figure 6.20.

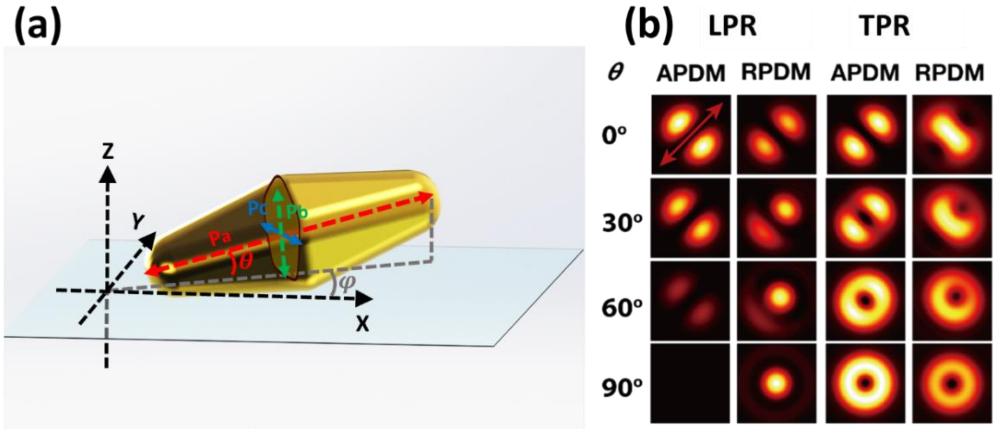

Figure 6.20 Diagramme schématique 3D d'un seul AuBP déposé sur le substrat. Les flèches bleue et verte indiquent l'orientation du mode de résonance plasmonique transversal (TPRM) et du mode de résonance plasmonique longitudinal (LPRM). φ et sont respectivement l'angle dans le plan et l'angle hors plan. (b) Modèles de photoluminescence simulés de AuBP d'or en utilisant un mode APDM et un mode RPDM séparément. La flèche rouge indique la projection du grand axe de AuBP sur le plan d'échantillonnage.

La Figure 6.21 illustre un groupe de résultats, y compris les spectres PL des AuBP et les motifs PL corrélés obtenus par APDM et RPDM en utilisant différentes longueurs d'onde d'excitation. Les modèles d'excitation en forme de double lobes excités par 632 nm (Figure 6.19 (b) rangée du bas) prouvent que cette longueur d'onde peut exciter le mode de résonance plasmonique longitudinal (LPRM) des AuBPs et le conduire fonctionne comme un dipôle avec un moment de transition le long du grand axe. Les motifs asymétriques excités avec RPDM sur la Figure 6.21 (b) (image en bas à droite) révèlent une inclinaison hors plan. L'orientation indiquée à partir des doubles lobes concorde entièrement avec l'image MEB des AuBPs sur la Figure 6.21 (a). Alors que le laser d'excitation passait à 530 nm, des motifs en forme d'anneau parfaits ont été obtenus sous APDM et des motifs en forme de points ont été obtenus sous RPDM, représentés sur la Figure 6.21 (b) (rangée du haut). Ainsi, les modèles PL sous APDM et RPDM ne montrent aucune directionnalité. L'orientation hors plan d'une seule bipyramide peut être déterminée de manière ambiguë via une excitation RPDM sous une excitation de 632 nm. Sur la *Figure 6.21* (c), l'image polaire a une symétrie circulaire excitée par 530 nm et une anisotropie évidente sous une excitation de 632 nm. La Figure 6.21 (d) montre les spectres PL excités par différentes longueurs d'onde. En comparant la Figure 6.21 (d) et la Figure 6.19 (e), les spectres PL suivent approximativement la diffusion du champ noir, à savoir les spectres LPRM. Cependant, les pics PL ont un décalage vers le bleu par rapport aux pics de diffusion qui sont liés au rapport d'aspect[193,194],, qui peuvent provenir d'une densité électronique élevée[195]. Le spectre PL (Figure 6.21 (e)) n'a pas de phénomène de clignotement. Cela peut aider à distinguer et à exclure les signaux de fluorescence des QD de PL après avoir introduit des QD autour des AuBPs dans des expériences ultérieures.

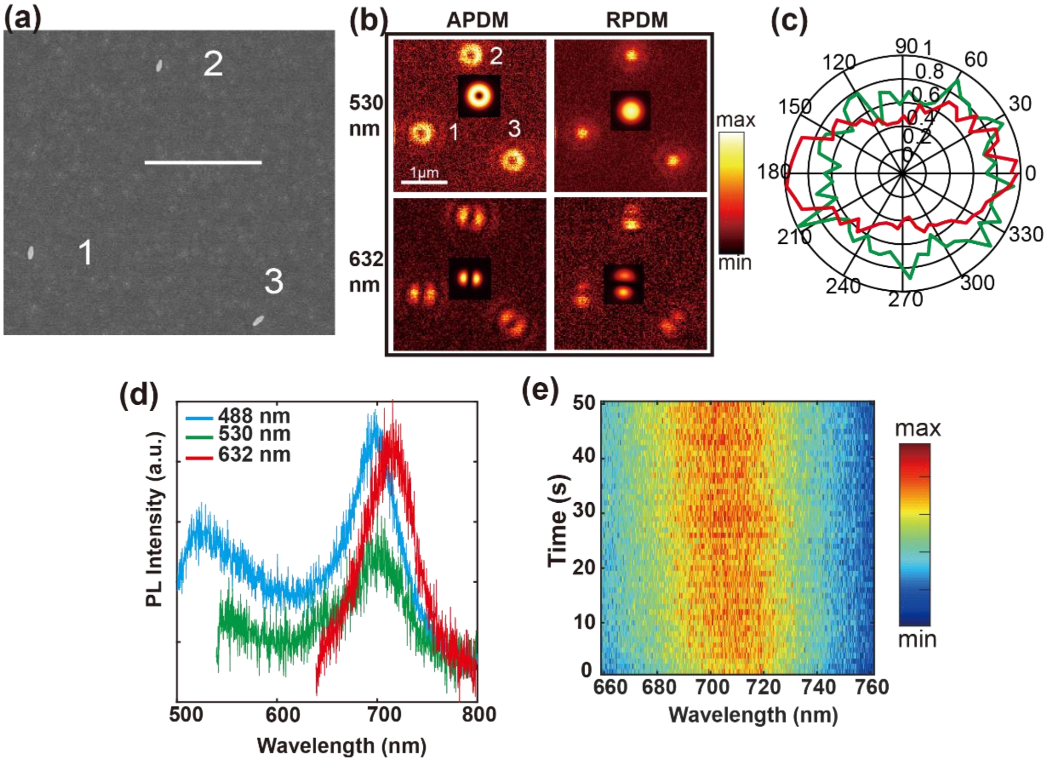

Figure 6.21 Image MEB de trois AuBPs séparés. (b) Les modèles d'excitation de photoluminescence (PL) des AuBP sont représentés en (a) excités par 530 nm (rangée du haut) et 632 nm (rangée du bas) en utilisant les modes APDM et RPDM. Les petites images insérées donnent les modèles PL simulés de AuBP No.1. (c) Le tracé polaire correspondant de la valeur d'extinction normalisée à partir des motifs PL de AuBP no.1 dans (b) en utilisant le mode APDM, les lignes vertes et rouges représentent la longueur d'onde

d'excitation de 530 nm et 632 nm séparément. (d) Spectres PL de l'AuBP No.1 unique en (a) qui ont été obtenus en utilisant différentes longueurs d'onde d'excitation. La puissance du laser d'excitation a été réglée à 25 uW. (e) Trace temporelle des spectres PL de AuBP No.1 acquis sous une excitation de 530 nm.

Comme nous l'avons fait sur les nanocubes d'or, le TPP en champ proche déclenché par plasmon est également appliqué sur les AuBPs. Considérons les pics LSPR des AuBPs avec l'inévitable red-shifter, nous avons choisi 800 nm comme longueur d'onde utilisée pour le TPP. Un groupe typique de résultats est présenté à la Figure 6.22.

La distribution en champ proche des AuBP est plus localisée que celle des Au nano-cubes ; et le facteur d'amélioration est plus élevé. La formulation utilisée pour les AuBP se compose également de trois composants, le PETA, 1% wt IRG 819 et QDs (670 nm).

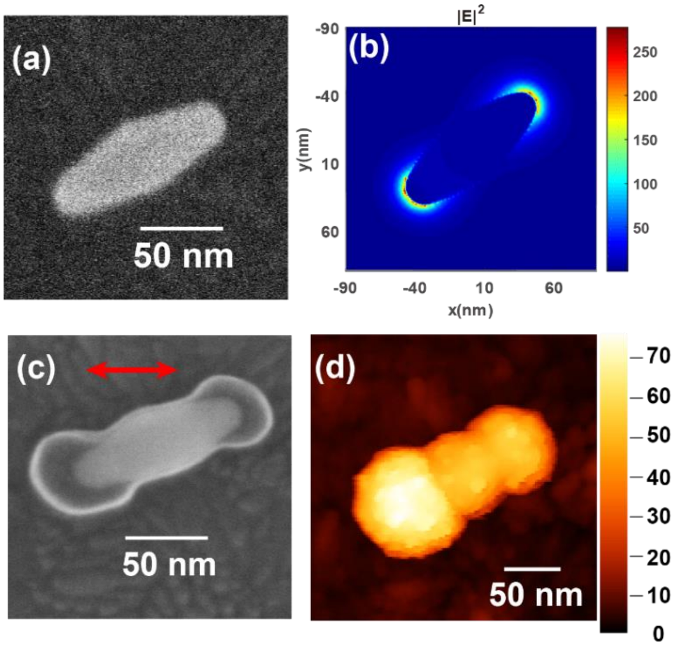

Figure 6.22 Structure hybride basée sur des AuBP fabriqués par TPP en champ proche. (a) Image MEB de AuBP simple nu. (b) Distribution de champ proche simulée autour de AuBP excité par 800 nm. Image MEB (c) et image AFM (d) de la structure hybride fabriquée par laser à polarisation linéaire basée sur l'AuBP en (a). La flèche rouge en (c) indique la direction de polarisation du laser de durcissement.

Après polymérisation, les AuBPs recouverts de polymère contenant des QDs hybrides résultants ont été scannés par le même montage en utilisant les modes APDM et RPMD; leurs schémas de fluorescence ont été présentés sur la *Figure 6.23*. Comparez les modèles PL des AuBPs purs et des AuBPs hybrides (contenus QDs). Nous constatons que les schémas d'émission des AuBP hybrides excités par 532 nm en utilisant l'APDM montrent une directionnalité au lieu de schémas d'anneaux isotropes dans des AuBPs purs. On peut le voir plus clairement sur les images polaires correspondantes de la Figure 6.23(c) et (d).

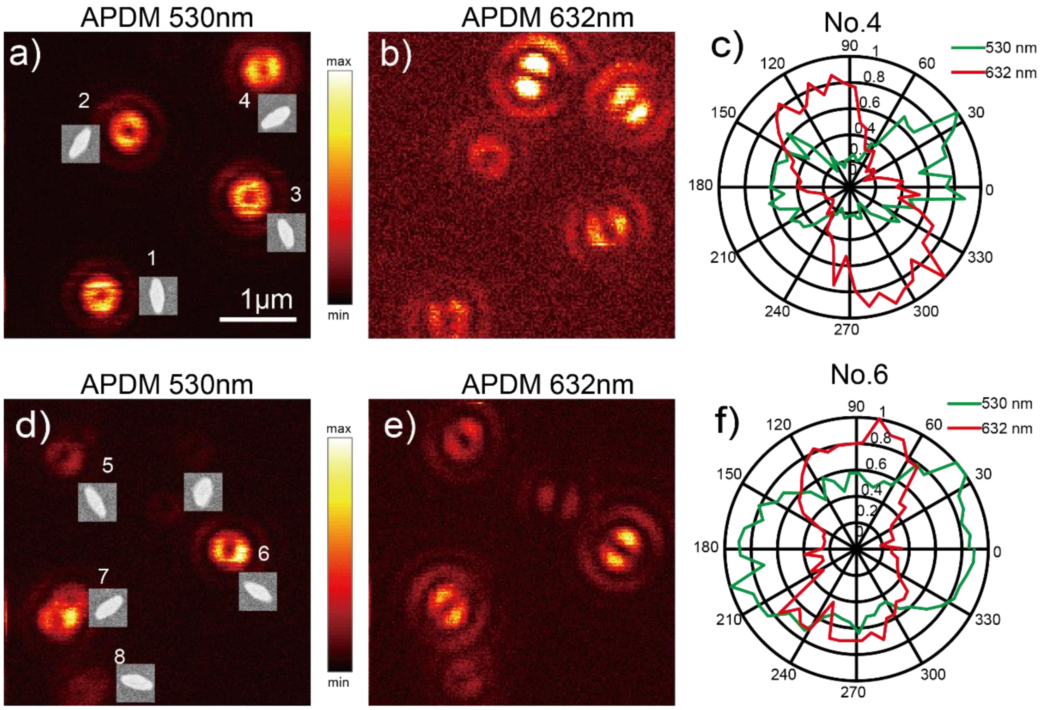

Figure 6.23 (a) (b) sont les modèles d'excitation mesurés à partir du premier groupe d'AuBP hybrides (NO. 1 ~ NO. 4) avec APDM excité en utilisant 530 nm et 632 nm ; de petites images insérées donnent les images MEB originales des AuBP correspondants. (c) L'image polaire correspondante des diagrammes d'émission de AuBP hybride NO 4 en (a) (b). (d) (e) sont les diagrammes d'émission du deuxième groupe d'AuBP hybrides (NO.5 ~ NO. 8) excités séparément à 530 nm et 632 nm. (f) Montre l'image polaire correspondante des diagrammes d'émission de AuBP hybride NO.6 en (d) (e).

La Figure 6.24 (a) donne les spectres de trace temporelle des QD en vrac, montrant une émission stable. Nous avons trouvé des QD uniques et enregistré les spectres de traces temporelles à partir d'un seul QD illustré à la Figure 6.24(b). Les Figure 6.24(c), (d) et (e) affichent les spectres de trace temporelle de trois AuBPs hybrides actifs différents. Le spectre de fluorescence du premier AuBP hybride a un pic principal clair, tandis que les deux autres AuBPs hybrides présentent deux pics d'émission évidents ou moins évidents. La Figure 6.24(f), qui donne les spectres de fluorescence des QD en vrac, des QD simples et des AuBPs hybrides actifs, révèle clairement la différence entre ces différentes situations. Nous avons des raisons de douter que ce phénomène à deux pics soit le clivage de Rabi, qui pourrait résulter du fort couplage entre AuBP et QDs. Cependant, jusqu'à présent, il n'y a pas suffisamment de preuves pour confirmer cette spéculation. Davantage de données expérimentales et de données de calcul doivent être obtenues.

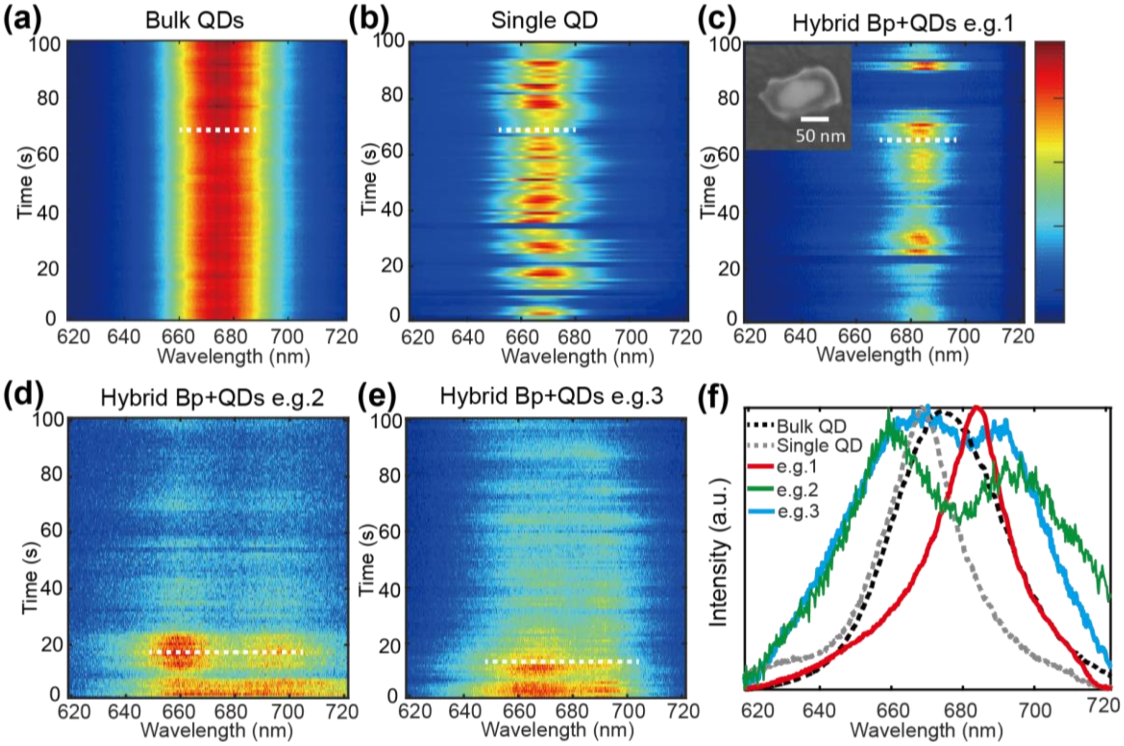

Figure 6.24 Spectres de QD purs et AuBP hybrides contenant des QD. (a) Trace temporelle des spectres de fluorescence des QD en vrac. (b) Trace temporelle des spectres de fluorescence d'un seul QD. (c) (d) (e) trois exemples de spectres de fluorescence à trace temporelle provenant d'AuBP hybrides avec des QD à l'intérieur du polymère. (f) Prenez un moment du spectre à partir d'images antérieures (a) ~ (e), position temporelle indiquée par une ligne blanche en pointillés.

De plus, il convient de noter que nous avons observé un antibunching avec une valeur g (2) d'environ 0.45 à partir d'AuBP hybride e.g.3, révélant qu'il n'y a que quelques QD (fermés à un seul QD). La fonction d'autocorrélation de l'AuBP hybride, par exemple 3, est illustrée à la Figure 6.25. À partir de la variance de la durée de vie entre les QD isolés (environ 8 ns) et les QD dans les AuBPs hybrides (moins de 0.23 ns peuvent être obtenus), un facteur de Purcell élevé (plus de 30) serait révélé, suggérant une modification significative des caractères de rayonnement des QD par couplage entre AuBP.

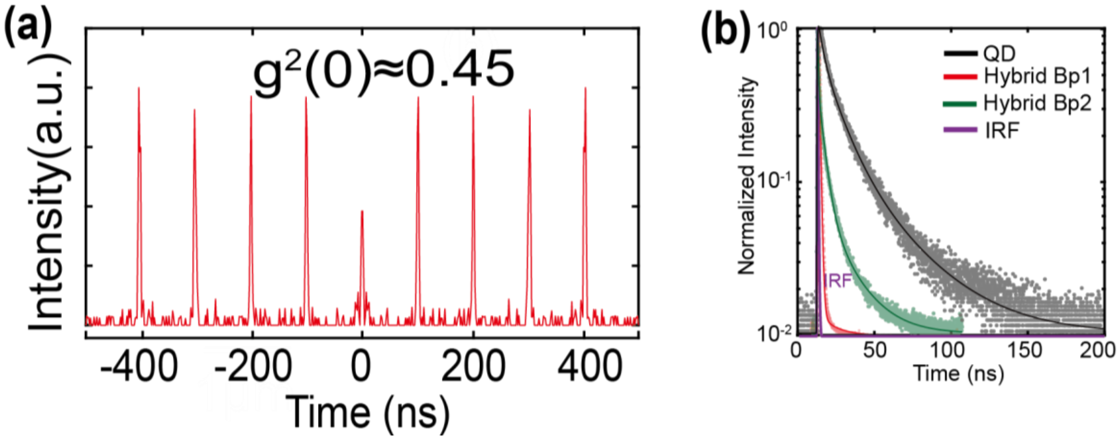

Figure 6.25 g $^{(2)}$ mesure de la fonction d'autocorrélation des AuBP hybrides contenant des QD sur la Figure 6.24(e) (puissance incidente de 15uw avec un laser de 530 nm, taux de répétition de 10 MHz). (b) Mesure de la durée de vie : comparaison entre un QD unique sans AuBP (courbe noire, 8 ns), des AuBP hybrides avec un QD unique à l'intérieur de son polymère (courbe rouge, environ 0.98 ns) et un autre exemple d'AuBP hybride avec peu de QD en polymère courbe, environ 0.23 ns).

6.4 conclusion

Au cours de la thèse, nous avons développé et étudié des nano-émetteurs plasmoniques hybrides anisotropes via une polymérisation à deux photons en champ proche qui est déclenchée par une amélioration localisée du champ à partir d'un plasmon de surface soutenu par des nanoparticules métalliques.

L'idée clé est que les émetteurs actifs, en particulier les QD semi-conducteurs, sont contenus dans le polymère, ce qui entraîne une distribution anisotrope du polymère qui reflète la distribution anisotrope des nano-émetteurs.

En utilisant des nanocubes et des nanodisques d'or et différents modes d'excitation plasmon, et différentes distributions de champ proche associées, nous avons réussi à fabriquer différents nanosystèmes présentant différentes distributions de polymères avec différents degrés de symétrie à proximité immédiate des nanoparticules métalliques. La reproductibilité de la méthode nous a permis de réaliser des études de paramètres et de discuter et quantifier la sensibilité de polarisation de la photoluminescence des nanosources hybrides en termes de chevauchement spatial entre le champ proche optique excitant et le milieu actif nanométrique. En particulier, la dépendance de polarisation résultante de la photoluminescence a été analysée et quantifiée sur la base de nouveaux paramètres spécifiques dont la définition et l'utilisation ont été rendues possibles pour la première fois: i) répartition spatiale des nano-émetteurs incluant la répartition angulaire du milieu actif, ii) intégrale de chevauchement spatial à l'échelle nanométrique entre le milieu actif et le champ proche d'excitation, et iii) le contraste de polarisation de photoluminescence associé. La nanostructure hybride à base de nanocubes qui est fabriquée à l'aide d'un laser à polarisation linéaire avec une direction de polarisation le long de la diagonale du cube s'est avérée être le nanosystème le plus sensible à la polarisation avec un contraste de polarisation PL de 0,7.

Sur la base de cela, nous avons diminué le nombre de QD à l'intérieur des lobes de polymère en diminuant la concentration de QD dans la formulation photosensible, et finalement réduit le nombre de QD à un seul niveau. En conséquence, nous avons démontré pour la première fois la capacité de faire de tels systèmes hybrides jusqu'au niveau de photon unique avec un facteur de Purcell associé d'environ 30. Ainsi, un résultat préliminaire de commutateur de photon unique commandé par polarisation a été rapporté.

La même méthode de TPP plasmonique en champ proche a également été utilisée sur les bipyramides en or qui ont deux extrémités pointues. Nous avons d'abord étudié les orientations des bipyramides nus via l'imagerie de leur photoluminescence résultant d'une excition présentant des modes beignets polarisés azimutalement ou radialement. Ensuite, nous avons réussi à fabriquer pour la première fois des nanostructures hybrides bipyramides / polymères mono-QD dont la caractérisation PL a révélé des effets intéressants suggérant un contraste de polarisation singulier et la possibilité d'obtenir un couplage fort au niveau de QD unique.

Reference :

1. Nicoli, F. *et al.* DNA-Mediated Self-Assembly of Plasmonic Antennas with a Single Quantum Dot in the Hot Spot. *Small* **15**, 1804418 (2019).
2. Busson, M. P., Rolly, B., Stout, B., Bonod, N. & Bidault, S. Accelerated single photon emission from dye molecule-driven nanoantennas assembled on DNA. *Nat. Commun.* **3**, 1–6 (2012).
3. Groß, H., Hamm, J. M., Tufarelli, T., Hess, O. & Hecht, B. Near-field strong coupling of single quantum dots. *Sci. Adv.* **4**, (2018).
4. Kolchin, P. *et al.* High Purcell Factor Due To Coupling of a Single Emitter to a Dielectric Slot Waveguide. *Nano Lett.* **15**, 464–468 (2015).
5. Belacel, C. *et al.* Controlling Spontaneous Emission with Plasmonic Optical Patch Antennas. *Nano Lett.* **13**, 1516–1521 (2013).
6. Deeb, C. *et al.* Mapping the Electromagnetic Near-Field Enhancements of Gold Nanocubes. *J. Phys. Chem. C* **116**, 24734–24740 (2012).
7. Zhou, X. *et al.* Two-Color Single Hybrid Plasmonic Nanoemitters with Real Time Switchable Dominant Emission Wavelength. *Nano Lett.* **15**, 7458–7466 (2015).
8. Cao, J., Sun, T. & Grattan, K. T. V. Gold nanorod-based localized surface plasmon resonance biosensors: A review. *Sens. Actuators B Chem.* **195**, 332–351 (2014).
9. Bauch, M., Toma, K., Toma, M., Zhang, Q. & Dostalek, J. Plasmon-Enhanced Fluorescence Biosensors: a Review. *Plasmonics* **9**, 781–799 (2014).
10. Jeong, Y., Kook, Y.-M., Lee, K. & Koh, W.-G. Metal enhanced fluorescence (MEF) for biosensors: General approaches and a review of recent developments. *Biosens. Bioelectron.* **111**, 102–116 (2018).
11. Clavero, C. Plasmon-induced hot-electron generation at nanoparticle/metal-oxide interfaces for photovoltaic and photocatalytic devices. *Nat. Photonics* **8**, 95–103 (2014).
12. Hou, W. & Cronin, S. B. A Review of Surface Plasmon Resonance-Enhanced Photocatalysis. *Adv. Funct. Mater.* **23**, 1612–1619 (2013).
13. Maier, S. A. Plasmonics: The Promise of Highly Integrated Optical Devices. *IEEE J. Sel. Top. Quantum Electron.* **12**, 1671–1677 (2006).

14. Du, W., Wang, T., Chu, H.-S. & Nijhuis, C. A. Highly efficient on-chip direct electronic–plasmonic transducers. *Nat. Photonics* **11**, 623–627 (2017).
15. Wang, F. *et al.* Nanoscale on-chip all-optical logic parity checker in integrated plasmonic circuits in optical communication range. *Sci. Rep.* **6**, 24433 (2016).
16. Visser, E. W. A., Horáček, M. & Zijlstra, P. Plasmon Rulers as a Probe for Real-Time Microsecond Conformational Dynamics of Single Molecules. *Nano Lett.* **18**, 7927–7934 (2018).
17. Sönnichsen, C., Reinhard, B. M., Liphardt, J. & Alivisatos, A. P. A molecular ruler based on plasmon coupling of single gold and silver nanoparticles. *Nat. Biotechnol.* **23**, 741–745 (2005).
18. Drexhage, K. H. IV interaction of light with monomolecular dye layers. in *Progress in optics* vol. 12 163–232 (Elsevier, 1974).
19. Bharadwaj, P. & Novotny, L. Spectral dependence of single molecule fluorescence enhancement. *Opt. Express* **15**, 14266–14274 (2007).
20. Liu, S.-Y. *et al.* Simultaneous Excitation and Emission Enhancement of Fluorescence Assisted by Double Plasmon Modes of Gold Nanorods. *J. Phys. Chem. C* **117**, 10636–10642 (2013).
21. Rousseaux, B., Baranov, D. G., Käll, M., Shegai, T. & Johansson, G. Quantum description and emergence of nonlinearities in strongly coupled single-emitter nanoantenna systems. *Phys. Rev. B* **98**, 045435 (2018).
22. Purcell, E. M., Torrey, H. C. & Pound, R. V. Resonance absorption by nuclear magnetic moments in a solid. *Phys. Rev.* **69**, 37 (1946).
23. Anger, P., Bharadwaj, P. & Novotny, L. Enhancement and Quenching of Single-Molecule Fluorescence. *Phys. Rev. Lett.* **96**, 113002 (2006).
24. Viste, P. *et al.* Enhancement and Quenching Regimes in Metal−Semiconductor Hybrid Optical Nanosources. *ACS Nano* **4**, 759–764 (2010).
25. Shimizu, K. T., Woo, W. K., Fisher, B. R., Eisler, H. J. & Bawendi, M. G. Surface-Enhanced Emission from Single Semiconductor Nanocrystals. *Phys. Rev. Lett.* **89**, 117401 (2002).
26. Pan, J. *et al.* Surface plasmon-enhanced quantum dot light-emitting diodes by incorporating gold nanoparticles. *Opt. Express* **24**, A33–A43 (2016).
27. Guzatov, D. V. *et al.* Plasmonic Enhancement of Molecular Fluorescence near Silver Nanoparticles: Theory, Modeling, and Experiment. *J. Phys. Chem. C* **116**, 10723–10733 (2012).

28. Khatua, S. *et al.* Resonant Plasmonic Enhancement of Single-Molecule Fluorescence by Individual Gold Nanorods. *ACS Nano* **8**, 4440–4449 (2014).

29. Zhou, X. *et al.* Polarization-dependent fluorescence from an anisotropic gold/polymer hybrid nano-emitter. *Appl. Phys. Lett.* **104**, 023114 (2014).

30. Cooper, C. T., Rodriguez, M., Blair, S. & Shumaker-Parry, J. S. Polarization Anisotropy of Multiple Localized Plasmon Resonance Modes in Noble Metal Nanocrescents. *J. Phys. Chem. C* **118**, 1167–1173 (2014).

31. Zuo, T., Goldwyn, H. J., Isaacoff, B. P., Masiello, D. J. & Biteen, J. S. Rotation of Single-Molecule Emission Polarization by Plasmonic Nanorods. *J. Phys. Chem. Lett.* **10**, 5047–5054 (2019).

32. Ming, T. *et al.* Strong Polarization Dependence of Plasmon-Enhanced Fluorescence on Single Gold Nanorods. *Nano Lett.* **9**, 3896–3903 (2009).

33. Lee, D. & Yoon, S. Gold Nanocube–Nanosphere Dimers: Preparation, Plasmon Coupling, and Surface-Enhanced Raman Scattering. *J. Phys. Chem. C* **119**, 7873–7882 (2015).

34. Chen, F., Alemu, N. & Johnston, R. L. Collective plasmon modes in a compositionally asymmetric nanoparticle dimer. *AIP Adv.* **1**, 032134 (2011).

35. Kinkhabwala, A. *et al.* Large single-molecule fluorescence enhancements produced by a bowtie nanoantenna. *Nat. Photonics* **3**, 654–657 (2009).

36. Ueno, K. *et al.* Control of plasmon dephasing time using stacked nanogap gold structures for strong near-field enhancement. *Appl. Mater. Today* **14**, 159–165 (2019).

37. Lumdee, C., Yun, B. & Kik, P. G. Gap-Plasmon Enhanced Gold Nanoparticle Photoluminescence. *ACS Photonics* **1**, 1224–1230 (2014).

38. Russell, K. J., Liu, T.-L., Cui, S. & Hu, E. L. Large spontaneous emission enhancement in plasmonic nanocavities. *Nat. Photonics* **6**, 459–462 (2012).

39. Qi, Z. *et al.* Plasmon-enhanced energy transfer between quantum dots and tunable film-coupled nanoparticles. *J. Phys. Appl. Phys.* **49**, 235103 (2016).

40. Li, G.-C., Zhang, Q., Maier, S. A. & Lei, D. Plasmonic particle-on-film nanocavities: a versatile platform for plasmon-enhanced spectroscopy and photochemistry. *Nanophotonics* **7**, 1865–1889 (2018).

41. Muskens, O. L., Giannini, V., Sánchez-Gil, J. A. & Gómez Rivas, J. Strong Enhancement of the Radiative Decay Rate of Emitters by Single Plasmonic Nanoantennas. *Nano Lett.* **7**, 2871–2875 (2007).

42. Akselrod, G. M. *et al.* Probing the mechanisms of large Purcell enhancement in plasmonic nanoantennas. *Nat. Photonics* **8**, 835–840 (2014).
43. Kholmicheva, N., Romero, L. R., Cassidy, J. & Zamkov, M. Prospects and applications of plasmon-exciton interactions in the near-field regime. *Nanophotonics* **8**, 613–628 (2018).
44. Noginov, M. A. *et al.* Demonstration of a spaser-based nanolaser. *Nature* **460**, 1110–1112 (2009).
45. Bergman, D. J. & Stockman, M. I. Surface Plasmon Amplification by Stimulated Emission of Radiation: Quantum Generation of Coherent Surface Plasmons in Nanosystems. *Phys. Rev. Lett.* **90**, 027402 (2003).
46. Ma, R.-M., Oulton, R. F., Sorger, V. J., Bartal, G. & Zhang, X. Room-temperature sub-diffraction-limited plasmon laser by total internal reflection. *Nat. Mater.* **10**, 110–113 (2011).
47. Meng, X., Kildishev, A. V., Fujita, K., Tanaka, K. & Shalaev, V. M. Wavelength-Tunable Spasing in the Visible. *Nano Lett.* **13**, 4106–4112 (2013).
48. Wang, J.-H. *et al.* How Gain Layer Design Determines Performance of Nanoparticle-Based Spaser. *J. Phys. Chem. C* **124**, 16553–16560 (2020).
49. Song, P. *et al.* quantum. *Sci. Adv.* **4**, eaat0292 (2018).
50. Törmä, P. & Barnes, W. L. Strong coupling between surface plasmon polaritons and emitters: a review. *Rep. Prog. Phys.* **78**, 013901 (2014).
51. Khitrova, G., Gibbs, H. M., Kira, M., Koch, S. W. & Scherer, A. Vacuum Rabi splitting in semiconductors. *Nat. Phys.* **2**, 81–90 (2006).
52. Yoshie, T. *et al.* Vacuum Rabi splitting with a single quantum dot in a photonic crystal nanocavity. *Nature* **432**, 200–203 (2004).
53. Chikkaraddy, R. *et al.* Single-molecule strong coupling at room temperature in plasmonic nanocavities. *Nature* **535**, 127–130 (2016).
54. Zengin, G. *et al.* Realizing strong light-matter interactions between single-nanoparticle plasmons and molecular excitons at ambient conditions. *Phys. Rev. Lett.* **114**, 157401 (2015).
55. Shi, L. *et al.* Spatial Coherence Properties of Organic Molecules Coupled to Plasmonic Surface Lattice Resonances in the Weak and Strong Coupling Regimes. *Phys. Rev. Lett.* **112**, 153002 (2014).
56. Santhosh, K., Bitton, O., Chuntonov, L. & Haran, G. Vacuum Rabi splitting in a plasmonic cavity at the single quantum emitter limit. *Nat. Commun.* **7**, (2016).

57. Waks, E. *et al.* Quantum cryptography with a single photon source. in *Quantum Communications and Quantum Imaging* vol. 5161 76–86 (International Society for Optics and Photonics, 2004).
58. Stevenson, R. M. *et al.* Quantum dots as a photon source for passive quantum key encoding. *Phys. Rev. B* **66**, 081302 (2002).
59. Takemoto, K. *et al.* Quantum key distribution over 120 km using ultrahigh purity single-photon source and superconducting single-photon detectors. *Sci. Rep.* **5**, 14383 (2015).
60. O'brien, J. L. Optical quantum computing. *Science* **318**, 1567–1570 (2007).
61. Varnava, M., Browne, D. E. & Rudolph, T. How good must single photon sources and detectors be for efficient linear optical quantum computation? *Phys. Rev. Lett.* **100**, 060502 (2008).
62. Lian, H. *et al.* Efficient Single Photon Emission and Collection Based on Excitation of Gap Surface Plasmons. *Phys. Rev. Lett.* **114**, 193002 (2015).
63. Esteban, R., Teperik, T. V. & Greffet, J. J. Optical Patch Antennas for Single Photon Emission Using Surface Plasmon Resonances. *Phys. Rev. Lett.* **104**, 026802 (2010).
64. Bulu, I., Babinec, T., Hausmann, B., Choy, J. T. & Loncar, M. Plasmonic resonators for enhanced diamond NV-center single photon sources. *Opt. Express* **19**, 5268–5276 (2011).
65. Almog, I. F., Bradley, M. S. & Bulovic, V. The Lorentz oscillator and its applications. *Mass. Inst. Technol.* (2011).
66. Tip, A. Linear dispersive dielectrics as limits of Drude-Lorentz systems. *Phys. Rev. E* **69**, 016610 (2004).
67. Hazra, B. *et al.* Hollow Gold Nanoprism as Highly Efficient "Single" Nanotransducer for Surface-Enhanced Raman Scattering Applications. *J. Phys. Chem. C* **120**, 25548–25556 (2016).
35. Attia, Y. A., Buceta, D., Requejo, F. G., Giovanetti, L. J. & López-Quintela, M. A. Photostability of gold nanoparticles with different shapes: the role of Ag clusters. *Nanoscale* (2015).
69. Willets, K. A. & Van Duyne, R. P. Localized Surface Plasmon Resonance Spectroscopy and Sensing. *Annu. Rev. Phys. Chem.* **58**, 267–297 (2007).
70. Kreibig, U. & Vollmer, M. *Optical Properties of Metal Clusters*. (Springer Science & Business Media, 2013).
71. Miller, M. M. & Lazarides, A. A. Sensitivity of Metal Nanoparticle Surface Plasmon Resonance to the Dielectric Environment. *J. Phys. Chem. B* **109**, 21556–21565 (2005).
72. Sekhon, J. S. & Verma, S. S. Refractive index sensitivity analysis of Ag, Au, and Cu nanoparticles. *Plasmonics* **6**, 311–317 (2011).

73. Hergert, W. & Wriedt, T. *The Mie Theory: Basics and Applications*. (Springer, 2012).

74. Maier, S. A. *Plasmonics: Fundamentals and Applications.* (Springer Science & Business Media, 2007).

75. Kravets, V. G., Kabashin, A. V., Barnes, W. L. & Grigorenko, A. N. Plasmonic Surface Lattice Resonances: A Review of Properties and Applications. *Chem. Rev.* **118**, 5912–5951 (2018).

76. Colas des Francs, G., Derom, S., Vincent, R., Bouhelier, A. & Dereux, A. Mie Plasmons: Modes Volumes, Quality Factors, and Coupling Strengths (Purcell Factor) to a Dipolar Emitter. *Int. J. Opt.* **2012**, 1–8 (2012).

77. Lermé, J. *et al.* Size Dependence of the Surface Plasmon Resonance Damping in Metal Nanospheres. *J. Phys. Chem. Lett.* **1**, 2922–2928 (2010).

78. Hou, B. *et al.* Microsphere Assisted Super-resolution Optical Imaging of Plasmonic Interaction between Gold Nanoparticles. *Sci. Rep.* **7**, 13789 (2017).

79. Zohar, N., Chuntonov, L. & Haran, G. The simplest plasmonic molecules: Metal nanoparticle dimers and trimers. *J. Photochem. Photobiol. C Photochem. Rev.* **21**, 26–39 (2014).

80. Akimov, A. V. *et al.* Generation of single optical plasmons in metallic nanowires coupled to quantum dots. *Nature* **450**, 402–406 (2007).

81. Bardhan, R., Grady, N. K., Cole, J. R., Joshi, A. & Halas, N. J. Fluorescence Enhancement by Au Nanostructures: Nanoshells and Nanorods. *ACS Nano* **3**, 744–752 (2009).

82. Ming, T. *et al.* Experimental Evidence of Plasmophores: Plasmon-Directed Polarized Emission from Gold Nanorod–Fluorophore Hybrid Nanostructures. *Nano Lett.* **11**, 2296–2303 (2011).

83. Cohen-Hoshen, E., Bryant, G. W., Pinkas, I., Sperling, J. & Bar-Joseph, I. Exciton–Plasmon Interactions in Quantum Dot–Gold Nanoparticle Structures. *Nano Lett.* **12**, 4260–4264 (2012).

84. Chen, H. *et al.* Plasmon–molecule interactions. *Nano Today* **5**, 494–505 (2010).

85. Leng, H., Szychowski, B., Daniel, M.-C. & Pelton, M. Strong coupling and induced transparency at room temperature with single quantum dots and gap plasmons. *Nat. Commun.* **9**, (2018).

86. Stockman, M. I. The spaser as a nanoscale quantum generator and ultrafast amplifier. *J. Opt.* **12**, 024004 (2010).

87. Stockman, M. I. Spasers explained. *Nat. Photonics* **2**, 327–329 (2008).

74. Norris, D. Colloidal Quantum-Dot Spasers and Plasmonic Amplifiers. in *Advanced Photonics 2017 (IPR, NOMA, Sensors, Networks, SPPCom, PS)* NoM2C.2 (OSA, 2017).

89. Gu, Y., Huang, L., Martin, O. J. & Gong, Q. Resonance fluorescence of single molecules assisted by a plasmonic structure. *Phys. Rev. B* **81**, 193103 (2010).
90. Hugall, J. T., Singh, A. & van Hulst, N. F. Plasmonic Cavity Coupling. *ACS Photonics* **5**, 43–53 (2018).
91. Pelton, M., Storm, S. D. & Leng, H. Strong coupling of emitters to single plasmonic nanoparticles: exciton-induced transparency and Rabi splitting. *Nanoscale* **11**, 14540–14552 (2019).
92. Valeur, B. & Berberan-Santos, M. N. *Molecular Fluorescence: Principles and Applications*. (John Wiley & Sons, 2012).
93. Fort, E. & Grésillon, S. Surface enhanced fluorescence. *J. Phys. Appl. Phys.* **41**, 013001 (2008).
94. *Nuclear Physics*.
95. Chizhik, A. I., Chizhik, A. M., Khoptyar, D., Bär, S. & Meixner, A. J. Excitation isotropy of single CdSe/ZnS nanocrystals. *Nano Lett.* **11**, 1131–1135 (2011).
96. Dong, L. *et al.* Fluorescence quenching and photobleaching in Au/Rh6G nanoassemblies: impact of competition between radiative and non-radiative decay. *J. Eur. Opt. Soc. - Rapid Publ.* **6**, (2011).
97. Shubina, T. V. *et al.* Plasmon-induced Purcell effect in InN/In metal-semiconductor nanocomposites. *Phys. Rev. B* **82**, 073304 (2010).
98. Kühn, S., Håkanson, U., Rogobete, L. & Sandoghdar, V. Enhancement of Single-Molecule Fluorescence Using a Gold Nanoparticle as an Optical Nanoantenna. *Phys. Rev. Lett.* **97**, 017402 (2006).
99. Carminati, R. *et al.* Electromagnetic density of states in complex plasmonic systems. *Surf. Sci. Rep.* **70**, 1–41 (2015).
100. Francs, G. C. des *et al.* Plasmonic Purcell factor and coupling efficiency to surface plasmons. Implications for addressing and controlling optical nanosources. *J. Opt.* **18**, 094005 (2016).
101. Koenderink, A. F. On the use of Purcell factors for plasmon antennas. *Opt. Lett.* **35**, 4208–4210 (2010).
102. Ringler, M. *et al.* Shaping emission spectra of fluorescent molecules with single plasmonic nanoresonators. *Phys. Rev. Lett.* **100**, 203002 (2008).
103. Aouani, H. *et al.* Plasmonic antennas for directional sorting of fluorescence emission. *Nano Lett.* **11**, 2400–2406 (2011).
104. Novotny, L. & Van Hulst, N. Antennas for light. *Nat. Photonics* **5**, 83–90 (2011).

105. Jaynes, E. T. & Cummings, F. W. Comparison of quantum and semiclassical radiation theories with application to the beam maser. *Proc. IEEE* **51**, 89–109 (1963).

106. Wurtz, G. A. *et al*. Molecular Plasmonics with Tunable Exciton- Plasmon Coupling Strength in J-Aggregate Hybridized Au Nanorod Assemblies. *Nano Lett.* **7**, 1297–1303 (2007).

107. Song, T. *et al.* Compounding Plasmon–Exciton Strong Coupling System with Gold Nanofilm to Boost Rabi Splitting. *Nanomaterials* **9**, 564 (2019).

108. Zengin, G. *et al.* Approaching the strong coupling limit in single plasmonic nanorods interacting with J-aggregates. *Sci. Rep.* **3**, 1–8 (2013).

109. Chen, X. *et al.* Mode Modification of Plasmonic Gap Resonances Induced by Strong Coupling with Molecular Excitons. *Nano Lett.* **17**, 3246–3251 (2017).

110. Gupta, S. N. *et al.* Plasmon-exciton polaritonics shed light on quantum dot dark-state dynamics. *ArXiv Prepr. ArXiv190910231* (2019).

111. Bitton, O. *et al.* Vacuum Rabi splitting of a dark plasmonic cavity mode revealed by fast electrons. *Nat. Commun.* **11**, 1–7 (2020).

112. Vasa, P. & Lienau, C. Strong Light–Matter Interaction in Quantum Emitter/Metal Hybrid Nanostructures. in (2017). doi:10.1021/acsphotonics.7b00650.

113. Zwiller, V. *et al.* Single quantum dots emit single photons at a time: Antibunching experiments. *Appl. Phys. Lett.* **78**, 2476–2478 (2001).

114. Strauf, S. *et al.* High-frequency single-photon source with polarization control. *Nat. Photonics* **1**, 704 (2007).

115. Beveratos, A. *et al*. Room temperature stable single-photon source. *Eur. Phys. J. -At. Mol. Opt. Plasma Phys.* **18**, 191–196 (2002).

116. Kurtsiefer, C., Mayer, S., Zarda, P. & Weinfurter, H. Stable solid-state source of single photons. *Phys. Rev. Lett.* **85**, 290 (2000).

117. Rezus, Y. L. A. *et al.* Single-photon spectroscopy of a single molecule. *Phys. Rev. Lett.* **108**, 093601 (2012).

118. Steiner, M., Hartschuh, A., Korlacki, R. & Meixner, A. J. Highly efficient, tunable single photon source based on single molecules. *Appl. Phys. Lett.* **90**, 183122 (2007).

119. Ropp, C. *et al.* Nanoscale probing of image-dipole interactions in a metallic nanostructure. *Nat. Commun.* **6**, 6558 (2015).

120. Boutelle, R. C., Neuhauser, D. & Weiss, S. Far-field super-resolution detection of plasmonic near-fields. *ACS Nano* **10**, 7955–7962 (2016).

121. Dadosh, T. *et al.* Plasmonic Control of the Shape of the Raman Spectrum of a Single Molecule in a Silver Nanoparticle Dimer. *ACS Nano* **3**, 1988–1994 (2009).

122. Savasta, S. *et al.* Nanopolaritons: Vacuum Rabi Splitting with a Single Quantum Dot in the Center of a Dimer Nanoantenna. *ACS Nano* **4**, 6369–6376 (2010).

123. Kongsuwan, N. *et al.* Suppressed quenching and strong-coupling of purcell-enhanced single-molecule emission in plasmonic nanocavities. *Acs Photonics* **5**, 186–191 (2018).

124. Liu, R. *et al.* Strong light-matter interactions in single open plasmonic nanocavities at the quantum optics limit. *Phys. Rev. Lett.* **118**, 237401 (2017).

125. Resch-Genger, U., Grabolle, M., Cavaliere-Jaricot, S., Nitschke, R. & Nann, T. Quantum dots versus organic dyes as fluorescent labels. *Nat. Methods* **5**, 763 (2008).

126. Bitton, O., Gupta, S. N. & Haran, G. Quantum dot plasmonics: from weak to strong coupling. *Nanophotonics* **0**, (2019).

127. Jun, Y. C., Pala, R. & Brongersma, M. L. Strong Modification of Quantum Dot Spontaneous Emission via Gap Plasmon Coupling in Metal Nanoslits. *J. Phys. Chem. C* **114**, 7269–7273 (2010).

128. Fons, R. *et al.* All-Optical Mapping of the Position of Quantum Dots Embedded in a Nanowire Antenna. *Nano Lett.* **18**, 6434–6440 (2018).

129. Meixner, A. J. *et al.* Coupling single quantum dots to plasmonic nanocones: optical properties. *Faraday Discuss.* **184**, 321–337 (2015).

130. Yuan, C. T., Yu, P. & Tang, J. Blinking suppression of colloidal CdSe/ZnS quantum dots by coupling to silver nanoprisms. *Appl. Phys. Lett.* **94**, 243108 (2009).

131. Park, K.-D. *et al.* Tip-enhanced strong coupling spectroscopy, imaging, and control of a single quantum emitter. *Sci. Adv.* **5**, eaav5931 (2019).

132. Hoang, T. B., Akselrod, G. M. & Mikkelsen, M. H. Ultrafast room-temperature single photon emission from quantum dots coupled to plasmonic nanocavities. *Nano Lett.* **16**, 270–275 (2016).

133. Hoang, T. B. *et al.* Ultrafast spontaneous emission source using plasmonic nanoantennas. *Nat. Commun.* **6**, 7788 (2015).

134. Song, J.-H., Atay, T., Shi, S., Urabe, H. & Nurmikko, A. V. Large Enhancement of Fluorescence Efficiency from CdSe/ZnS Quantum Dots Induced by Resonant Coupling to Spatially Controlled Surface Plasmons. *Nano Lett.* **5**, 1557–1561 (2005).

135. Deeb, C. *et al.* Off-Resonant Optical Excitation of Gold Nanorods: Nanoscale Imprint of Polarization Surface Charge Distribution. *J. Phys. Chem. Lett.* **2**, 7–11 (2011).

136. Deeb, C. *et al.* Size dependence of the plasmonic near-field measured via single-nanoparticle photoimaging. *J. Phys. Chem. C* **117**, 10669–10676 (2013).

137. El Ahrach, H. I. *et al.* Spectral degeneracy breaking of the plasmon resonance of single metal nanoparticles by nanoscale near-field photopolymerization. *Phys. Rev. Lett.* **98**, 107402 (2007).

138. Zhou, X. *et al.* Selective functionalization of the nanogap of a plasmonic dimer. *ACS Photonics* **2**, 121–129 (2014).

139. Grzelczak, M., Pérez-Juste, J., Mulvaney, P. & Liz-Marzán, L. M. Shape control in gold nanoparticle synthesis. *Chem. Soc. Rev.* **37**, 1783–1791 (2008).

140. González-Rubio, G., Scarabelli, L., Guerrero-Martínez, A. & Liz-Marzán, L. M. Surfactant-Assisted Symmetry Breaking in Colloidal Gold Nanocrystal Growth. *ChemNanoMat* **6**, 698–707 (2020).

141. Ge, D. *et al.* Hybrid plasmonic nano-emitters with controlled single quantum emitter positioning on the local excitation field. *Nat. Commun.* **11**, 3414 (2020).

142. McCarthy, S. A., Ratkic, R., Purcell-Milton, F., Perova, T. S. & Gun'ko, Y. K. Adaptable surfactant-mediated method for the preparation of anisotropic metal chalcogenide nanomaterials. *Sci. Rep.* **8**, 2860 (2018).

143. Bakshi, M. S. How Surfactants Control Crystal Growth of Nanomaterials. *Cryst. Growth Des.* **16**, 1104–1133 (2016).

144. Mitiche, S., Marguet, S., Charra, F. & Douillard, L. Near-Field Localization of Single Au Cubes, a Group Theory Description. *J. Phys. Chem. C* (2017).

145. Chateau, D. *et al.* From gold nanobipyramids to nanojavelins for a precise tuning of the plasmon resonance to the infrared wavelengths: experimental and theoretical aspects. *Nanoscale* **7**, 1934–1943 (2015).

146. Kirschner, M. S. *et al.* Size-Dependent Coherent-Phonon Plasmon Modulation and Deformation Characterization in Gold Bipyramids and Nanojavelins. *ACS Photonics* **3**, 758–763 (2016).

147. Pittenger, B., Erina, N. & Su, C. Quantitative mechanical property mapping at the nanoscale with PeakForce QNM. *Appl. Note Veeco Instrum. Inc* **1**, (2010).

148.Wuhrer, R. & Moran, K. Low voltage imaging and X-ray microanalysis in the SEM: challenges and opportunities. in *IOP Conf. Ser. Mater. Sci. Eng* vol. 109 012019 (2016).

149.Kane Yee. Numerical solution of initial boundary value problems involving maxwell's equations in isotropic media. *IEEE Trans. Antennas Propag.* **14**, 302–307 (1966).

150.Southorn, P. A. & Powis, G. Free radicals in medicine. I. Chemical nature and biologic reactions. in *Mayo Clinic Proceedings* vol. 63 381–389 (Elsevier, 1988).

152.Zhou, X., Hou, Y. & Lin, J. A review on the processing accuracy of two-photon polymerization. *AIP Adv.* **5**, 030701 (2015).

153.Juodkazis, S., Mizeikis, V., Seet, K. K., Miwa, M. & Misawa, H. Two-photon lithography of nanorods in SU-8 photoresist. *Nanotechnology* **16**, 846 (2005).

154.Quan, H. *et al.* Photo-curing 3D printing technique and its challenges. *Bioact. Mater.* **5**, 110–115 (2020).

155.Taking Commercial 3DP into the Nano Dimension. *3D Printing Industry* https://3dprintingindustry.com/news/nanoscribe-taking-commercial-3d-printing-nano-dimension-24848/ (2014).

156.Li, J. J. *et al.* Large-Scale Synthesis of Nearly Monodisperse CdSe/CdS Core/Shell Nanocrystals Using Air-Stable Reagents via Successive Ion Layer Adsorption and Reaction. *J. Am. Chem. Soc.* **125**, 12567–12575 (2003).

157.Peng, Y. *et al.* 3D Photoluminescent Nanostructures Containing Quantum Dots Fabricated by Two-Photon Polymerization: Influence of Quantum Dots on the Spatial Resolution of Laser Writing. *Adv. Mater. Technol.* **4**, 1800522 (2019).

158.Brown, R. H. & Twiss, R. Q. Correlation between Photons in two Coherent Beams of Light. *Nature* **177**, 27–29 (1956).

159.Senellart, P., Solomon, G. & White, A. High-performance semiconductor quantum-dot single-photon sources. *Nat. Nanotechnol.* **12**, 1026 (2017).

160.Grünwald, P. Effective second-order correlation function and single-photon detection. *New J. Phys.* **21**, 093003 (2019).

161.Becker, W. *Advanced time-correlated single photon counting techniques.* vol. 81 (Springer Science & Business Media, 2005).

162.Sharma, V. *et al.* A dual-modality optical biopsy approach for in vivo detection of prostate cancer in rat model. *J. Innov. Opt. Health Sci.* **4**, 269–277 (2011).

163. Trinel, D., Leray, A., Spriet, C., Usson, Y. & Héliot, L. Upgrading time domain FLIM using an adaptive Monte Carlo data inflation algorithm. *Cytometry A* **79A**, 528–537 (2011).

90. McGinty, J. *et al.* Fluorescence Lifetime Imaging: Microscopy, Endoscopy, and Tomography. *Handbook of Biomedical Optics* 609–636 https://www.taylorfrancis.com/ (2016).

165. Ntziachristos, V., Ma, X., Yodh, A. G. & Chance, B. Multichannel photon counting instrument for spatially resolved near infrared spectroscopy. *Rev. Sci. Instrum.* **70**, 193–201 (1999).

166. Deeb, C. *et al.* Quantitative Analysis of Localized Surface Plasmons Based on Molecular Probing. *ACS Nano* **4**, 4579–4586 (2010).

167. Ding, T., Mertens, J., Lombardi, A., Scherman, O. A. & Baumberg, J. J. Light-Directed Tuning of Plasmon Resonances via Plasmon-Induced Polymerization Using Hot Electrons. *ACS Photonics* (2017) doi:10.1021/acsphotonics.7b00206.

168. Tijunelyte, I. *et al.* Multi-functionalization of lithographically designed gold nanodisks by plasmon-mediated reduction of aryl diazonium salts. *Nanoscale Horiz.* **3**, 53–57 (2018).

169. Wang, Y. *et al.* Plasmon-directed polymerization: Regulating polymer growth with light. *Nano Res.* **11**, 6384–6390 (2018).

170. Johnson, P. B. & Christy, R.-Wjp. Optical constants of the noble metals. *Phys. Rev. B* **6**, 4370 (1972).

171. Zhang, S., Bao, K., Halas, N. J., Xu, H. & Nordlander, P. Substrate-Induced Fano Resonances of a Plasmonic Nanocube: A Route to Increased-Sensitivity Localized Surface Plasmon Resonance Sensors Revealed. *Nano Lett.* **11**, 1657–1663 (2011).

99. Cherqui, C. *et al.* Multipolar Nanocube Plasmon Mode-Mixing in Finite Substrates (2018).

173. Zayats, A. V. & Richards, D. *Nano-optics and Near-field Optical Microscopy*. (Artech House, 2009).

174. Tiecke, T. G. *et al.* Nanophotonic quantum phase switch with a single atom. *Nature* **508**, 241–244 (2014).

175. Kimble, H. J. The quantum internet. *Nature* **453**, 1023–1030 (2008).

176. Shomroni, I. *et al.* All-optical routing of single photons by a one-atom switch controlled by a single photon. *Science* **345**, 903–906 (2014).

177. Efros, A. L. & Rosen, M. Random telegraph signal in the photoluminescence intensity of a single quantum dot. *Phys. Rev. Lett.* **78**, 1110 (1997).

178.Medintz, I. L., Uyeda, H. T., Goldman, E. R. & Mattoussi, H. Quantum dot bioconjugates for imaging, labelling and sensing. *Nat. Mater.* **4**, 435–446 (2005).

179.Wu, X. *et al.* High-Photoluminescence-Yield Gold Nanocubes: For Cell Imaging and Photothermal Therapy. *ACS Nano* **4**, 113–120 (2010).

180.Young Lee, S., Han, Y., Wook Hong, J. & Won Ha, J. Single gold bipyramids with sharp tips as sensitive single particle orientation sensors in biological studies. *Nanoscale* **9**, 12060–12067 (2017).

181.Zhang, T. *et al.* Single Bipyramid Plasmonic Antenna Orientation Determined by Direct Photoluminescence Pattern Imaging. *Adv. Opt. Mater.* **1**, 335–342 (2013).

182.Ha, J. W., Sun, W., Wang, G. & Fang, N. Differential interference contrast polarization anisotropy for tracking rotational dynamics of gold nanorods. *Chem. Commun.* **47**, 7743–7745 (2011).

183.Ha, J. W., Marchuk, K. & Fang, N. Focused orientation and position imaging (FOPI) of single anisotropic plasmonic nanoparticles by total internal reflection scattering microscopy. *Nano Lett.* **12**, 4282–4288 (2012).

184.Piwonski, H. *et al.* Polarized spectroscopy studies of single molecules of porphycenes: tautomerism and orientation. *J. Phys. Chem. C* **113**, 11514–11519 (2009).

185.Failla, A. V., Qian, H., Qian, H., Hartschuh, A. & Meixner, A. J. Orientational Imaging of Subwavelength Au Particles with Higher Order Laser Modes. *Nano Lett.* **6**, 1374–1378 (2006).

186.Li, X., Lan, T.-H., Tien, C.-H. & Gu, M. Three-dimensional orientation-unlimited polarization encryption by a single optically configured vectorial beam. *Nat. Commun.* **3**, 1–6 (2012).

187.Richards, B. & Wolf, E. Electromagnetic diffraction in optical systems, II. Structure of the image field in an aplanatic system. *Proc. R. Soc. Lond. Ser. Math. Phys. Sci.* **253**, 358–379 (1959).

188.Man, Z. *et al.* Optical cage generated by azimuthal-and radial-variant vector beams. *Appl. Opt.* **57**, 3592–3597 (2018).

189.Chizhik, A. M. *et al.* Optical imaging of excited-state tautomerization in single molecules. *Phys. Chem. Chem. Phys.* **13**, 1722–1733 (2011).

190.Bouhelier, A. *et al.* Surface plasmon characteristics of tunable photoluminescence in single gold nanorods. *Phys. Rev. Lett.* **95**, 267405 (2005).

191.Wackenhut, F., Failla, A. V. & Meixner, A. J. Multicolor Microscopy and Spectroscopy Reveals the Physics of the One-Photon Luminescence in Gold Nanorods. *J. Phys. Chem. C* **117**, 17870–17877 (2013).

192.Novotny, L. & Hecht, B. *Principles of nano-optics.* (Cambridge university press, 2012).

193.Lin, K.-Q. *et al.* Plasmonic photoluminescence for recovering native chemical information from surface-enhanced Raman scattering. *Nat. Commun.* **8**, (2017).

194.Hu, H., Duan, H., Yang, J. K. & Shen, Z. X. Plasmon-modulated photoluminescence of individual gold nanostructures. *Acs Nano* **6**, 10147–10155 (2012).

195.Novo, C., Funston, A. M. & Mulvaney, P. Direct observation of chemical reactions on single gold nanocrystals using surface plasmon spectroscopy. *Nat. Nanotechnol.* **3**, 598–602 (2008).

196.Tcherniak, A. *et al.* One-photon plasmon luminescence and its application to correlation spectroscopy as a probe for rotational and translational dynamics of gold nanorods. *J. Phys. Chem. C* **115**, 15938–15949 (2011).

197.Fröhlich, T., Schönenberger, C. & Calame, M. Additional peak appearing in the one-photon luminescence of single gold nanorods. *Opt. Lett.* **41**, 1325–1328 (2016).

198.Cai, Y.-Y. *et al.* Photoluminescence of Gold Nanorods: Purcell Effect Enhanced Emission from Hot Carriers. *ACS Nano* **12**, 976–985 (2018).

199.Fang, Y. *et al.* Plasmon Emission Quantum Yield of Single Gold Nanorods as a Function of Aspect Ratio. *ACS Nano* **6**, 7177–7184 (2012).

200.Empedocles, S. A., Neuhauser, R. & Bawendi, M. G. Three-dimensional orientation measurements of symmetric single chromophores using polarization microscopy. *Nature* **399**, 126–130 (1999).

201.Yu, H., Peng, Y., Yang, Y. & Li, Z.-Y. Plasmon-enhanced light–matter interactions and applications. *Npj Comput. Mater.* **5**, 1–14 (2019).

202.Szychowski, B., Pelton, M. & Daniel, M.-C. Preparation and properties of plasmonic-excitonic nanoparticle assemblies. *Nanophotonics* **8**, 517–547 (2019).

203.Xu, X. *et al.* Towards the integration of nanoemitters by direct laser writing on optical glass waveguides. *Photonics Res.* **8**, 1541–1550 (2020).

Dandan GE

Doctorat : Matériaux, Mécanique, Optique, Nanotechnologie

Année 2021

Nano-émetteurs plasmoniques hybrides anisotropes avancés

Bien que les nanosystèmes plasmoniques hybrides basés sur l'interaction entre les émetteurs quantiques et les nanostructures métalliques aient suscité beaucoup d'attention en raison de la possibilité de développer des nanosources contrôlables, le contrôle de la position relative des nano-émetteurs et des nanostructures métalliques reste difficile. Cette thèse vise à développer des nano-émetteurs plasmoniques hybrides anisotropes via une polymérisation à deux photons en champ proche qui est déclenchée par une amélioration localisée du champ à partir de plasmon de surface supportés par des nanoparticules métalliques. En piégeant les nano-émetteurs (QD) à l'intérieur du polymère ou à sa surface, la distribution du nano-émetteur peut être contrôlée en conséquence en contrôlant la distribution spatiale du polymère au voisinage des nanostructures métalliques. En diminuant le nombre de QD à l'intérieur des lobes de polymère, on obtient un nano-émetteur hybride à base de cube avec un seul QD contenu.

Mots clés : optique en champ proche – plasmons – métallique nanostructures – photopolymérisation – fluorescence.

Advanced Anisotropic Hybrid Plasmonic Nano-emitters

Although the hybrid plasmonic nanosystems based on the interaction between quantum emitters and metallic nanostructures have been receiving much attention because of the possibility for developing controllable nanosources, controlling the relative position of nano-emitters and metal nanostructures remains challenging. This thesis has aimed at developing anisotropic hybrid plasmonic nano-emitters via near-field two-photon polymerization that is triggered by localized field enhancement from surface plasmon supported by metal nanoparticles. By trapping the nano-emitters (QDs) inside the polymer or at its surface, the distribution of the nano-emitter can be controlled accordingly by controlling the spatial distribution of the polymer in the vicinity of the metal nanostructures. By decreasing the number of QDs inside polymer lobes, a hybrid cube-based nano-emitters with only a single QD contained is achieved.

Keywords: near-field – plasmons (physics) – metallic nanostructures – photopolymerization – fluorescence.

Thèse réalisée en partenariat entre :

China Scholarship Council

utt
UNIVERSITÉ DE TECHNOLOGIE
TROYES

Ecole Doctorale "Sciences pour l'Ingénieur"